National Library
of Canada

Acquisitions and
Bibliographic Services Branch

395 Wellington Street
Ottawa, Ontario
K1A 0N4

Bibliothèque nationale
du Canada

Direction des acquisitions et
des services bibliographiques

395, rue Wellington
Ottawa (Ontario)
K1A 0N4

Your file Votre référence

Our file Notre référence

NOTICE

The quality of this microform is heavily dependent upon the quality of the original thesis submitted for microfilming. Every effort has been made to ensure the highest quality of reproduction possible.

If pages are missing, contact the university which granted the degree.

Some pages may have indistinct print especially if the original pages were typed with a poor typewriter ribbon or if the university sent us an inferior photocopy.

Reproduction in full or in part of this microform is governed by the Canadian Copyright Act, R.S.C. 1970, c. C-30, and subsequent amendments.

AVIS

La qualité de cette microforme dépend grandement de la qualité de la thèse soumise au microfilmage. Nous avons tout fait pour assurer une qualité supérieure de reproduction.

S'il manque des pages, veuillez communiquer avec l'université qui a conféré le grade.

La qualité d'impression de certaines pages peut laisser à désirer, surtout si les pages originales ont été dactylographiées à l'aide d'un ruban usé ou si l'université nous a fait parvenir une photocopie de qualité inférieure.

La reproduction, même partielle, de cette microforme est soumise à la Loi canadienne sur le droit d'auteur, SRC 1970, c. C-30, et ses amendements subséquents.

Canada

UNIVERSITY OF ALBERTA

MICROSTRUCTURE OF CLAY SEDIMENTS OR GELS

BY ©
KUNSONG MA

A THESIS SUBMITTED TO THE FACULTY OF GRADUATE STUDIES AND RESEARCH IN PARTIAL FULFILLMENT OF THE REQUIREMENTS FOR THE DEGREE OF DOCTOR OF PHILOSOPHY

IN
METALLURGICAL ENGINEERING

DEPARTMENT OF MINING, METALLURGICAL AND PETROLEUM ENGINEERING

EDMONTON, ALBERTA
FALL, 1995

National Library of Canada
Acquisitions and Bibliographic Services Branch
395 Wellington Street
Ottawa, Ontario
K1A 0N4

Bibliothèque nationale du Canada
Direction des acquisitions et des services bibliographiques
395, rue Wellington
Ottawa (Ontario)
K1A 0N4

Your file Votre référence

Our file Notre référence

THE AUTHOR HAS GRANTED AN IRREVOCABLE NON-EXCLUSIVE LICENCE ALLOWING THE NATIONAL LIBRARY OF CANADA TO REPRODUCE, LOAN, DISTRIBUTE OR SELL COPIES OF HIS/HER THESIS BY ANY MEANS AND IN ANY FORM OR FORMAT, MAKING THIS THESIS AVAILABLE TO INTERESTED PERSONS.

L'AUTEUR A ACCORDE UNE LICENCE IRREVOCABLE ET NON EXCLUSIVE PERMETTANT A LA BIBLIOTHEQUE NATIONALE DU CANADA DE REPRODUIRE, PRETER, DISTRIBUER OU VENDRE DES COPIES DE SA THESE DE QUELQUE MANIERE ET SOUS QUELQUE FORME QUE CE SOIT POUR METTRE DES EXEMPLAIRES DE CETTE THESE A LA DISPOSITION DES PERSONNE INTERESSEES.

THE AUTHOR RETAINS OWNERSHIP OF THE COPYRIGHT IN HIS/HER THESIS. NEITHER THE THESIS NOR SUBSTANTIAL EXTRACTS FROM IT MAY BE PRINTED OR OTHERWISE REPRODUCED WITHOUT HIS/HER PERMISSION.

L'AUTEUR CONSERVE LA PROPRIETE DU DROIT D'AUTEUR QUI PROTEGE SA THESE. NI LA THESE NI DES EXTRAITS SUBSTANTIELS DE CELLE-CI NE DOIVENT ETRE IMPRIMES OU AUTREMENT REPRODUITS SANS SON AUTORISATION.

ISBN 0-612-06251-1

Canada

UNIVERSITY OF ALBERTA

RELEASE FORM

NAME OF AUTHOR: KUNSONG MA

TITLE OF THESIS: **MICROSTRUCTURE OF CLAY SEDIMENTS OR GELS**

DEGREE: DOCTOR OF PHILOSOPHY

YEAR THIS DEGREE GRANTED: 1995

PERMISSION IS HEREBY GRANTED TO THE UNIVERSITY OF ALBERTA LIBRARY TO REPRODUCE SINGLE COPIES OF THIS THESIS AND TO LEND OR SELL SUCH COPIES FOR PRIVATE, SCHOLARLY OR SCIENTIFIC RESEARCH PURPOSES ONLY.

THE AUTHOR RESERVES ALL OTHER PUBLICATION AND OTHER RIGHTS IN ASSOCIATION WITH THE COPYRIGHT IN THE THESIS, AND EXCEPT AS HEREINBEFORE PROVIDED NEITHER THE THESIS NOR ANY SUBSTANTIAL PORTION THEREOF MAY BE PRINTED OR OTHERWISE REPRODUCED IN ANY MATERIAL FORM WHATEVER WITHOUT THE AUTHOR'S PRIOR WRITTEN PERMISSION.

SIGNATURE: ____________
KUNSONG MA

ADDRESS:

606# CHEMICAL/MINERAL
ENGINEERING BUILDING
116 STREET - 92 AVENUE
EDMONTON, ALBERTA T6G 2G6

DATE: July 17, 1995

UNIVERSITY OF ALBERTA

FACULTY OF GRADUATE STUDIES AND RESEARCH

THE UNDERSIGNED CERTIFY THAT THEY HAVE READ, AND RECOMMEND TO THE FACULTY OF GRADUATE STUDIES AND RESEARCH FOR ACCEPTANCE, A THESIS ENTITLED, **MICROSTRUCTURE OF CLAY SEDIMENTS OR GELS,** SUBMITTED BY KUNSONG MA IN PARTIAL FULFILLMENT OF THE REQUIREMENTS FOR THE DEGREE OF DOCTOR OF PHILOSOPHY IN METALLURGICAL ENGINEERING.

DR. K. BARRON, COMMITTEE CHAIRMAN

DR. A.C. PIERRE, SUPERVISOR

DR. D.G. IVEY, COMMITTEE MEMBER

DR. T. ETSELL, COMMITTEE MEMBER

DR.J.H. MASLIYAH, COMMITTEE MEMBER

DR. L.L. SCHRAMM, COMMITTEE MEMBER

DATE: July 17, 1995

ABSTRACT

The sedimentation behavior of kaolinite and montmorillonite suspensions, comprising a substantial proportion of colloidal particles as well as non-colloidal ones, have been studied systemically with the addition of Fe and Al electrolytes. The microstructures of corresponding clay sediments were examined extensively in a scanning electron microscope (SEM) after a supercritical drying. Supplementary data such as zeta potentials, Bingham yield stress, and adsorbed Fe and Al on clay particles were also collected.

In kaolinite suspensions, treated with $Na_4P_2O_7$ to only have negative charges both on the faces and on the edges of particles, the sedimentation behavior could be classified into three types: (1) accumulation; (2) flocculation; and (3) mixed accumulation-flocculation.

The accumulated sediments were comprised, either of a random accumulation of individual kaolinite particles, or of an accumulation of dense aggregates mostly made by face to face (FF) association of the clay particles. The flocculated sediments were shown to be comprised of a network with a fractal aspect and a more frequent edge to edge (EE) association of the particles in the network. The mixed accumulated-flocculated sediments were comprised of one part with an accumulated structure and the other with a fractal flocculated structure.

The sedimentation behavior of montmorillonite suspensions mixed with Fe or Al electrolytes, or with hydroxoferric particles, could also be classified into accumulation sedimentation or flocculation sedimentation. The flocculated sediments also had a fractal type network.

In the cases where the kaolinite particles had opposite charges on the edges and on the faces, a bookhouse structure could be observed. This structure was comprised of

domains where the kaolinite particles were mostly associated in the FF mode, while the domains were themselves mostly associated by the EF or the EE mode.

The theoretical analysis shows that these results were at least in qualitative agreement with the DLVO theory. The Fe^{3+} or the Al^{3+} cations and their hydrolysis products, acted as counterions for the negatively charged clay particles. They compressed the electrical double layer of the clay and made it possible for flocculation to occur. However, at high Fe or Al electrolyte concentration, an Fe or an Al product is deposited on the clay particles. These coatings changed the sign of the clay particles from a negative one to a positive one. They also helped to link the clay particles to each other with the intermediate of an Fe or Al gel cement.

ACKNOWLEDGEMENTS

I am the most grateful to Professor Alain.C. Pierre for his supervision and guidance throughout this research and thesis writing, without which I could not finish this study and thesis.

My special appreciation is also given to Dr. R. Eadie for his help and encouragement and to Dr. D. Ivey for his suggestions and organization of the defence. I wish to acknowledge Dr. J. H. Masliyah for his advice and suggestions. Thanks are also extended to Dr. T. Barron, Dr. T. Etsell, and Dr. L. Schramm.

I would like to express my thanks to Ms. Tina Barker and Mr. Shiraz Merali for their help during the experiment.

I am deeply grateful to my wife Ding Yuan, and my parents and parents in law for all their support and encouragement during this study.

Special thanks to my friends Dr. Jianyun Wu and Dr. Shuisheng Wang for their help during my research.

TABLE OF CONTENT

Page

CHAPTER 1 - INTRODUCTION 1

1.1 - BACKGROUND OF THE PRESENT STUDY 1
1.2 - OBJECTIVE OF THE PRESENT STUDY 2

CHAPTER 2 - LITERATURE REVIEW 4

2.1 - BACKGROUND OF OIL SANDS TAILING SLUDGE 4
2.2 - THE COLLOIDS AND THEIR INTERACTIONS 6
  2.2.1 - Terminology 6
  2.2.1.1 - Colloid 6
  2.2.1.2 - Sol 6
  2.2.1.3 - Suspension 6
  2.2.1.4 - Floc 6
  2.2.1.5 - Stability 6
  2.2.1.6 - Flocculation 6
  2.2.1.7 - Gel 7
  2.2.1.8 - Gelation 7
  2.2.1.9 - Sedimentation 7
  2.2.1.10 - Sediment 7
  2.2.2 - The Electrostatic or Derjaguin, Landau, Verwey, and Overbeek (DLVO) Theory 7
  2.2.2.1 - Origins of the electric charge on colloidal particles 7
  2.2.2.2 - The Helmholtz model for an electric double layer 8
  2.2.2.3 - The Gouy-Chapman model 8

2.2.2.4 - The Stern model 13

2.2.2.5 - Zeta potential 15

2.2.2.6 - The electrostatic repulsion between two colloidal particles 16

2.2.2.7 - The van der Waals attraction 18

2.2.2.8 - Total interaction potential energy - Flocculation 20

2.2.2.9 - The Schulze-Hardy rule 20

2.2.2.10 - Steric effects 22

2.2.3 - Gels 22

2.2.3.1 - Gelation 22

2.2.3.2 - Fractal structures 25

2.2.4 - Sedimentation 27

2.2.4.1 - No Flocculation occurs during sedimentation 27

2.2.4.2 - Flocculation occurs at the beginning of sedimentation 29

2.2.5 - Rheological properties 33

2.2.5.1 - Types of flow 33

2.2.5.2 - Rheological properties of suspensions 35

2.3 COLLOIDAL PROPERTIES OF CLAYS 38

2.3.1 - Crystal structure and ion exchangeability of clays 38

2.3.2 - Electric double-layer structure of clay particles 41

2.3.2.1 - The double layer near the faces of clay particles 41

2.3.2.2 - The double layer near the edges of clay particles 42

2.3.2.3 - The zeta potential of clay particles 42

2.3.3 - Interactions between clay particles 44

2.3.3.1 - The edges and the faces have opposite electric charges 44

2.3.3.2 - The edges and the faces carry electric charges with the same sign 44

2.3.4 - Clay Sedimentation 47

2.3.5 - The rheology of clay suspensions 51

2.3.6 - The mixed clay -Fe systems 55

2.3.6.1 - The behavior of Fe^{3+} electrolytes in an aqueous medium 55

2.3.6.2 - Action of Fe additives on clay suspensions 57

2.3.7 - The mixed clay -Al Systems 60

2.3.7.1 - The behavior of Al^{3+} electrolytes in an aqueous medium 60

2.3.7.2 - Action of Al additives on clay suspensions 60

2.4 ARCHITECTURE OF CLAY SEDIMENTS 62

2.4.1- Proposed models for clay sediments 62

2.4.2 - Preparation of electron microscope samples, by drying 65

2.4.2.1 - Drying by evaporation 68

2.4.2.2 - Freeze-drying 69

2.4.2.3 - Supercritical-drying 70

2.4.3 - Electron Microscopy observations 72

CHAPTER 3 - DETAILED RESEARCH PLAN 81

3.1 - RESEARCH ORGANIZATION 81

3.2 - MATERIALS 83

3.2.1- Kaolinite 83

3.2.1.1 - Raw kaolinite 83

3.2.1.2 - Kaolinite with negatively charged faces and positively charged edges 84

3.2.1.3 - Kaolinite with negative charges on both the faces and the edges 84

3.2.2 - Montmorillonite 85

3.2.3 - Fe Additives 85

3.2.3.1 - Unaged Fe electrolyte solutions 85

3.2.3.2 - Aged Fe electrolyte solutions 87

3.2.3.3 - Hydroxoferric particles 87

3.2.4 - Al additives 90

3.2.4.1 - Unaged Al electrolytes 90

3.2.4.2 - Aged Al electrolyte 90

3.2.5 - SiO_2 additives 90

3.3 SEDIMENTATION PROCEDURE 95

3.3.1 - Kaolinite suspensions 95

3.3.1.1 - Kaolinite with negatively charged faces and positively charged edges 95

3.3.1.2 - Kaolinite with negative charges on both the faces and the edges 96

3.3.2 - Montmorillonite suspensions 97

3.3.3 Mixed kaolinite - colloidal SiO_2 samples 98

3.3.3.1 - Kaolinite with negatively charged faces and positively charged edges 98

3.3.3.2 - Kaolinite with negative charges on both the faces and the edges 99

3.3.4 - Supercritical Drying of Sediments 99

3.4 CHARACTERIZATION TECHNIQUES 101

3.4.1 - Rheological Properties 101

3.4.2 - Determination ot the zeta potential (ζ) 101

3.4.3 - Scanning Electron Microscope (SEM) Observations 103

3.4.4 - Transmission Electron Microscope (TEM) Observations 103

3.4.5 - Atomic Absorption Spectroscopy and Flame Photometry 105

3.4.6 - Phase Identification and X-Ray Diffractometer 106

CHAPTER 4 - SEDIMENTATION BEHAVIOR 107

4.1 - KAOLINITE WITH NEGATIVELY CHARGED FACES AND POSITIVELY CHARGED EDGES 107

4.2 - KAOLINITE WITH NEGATIVE CHARGES ON BOTH THE EDGES AND THE FACES 111

4.2.1 - Kaolinite suspensions with unaged Fe electrolytes 111

4.2.1.1 - Accumulation sedimentation with unaged $FeCl_3$ 111

4.2.1.2 - Flocculation sedimentation with unaged $FeCl_3$ 114

4.2.1.3 - Mixed accumulation-flocculation sedimentation with unaged $FeCl_3$ 115

4.2.1.4 - Diagram of the sedimentation behavior with unaged $FeCl_3$ 116

4.2.1.5 - Sedimentation behavior with unaged $Fe_2(SO_4)_3$ 116

4.2.1.6 - Compared influence of the cation and of the anion from the Fe electrolyte 116

4.2.2 - Kaolinite suspensions with aged Fe electrolytes 120

4.2.3 - Effect of the kaolinite particle size on the sedimentation behavior with unaged $FeCl_3$ 125

4.2.4 - Effect of the kaolinite proportion on the sedimentation behavior with unaged $FeCl_3$ 131

4.2.5 - Kaolinite suspensions with unaged Al electrolytes 135

4.2.6 - Kaolinite suspensions with aged $AlCl_3$ 139

4.3 - MONTMORILLONITE SUSPENSIONS 148

4.3.1 - Montmorillonite-unaged $FeCl_3$ suspensions 148

4.3.2 - Montmorillonite-aged $FeCl_3$ suspensions 148

4.3.3 - Montmorillonite - Hydroxoferric Particles 152

4.3.4 - Montmorillonite-unaged $AlCl_3$ suspensions 152

4.3.5 - **Montmorillonite-aged $AlCl_3$ Suspensions** 159

CHAPTER 5 - PHYSICAL CHEMISTRY CHARACTERIZATIONS 164

5.1 - DETERMINATION OF THE Al OR THE Fe ADSORBED ON THE CLAY PARTICLES BY ATOMIC ABSORPTION SPECTROPHOTOMETRY OR BY FLAME ANALYSIS 164

5.1.1 - **Kaolinite suspensions** 164

5.1.1.1 - Fe or Al in the supernatant liquid after sedimentation 164

5.1.1.2 - Fe or Al adsorbed on the kaolinite particles 166

5.1.2 - **Montmorillonite suspensions** 166

5.1.2.1 - Al and Na in the supernatant liquid after sedimentation 166

5.1.2.2 - Al adsorbed on the montmorillonite particles 169

5.2 - T.E.M. OBSERVATIONS OF THE Fe DEPOSITS ON THE CLAY PARTICLES 171

5.2.1 - **Deposits from unaged $FeCl_3$** 171

5.2.1.1 - Deposits on kaolinite particles 171

5.2.1.2 - Deposits on montmorillonite particles 171

5.2.2 - **Deposits from the hydroxoferric particles** 171

5.3 - RHEOLOGICAL PROPERTIES 184

5.3.1 - **Kaolinite particles with initial negative charges on their faces and positive charges on their edges, mixed with unaged $FeCl_3$** 184

5.3.2 - **Montmorillonite suspensions mixed with hydroxoferric Particles** 184

5.4 - DETERMINATION OF THE ZETA POTENTIAL (ζ) 189

5.4.1 - Kaolinite particles initially treated to have negative charges on the faces and positive charges on the edges. 189

5.4.2 - Kaolinite initially treated with $Na_4P_2O_7$ to only have negative charges 189

5.4.2.1- Kaolinite suspensions mixed with unaged $FeCl_3$ 189

5.4.2.2- Kaolinite suspensions mixed with aged $FeCl_3$ 193

5.4.2.3 - Kaolinite suspensions mixed with unaged $AlCl_3$ 193

5.4.3 - Montmorillonite 193

5.4.3.1 - Montmorillonite suspensions mixed with hydroxoferric particles 193

5.4.3.2 - Montmorillonite suspensions mixed with unaged $AlCl_3$ 195

5.5 - S.E.M OBSERVATIONS OF KAOLINITE PARTICLES MIXED WITH COLLOIDAL SiO_2 PARTICLES 198

5.5.1 - Kaolinite with negatively charged faces and positively charged edges 198

5.5.2 - Kaolinite with negative charges on both the edges and the faces 201

CHAPTER 6 - S.E.M. OBSERVATIONS OF SEDIMENTS DRIED BY THE SUPERCRITICAL METHOD 203

6.1 - KAOLINITE WITH NEGATIVELY CHARGED FACES AND POSITIVELY CHARGED EDGES 203

6.1.1 - Kaolinite mixed without unaged $FeCl_3$ 203

6.1.2 - Kaolinite mixed with aged $FeCl_3$ 208

6.2 - KAOLINITE WITH NEGATIVE CHARGES ON BOTH THE EDGES AND THE FACES 213

6.2.1 - Kaolinite sediments made with unaged $FeCl_3$ 213

6.2.1.1 - Accumulated sediment 213

6.2.1.2 - Flocculated sediment 213

6.2.1.3 - Mixed accumulated-flocculated sediments 218

6.2.2 - Kaolinite sediments made with aged $FeCl_3$ 218

6.2.2.1 - Accumulated sediment 218

6.2.2.2 - Flocculated sediment 218

6.2.3 - Flocculated kaolinite sediments made with unaged $AlCl_3$ 218

6.3 - MONTMORILLONITE 228

6.3.1 - Montmorillonite-aged $FeCl_3$ sediments 228

6.3.1.1 - Accumulated sediment 228

6.3.1.2 - Flocculated sediment 228

6.3.2 - Montmorillonite - hydroxoferric particles flocculated sediments 228

6.3.3 - Montmorillonite-unaged $AlCl_3$ flocculated sediments 233

CHAPTER 7 - MATHEMATICAL MODELING 236

7.1 - INTRODUCTION TO THE MATHEMATICAL MODELING 236

7.2 - FORMULATION OF THE MATHEMATICAL MODEL 237

7.2.1 - Geometrical configuration 237

7.2.2 - Formulation of the van der Waals attraction energy 237

7.2.3 - Formulation of the electrostatic repulsion energy 239

7.2.3.1 - Elesctrostatic energy between two faces 239

7.2.3.2 - Electrostatic energy between a face and an edges 241

7.2.4 - Total interaction energy for the general rotation case 242

7.2.5 - Total interaction energy for a few important modes of particles association 242

7.2.5.1 - Face-to-face (FF) association mode 242

7.2.5.2 - Edge-to-face (EF) association mode 244

7.2.5.3 - Edge-to-edge (EE) association mode 245

7.3 - RESULTS OF THE COMPUTATION OF INTERACTIONS IN A FEW CASES 247

7.3.1 - Computation for experimental conditions where accumulation sedimentation occurred 247

7.3.1.1 - Computation parameters 247

7.3.1.2 - Comparison of the FF, the EF and the EE association modes 248

7.3.1.3 - Effect of the platelike particles thickness on EE aggregation 248

7.3.2 - Computation for experimental conditions where flocculation sedimentation occurred 252

7.3.2.1 - Computation parameters 252

7.3.2.2 - Comparison of the FF, the EF and the EE association modes 252

7.3.3 - Computation for experimental conditions where mixed accumulation-flocculation sedimentation occurs 255

7.3.3.1 - Computation parameters 255

7.3.3.2 - Comparison of the FF, the EF and the EE association modes 255

7.3.4 - Summary 258

7.3.5 - Angle at stair-step configuration 259

7.3.5.1 - Edges and faces with the relatively low surface potentials 259

7.3.5.2 - Edges and faces with the relatively high surface potentials 259

CHAPTER 8 - DISCUSSION 262

8.1 - AGGREGATION OF Na-KAOLINITE WITH NEGATIVE CHARGES ON BOTH THE EDGES AND THE FACES 262

8.1.1 - Aggregation with unaged Fe electrolyte 262

8.1.1.1 - Typical randomly accumulated sediment 262

8.1.1.2 - Typical flocculated sediment 264

8.1.1.3 - Typical packed accumulated sediment 265

8.1.1.4 - Mixed sediments 266

8.1.1.5 - Effect of the kaolinite content 267

8.1.1.6 - Effect of the kaolinite particles size 268

8.1.2 - Action of Fe on the aggregation of kaolinite particles 269

8.1.2.1 - Possible actions of Fe additives 269

8.1.2.2 - Fe additives as counterions for kaolinite 269

8.1.2.3 - Fe additives as an exchangeable cation source for kaolinite 270

8.1.2.4 - Fe additives as bonding intermediates between the kaolinite particles 271

8.1.3 - Aggregation of kaolinite particles with the help of Al electrolytes 272

8.2 - AGGREGATION OF Na-MONTMORILLONITE 275

8.2.1 - Aggregation with aged Fe electrolyte 275

8.2.2 - Aggregation with hydroxoferric particles 276

8.2.3 - Action of Fe on the aggregation of montmorillonite particles 277

8.2.4 - Aggregation of Na-montmorillonite particles with the help of Al electrolytes 278

8.3 - AGGREGATION OF Na-KAOLINITE WITH NEGATIVELY CHARGED FACES AND POSITIVELY CHARGED EDGES 280

8.3.1- Aggregation of kaolinite suspensions without Fe additives 280

8.3.2 - Aggregation of kaolinite suspensions with unaged $FeCl_3$ 281

CHAPTER 9 - CONCLUSIONS 282

CHAPTER 10 - REFERENCES 284

LIST OF SYMBOLS

LATIN SYMBOLS

a/b - Axial ratio of an ellipsoid.

A_p - Surface area of a flat plate.

A - Hamaker constant.

c_0, c_i - Concentration of an electrolyte in mole.

C_{Ap} - Ratio of aggregate volume fraction to particle volume fraction.

d - Euclidean dimension.

e - Charge of an electron.

E - Electric field.

f - Fractal dimension.

F - Faraday constant

F - Repulsion force between two particles.

g - Acceleration of gravity.

G - Elastic shear modulus of a gel.

h_0 - 1/2 separation gap between two particles plates.

H- Height of sharp interface between a sediment and a supernatant.

H_0 - Initial sediment height.

$\frac{dH}{dt}$ - Settling rate of a sharp interface.

I - Ionic strength.

k - Boltzmann constant.

L_i - Edge length of a platelike particle.

M_{ave}- Average mass of a cluster.

n_0, n_{io} - Concentration of each ion type far from a particle.

n_+ - Cation concentration.

n_- - Anion concentration.

N_s - Number of sites for adsorption.

$N(R)$ - Minimum number of spheres of radius R to completely cover all of an object.

p - Proportion of bonds.

p_c - Critical proportion of bonds at the gel point.

P - Pressure.

$P(M)$ - Probability that a cluster may have a mass M.

R_{ave} - Average size of a cluster.

R - Radius of a cluster.

R_A - Average spherical diameter of one aggregate.

$R(\Phi_p)$-Dimensionless hydrodynamic interaction parameter.

R_s - Gas constant.

t_c- Gel point or gelation time.

T - Absolute temperature.

u - Electrophoretic mobility.

$U_R^{\sigma-\sigma}$- Interaction energy due to repulsion force between two particles with constant surface charge densities.

$U_R^{\psi-\sigma}$ - Interaction energy due to repulsion force between two particles where one is with constant surface potential and the other with constant surface charge density .

$U_R^{\psi-\psi}$- Interaction energy due to repulsion force between two particles with constant surface potentials.

U_R^{FF} - Interaction energy due to repulsion force between faces of two particles.

U_R^{EE} - Interaction energy due to repulsion force between edges of two particles.

U_R^{EF} - Interaction energy due to repulsion force between edge and face of two particles.

U_A - Interaction energy between two particles due to van der Waals force.

U_{total} -Total energy between two particles.

v_a - Rate of adhesion of the particles.

v_s - Stokes' settling velocity of a spherical particle.

v_{sA} - Stokes' settling velocity for a single aggregate.

V_o - Initial suspension volume.

V_F - Final sediment volume.

ΔV - Applied voltage.

z, z_i - Valence of an ion.

z_+ - Valence of a cation.

z_- - Valence of an anion.

GREEK SYMBOLS

$\gamma,\ \gamma_0$- Defined by the equation (2.2-14)

$\frac{d\gamma}{dt}$ - Shear rate.

δ_d - Thickness of Stern layer.

δ - Thickness of a platelike particle.

ε - Relative dielectric constant of a material.

ε_0 - Dielectric permittivity of vacuum.

ε_s - Relative dielectric constant in the Stern layer.

ϕ - Addition chemical potential for adsorption.

ζ - Zeta potential.

η - Viscosity.

η_Δ - Differential viscosity.

η_L - Viscosity of the suspending medium.

$[\eta]$ - Intrinsic viscosity or limiting viscosity number.

θ - Angle between two faces of two platelike particles.

κ^{-1} - Debye-Hückel parameter or Electric double layer thickness.

λ - Shape factor.

ρ - Volume charge density.

ρ_L - Density of a liquid.

ρ_p - Density of a particle.

σ, σ_i - Surface charge density.

σ_f - Surface electric charge density on faces of a particle.

σ_s - Surface charge density of occupied sites in the Stern layer.

τ - Shear stress.

τ_B - Bingham yield stress.

$\tau_B(\Phi_p)$ - Estimate of the yield stress of the network of particles.

Φ_A - Aggregate volume fraction.

Φ_p - Particles volume fraction.

ψ - Electrical potential.

ψ_0, ψ_{i0} - Electric potential at the surface of a particle.

ψ_d - Stern potential.

ψ_e - Electric potential on edges of a platelike particle.

ψ_f - Electric potential on faces of a platelike particle.

LIST OF TABLES

Page

Table 2.3-1 - Ideal chemical composition of common clays. After Kingery, et al. [47]. 38

Table 2.3-2 - Cation exchange capacity of clay minerals. After Brindley [48]. 40

Table 2.4-1 - List of liquids miscible with carbon dioxide. From McHugh [107]. 71

Table 3.2-1 - Typical physical characteristics of HUF and HR kaolinites. From Georgia Kaolin Company [117]. 83

Table 3.2-2- Semiquantitative EDX analysis of the precipitates from aged $FeCl_3$ solutions. 87

Table 3.2-3 - Molar ratio of the reagents used to prepare monodispersed SiO_2 particles, and size of the particles which were obtained by the Stöber method [119] 93

Table 5.1-1 - Concentration of Fe (in ppm) in the liquid of 0.5 % by mass kaolinite suspensions mixed with unaged $FeCl_3$, after 24 hours sedimentation, as determined by the Atomic Absorption (AA) method. 165

Table 5.1-2 - Concentration of Fe (in ppm) in the liquid of 0.5 % by mass kaolinite suspensions mixed with aged $FeCl_3$, after 24 hours sedimentation, as determined by AA. 165

Table 5.1-3 - Concentration of Al (in ppm) in the liquid of 0.5 % by mass kaolinite suspensions mixed with unaged $AlCl_3$, after 24 hours sedimentation, as determined by AA. 165

Table 5.1-4 - Concentration of Al (in ppm) in the liquid of 0.5 % by mass kaolinite suspensions mixed with aged $AlCl_3$, after 24 hours sedimentation, as determined by AA. 165

Table 5.1-5 - Concentration of Al (in ppm) in the liquid of 1 % (by mass) montmorillonite suspensions mixed with unaged $AlCl_3$, after 24 hours sedimentation, as determined by AA. 166

Table 5.1-6 - Concentration of Al (in ppm) in the liquid of 1 % (by mass) montmorillonite suspensions mixed with aged $AlCl_3$, after 24 hours sedimentation, as determined by AA. 169

Table 5.1-7 - Concentration of Na (in ppm) in the liquid of 1 % (by mass) montmorillonitesuspensions mixed with aged $AlCl_3$, after 24 hours sedimentation, as determined by AA. 169

LIST OF FIGURES

Page

Fig. 1.2-1 - Relationship between the microstructure of a clay sediment and its formation conditions. 3

Fig. 2.2-1 - Schematic representation of the Helmholtz model: (a) the Helmholtz model of electric double layer; (c) distribution of electric potential near the flat surface. After Hunter [19] and Hiemenz [10]. 9

Fig. 2.2-2 - Schematic representation of the Gouy model: (a) electrical double layer; (b) distribution of the ions around a particle; (c) dependence of the electric potential on the distance from the particle surface. From Shaw [22] 9

Fig. 2.2-3 - Schematic illustration of the Stern model: (a) electrical double layer; (b) dependence of the electric potential on the distance form the particle surface. From Shaw [22]. 14

Fig. 2.2-4 - Schematic illustration of the Grahame model and a possible electric potential distribution near the particle surface. After Hunter [18] and Adamson [24]. 14

Fig. 2.2-5 - Schematic illustration of two overlapping electric double layers: (a) particles with an identical electric surface potential; (b) particles with a different electric potential. 17

Fig. 2.2-6 - Electrostatic potential energy as a function of the separation gap between two dissimilar platelike particles for different surface conditions, when $\psi_{10} = 0.01$ V, $\psi_{20} = 0.03$ V and $\kappa = 1 \times 10^8$ m^{-1}. From Wang [29]. 19

Fig. 2.2-7 - Qualitative sketch of the potential energy as a function of the separation gap between two particles: (a) U_{total}, U_R and U_A; (b) 3 possible different shapes of U_{total}. After Hiemenz [10]. 21

Fig. 2.2-8 - Schematic representation of the steady state shear viscosity and of the elastic modulus of a colloid during the sol-gel transition. From Pierre [12]. 23

Fig. 2.2-9 - Compared densities of fractal solids and of crystalline solids, as a function of their size R. From Hench and West [32]. 23

Fig. 2.2-10- Bi-dimensional illustration of: (a) a conventional object (f=d=2); and (b) a fractal object (f < 2). 26

Fig. 2.2-11 - Structural aspect of 2-dimensional clusters obtained from various computer simulation growth models. The fractal dimensions which are listed are for the equivalent 3-d clusters. From Brinker, et al.[40]. 28

Fig. 2.2-12 - Space-filling clusters. From Brinker et al. [40]. 28

Fig. 2.2-13 - Sedimentation from: (a) a dispersed suspension; (b) a flocculated suspension. From Van Olphen [27]. 30

Fig. 2.2-14 - Floc-aggregate structure from Michaels and Bolger [42]. 30

Fig. 2.2-15 - Different types of flow behavior for a fluid. After van Olphen [27]. 34

Fig. 2.2-16 - Typical hysteresis loop in the flow curve for a thixotropic fluid. After Moore [44]. 34

Fig. 2.2-17 - Platelike particles aggregation modes: (a) FF association and (b) its effect on the suspension viscosity; (c) bookhouse aggregation and (d) its effect on the suspension viscosity; (e) card-house aggregation and (f) its effect on the suspension viscosity. After Michaels [45]. 37

Fig. 2.3-1- Layer structures of kaolinite, of mica (illite with $x=y=0$ in Table 2.3-1) and of montmorillonite. After Brindley [48]. 39

Fig. 2.3-2 - Relationship between the pH and the zeta potential, in an aqueous medium, of Na-kaolinite (after Yong et al. [54]) and of Na-illite (after Ohtsubo et al. [61]), of Na-Montmorillonite (after Avena et al. [62]). 43

Fig. 2.3-3 - Total potential interaction energy U_{total}, as a function of the separation gap $2h_0$ between the parallel surfaces of two kaolinite particles, for different surface electric potentials ψ_{f0} on the faces, and ψ_{e0} on the edges: (a) opposite charges ψ_{f0} = - 0.031 V and ψ_{e0} = 0.02 V; (b) charges of same sign ψ_{f0} = - 0.046 V and ψ_{e0} = -0.01 V. The electrolyte was NaCl at 10^{-4} M, and the plate thickness was 1.6 x 10^{-7} m. After Flegmann et al. [63]. 45

Fig. 2.3-4 - Total potential energy of interaction between two platelike particles, as a function of the EF inclination angle θ between the 2 particles surfaces and for various values of the plate thickness δ. From Tateyama et al. [64]. Value of the Hamaker constant $A = -2\times10^{-20}$ J., electrolyte : 1M NaCl. 46

Fig. 2.3-5 - Possible association modes of platelike particles with the same type of charges on the edges and on the faces: (a) face-to-face; (b) edge-to-face; (c) in plane edge-to-edge; (d) crossed edge-to-edge; (e) corner-to-edge; (f) corner-to-corner. From Pierre [36]. 48

Fig. 2.3-6 - Total potential energy of interaction between two platelike particles, as a function of the separation distance $2h_0$ between the 2 particles surfaces and for various values of the plate thickness δ. From Tateyama et al. [64]. Value of the Hamaker constant $A = -2\times10^{-20}$ J., electrolyte : 1M NaCl. 49

Fig. 2.3-7 - The three types of settling kinetics of flocculated kaolinite suspensions. From Michaels and Bolger [42]. 50

Fig. 2.3-8 - Density distribution in a kaolinite suspension with a particles volume fraction $\Phi_p = 0.019$, and a CaO content of 0.1% by mass. From Michaels and Bolger [42]. 52

Fig. 2.3-9 - Shear stress τ as a function of the shear rate $\frac{d\gamma}{dt}$ of 5% by mass Na-kaolinite suspensions, in a 10^{-4} M NaCl solution. After Flegmann et al. [63]. 53

Fig. 2.3-10 - Relationship between the pH and the Bingham yield stress of 9% (by mass) kaolinite suspensions and interpretation in terms of the mode of particles association. From Rand et al. [60]. 54

Fig. 2.3-11 - Relationship between the Bingham shear stress τ_B and the NaCl concentration for a 2% by mass suspension of Na-montmorillonite. The pH decreased from 8.5 to 7 as the NaCl content increased. After Chen et al. [67] and van Olphen [27]. 54

Fig. 2.3-12 - Bingham yield stress for kaolinite, ferrihydrite and mixed kaolinite ferrihydrite suspensions of initial pH3.0 and 9.5, at various pH values. The solid content of the suspensions was 10% by mass and the proportion of ferrihydrite to kaolinite was 1/19 in the mixed systems. From Yong et al. [54]. 59

Fig. 2.3-13 - Variation of the Bingham yield stress with pH for mixed illite-ferrihydrite suspensions of initial pH3.0 and 9.5 with different ferrihydrite contents. The solid content of the suspensions was 8% by mass. From Ohtsubo et al. [61] 59

Fig. 2.4-1 - Domain structures: (a) Book domains. From Sloan et al.[80; (b,c) Stepped face-to-face domains. From Smalley et al. [81]. 63

Fig. 2.4-2 - Proposed schemes to explain the formation of domains in clay sediments: (a) Open, random arrangement of packets of particles; (b) Increased parallelism of domains and increasing incorporation of particles inside each domain. After Moon [82]. 63

Fig. 2.4-3 - Models for the fabric of clay sediments: (a) Cardhouse structure, form Lambe [83]; (b) Bookhouse structure, from Sloan et al. [80]; (c) Honeycomb structure, from Terzaghi [84] and Casagrande [85]; (d) Turbostratic structure, from Aylmore and Quik [86]. 64

Fig. 2.4-4 - Structure models for clay sediments: (a) and (b) Stair-step structure. From O'Brien [88]. (c) Tactoid structure. From Ingles [89]; (d) Aggregates and links structure. From Pusch [90]. 66

Fig. 2.4-5 - Possible association modes of clay particles according to van Olphen [11]: (a) dispersed particles; (b) Dispersed domains; (c) EF flocculation of particles (cardhouse); (d) EE flocculation of particles; (e) EF flocculation of domains (bookhouse); (f) EE flocculation of domains; (g) mixed EE and EF flocculation of domains. 67

Fig. 2.4-6 - Schematic drawing of SEM micrographs of flocculated kaolinite sediments dried by freeze-drying: (a) from Mattiat [111]; (b) from O'Brien [88] with 100g/L of clay in distilled water; or (c) with 10g/L of clay concentration in a 1 g/L NaCl solution. 74

Fig. 2.4-7 - Schematic drawing of SEM micrographs of kaolinite sediments dried by the freeze-drying technique, after uniaxial consolidation at: (a) 0 kPa; (b) 200 kPa; (c) 500 kPa. Drawn after Smart and Tovey [113]. 75

Fig. 2.4-8 - Schematic drawing of SEM micrographs of a regular EF bookhouse structure in a kaolinite based "sludge" sediment, such as made after the extraction of oil from Alberta oil sands. Drawn after Mikula et al. [103]. 77

Fig. 2.4-9 - Schematic drawing of SEM micrographs of kaolinite sediments dried by the supercritical drying technique, and made : (a) in distilled water; (b) in a 3% NaCl solution. Drawn after Lanier et al. [114]. 76

Fig. 2.4-10 - Schematic drawing of SEM micrographs of montmorillonite sediments made by: (a) freeze drying in propane; and (b) supercritical drying. Drawn after Smart and Tovey [92]. 79

Fig. 3.2-1 - Relationship between the pH and the zeta potential, in an aqueous clay suspensions: (a) Na-kaolinite (Hydrite PX) after Yong et al. [54], compared with the present measurements on: (b) HUF Na-kaolinite treated with $Na_4P_2O_7$; and (c) untreated Na-montmorillonite. 86

Fig. 3.2-2 - X-ray diffraction patterns (Cu $K\alpha$, Ni filtered) of the precipitates from aged $FeCl_3$ solution with the X-ray diffractometer (Rigaku Rotating Anode XRD). The precipitates include phases: (a) Hematite Fe_2O_3; (b) Akaganéite FeOOH; (c) Feroxyhite FeOOH; (d) Iron oxide hydrate $Fe_2O_3.H_2O$; (e) Molysite $FeCl_3$. 89

Fig. 3.2-3 - X-ray diffraction patterns (CuKa, Ni filtered) of hydroxoferric particles with the X-ray diffractometer (Rigaku-Denki XRD). 91

Fig. 3.2-4 - SEM micrographs of the precipitates from aged $FeCl_3$ solutions: (a) needle-like particles; (b) platelike particles. (c) TEM micrograph of hydroxoferric particles; (d) the pattern of selected area diffraction (the selected are is from the center of (c), the rings corresponding to β-FeOOH. 92

Fig. 3.2-5 - SEM micrographs of the SiO_2 particles prepared by the Stöber method [119] in the conditions listed in Table.3.2-3: (a) Sample 1; (b) Sample 2; (c) Sample 3. 94

Fig. 3.4-1 - Directions in which supercritical-dried clay sediment samples were observed. 95

Fig. 4.1-1 - Kinetics of sedimentation of 0.5% Na-kaolinite suspensions treated by the method of Schofield and Samson [59]: (a) without Fe electrolyte; (b) with 0.67 mM unaged $FeCl_3$. 108

Fig. 4.1-2 - Final thickness of the sediments made from 0.5% Na-kaolinite suspensions treated by the method of Schofield and Samson [59], as a function of the pH. 110

Fig. 4.2-1 -Types of sedimentation behavior of 0.5% Na-kaolinite suspensions treated with $Na_4P_2O_7$, at pH = 4.0 and after 3 days settling: (a) accumulation-sedimentation with a concentration [$FeCl_3$] = 3.3 mM; (b) flocculation-sedimentation with [$FeCl_3$] = 0.33 mM; (c) mixed accumulation-flocculation sedimentation with [$FeCl_3$] = 1.67 mM. 112

Fig. 4.2-2 - Sediment kinetics, as measured by the displacement of sharp interfaces, in 0.5% Na-Kaolinite suspensions treated with $Na_4P_2O_7$ at pH = 4.0: (a) interface between the flocculated sediment and the supernatant liquid in flocculation sedimentation with [$FeCl_3$] = 0.33 and 0.67mM; (b) interface between the accumulated sediment and the remaining suspension in accumulation sedimentation with [$FeCl_3$] = 0.0 and 3.33 mM ; (c) interfaces accumulated sediment-remaining suspension and flocculated sediment-supernatant liquid in mixed sedimentation with [$FeCl_3$] = 0.17 and 1.67 mM. 113

Fig. 4.2-3 - Diagrams of the sedimentation behavior of 0.5% Na-kaolinite suspensions treated with $Na_4P_2O_7$ and mixed with: (a) unaged $FeCl_3$; (b) unaged $Fe_2(SO_4)_3$. The solid, open, and semi-open dots respectively indicate accumulation, flocculation, and mixed behavior. 117

Fig. 4.2-4 - Sedimentation of 0.5% Na-kaolinite suspensions treated with $Na_4P_2O_7$ as a function of the $Fe_2(SO_4)_3$ concentration: (a) Initial settling rate; (b) Final sediment thickness. 118

Fig. 4.2-5 - Compared sedimentation data of 0.5% Na-kaolinite suspensions treated with $Na_4P_2O_7$, at pH = 2, when mixed with different electrolytes: (a) Initial settling rate; (b) Final sediment thickness. 119

Fig. 4.2-6 - Sediments of 0.5% Na-kaolinite as a function of the aged $FeCl_3$ concentration: (a) at pH = 4 after a week; (b) at pH=9.5 after 20 days. From left to right, the aged $FeCl_3$ concentration was 0.17, 0.33, 0.67, 1.67, 3.33, 5, 10, 20 mM. 121

Fig. 4.2-7 - Sediment kinetics, as measured by the displacement of sharp interfaces, in 0.5% Na-Kaolinite suspensions treated with $Na_4P_2O_7$ at pH = 4.0: (a) with aged $FeCl_3$ concentrations of 1.67mM and 10.0 mM; (b) with aged $FeCl_3$ concentrations of 0.0 and 3.3 mM; (c) with aged $FeCl_3$ concentrations of 0.17 and 5.0 mM. 122

Fig. 4.2-8 - Diagram of the sedimentation behavior in 0.5% Na-kaolinite suspensions treated with $Na_4P_2O_7$, mixed with aged $FeCl_3$. The solid, open, and semi-open dots respectively indicate accumulation, flocculation, and mixed behavior. 123

Fig. 4.2-9 - Compared sedimentation behavior of 0.5% Na-kaolinite suspensions treated with $Na_4P_2O_7$, as a function of the concentration of unaged or of aged $FeCl_3$ at pH=2: (a) Initial settling rate; (b) Final sediment thickness. 124

Fig. 4.2-10 - Initial settling rate of Na kaolinite suspensions treated with $Na_4P_2O_7$ and flocculated with unaged $FeCl_3$: (a) Na-HR kaolinite at concentrations of 1%, 2% and 5% by mass; (b) Na-HUF kaolinite at the concentration of 1 %. 126

Fig. 4.2-11 - Initial settling rate of 2% Na-kaolinite suspensions treated with $Na_4P_2O_7$ and flocculated with unaged $FeCl_3$: (a) Na-HR kaolinite; (b) Na-HUF kaolinite. 127

Fig. 4.2-12 - Initial settling rate of 5% kaolinite suspensions treated with $Na_4P_2O_7$ and flocculated with unaged $FeCl_3$; (a) Na-HR kaolinite; (b) Na-HUF kaolinite. 128

Fig. 4.2-13 - Final sediment thickness of kaolinite suspensions treated with $Na_4P_2O_7$, as a function of the concentration of unaged $FeCl_3$ and at different pH: (a) 2% Na-HR kaolinite; (b) 1% Na-HUF kaolinite. The solid lines indicate flocculated sediments while the dashed lines indicate mixed accumulated-flocculated sediments. 129

Fig. 4.2-14 - Final sediment thickness of 5% kaolinite suspensions treated with $Na_4P_2O_7$, as a function of the concentration of unaged $FeCl_3$ concentration: (a) Na-HR kaolinite; (b) Na-HUF kaolinite. 130

Fig. 4.2-15 - Ratio C_{Ap} between the volume occupied by the flocs and the volume occupied by the primary particles, in HUF kaolinite suspensions treated with $Na_4P_2O_7$, as a function of the concentration of unaged $FeCl_3$. 132

Fig. 4.2-16 - Diagrams of the sedimentation behavior of Na-HUF kaolinite suspensions with unaged $FeCl_3$: (a) 1% kaolinite; (b) 2% kaolinite; (c) 5% kaolinite. The solid, open, and semi-open dots respectively indicate accumulation, flocculation, and mixed behavior. 133

Fig. 4.2-17 - Diagrams of the sedimentation behavior of Na-HR kaolinite suspensions with unaged $FeCl_3$: (a) 0.5% kaolinite; (b) 1% kaolinite; (c) 2% kaolinite; (d) 5% kaolinite. The solid, open, and semi-open dots respectively indicate accumulation, flocculation and mixed behavior. 134

Fig. 4.2-18 - Sedimentation of 0.5% Na-HUF kaolinite suspensions with a concentration of unaged $Al(NO_3)_3$ of 5.0mM: (a) accumulation sedimentation at pH=12; (b) flocculation sedimentation at pH=2; (c) mixed sedimentation at pH=9.5. 136

Fig. 4.2-19 - Sedimentation kinetics of 0.5% Na-HUF Kaolinite suspensions with unaged Al electrolytes: (a) Concentration $[Al(NO_3)_3]$ = 5 and 10 mM at pH=2; (b) $[Al(NO_3)_3]$ =5 mM at pH=12 ; (c) $[Al(NO_3)_3]$ = 5 and 10 mM at pH=9.4; (d)$[AlCl_3]$ = 2 and 10 mM at pH= 6; (e) $[AlCl_3]$ = 0 mM at pH= 6; (f)$[AlCl_3]$ =1 mM at pH= 6. 137

Fig. 4.2-20 - Diagrams of the sedimentation behavior of 0.5 % (by mass) Na-HUF kaolinite suspensions with unaged Al electrolytes: (a) $AlCl_3$; (b) $Al(NO_3)_3$; (c) $Al_2(SO_4)_3$. The solid, open, and semi-open dots respectively indicate accumulation, flocculation, and mixed behavior. 138

Fig. 4.2-21 - Initial settling rate of 0.5% Na-kaolinite suspensions treated with $Na_4P_2O_7$ suspensions, when flocculated with three different unaged Al electrolytes: (a) at pH = 2 ; (b) at pH = 6. 140

Fig. 4.2-22 - Final sediment thickness of 0.5% Na-kaolinite suspensions treated with $Na_4P_2O_7$ and flocculated with three different unaged Al electrolytes: (a) at pH = 2; (b) at pH = 6. 141

Fig. 4.2-23- Sedimentation behavior of 0.5% Na-Kaolinite suspensions treated with $Na_4P_2O_7$, as a function of the concentration of unaged $AlCl_3$, at different pH: (a) Initial settling rate; (b) Final sediment thickness. 142

Fig. 4.2-24 - Aspect of 0.5% Na-kaolinite suspensions, treated with $Na_4P_2O_7$ and mixed with the unaged $AlCl_3$ concentrations of 1, 2, 5, 10 and 50 mM from the left to the right, after 3 days of sedimentation: (a) at pH=4 ; (b) at pH=9.5. 143

Fig. 4.2-25 - Displacement kinetics of sharp interfaces in 0.5 % (by mass) Na-kaolinite suspensions: (a) flocculated sediment-supernatant liquid interface with the aged $AlCl_3$ concentrations of 1mM and 10mM at pH=6. (b) accumulated sediment-diffuse suspension interface with the aged $AlCl_3$ concentrations of 1 and 10mM at pH=11. 144

Fig. 4.2-26 - Diagram of the sedimentation behavior in 0.5% HUF Na-kaolinite suspensions treated with $Na_4P_2O_7$ and mixed with aged $AlCl_3$. The solid, open, and semi-open dots respectively indicate accumulation and flocculation behavior. 146

Fig. 4.2-27 - Sedimentation data of 0.5% HUF Na-kaolinite suspensions flocculated with aged $AlCl_3$ at different pH values: (a) Initial settling rate; (b) Final sediment thickness. 147

Fig. 4.3-1 - Displacement rates of the sharp interfaces in Na-montmorillonite suspensions at pH=9.5 with: (a) a low content of Fe additives; (b) a higher content of Fe additives. 149

Fig. 4.3-2 - Aspect of the sediments made from 1% by mass Na-montmorillonite suspensions, with the aged $FeCl_3$ concentrations of 0.33, 1, 2, 3.3, 5 and 10mM, from left to right, after 10 days sedimentation: (a) at pH = 4; (b) at pH = 9.5. 150

Fig. 4.3-3 - Displacement kinetics of the sharp interfaces in 1% Na-montmorillonite suspensions at pH=9.5, with different aged $FeCl_3$ concentrations: (a) flocculated sediment-supernatant liquid interface with $FeCl_3$ = 1mM, 3.3mM and 10mM; (b) accumulated sediment-diffuse suspension interface with aged $FeCl_3$ = 0.33 mM. 151

Fig. 4.3-4 - Diagrams of the sedimentation behavior in 1% Na-montmorillonite suspensions: (a) with aged $FeCl_3$; (b) with hydroxoferric particles. The solid, open, and semi-open dots respectively indicate accumulation and flocculation sedimentation. 153

Fig. 4.3-5 - Sedimentation kinetics of 1% Na-montmorillonite suspensions flocculated with aged $FeCl_3$ at different pH: (a) Initial settling rate; (b) Final sediment thickness. 154

Fig. 4.3-6 - Displacement rate of sharp interface between the flocculated sediment and the supernatant liquid, in 1 % (by mass) Na-montmorillonite suspensions flocculated with 0.25% (by mass) of hydroxoferric particles at pH = 12, 9.5 and 4. 155

Fig. 4.3-7 - Sedimentation of 1 % (by mass) montmorillonite suspensions with hydroxoferric particles at different pH values: (a) Initial settling rate; (b) Final sediment thickness. 156

Fig. 4.3-8 - Sedimentation of 1% (by mass) Na-montmorillonite suspensions after 10 days, for the unaged $AlCl_3$ concentrations of 0.165, 0.33, 1, 1.65, 3.3, 5, 10 and 20mM, from the left to the right: (a) pH = 4.0; (b) at pH = 9.5. 157

Fig. 4.3-9 - Displacement rate of the sharp interface between the flocculated sediment and the supernatant liquid, in 1% Na-montmorillonite suspensions at pH=9.5, for the unaged $AlCl_3$ concentrations of 0.33mM, 3.3mM and 10mM. 158

Fig. 4.3-10 - Diagram of the sedimentation behavior of 1% Na-montmorillonite suspensions: (a) with unaged $AlCl_3$; (b) with aged $AlCl_3$. The solid, open, and semi-open dots respectively indicate accumulation and flocculation. 160

Fig. 4.3-11 - Sedimentation characteristics of 1% Na-montmorillonite suspensions flocculated with unaged $AlCl_3$ at different pH: (a) Initial settling rate; (b) Final sediment thickness. 161

Fig. 4.3-12 - Displacement kinetics of sharp interfaces in 1% Na-montmorillonite suspensions at pH=9.5: (a) interface between the flocculated sediment and the supernatant liquid with the aged $AlCl_3$ concentrations of 5mM and 2mM; (b) interface between the accumulated sediment and the diffuse suspension with an aged $AlCl_3$ concentration of 0.33 mM. 162

Fig. 4.3-13 - Sedimentation characteristics of 1% (by mass) Na-montmorillonite suspensions flocculated with aged $AlCl_3$ at different pH: (a) Initial settling rate; (b) Final sediment thickness. 163

Fig. 5.1-1 - Amount of Fe adsorbed on the kaolinite particles from $FeCl_3$, at different pH: (a) from unaged $FeCl_3$; (b) from aged $FeCl_3$. 167

Fig. 5.1-2 - Amount of Al adsorbed on the kaolinite particles from $AlCl_3$, as a function of the pH: (a) unaged $AlCl_3$; (b) aged $AlCl_3$. 168

Fig. 5.1-3 - Amount of Al adsorbed on the montmorillonite particles from $AlCl_3$, as a function of the pH: (a) unaged $AlCl_3$; (b) aged $AlCl_3$. 170

Fig. 5.2-1 - TEM micrographs of the Fe materials deposited on the kaolinite particles, in sediments made with 10mM $FeCl_3$ at pH 9.5: (a) rodlike and platelike particles; (b) thin film; (c) small spherical particles. 172

Fig. 5.2-2 - EDX spectrum of the surface of the kaolinite particles shown in Fig. 5.2-1: (a), (b), and (c) respectively correspond to each circle in the (a), (b), and (c) micrographs in Fig. 5.2-1. 173

Fig. 5.2-3 - TEM micrographs of the Fe compound deposited on montmorillonite particles in sediments made with 10mM $FeCl_3$ at pH=9.5: (a) thin films; (b) rod-like particles. 174

Fig. 5.2-4 - EDX spectrum of selected areas on the surface of the montmorillonite particles shown in Fig. 5.2-3: (a) and (b) respectively correspond to the circled areas in the (a) and (b) micrographs in Fig. 5.2-3. 175

Fig. 5.2-5 - TEM micrographs of the hydroxoferric particles deposited on montmorillonite particles, in a sediment made from a 1% Na-montmorillonite suspension mixed with 0.125% (by mass) of hydroxoferric particles, at pH=2: (a) near the edge of a montmorillonite particle; (b) far from the edges of a montmorillonte particle. 176

Fig. 5.2-6 - TEM micrographs of the hydroxoferric particles deposited on montmorillonite particles, in a sediment made from a 1% Na-montmorillonite suspension mixed with 0.5% (by mass) of hydroxoferric particles, at pH=2 and at 2 different scales. 177

Fig. 5.2-7 - TEM micrographs of the hydroxoferric particles deposited on the faces of montmorillonite particles, in a sediment made from a 1% (by mass) Na-montmorillonite suspension mixed with 0.125% (by mass) of hydroxoferric particles, at pH=6 and at 2 different scales. 180

Fig. 5.2-8 - TEM micrographs of the hydroxoferric particles deposited on montmorillonite particles, in a sediment made from a 1% Na-montmorillonite suspension, mixed with 0.125% by mass of hydroxoferric particles, at pH=9.5 and at 2 different scales. 181

Fig. 5.2-9 - TEM micrographs of the hydroxoferric particles deposited on montmorillonite particles, in a sediment made from a 1% Na-montmorillonite suspension mixed with 0.5% (by mass) of hydroxoferric particles, at pH=9.5 and at 2 different scales. 182

Fig. 5.2-10 - TEM micrographs of the hydroxoferric particles clusters settled with the montmorillonite particles, in a sediment made from a 1% Na-montmorillonite suspension, mixed with 0.5% (by mass) of hydroxoferric particles, at pH=12. 183

Fig. 5.3-1 - Bingham yield stress of 10% (by mass) kaolinite suspensions with initial negative charges on the particles faces and positive charges on their edges, as a function of the pH. 185

Fig. 5.3-2 - Typical flow data of data Na-montmorillonite suspensions mixed with hydroxoferric particles: (a) flow curve for a suspension comprised of 0.500% (by mass) of hydroxoferric particles; (b) Bingham yield stress τ_B for suspensions comprised of 0.125% (by mass) of hydroxoferric particles. 186

Fig. 5.3-3 - Bingham yield stress τ_B as a function of the pH, for 1% Na-montmorillonite suspensions mixed with different hydroxoferric particles proportions. 188

Fig. 5.4-1 - Zeta potential of kaolinite particles treated by the method of Schofield and Samson [59]. 190

Fig. 5.4-2 - Variation of the zeta potential with the concentration of $FeCl_3$ at different pH values in 0.5% (by mass) kaolinite suspensions treated with $Na_4P_2O_7$: (a) unaged $FeCl_3$; (b) aged $FeCl_3$. 191

Fig. 5.4-3 - Diagram of the sedimentation behavior in 0.5% kaolinite suspensions treated with $Na_4P_2O_7$ and mixed with unaged $FeCl_3$: (a) observed results reproduced from Fig. 4.2-3a; (b) prediction from the measured zeta potential ζ. The open dots are for $|\zeta| < 0.01$V, the solid dots for $|\zeta| > 0.015$ V, the semi-open dots for $0.01 \text{ V} \le |\zeta| \le 0.015$ V. 192

Fig. 5.4-4 - Diagram of the sedimentation behavior in 0.5% kaolinite suspensions treated with $Na_4P_2O_7$ and mixed with aged $FeCl_3$: (a) observed results reproduced from Fig. 4.2-8; (b) prediction from the measured zeta potential ζ. The open dots are for $|\zeta| < 0.01$ V, the solid dots for $|\zeta| > 0.015$V, the semi-open dots for $0.01 \text{ V} \le |\zeta| \le 0.015$ V. 194

Fig. 5.4-5 - Variation of the zeta potential with the concentration of unaged $AlCl_3$ at different pH values in 0.5% (by mass) kaolinite suspensions treated with $Na_4P_2O_7$. 196

Fig. 5.4-6 - Zeta potential of montmorillonite particles from mixed montmorillonite hydroxoferric suspensions, as a function of the pH. 196

Fig. 5.4-7 - Relationship between the zeta potential and the Bingham yield stress in mixed montmorillonite-hydroxoferric particles suspensions. 197

Fig. 5.4-8 - Dependence of the zeta potential of montmorillonite particles on the concentration of unaged $AlCl_3$ in the suspension, at different pH. 197

Fig. 5.5-1 - SEM micrographs of kaolinite particles treated by the method of Schofield and Samson [59], and mixed with SiO_2 particles at pH=2. SiO_2 particles size: (a) 0.2μm; (b) 0.35μm; (c) 0.65μm. 199

Fig. 5.5-2 - SEM micrographs of kaolinite particles treated by the method of Schofield and Samson [59], and mixed with SiO_2 particles at pH=4. SiO_2 particles size: (a) 0.2μm; (b) 0.35μm; (c) 0.65μm. 200

Fig. 5.5-3 - SEM micrographs of kaolinite particles mixed with SiO_2 particles at pH=10. In (a) and (b) the kaolinite was first treated by the method of Schofield and Samson [59], while in (c) it was treated with $Na_4P_2O_7$. The SiO_2 particles size was: (a) 0.2μm; (b) 0.35μm; (c) 0.65μm. 202

Fig. 6.1-1 - SEM micrographs at 10 kV of the sediments made from 0.5 % (by mass) kaolinite suspensions treated by the method of Schofield and Samson [59], and mixed with 0.67 mM unaged $FeCl_3$, at pH 2. (a), (b) and (c) are at increasing magnification. 204

Fig. 6.1-2 - SEM micrographs at 10 kV of the sediments made from 0.5 % (by mass) kaolinite suspensions treated by the method of Schofield and Samson [59], and mixed with 0.67 mM unaged $FeCl_3$, at pH 4. (a), (b) and (c) are at increasing magnification. 205

Fig. 6.1-3 - SEM micrographs at 10 kV of the sediments made from 0.5 % (by mass) kaolinite suspensions treated by the method of Schofield and Samson [59], and mixed with 0.67 mM unaged $FeCl_3$, at pH 6. (a), (b) and (c) are at increasing magnification. 206

Fig. 6.1-4 - SEM micrographs at 10 kV of the sediments made from 0.5 % (by mass) kaolinite suspensions treated by the method of Schofield and Samson [59], and mixed with 0.67 mM unaged $FeCl_3$, at pH 9.5. (a), (b) and (c) are at increasing magnification. 207

Fig. 6.1-5 - SEM micrographs at 10 kV of the sediments made from 0.5 % (by mass) kaolinite suspensions treated by the method of Schofield and Samson [59], and mixed with 0.67 mM aged $FeCl_3$, at pH 2. (a), (b) and (c) are at increasing magnification. 209

Fig. 6.1-6 - SEM micrographs at 10 kV of the sediments made from 0.5 % (by mass) kaolinite suspensions treated by the method of Schofield and Samson [59], and mixed with 0.67 mM aged $FeCl_3$, at pH 4. (a), (b) and (c) are at increasing magnification. 210

Fig. 6.1-7 - SEM micrographs at 10 kV of the sediments made from 0.5 % (by mass) kaolinite suspensions treated by the method of Schofield and Samson [59], and mixed with 0.67 mM aged $FeCl_3$, at pH 6. (a), (b) and (c) are at increasing magnification. 211

Fig. 6.1-8 - SEM micrographs at 10 kV of the sediments made from 0.5 % (by mass) kaolinite suspensions treated by the method of Schofield and Samson [59], and mixed with 0.67 mM aged $FeCl_3$, at pH 9.5. (a), (b) and (c) are at increasing magnification. 212

Fig. 6.2-1 - SEM micrographs made at 10 kV and at several magnifications, of the accumulated kaolinite sediment without $FeCl_3$, at pH = 4.0. 214

Fig. 6.2-2 - SEM micrographs made at 10 kV and at several magnifications, of the accumulated kaolinite sediment without $FeCl_3$, at pH = 9.5. 215

Fig. 6.2-3 - SEM micrographs made at 10 kV and at several magnifications, of the accumulated kaolinite sediment made at pH = 4.0 with unaged $FeCl_3$ at a concentration of 3.33 mM. 216

Fig. 6.2-4 - SEM micrographs made at 10 kV and at several magnifications, of the flocculated kaolinite sediment made at pH = 4.0 with unaged $FeCl_3$ at a concentration of 0.67mM. 217

Fig. 6.2-5 - SEM micrographs at several magnifications, of the mixed accumulated-flocculated kaolinite sediment made at pH 4 with unaged $FeCl_3$ at a concentration of 1.67mM; (a) top part of the sediment; (b) bottom part of the sediment. 219

Fig. 6.2-6 - SEM micrographs made at 10 kV and at several magnifications, of the accumulated kaolinite sediment made at pH 9.5 with aged $FeCl_3$ at a concentration of 10mM. 220

Fig. 6.2-7 - SEM micrographs made at 10 kV and at several magnifications, of the accumulated kaolinite sediment made at pH 9.5 with aged $FeCl_3$ at a concentration of 3.3mM. 221

Fig. 6.2-8 - SEM micrographs made at 10 kV and at several magnifications, of the flocculated kaolinite sediment made at pH 2 without $AlCl_3$. 222

Fig. 6.2-9 - SEM micrographs made at 10 kV and at several magnifications, of the flocculated kaolinite sediment made at pH 2 with unaged $AlCl_3$ at a concentration of 2mM. 223

Fig. 6.2-10 - SEM micrographs made at 10 kV and at several magnifications, of the flocculated kaolinite sediment made at pH 2 with unaged $AlCl_3$ at a concentration of 50mM. 224

Fig. 6.2-11 - SEM micrographs made at 10 kV and at several magnifications, of the flocculated kaolinite sediment made at pH 9.5 with unaged $AlCl_3$ at a concentration of 2mM. 226

Fig. 6.2-12 - SEM micrographs made at 10 kV and at several magnifications, of the flocculated kaolinite sediment made at pH 9.5 with unaged $AlCl_3$ at a concentration of 50mM. 227

Fig. 6.3-1 - SEM micrographs made at 10 kV and at several magnifications, of the accumulated montmorillonite sediment made at pH = 9.5 with aged $FeCl_3$ at a concentration of 3.33mM. 229

Fig. 6.3-2 - SEM micrographs made at 10 kV and at several magnifications, of the flocculated montmorillonite sediment made at pH = 9.5 with aged $FeCl_3$ at a concentration of 5mM. 230

Fig. 6.3-3 - SEM micrographs made at 15 kV and at several magnifications, of the flocculated montmorillonite sediment made at pH = 9.5 with hydroxoferric particles at a solid content of 0.125 % by mass. 231

Fig. 6.3-4 - SEM micrographs made at 15 kV and at several magnifications, of the flocculated montmorillonite sediment made at pH = 9.5 with hydroxoferric particles at a solid content of 0.5 % by mass. 234

Fig. 6.3-5 - SEM micrographs made at 10 kV and at several magnifications, of the flocculated montmorillonite sediment made at pH = 9.5 with unaged $AlCl_3$ at a concentration of 2mM. 234

Fig. 6.3-6 - SEM micrographs made at 15 kV and at several magnifications, of the flocculated montmorillonite sediment made at pH = 9.5 with unaged $AlCl_3$ at a concentration of 5mM. 235

Fig. 7.2-1 - Illustration of the geometrical model used to compute the interaction between two platelike particles at an angle θ. 238

Fig. 7.2-2 - Platelike particles association modes: (a) FF mode; (b) EF mode; (c) EE mode. 243

Fig. 7.3-1 - Total interaction energy between two platelike particles, as a function of the nearest separation distance between the particles, for the FF, the EF, and the EE configurations. General conditions: $L_1 = L_2 = 0.4 \times 10^{-6}$ m, $\delta = 0.05 \times 10^{-6}$ m, T = 298K, $\psi_f = -0.03$ V, $\psi_e = -0.02$ V, A = 2×10^{-20}J, 1:1 type electrolyte at the concentrations: (a) 10mM; (b) 30mM; (c) 60mM. 249

Fig. 7.3-2 - Total interaction energy between two platelike particles, as a function of the nearest separation distance between the particles, for the FF, the EF, and the EE configurations. General conditions: $L_1 = L_2 = 0.4 \times 10^{-6}$ m, $\delta = 0.05 \times 10^{-6}$ m, T = 298K, A = 2×10^{-20}J : (a) $\psi_f = -0.02$ V and $\psi_e = -0.03$ V, 1:1 type electrolyte at the concentrations of 5 mM; (b) $\psi_f = \psi_e = -0.025$ V, 1:1 type electrolyte at the concentrations of 10 mM. 250

Fig. 7.3-3 - Total interaction energy between two platelike particles, as a function of the nearest separation distance between the particles, for the EE configuration. General conditions: $L_1 = L_2 = 0.4 \times 10^{-6}$ m, $\delta = 0.05 \times 10^{-6}$ m, T = 298K, A = 2×10^{-20}J, $\psi_f = \psi_e = -0.025$ V, 1:1 type electrolyte at the concentration of 10mM. 251

Fig. 7.3-4 - Total interaction energy between two platelike particles, as a function of the nearest separation distance between the particles, for the FF, the EF, and the EE configurations. General conditions: $L_1 = L_2 = 0.4 \times 10^{-6}$ m, $\delta = 0.05 \times 10^{-6}$ m, T = 298K, A = 2×10^{-20}J, $\psi_f = -0.015$ V, $\psi_e = -0.005$ V, 1:1 type electrolyte at the concentrations: (a) 0.1 mM; (b) 10mM; (c) 20mM. 253

Fig. 7.3-5 - Total interaction energy between two platelike particles, as a function of the nearest separation distance between the particles, for the FF, the EF, and the EE configurations. General conditions: $L_1 = L_2 = 0.4 \times 10^{-6}$ m, $\delta = 0.05 \times 10^{-6}$ m, T = 298K, A = 2×10^{-20}J : (a) $\psi_f = -0.005$ V and $\psi_e = -0.015$ V, 1:1 type electrolyte at the concentrations of 0.1 mM; (b) $\psi_f = \psi_e = -0.01$ V, 1:1 type electrolyte at the concentrations of 0.1 mM. 254

Fig. 7.3-6 - Total interaction energy between two platelike particles, as a function of the nearest separation distance between the particles, for the FF, the EF, and the EE configurations. General conditions: $L_1 = L_2 = 0.4 \times 10^{-6}$ m, $\delta = 0.05 \times 10^{-6}$ m, T = 298K, A = 2×10^{-20}J, $\psi_f = -0.02$ V, $\psi_e = -0.01$ V, 1:1 type electrolyte at the concentrations: (a) 1 mM; (b) 5 mM; (c) 60 mM. 256

Fig. 7.3-7 - Total interaction energy between two platelike particles, as a function of the nearest separation distance between the particles, for the FF, the EF, and the EE configurations. General conditions: $L_1 = L_2 = 0.4 \times 10^{-6}$ m, $\delta = 0.05 \times 10^{-6}$ m, T = 298K, A = 2×10^{-20}J : (a) $\psi_f = -0.01$ V and $\psi_c = -0.02$ V, 1:1 type electrolyte at the concentrations of 0.1 mM; (b) $\psi_f = \psi_c = -0.015$ V, 1:1 type electrolyte at the concentrations of 0.5 mM. 257

Fig. 7.3-8 - Total interaction energy between two platelike particles, as a function of the nearest separation distance and on the angle θ between them, for the configuration in Fig. 7.2-1. General conditions: $L_1 = L_2 = 0.4 \times 10^{-6}$ m, $\delta = 0.05 \times 10^{-6}$ m, T = 298K, A = 2×10^{-20}J, $\psi_f = 0.012$ V, $\psi_c = 0.02$ V, 1:1 type electrolyte at the concentration of 1mM. 260

Fig. 7.3-9 - Total interaction energy between two platelike particles, as a function of the nearest separation distance and on the angle θ between them, for the configuration in Fig. 7.2-1. General conditions: $L_1 = L_2 = 0.4 \times 10^{-6}$ m, $\delta = 0.05 \times 10^{-6}$ m, T = 298K, A = 2×10^{-20}J, $\psi_f = 0.03$V, $\psi_c = 0.05$ V, 1:1 type electrolyte at the concentration of 30mM. 261

CHAPTER 1 - INTRODUCTION

1.1 - BACKGROUND OF THE PRESENT STUDY

The reason to study the microstructure of platelike particle clay sediments is related to the treatment of oil sands tailings sludge.

Oil sands deposits are abundant in Alberta. As the bitumen is extracted from the oil sands by a commercial hot water process, an increasing volume of oil sands tailings sludge is being produced. This sludge is made to settle and to slowly consolidate in ponds, where it stays a fluid for a long time. As the sludge ponds occupy a large space, and as the sludge water cannot be recycled, this creates a serious environmental problem.

It is known that the long-term stability of the sludge is due, at least in part, to the clay components such as kaolinite. Hence, it is necessary to find an efficient and economical method to transform the large volume of fluid-like sediments made by these clay, to a compact form.

In his MSc studies, Zou [1] investigated the structure of montmorillonite sediments and of a real tailings sludge. The present study is a continuation of this effort and it mostly addresses the case of kaolinite.

1.2 - OBJECTIVE OF THE PRESENT STUDY

In the present study, two types of minerals are addressed - kaolinite and montmorillonite. Both minerals are comprised of platelike particles. The main objective was to determine the relationship between the microstructure of the sediments, which form in an aqueous medium, and the formation condition, such as the pH and the concentration of electrolytes.

The particle interactions in a colloidal system largely depend on some characteristics of the particles such as their surface electric charge density. The effect of the aqueous medium characteristics, the colloidal characteristics of the clay particles and the structure of clay sediments is summarized in Fig. 1.2-1.

Several methods can be used to determine a microstructure. In the present research, the main observation technique was scanning electron microscopy (SEM). Some transmission electron microscopy (TEM) was also performed to study the possible occurrence of precipitates from the electrolyte additives, onto the clay particles. A key experimental step is to maintain the original sediment microstructure during sample preparation.

In the present study, the technique of supercritical drying was used. Also, Fe and Al electrolytes are previously known to establish strong permanent connections between clay particles, in acidic medium [2,3]. Fe and Al salts are widely used as flocculants, and they are frequently present in kaolinite and in montmorillonite minerals. However, these Fe and Al compounds undergo hydrolysis, which has a complex effect on the colloidal properties and the microstructure of the sediments.

The main aqueous medium parameters which are addressed in this study are, the pH and the concentration of Fe and of Al electrolytes, in an unaged and in an aged state. The sedimentation kinetics as well as some aqueous medium characteristics such as the zeta potential were measured.

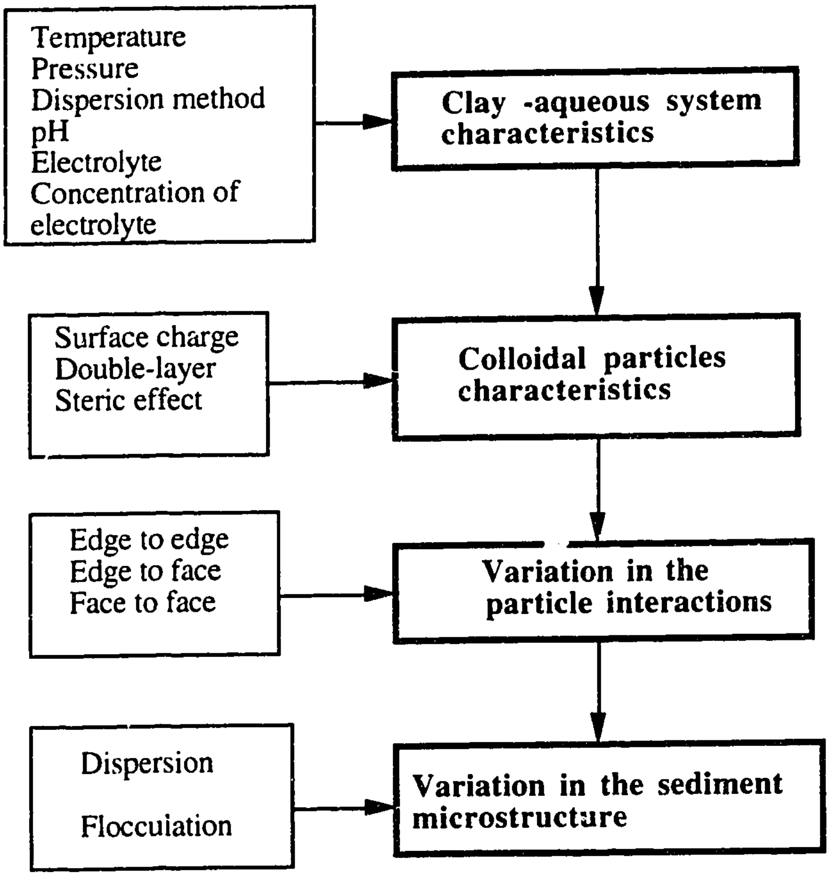
Temperature
Pressure
Dispersion method
pH
Electrolyte
Concentration of electrolyte
Clay -aqueous system characteristics
Surface charge
Double-layer
Steric effect
Colloidal particles characteristics
Edge to edge
Edge to face
Face to face
Variation in the particle interactions
Dispersion
Flocculation
Variation in the sediment microstructure

Fig. 1.2-1- Relationship between the microstructure of a clay sediment and its formation conditions.

CHAPTER 2 - LITERATURE REVIEW

Three domains are reviewed in this chapter: the colloids at large; the properties of clays; and the microstructure of the clay sediments.

2.1 - BACKGROUND OF OIL SANDS TAILING SLUDGE

The oil sands tailing sludge produced in Alberta after bitumen extraction from oil sands by the Hot Water Process. is a complex system. Two major components of the tailing sludge are water and clay minerals. For instance, the tailing sludge in Athabasca contains several clay minerals such as kaolinite, illite and montmorillonite, mixed with quartz [4]. Other minerals including chlorite, calcite, dolomite, siderite, feldspar and ankerite as well as zircon, ilmenite, leucoxene and rutile, were also reported [4, 5].

In relation with these minerals, various cations and anions are present in Alberta's oil sands tailing sludge. The cations include Na^+, K^+, Ca^{2+}, Mg^{2+}, Fe^{2+}, Al^{3+}, Fe^{3+}, and NH^{4+}. The major anions are Cl^-, SO_4^{2-}, and HCO_3^-.

Moreover, various organic compounds, either dissolved in the liquid or associated with clays, including residual bitumen, were detected. The organic composition of a tailing sludge is rather complex. However, the major components are organic acids and polyphenolic compounds [6, 7].

The sedimentation behavior and sediments' microstructure of the oil sands tailing sludge depend on many factors such as the temperature, pH, nature and amount of cations and anions, shape and size of the solid particles, electrical properties of the particle surfaces, and solid content. The pH value of oil sands tailing sludge is higher than 8 [1]. The particle shape of major clay minerals is platelike. The particle size of these minerals covers a wide range. About 12% of the particles have a size smaller than one micron [8, 9]. Clay particles in the oil sands tailing sludge have a zeta potential absolute value as high as 60 mV [6]. The slow settling behavior of the oil sands tailing sludge is partially due to the small size particles and their high zeta potential, in other words, the colloidal properties. Hence, basic knowledge of Colloid Science is first addressed in the following sections.

2.2 - THE COLLOIDS AND THEIR INTERACTIONS

2.2.1 - Terminology

2.2.1.1 - Colloid

A colloid is a material comprised of particles, droplets or bubbles which have a dimension from 10^{-9}m (1nm) to 10^{-6}m (1 μm) [10].

2.2.1.2 - Sol

A sol is a kinetically dispersion of colloidal solid particles within a fluid, which is kinetically stable [10]. It remains dispersed for a relatively long time, by comparison with the time scale of an experiment.

2.2.1.3 - Suspension

A suspension is a dispersion of particles, but may also refer to dispersions of larger sized particles [11].

2.2.1.4 - Floc

A floc is a very open aggregate made with colloidal particles [10].

2.2.1.5 - Stability

A stable system in colloidal science means that the colloids and the liquid in this system do not separate into two phases after a given time, otherwise, this system is unstable [10]. The given time is different for different systems [10]. The data show that, during this given time, the suspension has a constant density over a large height in a cylinder. This constant density is the same as the initial suspension density.

2.2.1.6 - Flocculation

Flocculation is a phenomenon where colloidal particles cluster to form a floc. In sol-gel science, the term coagulation is often used as a synonym to flocculation [10]. In studies on clay microstructure, flocculation refers to edge to face (EF) or edge to edge (EE) linking of the clay particles.

2.2.1.7 - Gel

A gel can be defined as a 3-dimensionally interconnected solid network which is only limited in extent by the size of the container, and which has a high pore volume proportion [12].

2.2.1.8 - Gelation

Gelation is the phenomenon where colloidal particles aggregate to form a gel [13].

2.2.1.9 - Sedimentation

Sedimentation is the phenomenon where the particles in suspension settle under the influence of an external field (gravity or a centrifugal field).

2.2.1.10 Sediment

A sediment is a material deposit which is produced by the sedimentation of a suspension.

2.2.2 - The Electrostatic or Derjaguin, Landau, Verwey, and Overbeek (DLVO) Theory

This theory is well developed in books by P. Hiemenz [10], J. Masliyah [14], Derjaguin et al. [15], Verwey and Overbeek [16] and in a publication by Overbeek [17]. In the DLVO theory, the possible interactions between a pair of particles are limited to the electrostatic repulsion and the van der Waals attraction. The theory can be summarized as follows.

2.2.2.1 - Origins of the electric charge on colloidal particles

Colloidal particles can carry a positive electric charge or a negative electric charge on their surfaces, when in an aqueous medium. This electric charge arises from the following mechanisms [11, 18, 19]:

(1) A different affinity of each phase for ions of different charge. This concerns: (a) the distribution of anions and cations between two immiscible phases, e.g. oil and

water; (b) the different adsorption of different ions from an electrolyte solution onto a solid surface; (c) the different dissolution of different ions from a crystal lattice.

(2) Ionization of surface groups.

(3) Physical entrapment of non-mobile charge in one phase.

(4) Crystalline imperfections of particles.

Many important properties of colloidal systems are influenced by the electric charges on the particle surfaces. These charges can be modified in particular by modifying the pH value in a suspension, which leads to the definition of the pH value where particles are not charged as the zero point of charge (z.p.c.) [13]. This is an important characteristic for a colloid.

2.2.2.2 - The Helmholtz model for an electric double layer

When a particle in a sol is charged, this charge must be compensated for by an excess of ions with an opposite electric charge, in the surrounding liquid. Helmholtz [19] proposed that a charged particle with a surface potential ψ_0 was surrounded by ions of opposite charge at a fixed distance δ_H. These surrounding ions are held in solution by electrostatic forces (Fig. 2.2-1). The charged surface of a particle and the plane of opposite charge at the distance δ_H from the particle surface, form an electric double layer. For a positively charged particle, the electric potential decreases linearly with distance from the particle surface, in the electric double layer. The Helmholtz model allows a straightforward calculation of the electric potential of the charged particle with respect to its surroundings.

2.2.2.3 - The Gouy-Chapman model [10, 16 - 22]

Gouy [20] and Chapman [21] proposed a more realistic model, known as the Gouy-Chapman model, to describe the distribution of ions and electric potential outside of a charged particle in a liquid. In this model, the ions surrounding a particle are not fixed in a plane. Instead, these ions are subjected to electrostatic forces and to thermal diffusion forces. The ions with an opposite charge to the particle are termed the counterions, while

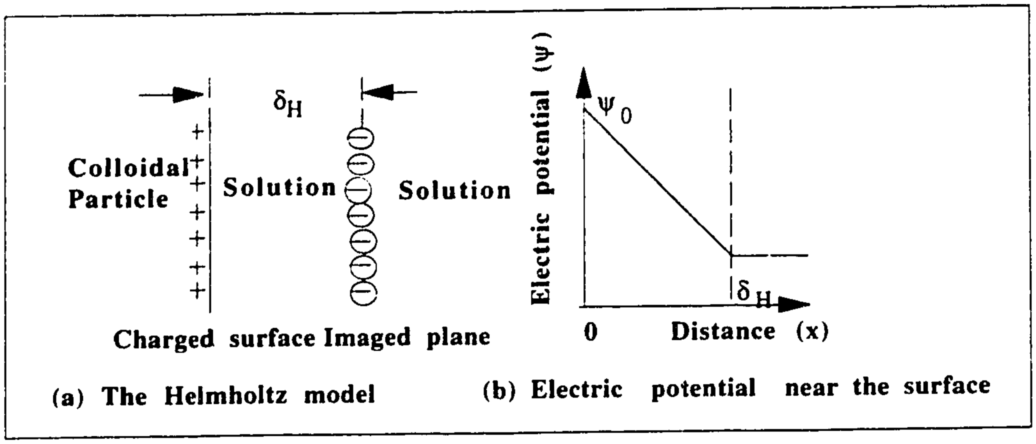
δH
Colloidal Particle
Solution
Solution
Charged surface
Imaged plane
(a) The Helmholtz model
Electric potential (ψ)
ψ0
δH
0
Distance (x)
(b) Electric potential near the surface

Fig. 2.2-1- Schematic representation of the Helmholtz model: (a) the Helmholtz model of electric double layer; (c) distribution of electric potential near the flat surface. After Hunter [19] and Hiemenz [10].

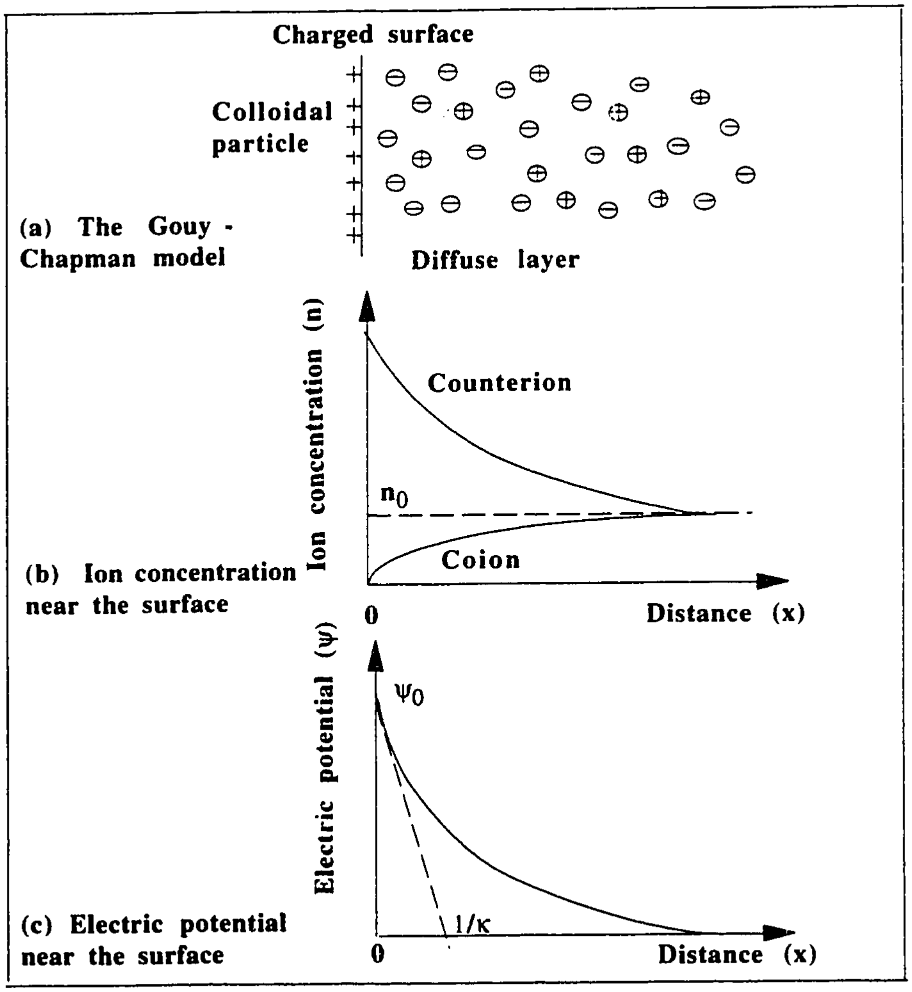
Charged surface
Colloidal particle
(a) The Gouy - Chapman model
Diffuse layer
Ion concentration (n)
Counterion
n0
Coion
(b) Ion concentration near the surface
0
Distance (x)
Electric potential (ψ)
ψ0
1/κ
(c) Electric potential near the surface
0
Distance (x)

Fig. 2.2-2 - Schematic representation of the Gouy-Chapman model: (a) electrical double layer; (b) distribution of the ions around a particle; (c) dependence of the electric potential on the distance from the particle surface. From Shaw [22].

the ions with the same charge as the particle are termed the co-ions (Fig. 2.2-2a). The counterions predominate near the charged surfaces of the particle and the co-ions are excluded. This region near the particle surface constitute an electric diffuse layer, termed the Gouy layer. The charged surface of a particle and the diffuse layer constitute an electric double layer around the particle (Fig. 2.2-2a).

According to this model, the fundamental electrostatic equation which makes it possible to derive the electric potential in this system, is Poisson's equation [10,16]:

$$\nabla^2\psi = -\frac{\rho}{\varepsilon\varepsilon_0} \qquad (2.2\text{-}1)$$

where $\nabla^2 = \frac{\partial 2}{\partial x^2} + \frac{\partial 2}{\partial v^2} + \frac{\partial 2}{\partial z^2}$ is the Laplace operator, ψ is the electrical potential outside the particle surface, ρ is the volume charge density, ε_0 is the dielectric permittivity of the vacuum and ε is the relative dielectric constant of the liquid [18,19].

The concentration of ions surrounding the particles is a function of the local electric potential, as given by the Boltzmann equation [10, 16]:

$$n_i = n_{i0}\exp(-z_i e\psi/kT) \qquad (2.2\text{-}2)$$

In this equation, n_{i0} is the concentration of each ion type i far from the particle, ψ is the local electrical potential, e is the absolute charge of an electron, k is the Boltzmann constant and T is the absolute temperature.

The volume charge density in the neighborhood of the surface is given by [18, 19]

$$\rho = \sum_i n_i z_i e \qquad (2.2\text{-}3)$$

where the summation is over all species i of present ion. After substituting equations (2.2-2) and (2.2-3) in (2.2-1), the Poisson-Boltzmann equation can be obtained:

$$\nabla^2\psi = -\frac{1}{\varepsilon\varepsilon_0}\sum_i n_{i0} z_i e \exp(-z_i e\psi/kT) \qquad (2.2\text{-}4)$$

If the electrical energy is small compared to the thermal energy ($| z_i e\psi | < kT$), it is possible to expand the exponential in the last equation in a series, and to neglect all but the first two terms. This gives [10, 18, 19]

$$\nabla^2\psi = -\frac{1}{\varepsilon\varepsilon_0}\left(\sum_i z_i e n_{i0} - \sum_i z_i^2 e^2 n_{i0}\psi/kT\right) \tag{2.2-5}$$

The first summation term must be zero to preserve electrical neutrality in the bulk solution. Hence

$$\nabla^2\psi = \left(\sum_i \frac{z_i^2 e^2 n_{i0}}{\varepsilon\varepsilon_0 kT}\right)\psi = \kappa^2\psi \tag{2.2-6}$$

where

$$\kappa^2 = \frac{e^2\sum_i z_i^2 n_{i0}}{\varepsilon_0\varepsilon kT} \tag{2.2-7}$$

κ is referred to as the Debye-Hückel parameter. This is an important parameter in colloidal science. Its significance will be discussed in more details below. The simplification which is made when assuming ψ to be very small is known as the Debye-Hückel approximation.

The solution to the equation (2.2-6) under the boundary conditions $\psi = \psi_0$ in the plane x=0, and $d\psi/dx = 0$ and $\psi=0$ in the bulk solution where $x=\infty$, is [10, 16]:

$$\psi = \psi_0 \exp(-\kappa x) \tag{2.2-8}$$

This solution shows an approximate form to the potential distribution near the surface of the particles. However, the approximation is based on the condition [18]

$$\psi_0 < 25.7\times 10^{-3}\ \mathrm{V}/z \ \text{ at } 25°\mathrm{C}$$

which is not satisfied in most situations of interest in colloidal science.

The more general equation (2.2-4) can also be solved in the case of a flat surface. For a symmetrical z:z electrolyte where the cations and anions have the same valence z, the cation concentration (n_+) and the anion concentration(n_-) obey the Boltzmann distribution statistics around a particle (Fig. 2.2-2b) [10, 16].

$$n_+ = n_0\exp(-ze\psi/kT) \text{ and } n_- = n_0\exp(ze\psi/kT) \tag{2.2-9}$$

If the equation (2.2-9) is introduced into the equation (2.2-4), then [10, 16]

$$\frac{d^2\psi}{dx^2} = \frac{2n_0ze}{\varepsilon\varepsilon_0}\sinh\frac{ze\psi}{kT} \tag{2.2-10}$$

where $n_0 = n_{+0} = n_{-0}$ and $z=z_+=-z_-$. Both sides of this equation can be multiplied by $2(d\psi/dx)$, which leads to [10,16]

$$\frac{2d\psi}{dx}\frac{d^2\psi}{dx^2} = \frac{4n_0ze}{\varepsilon\varepsilon_0}\sinh\frac{ze\psi}{kT}\frac{d\psi}{dx} \tag{2.2-11}$$

The equation (2.2-11) can be integrated, after keeping the boundary conditions which were mentioned in the Debye-Hückel approximation. The result is [10, 16].

$$\frac{d\psi}{dx} = -\frac{2\kappa kT}{ze}\sinh\frac{ze\psi}{2kT} \tag{2.2-12}$$

By solving the equation (2.2-12), it can be shown that the electrical potential ψ depends on the distance x from the particle surface, according to the following equation [10, 16] (Fig. 2.2-2c)

$$\gamma = \gamma_0\exp(-\kappa x) \tag{2.2-13}$$

where γ is defined as

$$\gamma = \frac{\exp[(ze\psi)/(2kT)]-1}{\exp[(ze\psi)/(2kT)]+1} \tag{2.2-14}$$

γ_0 is the value at γ near the surface of the particle, where the electric potential is ψ_0.

The electrolyte concentration has an effect on the parameter κ as [18,19]:

$$\kappa = \left(\frac{2000F^2}{\varepsilon\varepsilon_0 R_s T}\right)^{1/2}\sqrt{I} \text{ in units of m}^{-1} \tag{2.2-15}$$

or $$\kappa = 3.288\sqrt{I} \text{ in units of (nm)}^{-1} \tag{2.2-16}$$

for water at 25°C. In these equations , F is the Faraday charge, R_s is the gas constant per mole, and I is the ionic strength (mol L^{-1}) defined by the expression [18]:

$$I = 1/2\Sigma c_i z_i^2 \tag{2.2-17}$$

where c_i is the concentration of ion i in mole L^{-1}. The distance $1/\kappa$ is termed the electric double layer thickness. $1/\kappa$ is 9.6nm when a concentration of a 1:1 electrolyte solution is

1mM. For the systems of interest in colloid science, $1/\kappa$ ranges from a nanometer to about 100nm. If the ionic strength is increased, $1/\kappa$ decreases. The electric potential falls off more rapidly with distance. This effect is referred to as "compression of the electric double layer".

2.2.2.4 - The Stern model

In the Gouy-Chapman model, the size of ions is neglected. In real systems, the ions have a finite size and they can approach a surface to a distance which cannot be less than their radius. To take this size effect into account, Stern [23] proposed a model where the electric double layer near the surface of a particle, is comprised of two parts. First, the ions adsorbed on the surface of a particle form an compact inner boundary layer. This inner layer is termed the Stern layer and its thickness (δ_d) (Fig. 2.2-3a) is approximately given by the diameter of a hydrated ion. Secondly, beyond the compact layer, the ions form a diffuse layer as in the Gouy-Chapman model. The boundary between the Stern layer and the diffuse layer is referred to as the Stern plane. The electrical potential at this Stern plane is called the Stern potential ψ_d (Fig. 2.2-3b). According to the Stern model, the electric potential decreases linearly with the distance, in the Stern layer. Hence this electric potential is described by the equation (2.2-18) [10]:

$$\frac{\psi_0 - \psi_d}{\delta_d} = \frac{\sigma_s}{\varepsilon_0 \varepsilon_s} \tag{2.2-18}$$

where ε_0 is the dielectric permittivity of the vacuum, ε_s is the relative dielectric constant of the Stern layer, ψ_0 is the electric potential near the surface of the particle and σ_s is the surface charge density of occupied sites on the Stern surface. The Stern surface charge density can be calculated by the following equation [24]:

$$\frac{\sigma_s}{\sigma_0} = \frac{N_s \exp(\frac{ze\psi_d + \phi)}{kT})}{1 + N_s \exp(\frac{ze\psi_d + \phi)}{kT})} \tag{2.2-19}$$

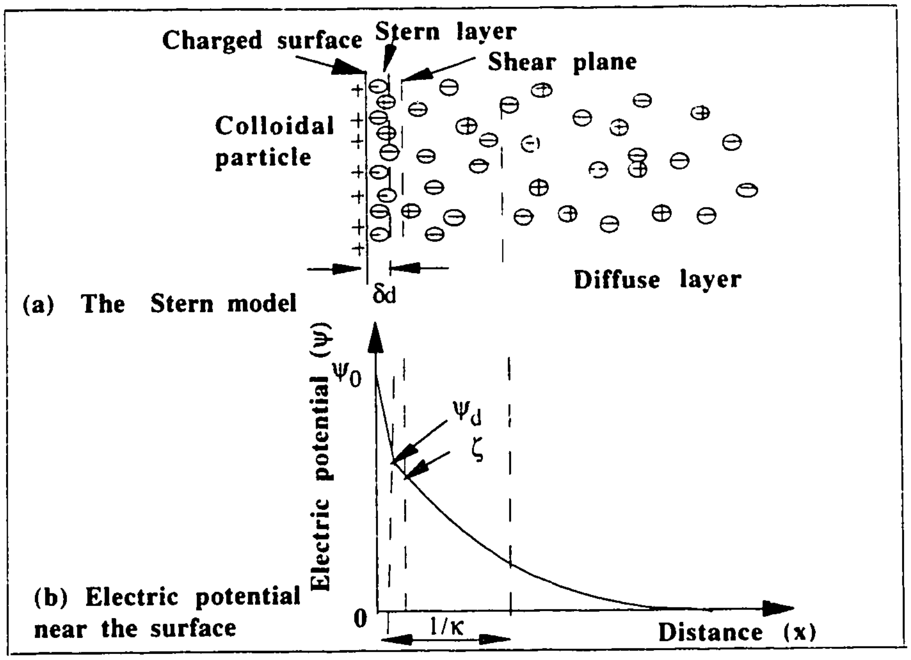
Charged surface
Stern layer
Shear plane
Colloidal particle
(a) The Stern model
δd
Diffuse layer
Electric potential (ψ)
ψ_0
ψ_d
ζ
(b) Electric potential near the surface
0
1/κ
Distance (x)

Fig. 2.2-3 - Schematic illustration of the Stern model: (a) electrical double layer; (b) electric potential as a function of the distance from a particle surface. From Shaw [22].

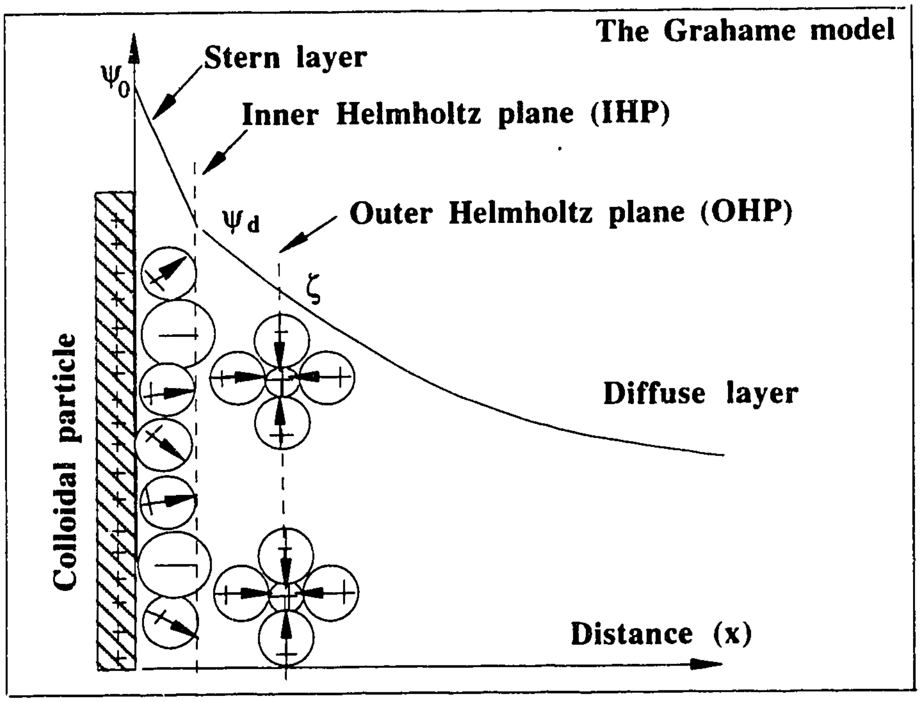
The Grahame model
ψ_0
Stern layer
Inner Helmholtz plane (IHP)
ψ_d
Outer Helmholtz plane (OHP)
ζ
Diffuse layer
Colloidal particle
Distance (x)

Fig. 2.2-4. Schematic illustration of the Grahame model and a possible electric potential distribution near the particle surface. After Hunter [18] and Adamson [24].

where σ_0 is the surface charge density of the particle surface, N_s is the number of adsorption sites, and ϕ is the addition chemical potential for adsorption. In the diffuse layer, the distribution of the electric potential follows the equation (2.2-2) where ψ_0 and x must be replaced by ψ_d and $x-\delta_d$.

2.2.2.5 - Zeta potential

In practice, a zeta potential is easy to measure experimentally. The zeta potential ζ is defined as the electric potential at the shear interface between the liquid which moves with a particle, and the surrounding liquid which does not move with the particle (Fig. 2.2.2b). ζ can be experimentally determined by measuring the velocity of a particle under an electric field, which gives the electrophoretic mobility, u, of the colloidal particles. This electrophoretic mobility is defined as the velocity of a particle per unit field [10, 18]. The classical equation to calculate the zeta potential is [10, 18]:

$$u = \frac{\varepsilon\varepsilon_0\zeta}{\eta} \qquad (2.2\text{-}20)$$

where ε and ε_0 are previously defined and η is the viscosity of the medium.

The Stern potential ψ_d was sometimes regarded as same as the zeta potential for a colloidal system in the previous section. Actually, they are different. Fig. 2.2-4 shows the schematic illustration of the Grahame model for the electric double layer [25], after modification by Bockris [26]. The plane which separates the unhydrated anions adsorbed on a positive particle surface, from the next hydrated cations, is termed the Inner Helmholtz Plane (IHP) [24]. The plane passing through the center position of the hydrated cations is termed the Outer Helmholtz Plane (OHP) [24]. The electric potential at the IHP corresponds to the Stern potential while the electric potential at the OHP corresponds to the zeta potential [18, 24].

Another important characteristic for a colloid is the pH for which the zeta potential is zero [27]. This pH is termed the isoelectric point (i.e.p). The i.e.p of a system is related to its z.p.c.. However, they are different in many colloidal systems [18].

2.2.2.6 - The electrostatic repulsion between two colloidal particles

Electrostatic repulsion arises from the interaction between the electric double layers of two particles. In the case of platelike particles, this is illustrated in Fig. 2.2-5.

Let us consider two flat particles which each have a constant electric surface potential, with the respective values ψ_{10} and ψ_{20}. These surface potentials remain constant irrespective of the separation gap $2h_o$ between the plates. The repulsion force (F) or the pressure (P) between the 2 plates, in a z:z electrolyte, can be described by the following equation which is obtained by solving the Poisson equation [14].

$$P = \frac{F}{A_p} = \frac{e^2z^2n_0}{kT}\left(\frac{2\psi_{10}\psi_{20}\cosh 2\kappa h_o - \psi_{10}^2 - \psi_{20}^2}{\sinh^2 2\kappa h_o}\right) \qquad (2.2\text{-}21)$$

where A_p is the surface area of the flat plate.

In the special case where $\psi_{10}=\psi_{20}=\psi_0$, the above expression reduces to

$$P = \frac{F}{A_p} = \frac{2e^2z^2n_0\psi_0^2}{kT}\left(\frac{\cosh 2\kappa h_o - 1}{\sinh^2 2\kappa h_o}\right) \qquad (2.2\text{-}22)$$

For small values of $2\kappa h_0$, that is to say for $2\kappa h_0 << 1$, one can write $\cosh 2\kappa h_0 \cong 1 + (2\kappa h_0)^2/2$ and $\sinh 2\kappa h_0 \cong 2\kappa h_0$. Then, equation (2.2-22) transforms to (2.2-23)

$$\frac{F}{A_p} = \frac{2e^2z^2n_0\psi_0^2}{kT} = \frac{1}{2}\varepsilon\varepsilon_0\kappa^2\psi_0^2 \qquad (2.2\text{-}23)$$

This equation indicates that for small κ, that is to say for a thick double layer, the force per unit area is proportional to ψ_0^2 and it is independent of the separation gap.

For $2\kappa h_0 >> 1$, $\cosh 2\kappa h_0 \approx \sinh 2\kappa h_0 \approx (1/2)e^{2\kappa h_o}$. Equation (2.2-22) became

$$\frac{F}{A_p} = \frac{4e^2z^2n_0\psi_0^2}{kT}e^{-2\kappa h_o} \qquad (2.2\text{-}24)$$

In the case where the 2 particles respectively have the constant surface electric potentials ψ_{10} and ψ_{20}, the repulsion energy is given by the following expression [28]:

$$U_R^{\psi-\psi} = \frac{\varepsilon\varepsilon_0\kappa}{2}\left(\left(\psi_{10}^2+\psi_{20}^2\right)(1 - \coth 2\kappa h_o) + 2\psi_{10}\psi_{20}\,\mathrm{cosech}\, 2\kappa h_o\right) \qquad (2.2\text{-}25)$$

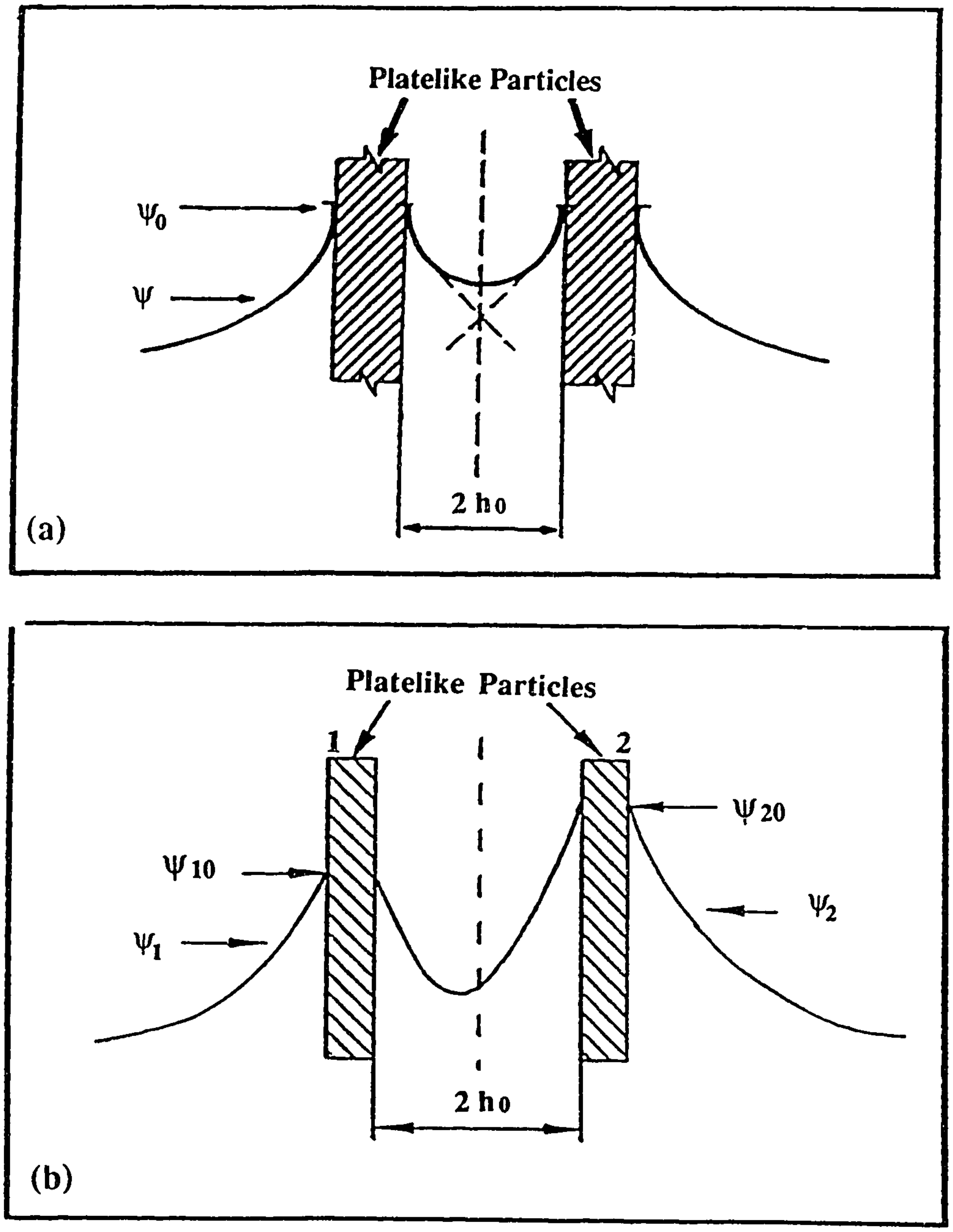
Platelike Particles
ψ0
ψ
2 ho
(a)
Platelike Particles
1
2
ψ10
ψ20
ψ1
ψ2
2 ho
(b)

Fig. 2.2-5 - Schematic illustration of two overlapping electric double layers: (a) particles with an identical electric surface potential; (b) particles with a different electric potential.

In the case of two parallel platelike particles with respective constant surface charge densities σ_1 and σ_2 [29,30]

$$U_R^{\sigma-\sigma} = \frac{1}{2\varepsilon\varepsilon_0\kappa}\left(\left(\sigma_1^2+\sigma_2^2\right)(\coth 2\kappa h_o - 1) + 2\sigma_1\sigma_2 \operatorname{cosech} 2\kappa h_o\right) \qquad (2.2\text{-}26)$$

The 2 surface charge densities can be replaced by the electric potentials ψ_{10} and ψ_{20} when the 2 particles are separated by an infinite gap, which gives:

$$U_R^{\sigma-\sigma} = \frac{\varepsilon\varepsilon_0\kappa}{2}\left(\left(\psi_{10}^2+\psi_{20}^2\right)(\coth 2\kappa h_o - 1) + 2\psi_{10}\psi_{20} \operatorname{cosech} 2\kappa h_o\right) \qquad (2.2\text{-}27)$$

If one particle has a constant surface electric potential ψ_{10} and the other particle has a constant surface charge density σ_2 [31].

$$U_R^{\psi-\sigma} = \frac{1}{2}\left(\left(\frac{\sigma_2^2}{\varepsilon\varepsilon_0\kappa} - \varepsilon\varepsilon_0\kappa\psi_{10}^2\right)(\tanh 2\kappa h_o - 1) + 2\psi_{10}\sigma_2 \operatorname{sech} 2\kappa h_o\right) \qquad (2.2\text{-}28)$$

Considering the electric potentials ψ_{20} of the constant charge particle when the 2 particles are at an infinite separation gap, the previous equation can be transformed to:

$$U_R^{\psi-\sigma} = \frac{\varepsilon\varepsilon_0\kappa}{2}\left(\left(\psi_{20}^2-\psi_{10}^2\right)(\tanh 2\kappa h_o - 1) + 2\psi_{10}\psi_{20} \operatorname{sech} 2\kappa h_o\right) \qquad (2.2\text{-}29)$$

Let us consider two platelike particles which have the respective electric surface potentials $\psi_{10} = 0.01$ V and $\psi_{20} = 0.03$ V and $\kappa = 1 \times 10^8\ \mathrm{m}^{-1}$, when their separation gap is infinite. The electrostatic potential energy, calculated from equations (2.2-25), (2.2-27) and (2.2-29), depends on the separation gap as shown in Fig. 2.2-6 [29]. This graph shows $U_R^{\psi-\sigma}$ and $U_R^{\psi-\psi}$ have negative values when κh_0 is small. This phenomenon is due to a charge reversal on the particle which has the lowest surface electric potential [14].

2.2.2.7 - The van der Waals attraction

The van der Waals attraction is caused by the dipole-dipole interaction of molecules in materials. The van der Waals attraction between two platelike particles of thickness δ and a separation gap $2h_0$ between their surfaces, is by the Hamaker summation method [10, 16, 19, 27]:

$$U_A = -\frac{A}{12\pi}\left[\frac{1}{(2h_0)^2} + \frac{1}{(2h_0+2\delta)^2} - \frac{2}{(2h_0+\delta)^2}\right] \qquad (2.2\text{-}30)$$

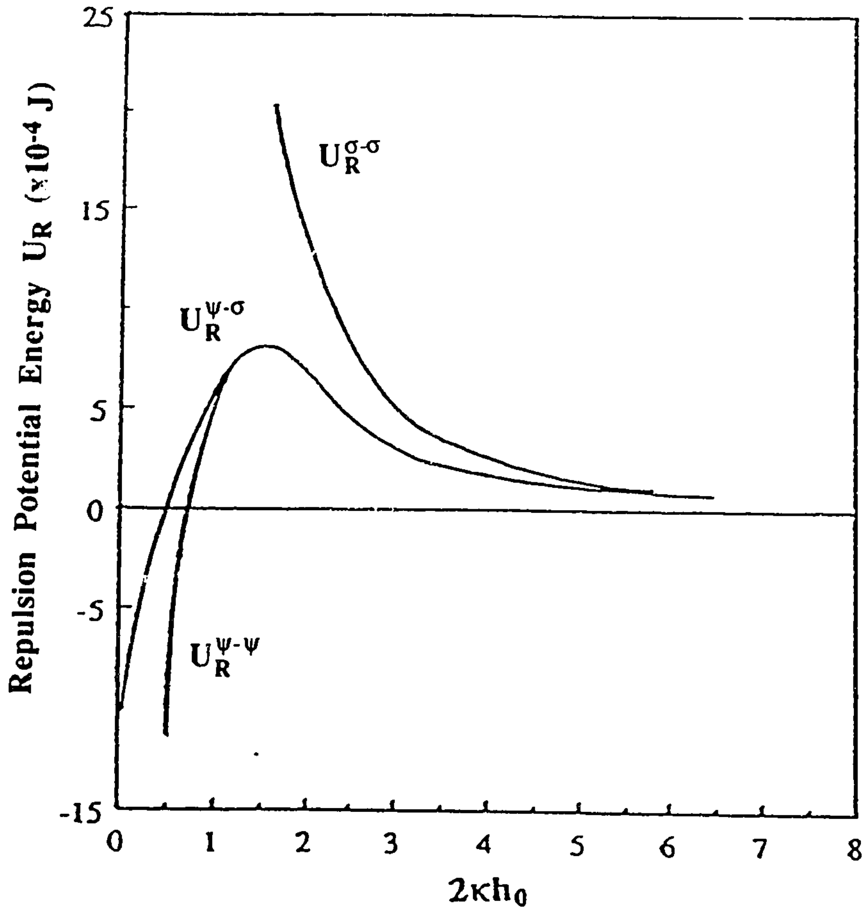

Fig. 2.2-6 - Electrostatic potential energy as a function of the separation gap between two dissimilar platelike particles for different surface conditions, when $\psi_{10} = 0.01$ V, $\psi_{20} = 0.03$ V and $\kappa = 1 \times 10^8$ m^{-1}. From Wang [29].

As $\delta \to 0$

$$U_A = -\frac{A}{12\pi(2h_0)^2} \qquad (2.2\text{-}31)$$

In the above two equations, A is termed the Hamaker constant. This constant is related to the properties of a material, especially the polarizability property and the number of molecules per unit volume in this material [10]. The Hamaker constant is measured with energy units, usually in the range of 10^{-20} to 10^{-19} J [10].

2.2.2.8 -Total interaction potential energy - Flocculation

Fig. 2.2-7 shows a qualitative sketch of the total potential energy, as a function of the separation gap. This total energy is the resultant of the repulsive and of the attractive forces [10, 16, 17]:

$$U_{total} = U_A + U_R \qquad (2.2\text{-}32)$$

The graph of U_{total} may show a maximum, termed the energy barrier, and two minima termed the primary minimum and the secondary minimum. Traditionally, it is considered that when the energy barrier is too high (>15kT [10]) to be overcome by the thermal agitation, as in the curve labeled "stable" in Fig. 2.1.5b, the colloidal system is stable. When an energy barrier smaller than 15kT exists [10], as in the curve labeled "metastable" (Fig. 2.2-7b) the energy barrier can be overcome with a non negligible probability by the Browian motion. In this case, a sol is not stable and a slow flocculation occurs. The system is unstable and rapid flocculation occurs when the energy barrier is wiped out as in the curve labeled "unstable" (Fig. 2.2-7b).

2.2.2.9 - The Schulze-Hardy rule

In the DLVO theory, the critical flocculation concentration (CFC) is defined as the concentration of electrolyte below which fast flocculation does not occur. The empirical Schulze-Hardy rule states that the valence z of only the counterions controls the value of the CFC. On the other hand, the valence of the co-ions is not important [10]. According to this rule:

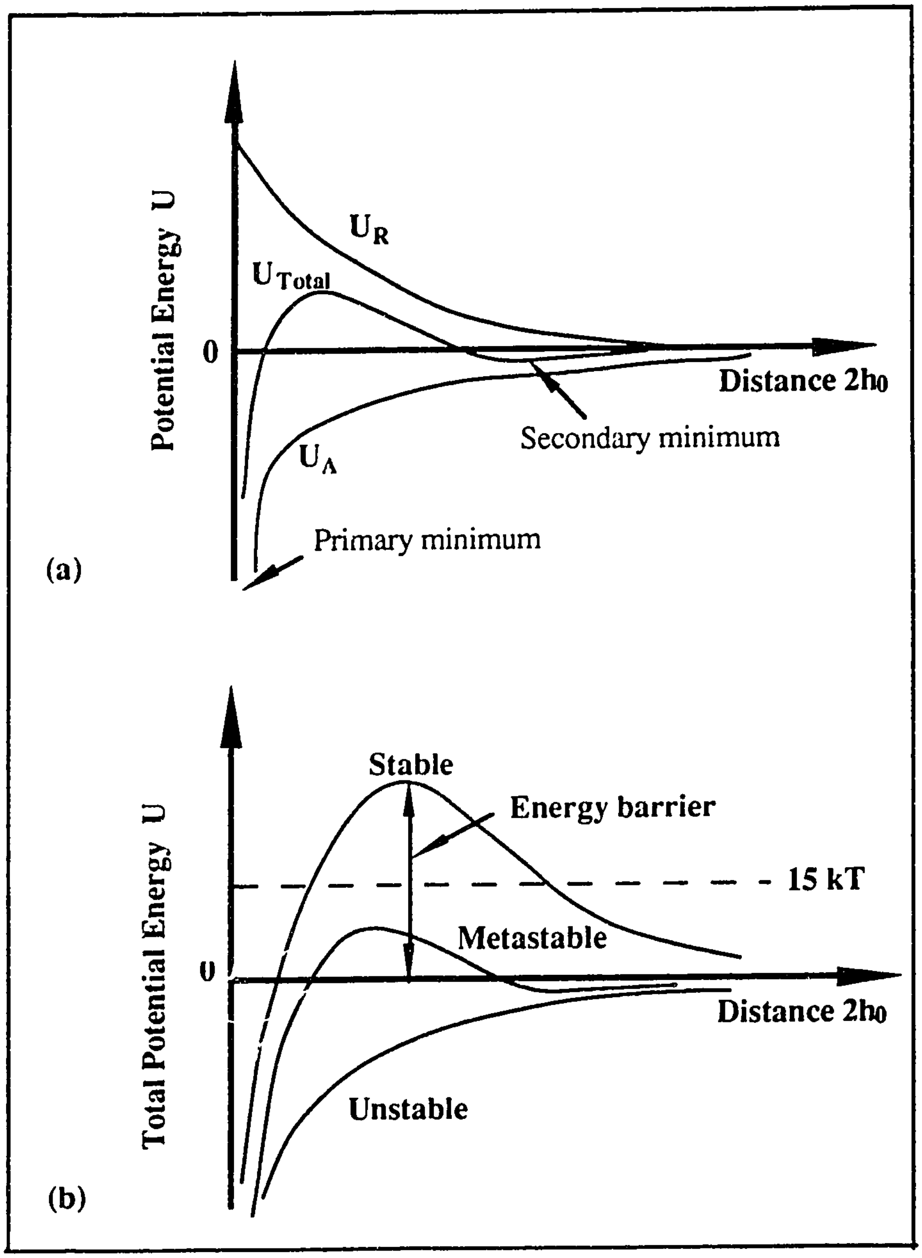
(a)
Potential Energy U
0
U_R
U_{Total}
U_A
Distance $2h_0$
Secondary minimum
Primary minimum
(b)
Total Potential Energy U
0
Stable
Energy barrier
15 kT
Metastable
Distance $2h_0$
Unstable

Fig. 2.2-7 - Qualitative sketch of the potential energy as a function of the separation gap between two particles: (a) U_{total}, U_R and U_A; (b) 3 possible different shapes of U_{total}. After Hiemenz [10].

$$CFC \propto z^{-6} \tag{2.2-33}$$

The great success of the DLVO theory is to provide an explanation for the Schulze-Hardy rule. If we consider two flat particles, rapid flocculation occurs under the following two conditions:

$$U_{total} = 0 \tag{2.2-34}$$

and

$$\frac{dU_{total}}{dh_0} = 0 \tag{2.2-35}$$

Solving these 2 previous equations for a z:z electrolyte, leads to the Schulze-Hardy relation.

2.2.2.10 - Steric effects

The stability of a colloidal system can also be influenced by the steric interactions. These interactions are due to the adsorption of macromolecules. They are beyond the scope of this thesis which is focused on the sediments made by clays with electrolytes.

2.2.3 - Gels

2.2.3.1 - Gelation

Gelation can occur in a polymeric or in a colloidal system. This is a critical phenomenon which occurs when a sol transforms to a gel. This phenomenon designates the successive addition of colloidal particles to an open floc which slowly builds up an infinite network. The gel point or the gelation time (t_c) is the time at which a network, forms in a polymeric or in a colloidal system, which is only limited in extent by the size of the container [12]. Fig. 2.2-8 shows how the viscosity η of a sol and the elastic shear modulus G of a gel change with the reaction time, in a sol-gel transition. At the gel point, the viscosity goes towards an infinite value and an elastic modulus appears. In this graph, the reaction time could be replaced with the proportion of inter-particle bonds. Consequently, a critical proportion p_c of bonds must establish to reach the gel point.

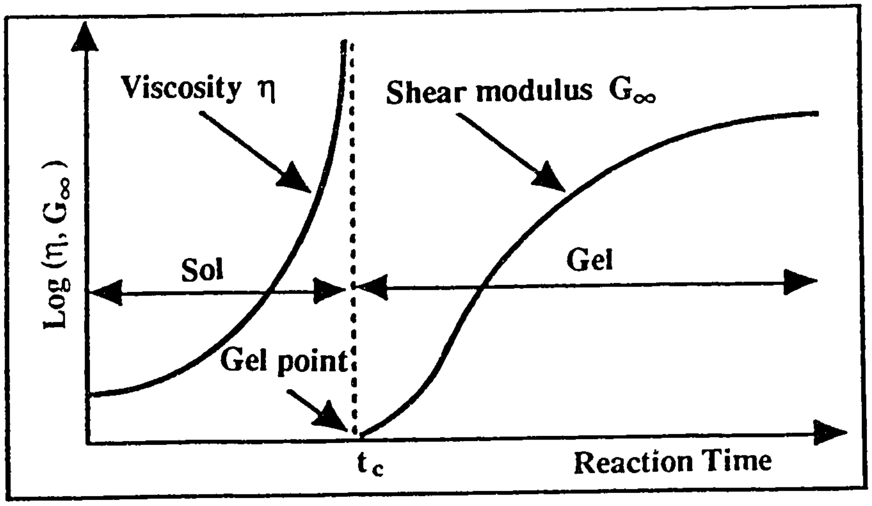

Fig. 2.2-8- Schematic representation of the steady state shear viscosity and of the elastic modulus of a colloid during the sol-gel transition. From Pierre [12].

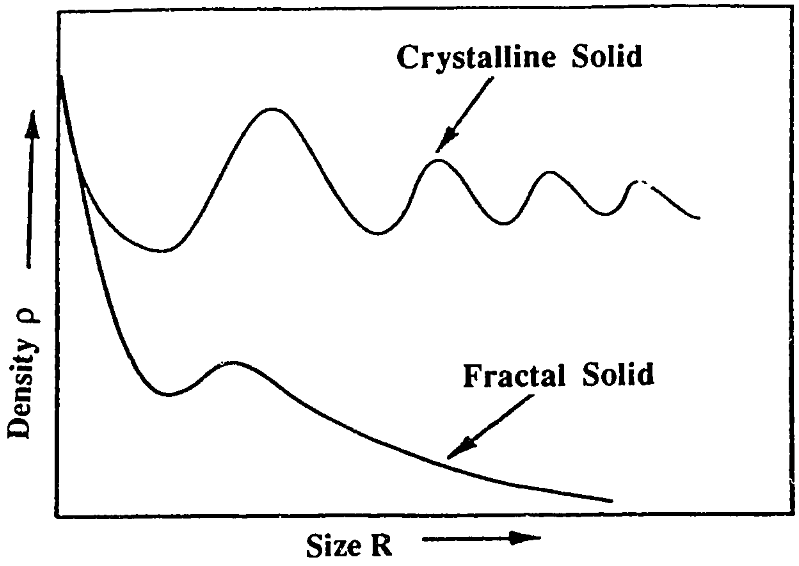

Fig. 2.2-9 - Compared densities of fractal solids and of crystalline solids, as a function of their size R. From Hench and West [32]

Near the gel point, the viscosity and the elastic modulus depend on the proportion of bonds as indicated in equations (2.2-36) and (2.2-37) [33]:

$$\eta \sim (p-p_c)^{-k} \qquad (2.2\text{-}36)$$

$$G \sim (p-p_c)^{\beta} \qquad (2.2\text{-}37)$$

Besides the viscosity and the elastic modulus, when approaching the critical probability point from the sol side ($p<p_c$) the average mass (M_{ave}) of a cluster approaches infinity according to equation (2.2-38). Also, the average size of a cluster (R_{ave}) approches an infinite value according to equation (2.2-39) [12]:

$$M_{ave} \sim (p-p_c)^{-\gamma} \qquad (2.2\text{-}38)$$

$$R_{ave} \sim (p-p_c)^{-\nu} \qquad (2.2\text{-}39)$$

Finally, at the gel point ($p = p_c$), a full range of clusters with a different size exists. However, only one cluster is unlimited in size. The probability P(M) that a cluster may have a mass M is given by equation (2.2-40). The geometry of the unique unlimited cluster is such that, from any colloidal particle in the cluster, chosen as the center of a sphere of radius R, the average mass M of the cluster which is inside this sphere depends on R according to equation (2.2-41) [12].

$$P(M) \sim M^{-\tau} \qquad (2.2\text{-}40)$$

$$R(M) \sim M^{1/f} \qquad (2.2\text{-}41)$$

The exponent "f" is termed a fractal dimension [34] and the cluster is termed a fractal object. The densities of a fractal solid and of a crystalline solid, as a function of their size R, are compared in Fig.2.2-9. Fractal structures are further analyzed in the next section.

Gelation can be regarded as a special case of flocculation in a colloidal system. In fact it is known that the gelation of colloidal dispersions obeys the Schulze-Hardy rule with respect to the influence of the concentration of electrolytes [12]. Besides the CFC previously introduced, a critical gelation concentration CGC can be defined. For an electrolyte which does not modify the electric state on the particle surfaces (indifferent or non-potential determining electrolyte), a colloidal dispersion is stable against gelation when the electrolyte concentration is $C < CGC$, while fast flocculation occurs when $C > CFC$. The colloidal dispersion slowly gels if $CGC < C < CFC$ [12].

If the rate of adhesion of the particles to each other (v_a) and the rate of sedimentation of flocs (v_s) are compared, $v_a >> v_s$ for gelation and $v_a \leq v_s$ for sedimentation [35]. Pierre [36] indicated that a linear bonding of colloidal particles, or an edge-to-edge (EE) association of the particles when they have platelike shape, can easily produce the phenomenon of gelation. According to the DLVO theory, a linear aggregation of particles to form a gel will more likely occur when the electric double layer thickness is comparable with the radius of curvature of the particles.

2.2.3.2 - Fractal structures.

The occurrence of fractal structures was introduced in the previous section. A fractal structure is a structure made of porous parts which have a shape similar to the complete structure [37]. The packing architecture of the particles which constitute a fractal structure is characterized by its fractal dimension, as this was introduced in equation (2.2-41). The fractal dimension can be further described as follows.

Let N(R) be the minimum number of spheres of radius R, which is necessary to completely cover all the matter in an object. Then the fractal dimension can be defined as the following mathematical limit [38,39]

$$f = \mathrm{Lim}_{R \to 0} \frac{\log N(R)}{\log R} \qquad (2.2\text{-}42)$$

This definition can be applied to a bi-dimensional object where the Euclidean dimension is d=2 or to a 3-dimensional object where d = 3. For a conventional, non fractal solid object f = d. However f no longer is an integer for a fractal object. The difference between a conventional object and a fractal object is illustrated in the bi-dimensional model in Fig. 2.2-10. This figures shows that f=d= 2 for a conventional object (Fig. 2.2-10a) and f < 2 for a fractal object in (Fig. 2.2-10b).

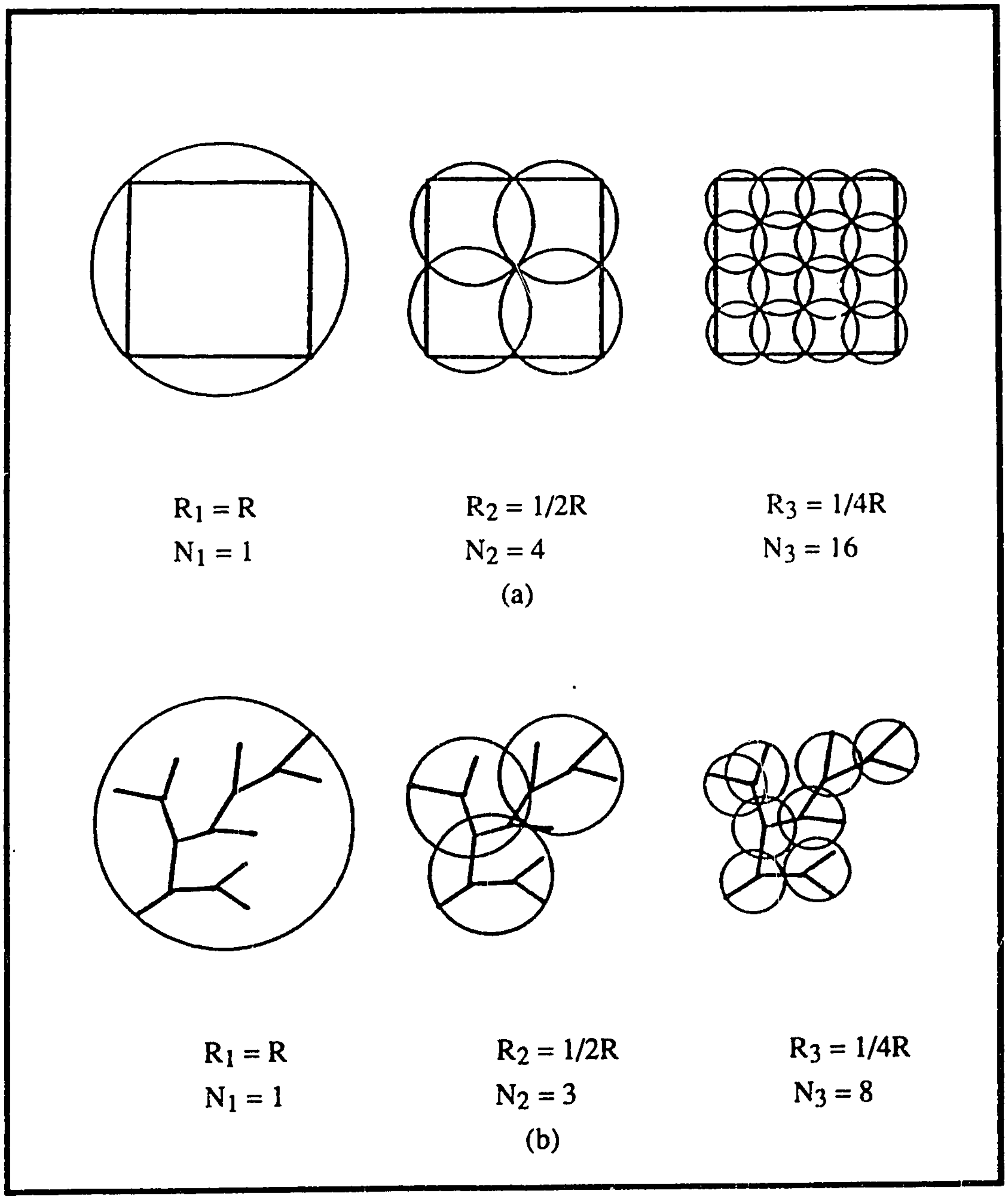
$R_1 = R$
$N_1 = 1$
$R_2 = 1/2R$
$N_2 = 4$
$R_3 = 1/4R$
$N_3 = 16$
(a)
$R_1 = R$
$N_1 = 1$
$R_2 = 1/2R$
$N_2 = 3$
$R_3 = 1/4R$
$N_3 = 8$
(b)

Fig. 2.2-10- Bi-dimensional illustration of: (a) a conventional object ($f=d=2$); and (b) a fractal object ($f < 2$).

The formation kinetics of fractal aggregates can be simulated on a computer. These computer simulations are known as growth-aggregation models. Several of these models were proposed and they can be classified into two types: the monomer-cluster aggregation models and the cluster-cluster aggregation models [40]. The monomer-cluster growth requires a continual source of monomers which undertake a random walk and which preferentially aggregate with a cluster when they meet one of them. In a cluster-cluster model, the clusters also undertake a random walk and they aggregate with each other.

The aspect of aggregates which are formed according to these models are shown in Fig. 2.2-11. The monomer-cluster model which is the best known is the diffusion-limited-aggregation model, or DLA [41], and the aggregates which are built are known as the DLA clusters or aggregates. The fractal dimension of DLA aggregates is $f \approx 1.71$, for the planar models and $f \approx 2.5$ for the 3-dimensional models [10]. The cluster-cluster models are also known as hierarchical models, because a hierarchy of aggregations of monomers to clusters and of clusters to clusters, occurs [40]. DLA growth does not produce the phenomenon of gelation in the thermodynamics sense, as this occurs with true polymers. However, as the clusters grow, they eventually fill up the available space, as this is illustrated in Fig. 2.2-12.

2.2.4 - Sedimentation

2.2.4.1 - No Flocculation occurs during sedimentation

Sedimentation tests are often carried out to study the stability of colloidal dispersions. If the particles in a dispersion do not flocculate, each particle settles individually. The settling velocity v_s of a spherical particle in a liquid medium can be calculated by the Stokes equation [10]:

$$v_s = \frac{2g(\rho_p - \rho_L)R^2}{9\eta} \qquad (2.2\text{-}43)$$

	REACTION-LIMITED	BASLLISTIC	DIFFUSION-LIMITED
MONOMER-CLUSTER	EDEN 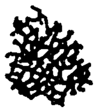 f = 3.00	VOLD 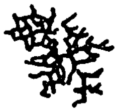 f = 3.00	WITTEN-SANDER 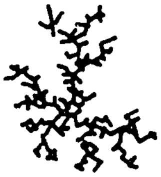 f = 2.50
CLUSTER-CLUSTER	RLCA 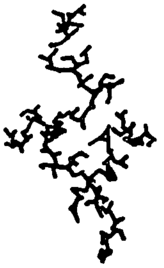 f = 2.09	SUTHERLAND 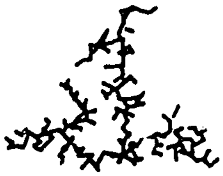 f = 1.95	DLCA 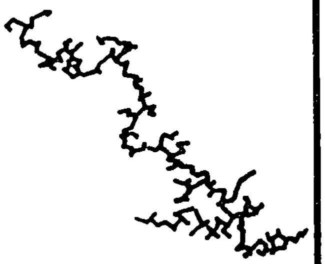 f = 1.80

Fig. 2.2-11 - Structural aspect of 2-dimensional clusters obtained from various computer simulation growth models. The fractal dimensions which are listed are for the equivalent 3-d clusters. From Brinker, et al.[40].

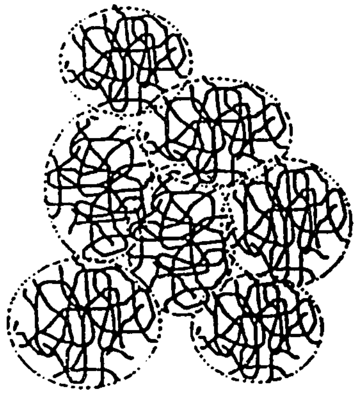

Fig. 2.2-12 - Space-filling clusters. From Brinker et al. [40]

In this equation, ρ_p and ρ_L are the densities of the particle and of the liquid, respectively, R is the particle radius, η is the liquid viscosity and g is the acceleration due to gravity.

The derivation of the Stokes equation is based on the following assumptions [10, 19] : (1) the velocity of particles is small and the fluid is kept laminar during sedimentation; (2) the liquid medium is a continuous phase compared with the size of the particles in the suspension; (3) the suspension is very dilute and there is no interaction between particles; (4) particles are rigid spheres; (5) no solvatation occurs.

The conditions (1) and (2) are always satisfied in a colloidal system [19]. In practice, the radius of particles (or the average radius for a distribution of particles) can be measured by a sedimentation method based on Stokes equation. However, actual particles are often solvated, non-spherical, or both. Hence, the radius of particles with a non-spherical shape derived from the Stokes equation is termed an equivalent radius in hydrodynamics [10]. The Stokes equation has to be revisited if a suspension is concentrated, which is discussed in detail in reference [19]. Also, when electrical double layers are developed around particles in a colloidal system, the electrical double layer interaction modifies the sedimentation behavior of particles and the viscosity of a suspension [18]. This is known as the electroviscous effect. Consequently, the Stokes equation has to be revised according to the electroviscous effect. In terms of the above assumptions, the Stokes equation can be applied up to particles with a radius of 100 μm [29]. The effect of diffusion on the sedimentation has to be reconsidered when the radius of particles is smaller than 0.1 μm [29].

2.2.4.2 - Flocculation occurs at the beginning of sedimentation

The difference between the particles packing in a sediment settled from a dispersed suspension and in a sediment settled from a flocculated suspension, is illustrated in Fig. 2.2-13 .

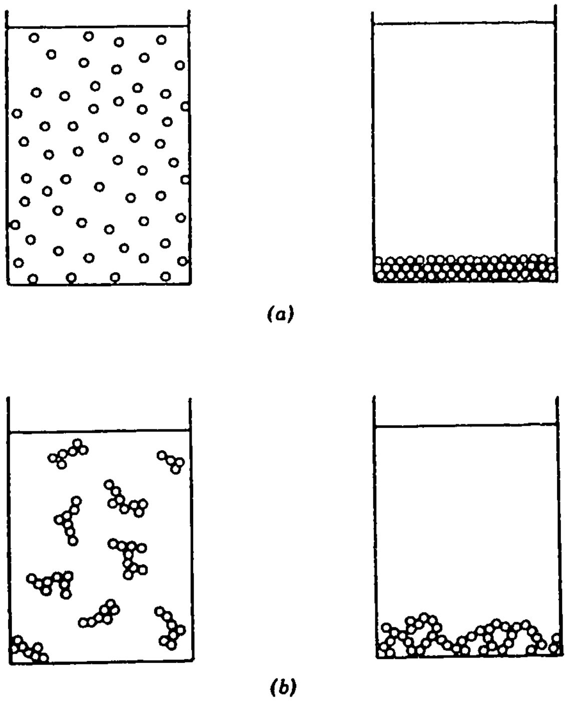

Fig. 2.2-13 - Sedimentation from: (a) a dispersed suspension; (b) a flocculated suspension. From Van Olphen [27].

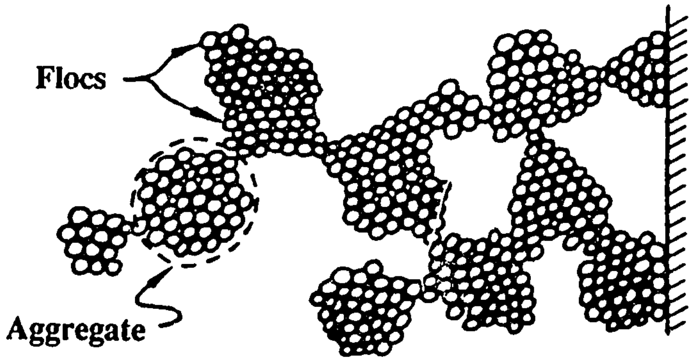
Flocs
Aggregate

Fig. 2.2-14 - Floc-aggregate structure from Michaels and Bolger [42]

The flocculated particles form a loose, voluminous sediment, whereas a relatively dense sediment of closely packed particles forms from a dispersed suspension. Actually, three phenomena can be in competition: (1) the formation of flocs; (2) the settling of these flocs; (3) the compacting of the sediment when the flocs form a wall to wall network.

Michaels and Bolger [42] developed a model to describe the sedimentation behavior of flocculated suspensions. In this model, the primary particles form small clusters, termed flocs. These flocs have a certain mechanical strength and they are capable of retaining their identity under very mild shear forces such as in the collisions experienced during settling. It is assumed that these flocs have a nearly spherical shape and that they tend to approach a uniform size under a given shear field. This size increases as the clay concentration increases or as the shear rate decreases. At low shear rates the flocs tend to group into clusters of flocs, designated by Michaels and Bolger as aggregates. These aggregates may join together to form an extended network as illustrated in Fig. 2.2-14. This network may extend from wall to wall in the container where sedimentation is performed, and it gives some plastic properties to the sediment. Also, a sharp interface is formed between the sediment network and the supernatant liquid.

In the model by Michaels and Bolger [42], for a dilute suspension of particles which undertakes flocculation, the settling rate $\frac{dH}{dt}$ for the sharp interface is described by the following equations [42]:

$$\frac{dH}{dt} = v_{SA}\ (1 - C_{Ap}\Phi_p)^{4.65} \tag{2.2-44}$$

$$v_{SA} = \frac{2g(\rho_p - \rho_L)R_A^2}{9\eta C_{Ap}} \tag{2.2-45}$$

In this equation, v_{SA} is the settling velocity for a single aggregate, R_A is the average spherical diameter of one aggregate, and $C_{Ap} = \frac{\Phi_A}{\Phi_p}$ where Φ_A is the aggregate volume fraction in the suspension while Φ_p is the particle volume fraction, η is the liquid medium viscosity and ρ_p and ρ_L are the densities of the particles and of the liquid.

Equations (2.2-44) and (2.2-45) make it possible to obtain some experimental characteristics on the aggregates density and on their size, by measuring the settling rate of a flocculated dilute suspension.

A more sophisticated theory of sedimentation was developed by Buscall and White [43]. In this theory, three forces were taken in consideration: (1) the gravitational or the centrifugal driving force, (2) the viscosity drag force associated with the flow of liquid in the sediment and (3) a particle or network stress developed as the result of direct particle-particle interactions. The initial settling rate is given approximately by:

$$\left(\frac{dH}{dt}\right)_0 = -\frac{(1-\Phi_p)v_s}{R(\Phi_p)}\left(1 - \frac{1}{B}\right) \qquad \text{when } B > 1 \qquad (2.2\text{-}46a)$$

$$\left(\frac{dH}{dt}\right)_0 = 0 \qquad \text{when } B < 1 \qquad (2.2\text{-}46b)$$

In these equations, $B = (\rho_p - \rho_L)\Phi_p H_0/\tau_B(\Phi_p)$, v_s is the sedimentation rate of an isolated particle, Φ_p is the initial volume fraction of.particles, $R(\Phi_p)$ is a dimensionless hydrodynamic interaction parameter, H_0 is the initial sediment height, $\tau_B(\Phi_p)$ is an estimate of the yield stress of the network of particles and $(\rho_p - \rho_L)$ is the density difference between the initial particles and the liquid.

Michaels and Bolger [42] showed that the final sediment volume V_F depends on the volume fraction of the flocs in the suspension ($C_{Ap}\Phi_p$) and on the initial suspension volume V_0 according to:

$$V_F = \frac{V_0 C_{Ap}\Phi_p}{0.62} + b \qquad (2.2\text{-}47)$$

where b is constant which describes the upper low density zone in the sediment.

2.2.5 - Rheological properties [27,42,44]

2.2.5.1 - Types of flow

A liquid is a Newtonian fluid when it flows at a shear rate $\frac{d\gamma}{dt}$ which depends on the applied shear stress τ according to the simple linear relation:

$$\tau = \eta\frac{d\gamma}{dt} \qquad (2.2\text{–}48)$$

η is a proportionality constant which is termed the viscosity. Such a Newtonian flow is illustrated in Fig. 2.2-15.

A suspension or liquid which does not flow according to equation (2.2-48) is a non-Newtonian liquid. Several types of non-Newtonian flow behavior are illustrated in Fig. 2.2-15. The viscosity of a non-Newtonian liquid may be time-dependent or shear rate dependent.

A fluid with a time-independent flow behavior is termed a dilatant fluid when its viscosity increases with the shear rate. It is termed a pseudo-plastic fluid when its viscosity decreases as the shear rate increases, and when no yield stress must be overcome to make the fluid flow. The fluid is termed a plastic, or a viscoplastic or a Bingham fluid when its viscosity decreases as the shear rate increases, and if it requires a stress higher than a yield stress to flow. In a Bingham (or plastic or viscoplastic) flow, the linear part of the curve in Fig. 2.2-15. is described by :

$$\tau - \tau_B = \eta_\Delta \frac{d\gamma}{dt} \qquad (2.2\text{-}49)$$

In this equation, τ_B is termed the Bingham yield stress and η_Δ is the differential viscosity. The yield stress is sensitive to the types of particle interaction in a suspension

A time-dependent flow behavior is termed rheopexy when the viscosity increases with the shear rate and with the time. It is termed thixotropy when the viscosity decreases as the shear rate and as the time increase. A typical flow curve for a thixotropic material is shown in Fig. 2.2-16. It is characterized by the occurrence of a hysteresis loop.

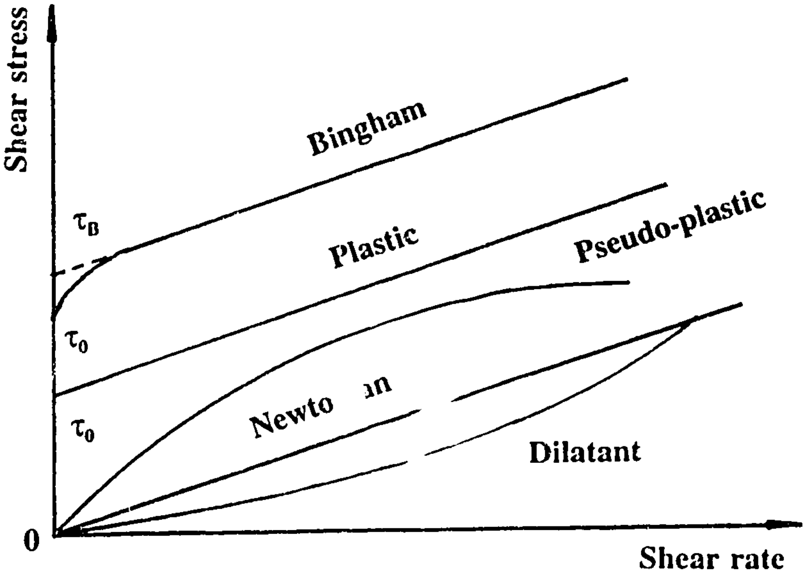

Fig. 2.2-15 - Different types of flow behavior for a fluid. After van Olphen [27].

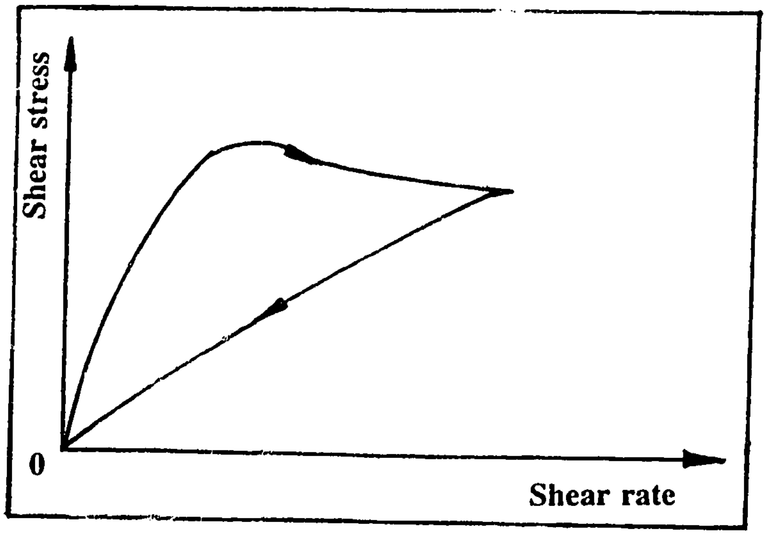

Fig. 2.2-16 - Typical hysteresis loop in the flow curve for a thixotropic fluid. After Moore [44].

2.2.5.2 - Rheological properties of suspensions [10, 44, 45]

The rheological behavior of suspensions is very sensitive to particle interactions. Hence, rheological studies make it possible to obtain some information on these particle interactions and on the modes of particle association.

In general, the rheological properties of a suspension depend on: (1) the viscosity of the liquid medium; (2) the solids content of the suspension; (3) the size and the shape of the particles; and (4) the colloidal interactions between the particles, since these interactions are responsible for the stability of a suspension, or for its flocculation.

A suspension of solid particles in a liquid is always characterized by a higner viscosity than the liquid alone. In most cases, the suspended particles have a spherical shape which is larger than the molecules of the suspending liquid. If these particles do not interact with each other or with the liquid, and if the solids content of the suspension is low, the viscosity η of this suspension is well described by the Einstein equation:

$$\eta /\eta_L = 1+2.5\Phi_p \qquad (2.2\text{-}50)$$

where η_L is the viscosity of the suspending medium and Φ_p is the volume fraction of the solid spheres.

For a high concentration of spheres, the previous relation must be replaced by [45]:

$$\frac{\eta}{\eta_L} = \left(1 + \frac{1.25\Phi_p}{1-\Phi_p/0.74}\right)^2 \qquad (2.2\text{-}51)$$

These relations indicate that the size of the suspended particles is unimportant. The only variable is the particles volume fraction. Also, such suspensions are Newtonian.

In a suspension, platelike particles can undertake random rotations. Hence, such particles can approach each other far more closely than spherical particles do, for a given particle volume fraction. In practice, the suspensions which are comprised of small platelike particles begin to show a marked non-Newtonian behavior even for a low particle volume fraction. Frisch and Simha [46] derived the following equation for the viscosity of a dispersion of prolate ellipsoids:

$$[\eta] = \frac{\eta/\eta_L - 1}{\Phi_p} = \frac{14}{15} + \frac{(a/b)^2}{15(\text{Ln } 2a/b - \lambda)} + \frac{(a/b)^2}{5(\text{Ln } 2a/b - \lambda + 1)} \quad (2.2\text{-}52)$$

In this equation, $[\eta]$ is termed the intrinsic viscosity or limiting viscosity number, a/b is the axial ratio of an ellipsoid and λ is a shape factor which has the value 1.5 for an ellipsoid and 1.8 for a cylindrical rod.

Equations (2.2- 51) and (2.2 - 52) concern suspensions of dispersed particles. If the particles attract each other and if they build some aggregates, the suspension behavior may be determined by the size, the structure and the properties of the aggregates rather than by the individual particles.

Let us assume that the individual particles are platelike. The chemical conditions in a suspension may be such that aggregation of particles in a face-to-face (FF) manner is favored (Fig. 2.2-17a). If the volume fraction of particles in the suspension is low, this kind of aggregation results in a decrease of the suspension viscosity as the proportion of particles which are associated in the FF manner increases (Fig. 2.2-17b). This is due to the fact that no structure is built by association of these FF aggregates. These FF aggregates behave as dispersed particles in a suspension [45].

On the other hand, if the volume fraction of the platelike particles is sufficiently high, these FF aggregates can build a structure termed bookhouse aggregation, illustrated in Fig. 2.2-17c. Such a construction greatly increases the viscosity by comparison with what would be expected from a dispersed suspension, for a given solid content, as illustrated in Fig. 2.2-17d [45].

Platelike particles can also flocculate by edge to face (EF) or edge to edge (EE) association. The resulting structure is termed a "card-house" and it is illustrated in Fig. 2.2-17e.

Such a structure occupies a high volume in the suspension. The viscosity of the suspension increases with the number of EE or EF links, as illustrated in Fig. 2.2-17f [11].

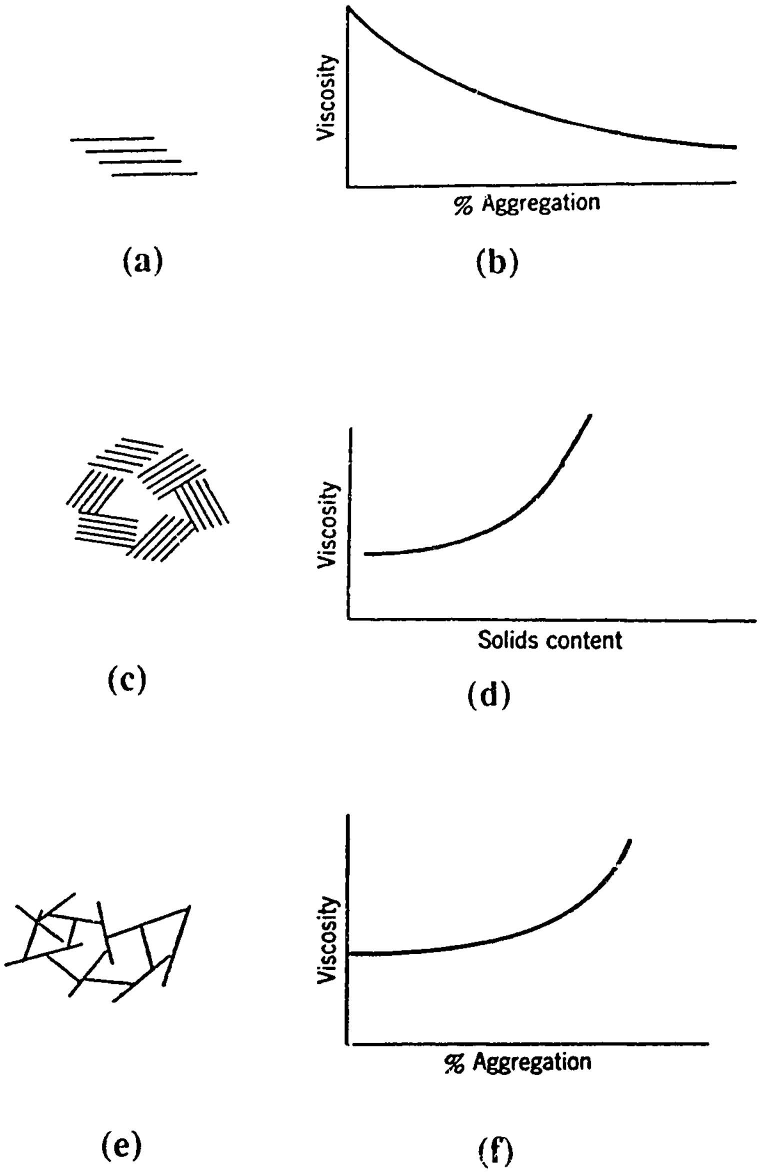
Viscosity
% Aggregation
(a)
(b)
Viscosity
Solids content
(c)
(d)
Viscosity
% Aggregation
(e)
(f)

Fig. 2.2-17. Platelike particles aggregation modes: (a) FF association and (b) its effect on the suspension viscosity; (c) bookhouse aggregation and (d) its effect on the suspension viscosity; (e) card-house aggregation and (f) its effect on the suspension viscosity. After Michaels [45].

2.3 COLLOIDAL PROPERTIES OF CLAYS

2.3.1 - Crystal structure and ion exchangeability of clays

Clays are aluminosilicate minerals, such as kaolinite, montmorillonite, and illite, which are comprised of platelike particles. The size of these particles can range from a few times 0.01μm to several μm. Consequently, clays may have a significant specific surface area which ranges from a value of the order $10 m^2/g$ for kaolinite, to a value of the order of $100 m^2/g$ for illite and for montmorillonite [27].

The ideal chemical formulas of kaolinite, montmorillonite and illite are given in Table 2.3-1 [47]. The crystal structures of these common clay minerals are based on a combination of $(Si_2O_5)_n$ sheets with $AlO(OH)_2$ sheets. A silica sheet is comprised of SiO_4 tetrahedra which are linked at their corners with the octahedra of a adjacent alumina sheet. In kaolinite, a layer is comprised of one silica sheet and of one alumina sheet. Hence this mineral is also termed a 1:1 layer clay. In montmorillonite and in illite, a central $AlO(OH)_2$ sheet is sandwiched in between two Si_2O_5 sheets and these clays are termed 2:1 layer clays. The layer structures of kaolinite, of montmorillonite and of illite are illustrated in the in Fig. 2.3-1 [48]. Mica is a special type of illite where x=y=0 in Table 2.3-1.

Table 2.3-1 - Ideal chemical composition of common clays. After Kingery, et al. [47]

Kaolinite	$Al_2(Si_2O_5)(OH)_4$
Montmorillonite	$\left(Al_{1.67}\begin{matrix}Na_{0.33}\\Mg_{0.33}\end{matrix}\right)(Si_2O_5)_2(OH)_2$
Illite (mica: x=y=0)	$Al_{2-x}Mg_xK_{1-x-y}(Si_{1.5-y}Al_{0.5+y}O_5)_2(OH)_2$

In clays, an isomorphous substitution of the cations is frequent. In this way, Al^{3+} and sometimes Fe^{3+} may substitute for some of the Si^{4+} ions in the silica tetrahedral sheets, while Mg^{2+} and Fe^{2+} may substitute for Al^{3+} in the alumina octahedral sheets.

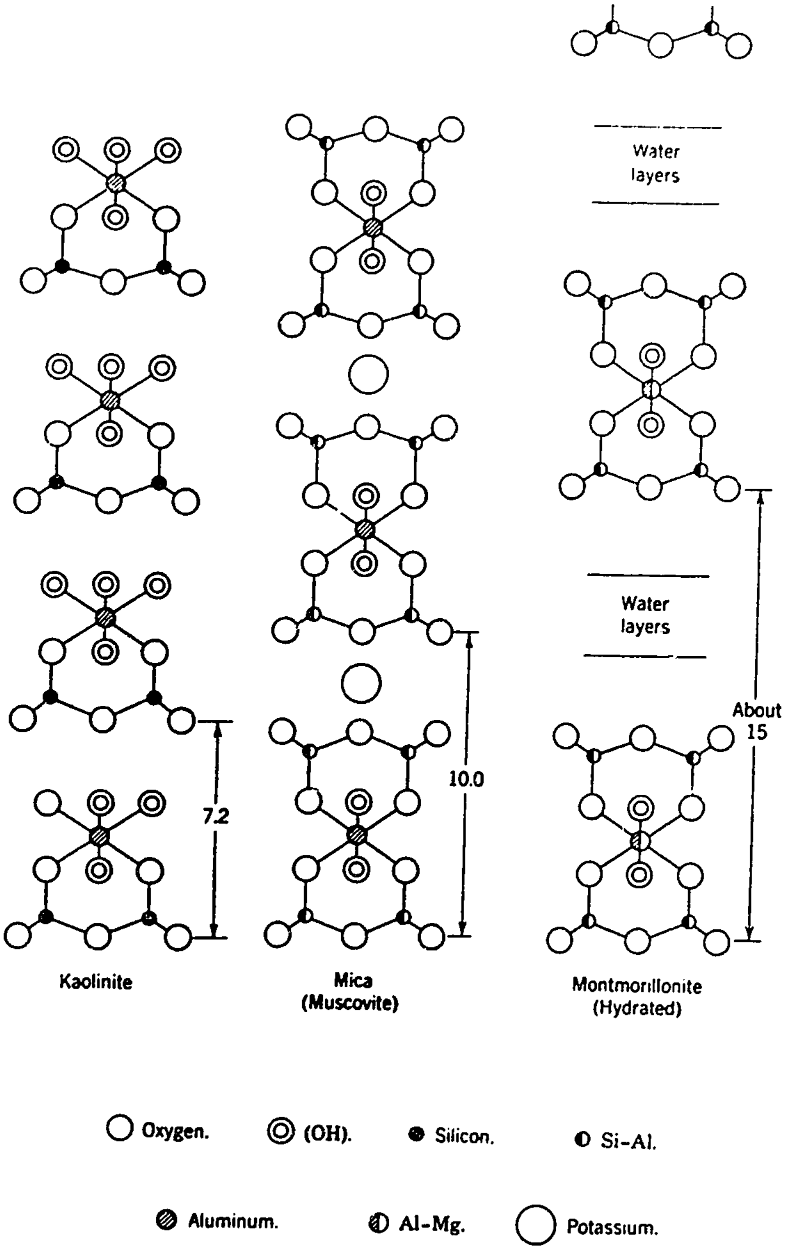
Water layers
Water layers
7.2
10.0
About 15
Kaolinite
Mica (Muscovite)
Montmorillonite (Hydrated)
Oxygen.
(OH).
Silicon.
Si-Al.
Aluminum.
Al-Mg.
Potassium.

Fig. 2.3-1- Layer structures of kaolinite, of mica (illite with x=y=0 in the Table 2.3-1) and of montmorillonite. After Brindley [48].

These isomorphous substitutions provide a net negative charge to a clay atomic layer. To balance this negative layer charge, some cations such as Na^+ or Ca^{2+} intercalate between the clay atomic layers and some are adsorbed on the faces of the clay particles. These face cations are loosely held by the clay particles. They can move away from the clay faces, when the clay is in dispersed in an aqueous medium. Hence the clay faces take a negative electric charge while the loosely held face cations participate in the counterion diffuse layer. Also, these cations can more or less readily be exchanged for other cations and they are responsible for the ion exchange capacity of clays.

When a clay which contains X^+ cations is immersed in a solution of an electrolyte which is comprised of Y^+ cations, a cation exchange between the clay and the electrolyte occurs. This exchange can be summarized by the reaction:

$$\text{X-clay} + Y^+ \Leftrightarrow \text{Y-clay} + X^+ \qquad (2.3\text{-}1)$$

The extent of the above exchange depends on the nature of the clay, X^+ and Y^+, and on the concentration of these reactants [49]. The cation exchange capacity (C.E.C.) of a clay is expressed in milliequivalent (meq) per gram, or per 100g, of the dry clay (meq/100 g). The equivalent mass of an element is defined as the mass of this element which combines with or displaces one mole of hydrogen ion, directly or indirectly [50]. The gram-equivalent of this element is expressed in gram. One equivalent gram is equal to 1000 milliequivalent grams. The ranges of typical C.E.C values for kaolinite, montmorillonite and illite are gathered in Table 2.3-2.

Table 2.3-2. Cation exchange capacity of clay minerals. After Brindley [48]

Minerals	C.E.C. (milliequivalents /100g dry clay)
Kaolinite	3 - 15
Montmorillonite	75 - 150
clay mica (illite)	10 - 40

Many studies have addressed the mechanism of cation exchange [27, 48, 49, 51]. For the same concentration, some cations are more readily adsorbed than others. The readiness of adsorption of cations decreases in the following order (termed lyotropic or Hofmeister series) [49]:

$$H>Al>Ba>Sr>Ca>Mg>NH_4>K>Na>Li \qquad (2.3\text{-}2)$$

The exchange of anions is also possible. However, this is not as prominent a phenomenon as cation exchange.

2.3.2 - Electric double-layer structure of clay particles

Generally, the net charge on a clay particle is negative in aqueous solutions. The zero point of charge (z.p.c.) of Na-kaolinite in aqueous media is between pH 2.8 and 4.8 [52], e.g., 3.9 according to Williams et al. [53] and 4.2 according to Yong et al. [54]. In a broad description, all the cations including the exchangeable cations are part of the counterions above the z.p.c. They form the diffuse and the Stern electrical layers, in the electrical double layer structure around the particles. However, in reality, the structures of the electric double layers near the faces and near the edges of clay particles, are quite different.

2.3.2.1 - The double layer near the faces of clay particles [27, 49]

The faces of platelike clay particles carry a net negative charge in an aqueous medium, as a result of the isomorphous substitutions which were mentioned previously. The exchangeable cations act as counterions in the electric double layer structure of these faces. In practice, the faces of clay particles have a constant electric charge density σ which is only determined by the type and the extent of isomorphous substitution. No z.p.c can be measured for these faces. As a function of the nature of the clay and on the experimental method used to determine this charge density, σ ranges from -0.100 to -0.700 Cm^{-2} [55].

Although usually the faces of clay particles are negatively charged, it is possible to reverse the sign of this charge by the adsorption of some polymeric organic cations, such as the long chain ammonium salts [11].

2.3.2.2 - The double layer near the edges of clay particles [11, 27, 48, 51]

The atomic structure of the clay particles edges is entirely different from the structure of their faces. At the edge, the tetrahedral silica sheet and the octahedral alumina sheet terminate with broken primary bonds. A broken bond, such as the aluminum-oxygen bond, can provide a positive charge to an edge, as a function of the pH. Moreover, it is possible to measure a z.p.c. for these edges. The z.p.c. of kaolinite particles edges is between pH=6.5 [56] and 7.8 [52], with a value of 7.2 according to Williams et al. [53].

Several experimental results support the existence of positive charges on the edges of kaolinite particles. The best known of these experiments consists of the observation in a transmission electron microscope of mixtures of kaolinite and negative gold sols, in conditions where the colloidal gold particles are negatively charged [57, 58]. The micrographs clearly showed the colloidal gold particles were only adsorbed on the edges of the kaolinite particles. Indirectly, the existence of positive charges on the edges of kaolinite particles is also supported by experimental results on the flocculation and the rheological behaviors[59, 60].

The sign of the charges on the edges of kaolinite can be reversed in two ways. One way consists of increasing the concentration of potential-determining OH ions by adding a base so as to increase the pH of a suspension beyond the z.p.c. of the particles edges. The second method consists of adding an electrolyte which is comprised of anions which are chemisorbed on the particle edges. These anions should form a complex with the clay cations, such as Al, which are exposed at the broken bonds of the edges. Such anions include the fluoride anion, the polymetaphosphate anions, and a number of organic anions[11].

2.3.2.3 - The zeta potential of clay particles

The global zeta potential measured on clays represents a balance of the electric charges on the faces and on the edges. Fig. 2.3-2 shows the relationship between this zeta potential and the pH for Na-illite , for Na-montmorillonite and for Na-kaolinite.

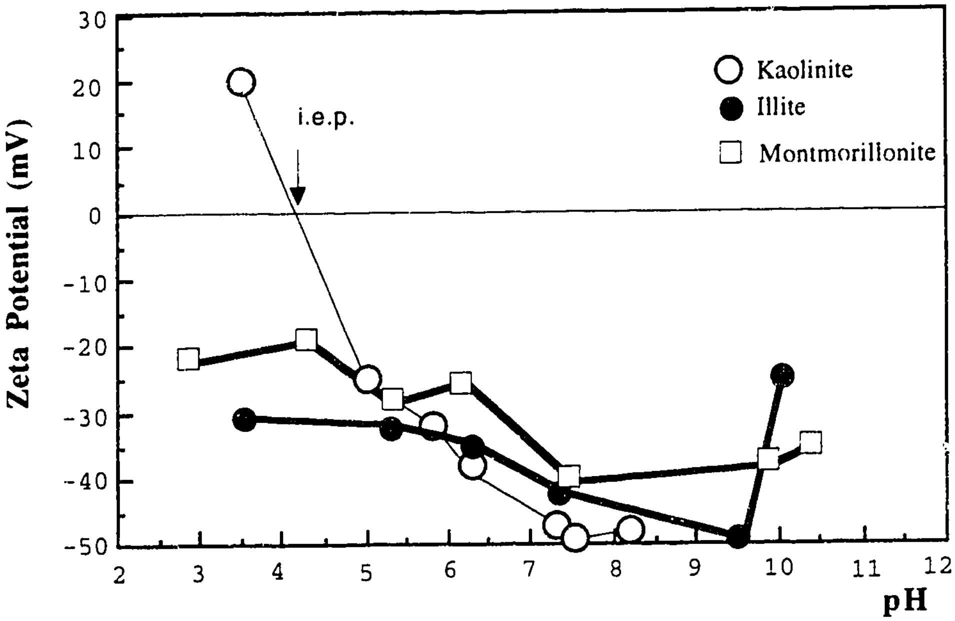

Fig. 2.3-2 - Relationship between the pH and the zeta potential, in an aqueous medium, of Na-kaolinite (after Yong et al. [54]) and of Na-illite (after Ohtsubo et al. [61]), of Na-Montmorillonite (after Avena et al. [62]).

The i.e.p. of Na-kaolinite is close to its global z.p.c., with a value of 4.2 according to Yong et al. [54]. No i.e.p. could be determined for Na-montmorillonite and for Na-illite, since their zeta potentials remain negative in the pH range from 3.0 to 10.5.

2.3.3 - Interactions between clay particles

A number of publications reported the results of calculations on the interactions between clay particles, according to the DLVO theory. These results can be classified in two groups, as a function of whether the electric charges on the faces and on the edges of the clay particles have the same sign, or if they have an opposite sign.

2.3.3.1 - The edges and the faces have opposite electric charges

When clay particles carry opposite charges on their edges and on their faces, the basic mode of particles association is edge-to-face (EF). For instance, such an association was considered by Flegmann et al. [63] and the result of their calculation of the total interaction energy U_{total} between two parallel surfaces is shown in Fig. 2.3-3a, as a function of the separation distance $2h_0$ between the 2 surfaces. This figure shows that no energy barrier opposes the EF aggregation, contrary to the face-to-face (FF) and the edge-to-edge (EE) association modes.

Tateyama et al. [64] studied the dependence of U_{total} on the EF inclination angle θ. They showed that U_{total} was negative (i.e., an attraction) for $\theta_{min} < \theta \leq 90°$ (Fig. 2.3-4). The attraction is maximum for $\theta = 90°$. The value of θ_{min} depends on the plate thickness δ, on the shortest separation gap $2h_0$ between the particles, and on the electrolyte concentration. The θ_{min} value typically is in a range from 20° to 45 °.

2.3.3.2 - The edges and the faces carry electric charges with the same sign

This case was also considered by Flegmann et al.[63] and it was compared with the previous one. The results of their calculation are shown in Fig. 2.3-3b. This figure

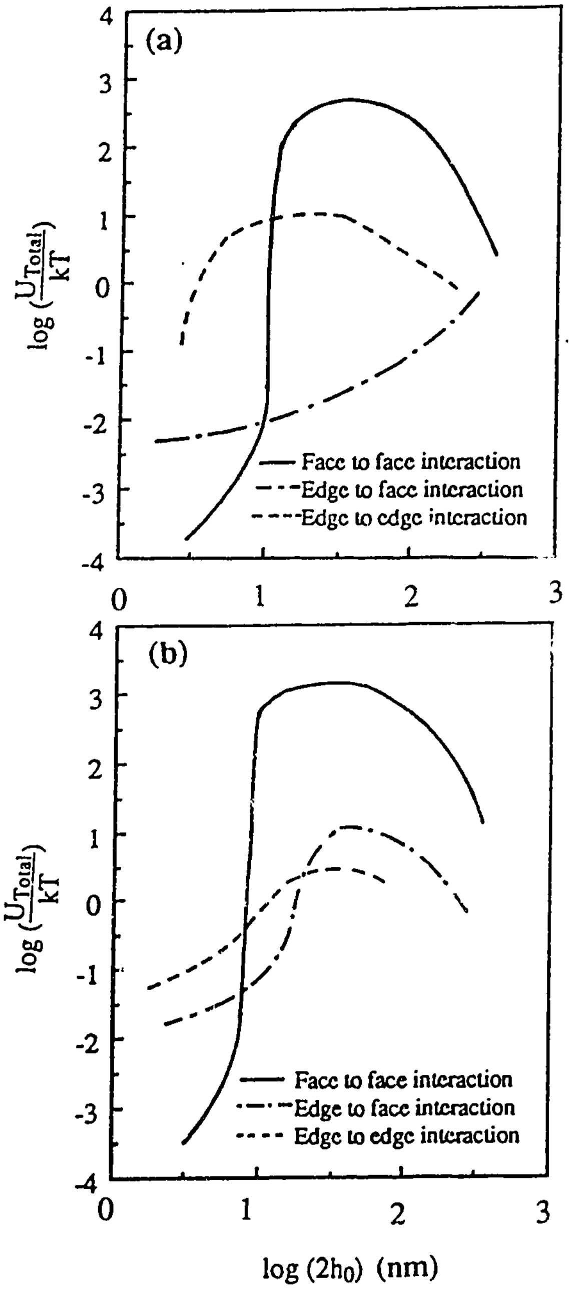

Fig. 2.3-3 - Total potential interaction energy U_{total}, as a function of the separation gap $2h_0$ between the parallel surfaces of two kaolinite particles, for different surface electric potentials ψ_{fo} on the faces, and ψ_{e0} on the edges: (a) opposite charges $\psi_{fo} = -0.031$ V and $\psi_{\varepsilon 0} = 0.02$ V; (b) charges of same sign $\psi_{fo} = -0.046$ V and $\psi_{e0} = -0.01$ V. The electrolyte was NaCl at 10^{-4} M, and the plate thickness was 1.6×10^{-7} m. After Flegmann et al. [63].

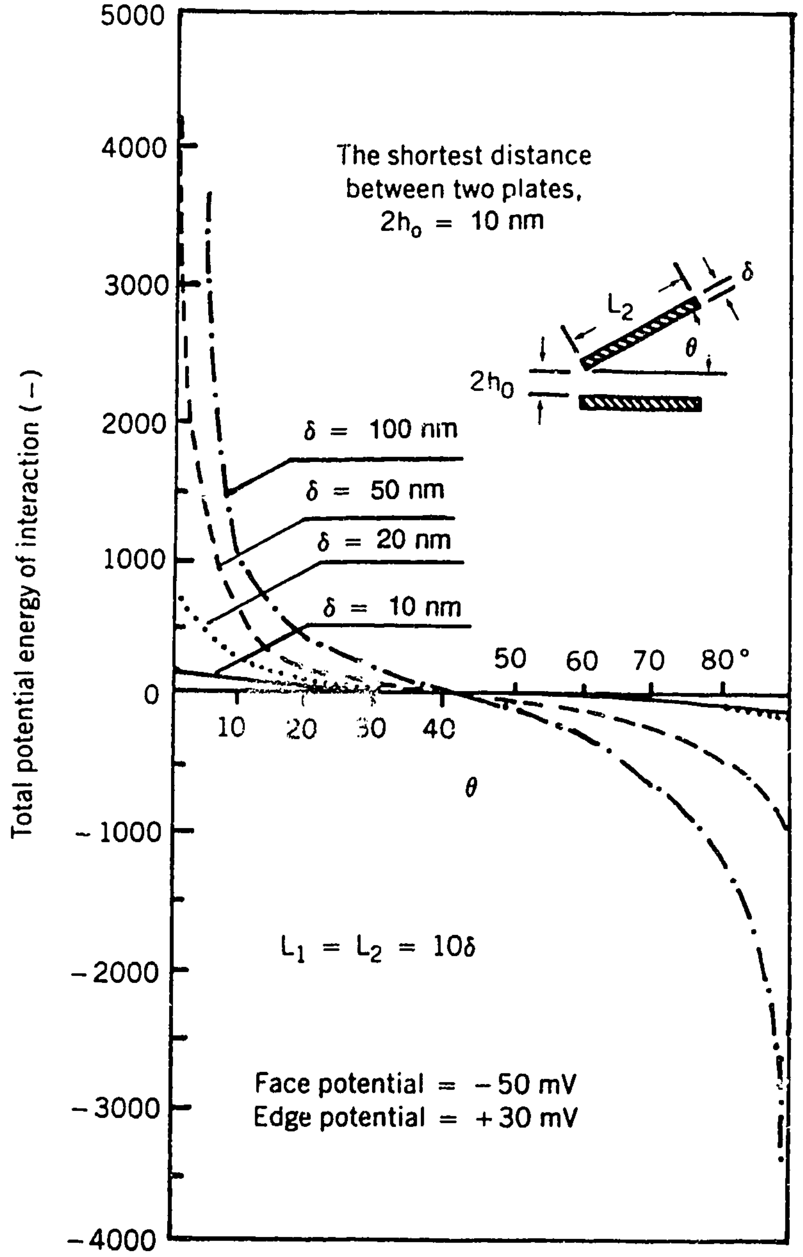

Fig. 2.3-4 - Total potential energy of interaction between two platelike particles, as a function of the EF inclination angle θ between the 2 particles surfaces and for various values of the plate thickness δ. From Tateyama et al. [64]. Value of the Hamaker constant A = $-2x10^{-20}$ J., electrolyte : 1M NaCl.

shows an energy barrier opposes the aggregation of two particles for all the modes of association. However the energy barrier is the smallest for the EE mode.

Considering the electrostatic repulsion U_R, it was also shown that this repulsion increases in the order [36]:

$$U_R^{CC} < U_R^{CE} < U_R^{EEc} < U_R^{EEp} < U_R^{EF} < U_R^{FF} \qquad (2.3\text{-}3)$$

In this series, CC, CE, EEc, EEp, EF, and FF, respectively stand for the association modes corner-to-corner, corner-to-edge, crossed edge-to-edge, in plane edge-to-edge, edge-to-face, and face-to-face. These modes are illustrated in Fig. 2.3-5.

In a previous section of this literature review, equation (2.2-30) indicated that the attraction energy U_A between two platelike particle depends on the plates thickness. Some calculations of the total interaction energy U_{total}, as a function of the plate thickness δ, were done by Tateyama et al. [64] for the EE and the FF association modes. Their results show that the total energy barrier decreases drastically for the EE mode, as the plate thickness decreases (Fig. 2.3-6).

2.3.4 - Clay Sedimentation

Michaels and Bolger [42] studied the sedimentation of colloidal kaolinite in conditions where flocculation occurred. As stated in Section 2.2.4.2, they found that a sharp interface appeared between a clear supernatant liquid and the suspension of flocculated particles. This interface kept moving downwards in the graduated cylinder where sedimentation was performed. On the condition that the graduated cylinder had a diameter larger than the average kaolinite aggregates, they found that the sediment height H decreased with the time according to one of three possible kinetic behaviors. These three behavior types are labeled a, b, and c in Fig. 2.3-7. The a-type only occurs with very dilute kaolinite suspensions (kaolinite volume fraction $\Phi_p < 0.007$). In such conditions, the kaolinite aggregates do not form a single network. As the kaolinite volume fraction

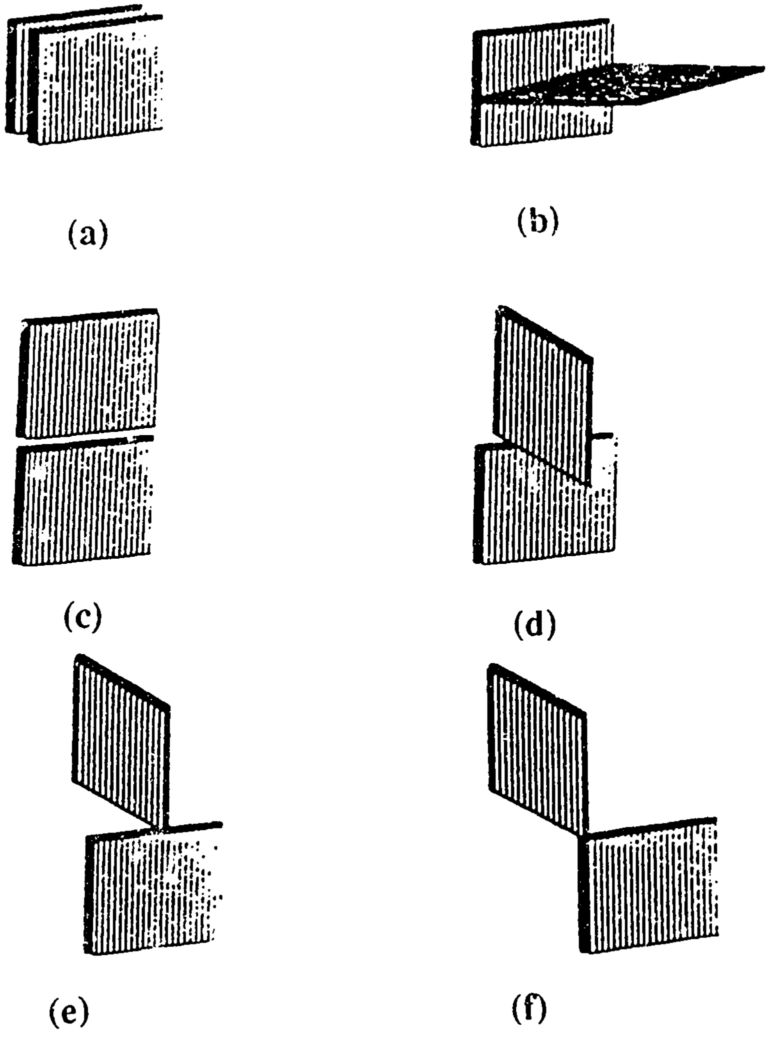

Fig. 2.3-5 - Possible association modes of platelike particles with the same type of charges on the edges and on the faces: (a) face-to-face; (b) edge-to-face; (c) in plane edge-to-edge; (d) crossed edge-to-edge; (e) corner-to-edge; (f) corner-to-corner. From Pierre [36].

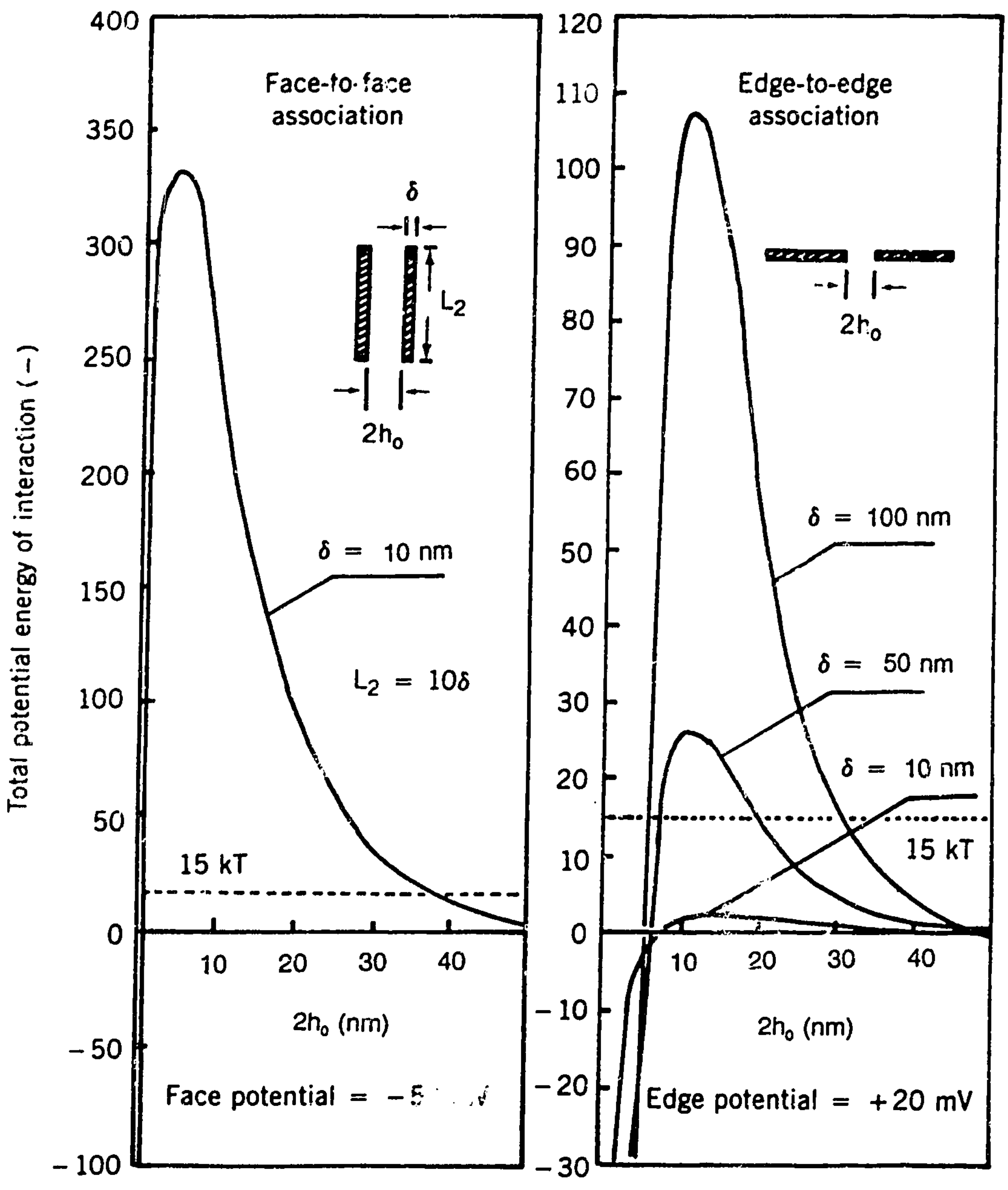

(a)

(b)

Fig. 2.3-6 - Total potential energy of interaction between two platelike particles, as a function of the separation distance $2h_0$ between the 2 particles surfaces and for various values of the plate thickness δ. From Tateyama et al. [64]. Value of the Hamaker constant $A = -2\times10^{-20}$ J., electrolyte : 1M NaCl.

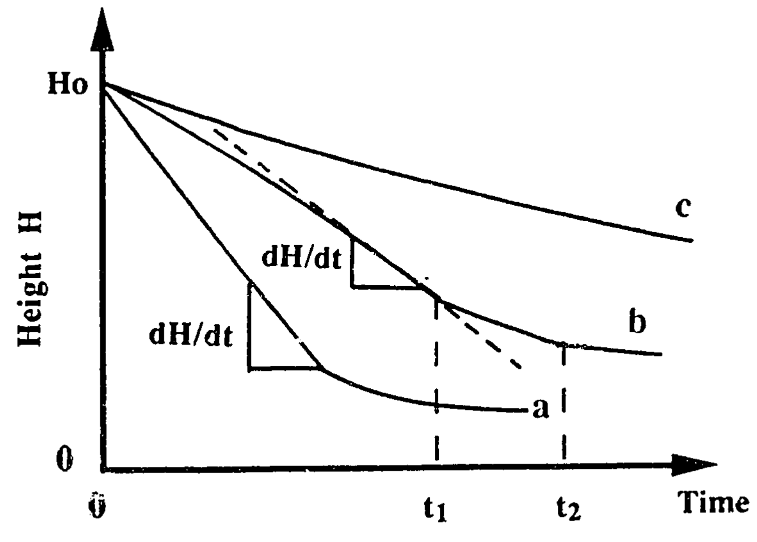

Fig. 2.3-7 - The three types of settling kinetics of flocculated kaolinite suspensions. From Michaels and Bolger [42].

increases, the particles form a single network and the settling behavior transforms to the b-type, then to the c-type.

The density in a suspension which corresponds to the b-type (e.g., $\Phi_p = 0.019$) could be measured by an X-ray transmission technique [65], and the data showed that it depended on the height H and on the time t as illustrated in Fig. 2.3-8 [42].

Rand et al. [60] studied the relationship between the final sediment volume, the pH and the amount of salts which were added to a kaolinite suspension. They interpreted their data, as well as other data on rheology, in terms of the kaolinite particles aggregation mode. Their interpretations were in qualitative agreement with the DLVO theory for kaolinite colloids. A similar work was also carried out on the montmorillonite-$FeCl_3$ system by Zou and Pierre [66].

2.3.5 - The rheology of clay suspensions

Dilute Na-kaolinite suspensions behave as Bingham fluids, as shown by the flow curves in Fig. 2.3-9 [63]. This rheological behavior is also found in montmorillonite [28] and in illite [61] suspensions.

The effect of pH on the rheological properties of aqueous clay suspensions was extensively investigated. For instance, kaolinite suspensions were studied by Rand et al. [60]. The relationship between the Bingham yield stress τ_B and the pH of such suspensions is shown in Fig. 2.3-10. This figure also shows how the data were interpreted in terms of the particles aggregation mode. At a pH below the z.p.c of the kaolinite particles edges, these edges were positively charged and they were attracted by the negative faces. Hence, a "card-house" structure with EF particle association is likely to occur. This type of association is consistent with a high Bingham yield stress.

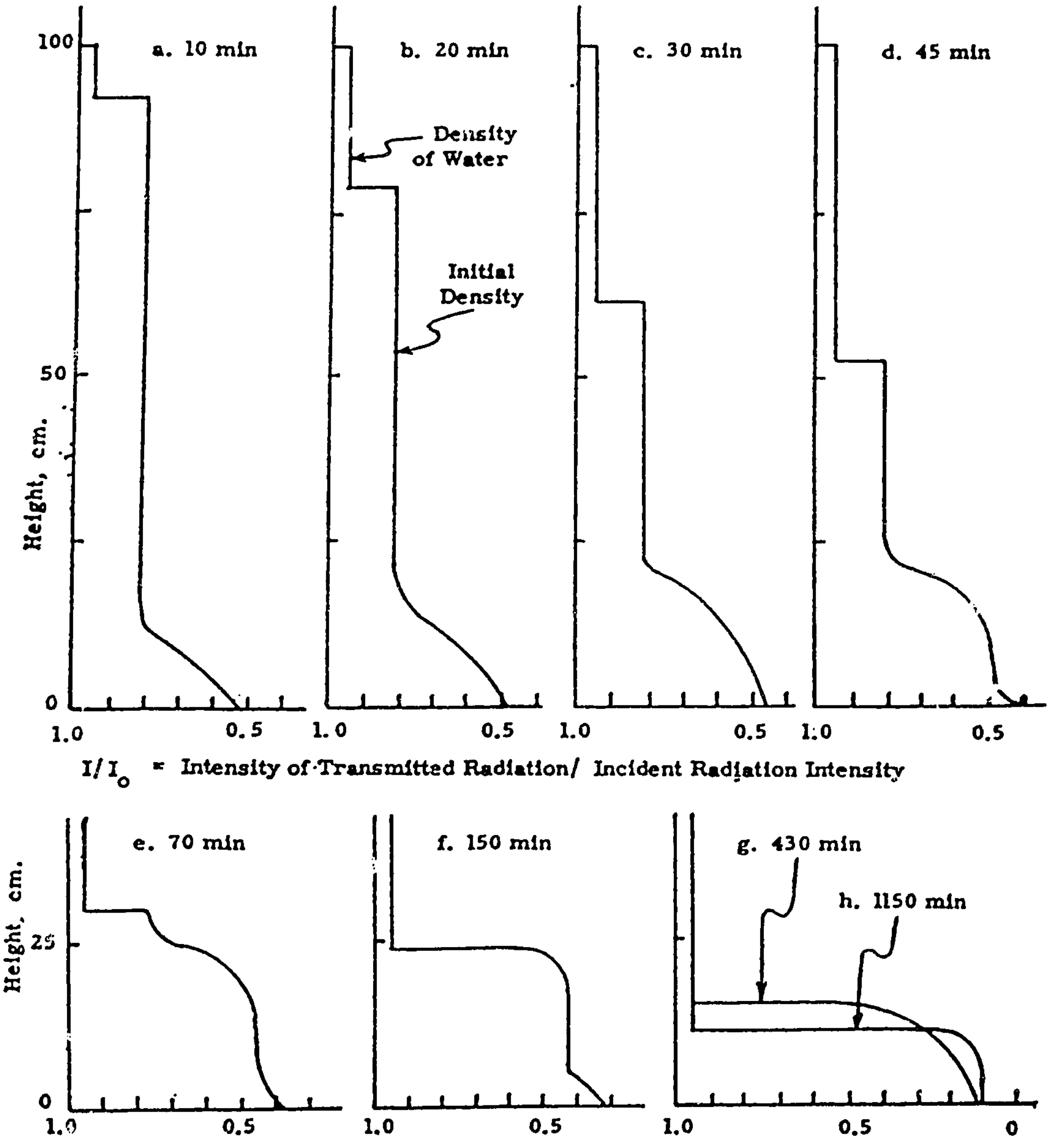

Fig. 2.3-8 - Density distribution in a kaolinite suspension with a particles volume fraction $\Phi_p = 0.019$, and a CaO content of 0.1% by mass. From Michaels and Bolger [42].

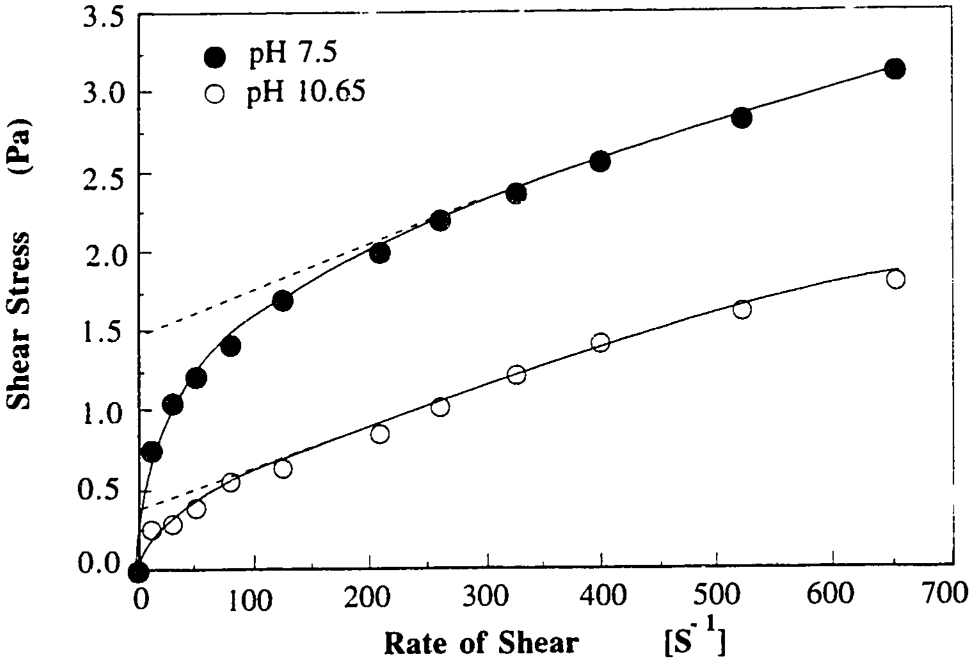

Fig. 2.3-9 - Shear stress τ dependence on the shear rate $\frac{d\gamma}{dt}$ of 5% by mass Na-kaolinite suspensions, in a 10^{-4} M NaCl solution. After Flegmann et al. [63].

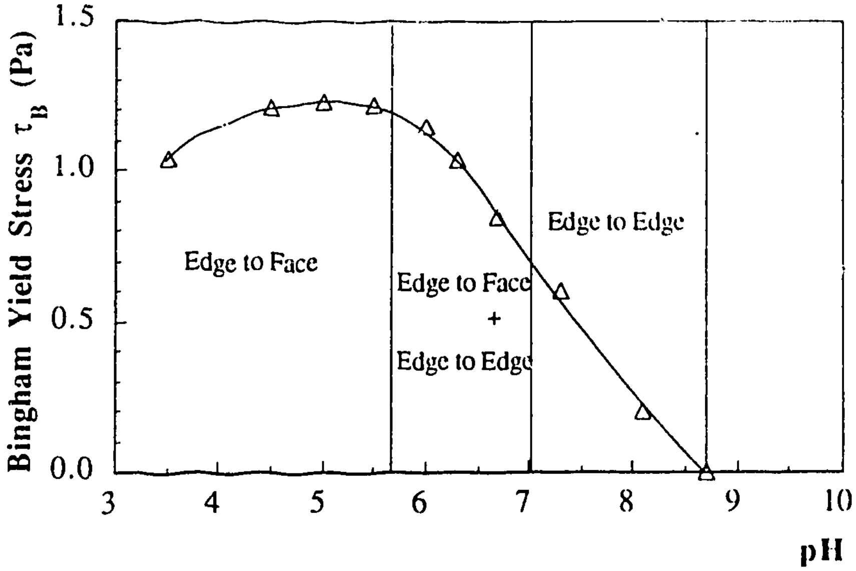

Fig. 2.3-10 - Relationship between the pH and the Bingham yield stress of 9% (by mass) kaolinite suspensions and interpretation in terms of the mode of particles association. From Rand et al. [60].

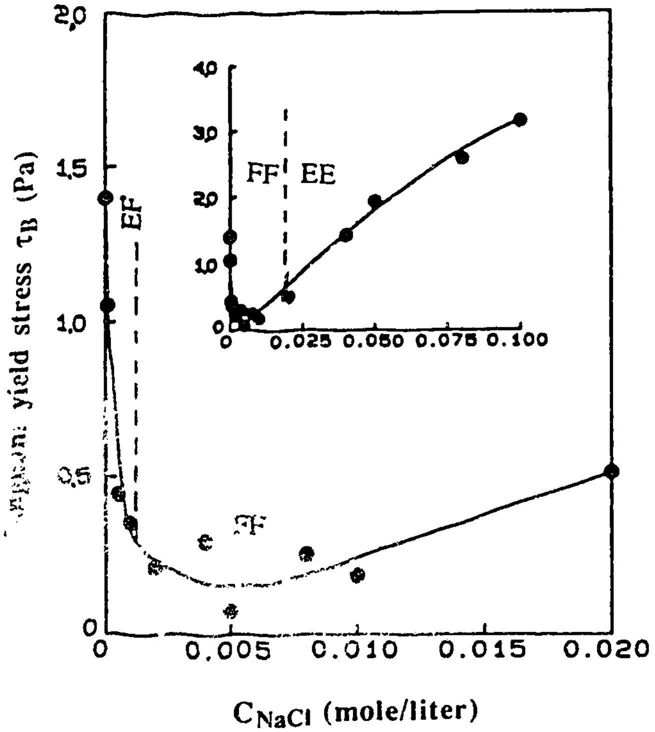

Fig. 2.3-11 - Relationship between the Bingham shear stress τ_B and the NaCl concentration for a 2% by mass suspension of Na-montmorillonite. The pH decreased from 8.5 to 7. as the NaCl content increased. After Chen et al. [67] and van Olphen [27].

Above the z.p.c. of edges, both the edges and the faces of kaolinite particles are negatively charged. The most probable particle association is EE, which is consistent with a lower Bingham yield stress. At high pH, the repulsion between the faces and the edges is strong and the Bingham yield stress disappears.

When an increasing concentration of indifferent electrolyte such as NaCl is added to a kaolinite suspension at a pH below the z.p.c. of the edges, the electrical double layers are increasingly compressed both on the edges and the faces of the clay particles. As a consequence, the EF association of the particles is less frequent. The viscosity and the yield stress of the suspension decreases. Above the edges' z.p.c., the EE association is promoted as the NaCl content increases. Hence the yield stress and the viscosity increase [60].

The effect of adding an indifferent electrolyte such NaCl is illustrated in the case of Na-montmorillonite suspensions in Fig. 2.3-11 from Chen et al. [67]. On this figure, the interpretation in terms of the mode of particles association according to van Olphen [27], is reported. Van Olphen suggested that the edges of montmorillonite particles are negatively charged while their faces are positively charged, as for kaolinite. Hence the effect of an increasing NaCl concentration is the same for both types of clay.

2.3.6 - The mixed clay - Fe systems

2.3.6.1 - The behavior of Fe^{3+} electrolytes in an aqueous medium

The behavior of Fe^{3+} electrolytes in an aqueous medium was summarized by Henry et al. [68] and by Livage et al. [69]. These electrolytes undertake complex chemical transformations through reactions of complexation, hydrolysis and condensation.

The trivalent cations Fe^{3+} are first solvated [68-71], by the dipolar water molecules which give the aquo-ions $[Fe(OH_2)_6]^{3+}$ in acidic conditions. These aquo-ions undertake deprotonation reactions such as:

$$[Fe(OH_2)_6]^{3+} + hH_2O \rightarrow [Fe(OH)_h(OH_2)_{6-h}]^{(3-h)+} + hH_3O^+ \qquad (2.3\text{-}4)$$

where h is the extent of hydrolysis.

Next, some condensation reactions occur, such as the olation type reaction (2.3-5) and the oxolation type reaction (2.3-6) [68]:

Olation: $M\text{-}OH + M\text{-}OH_2 \rightarrow M\text{-}OH\text{-}M + H_2O$ (2.3-5)

Oxolation: $M\text{-}OH + HO\text{-}M \rightarrow M\text{-}O\text{-}M + H_2O$ (2.3-6)

From the works of Henry et al., [68], Livage et al. [69], Baes and Mesmer [70], Schneider [71] and Sylva [72], the practical behavior of Fe^{3+} electrolytes can be summarized as follows.

Low pH (< 4) solutions are known to contain the hydroxylated monomer species $[Fe(OH)_2)_6]^{3+}$ and $[Fe(OH)(OH)_2)_5]^{2+}$ and the dimer species $[Fe_2(OH)_2(OH_2)_8]^{4+}$. The compound Lepidocrocite γ–FeO(OH) precipitates at low temperature, while the compound hematite $\alpha\text{–}Fe_2O_3$ forms at higher temperature [69].

Intermediate pH solutions (4 < pH < 6) are known to contain the monomer species $[Fe(OH)_2(OH_2)_4]^+$ at room temperature. Such monomers condense to a polycation which has the mean composition $[Fe_4O_3(OH)_4]_n^{2n+}$ with $n = 25$. Small spheres about 2-4 nm in diameter grow from these polycations and they are responsible for giving a brown-red color to the colloidal solution. Upon aging or if a base is added to the solution, these polycations aggregate so as to form β–FeO(OH) also known as akaganéite, or α–FeO(OH) needles also known as Goethite. The product which is formed depends on the nature of the anions. In turn, the needles can induce the phenomenon of gelation. At high temperature, no polycation is formed and $\alpha\text{–}Fe_2O_3$ directly precipitates[69].

At high pH (>6), the main monomeric species which is found in solution is $[Fe(OH)_3(OH_2)_3]^0$. From this monomer, α–FeO(OH) precipitates at pH > 10 [69].

The anions from the Fe^{3+} electrolytes participate in the complexation of these Fe species and they may change the nature of the solid products which precipitate. As an example, the chloride anions favor the formation of the intermediate product

$Fe(OH)_{2.7}Cl_{0.3}$ in the range $1.8<pH<3.1$, from which β–FeO(OH) needles precipitate [71]. The nitrate anions enhance the formation of α–FeO(OH).

2.3.6.2 - Action of Fe additives on clay suspensions

The Fe^{3+} electrolytes strongly interact with the clays and this phenomenon was investigated by several groups. Thomas and Swoboda suggested that these Fe^{3+} cations can first act as exchange cations. At 80°C, the global reaction between $FeCl_3$ and clay could be written [73]:

$$Fe^{3+} + 3Cl^- + clay + 3H_2O = Fe(OH)_3\text{-clay} + 3HCl \qquad (2.3\text{-}7)$$

More precisely, Blackmore [74] showed that a contact between the early hydrolysis products of Fe^{3+} electrolytes and a clay was necessary to establish stable bonds between the clay particles. These bonds were achieved by the intermediate Fe hydroxospecies. No strong bonds were established when the clay was mixed with the aged gelatinous precipitates of the Fe^{3+} electrolytes. However, a mixture of the early hydrolysis products and of the aged gelatinous Fe precipates was responsible for the strongest bonding between the clay particles. It must be noted that the hydrolysis of the Fe^{3+} electrolytes was complete in less than 250 s.

Rengasamv and Oades [3,75] used the techniques of ultrafiltration and of dialysis to separate the polycations from the monomers in hydrolyzed Fe^{3+} nitrate solutions. They found that the polycations chemisorbed on the OH groups of the clay particles faces and they were responsible for the flocculation of the clay. The charge on the clay faces could even be reversed to become positive. However, when Fe^{3+} hydrolysis monomer species were also present, these monomers acted as the double layer counterions. This double layer constituted a barrier which hindered the adsorption of the polycations by the clay faces. In this case, a separate precipitation of amorphous Fe hydroxide occurred. These Fe hydrolysis products flocculate in the pH range of 6 to 8.2 close to their z.p.c [52].

Oades showed that the Fe polycations consisted of colloidal spheres with a size from 1 to 10 nm [76]. Their structure is related to lepidocrocite and at pH < 5 they easily adsorb on the clay faces. In these conditions, the clay faces seem to be covered with a fine "pepper-like" spherical powder. When these colloidal spheres agglomerate, they first give needle-like particles, then a poorly crystallized Fe hydroxide, in some cases related to akaganéite β-FeO(OH) [61]. This poorly crystallized Fe hydroxide is often termed amorphous hydroxide or ferrihydrite [50]. Such a product can cover the clay faces [77]. At pH 8.5, goethite particles are formed and these particles do not associate with the clay particles.

In summary, strong bonding of clay particles by the intermediate Fe^{3+} hydrolysis products only occurs in acidic conditions [2]. This was confirmed by rheological studies on mixed aqueous kaolinite-ferrihydrite systems by Yong et al. [54]. If kaolinite and ferrihydrite are mixed at pH 3, the ferrihydrite particles chemisorb on the kaolinite faces. Then, the coated kaolinite particles agglomerate in a sense defined in Section 2.2.1.7, when the pH is raised in a range near pH 7, close to the z.p.c. of the ferrihydrite. On the other hand, if the kaolinite and the ferrihydrite are mixed at pH 9.5, the ferrihydrite builds a network when the pH is decreased to a value near 5.9, close its z.p.c. This network is independent of the kaolinite. In both cases the Bingham yield stress of the suspensions is higher in a range, from pH 5.9 to 7, which is close to the z.p.c of the ferrihydrite (Fig. 2.3-12). The highest Bingham yield stress occurred when the mixing was done at pH 9.5, possibly because the ferrihydrite gel network linked the clay particles. Similar results were obtained by Ohtsubo et al. [61] in their study on the rheology of mixed illite-ferrihydrite systems (Fig. 2.3-13).

The property of Fe hydroxospecies to build a strong network between clay particles was used by Zou [1] to investigate the structure of flocs made by flocculation of montmorillonite with unaged Fe^{3+} electrolyte solutions. The behavior of such mixed systems was qualitatively consistent with a triple action of the Fe hydroxospecies as

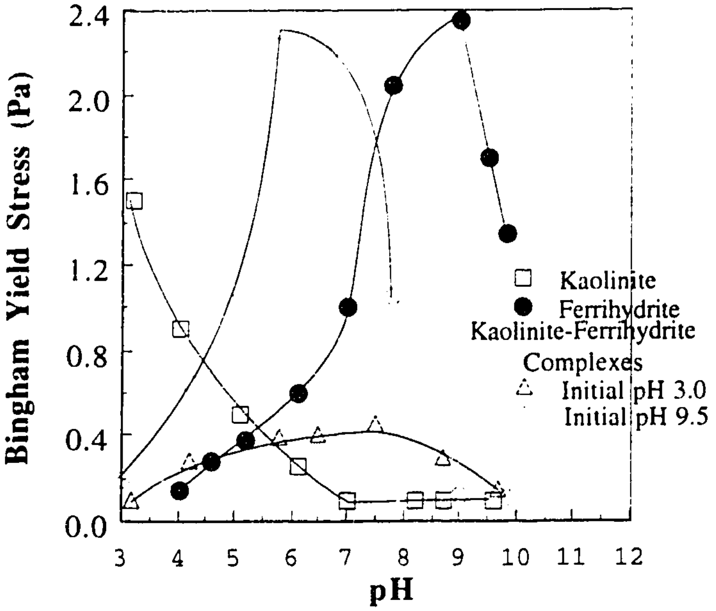

Fig. [illegible] - Bingham yield stress for kaolinite, ferrihydrite and mixed kaolinite ferrihydrite suspensions of initial pH 3.0 and 9.5, at various pH values. The solid content of the suspensions was 10% by mass and the proportion of ferrihydrite to kaolinite was 1/19 in the mixed systems. From Yong et al. [54].

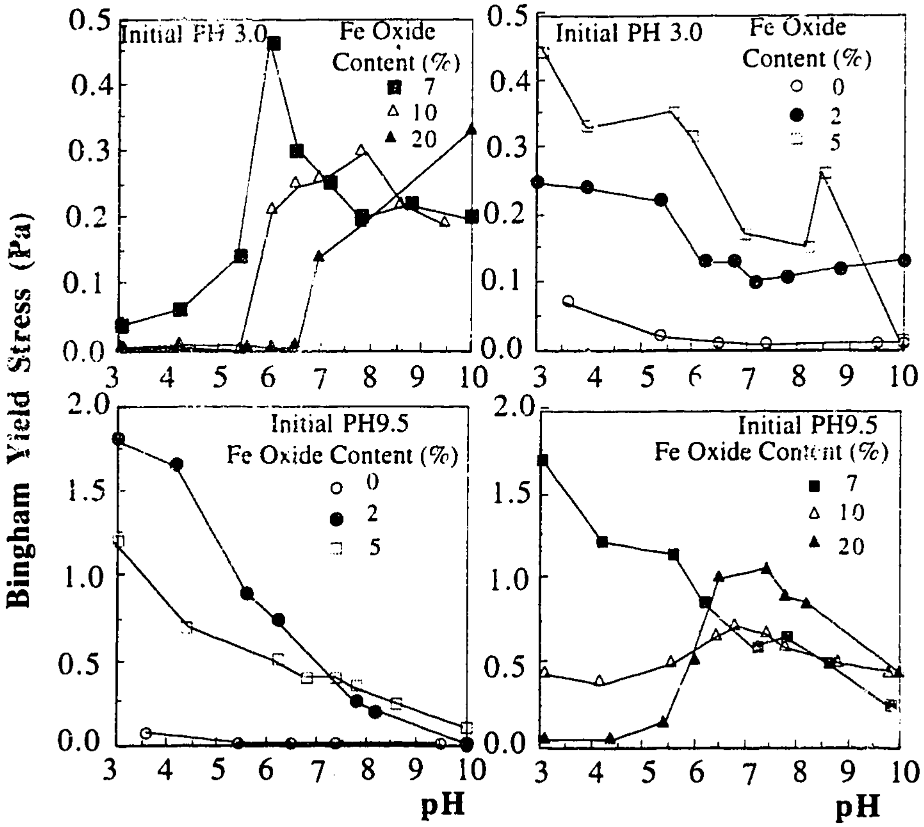

Fig. 2.3-13 - Variation of the Bingham yield stress with pH for mixed illite-ferrihydrite suspensions of initial pH 3.0 and 9.5 with different ferrihydrite contents. The solid content of the suspensions was 8% by mass. From Ohtsubo et al. [61]

counterions, as species which could adsorb on the clay faces and as possible bonding intermediates between the clay particles.

2.3.7 - The n[illegible] clay - Al Systems

2.3.7.1 - The behavior of Al^{3+} electrolytes in an aqueous medium

Electrolytes containing Al^{3+} undertake solvation reactions [68,69], hydrolysis reactions and polymerization reactions which are similar to the reactions of the Fe^{3+} electrolytes, when they are dissolved in an aqueous medium. For instance, hydrolysis involves reactions known as deprotonation reactions [68, 69, 70], such as:

$$[Al(OH_2)_6]^{3+} + hH_2O \rightarrow [Al(OH)_h(OH_2)_{6-h}]^{(3-h)+} + hH_3O^+ \qquad (2.3\text{-}8)$$

where h is the extent of hydrolysis.

The only small species which was really detected in solution is the trimer $[Al_3(OH)_4(OH_2)_{10}]^{5+}$. Such trimers rapidly condense with a monomer to form the species $[Al_{13}O_4(OH)_{24}(OH_2)_{12}]^{7}$ which contains 13 Al atoms [68].

When a base is added to such solutions below 80°C, the accepted mechanism involves the formation of hexameric units from the monomer $[Al(OH)_3(OH_2)_3]^0$. When an acid is added, trimers, tetramers and hexamers are formed from the monomer $[Al(OH)_3(OH_2)_3]^0$. The solids which can be precipitated is the trihydroxide $Al(OH)_3$, under the bayerite or the gibbsite forms [68].

At a temperature above 80°C, the monomer $[Al(OH)_3(OH_2)_3]^0$ leads to the trimer $[Al_3(OH)_9(OH_2)_4]^0$, then to the tetramer $[Al_4O(OH)_{10}(OH_2)_5]^0$. The solid product which is formed is mostly boehmite AlO(OH) which makes gels [67].

2.3.7.2 - Action of Al additives on clay suspensions

The clay particles terminate with Al-O broken bonds, on their edges. Hence the Al^{3+} cations are potential determining ions for these clay particles, contrary to the Fe^{3+} cations. However, as with Fe^{3+}, the Al^{3+} can exchange for Na^+ [18]. Also, the Al^{3+}

hydrolysis species in solution can have the same action as the Fe^{3+} species to coat the clay particles faces and to bond these particles [78].

The main difference between the two types of cations is that the Al^{3+} species make a thin uniform layer with an undetermined structure, which completely covers the clay faces. This coating is more active than the Fe coating to reverse the charge of the clay particles, and to make them flocculate in a larger pH range [52, 78].

The Al^{3+} polycations in solution are the Al_{13} oligomer and the planar hexagonal oligomer which were mentioned in the previous section [79]. The first species are fast reacting. They are more abundant in unaged Al^{3+} solutions. The planar species are present in aged solutions. They react more slowly but they are better adsorbed because of their shape and their high charge [76, 79]. These planar polycations can intercalate between the layers of montmorillonite to which they can give a high specific area [75, 76].

2.4 - ARCHITECTURE OF CLAY SEDIMENTS

2.4.1- Proposed models for clay sediments

The studies summarized in Section 2.3 led to the proposal of a number of models for the structure of clay flocs or aggregates by different scientists. These structures are sometimes referred to as the clay fabrics. These models describe the spatial distribution, the orientation of the particles, and the particle-to-particle association modes in the sediments [51].

The term "domain" is often used to designate a region of a sediment where the platelike particles of montmorillonite, of kaolinite or of illite are packed parallel to each other [51]. A domain is usually small. Different types of domains su [illegible] the "book" domains [80] and the stepped face-to-face domains [81] are illustrated in Fig. 2.4-1. Sloan et al. [80] described a model of clay sediment called "perfect stack" [81] in which the microstructure was comprised of large book domains.

Moon [82] proposed a model to explain the formation of such domains from a dispersed clay suspension, during the process of flocculation and of consolidation. These domains are first formed of loose and random groups of particles. Progressively, more particles are incorporated into each domain, and the preferred orientation of the particles inside each domain increases, as consolidation proceeds (Fig. 2.4-2). Finally, the domains are of the book and of the stepped face-to-face types.

On a larger scale, a few models proposed for the fabric of clay sediments are illustrated in Fig. 2.4-3. The cardhouse structure (Fig. 2.4-3a) is the most well known of these models. The walls of the cardhouse consist of single platelike particles which are connected in the EF manner [83]. The bookhouse model looks like the cardhouse model. However, the walls consist of book domains which are connected according to the EF mode (Fig. 2.4-3b) [80].

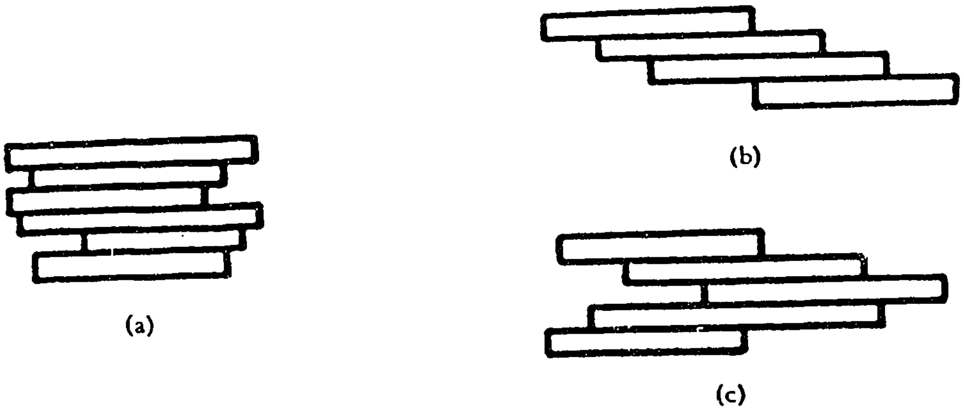

Fig. 2.4-1 - Domain structures: (a) Book domains. From Sloan et al.[80]; (b,c) Stepped face-to-face domains. From Smalley et al. [81].

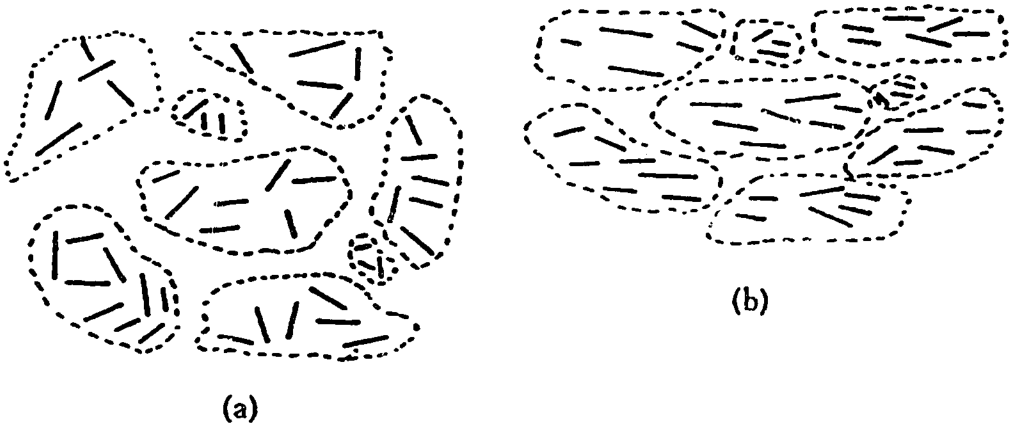

Fig. 2.4-2 - Proposed schemes to explain the formation of domains in clay sediments, : (a) Open, random arrangement of packets of particles ; (b) Increased parallelism of domains and increasing incorporation of particles inside each domain. After Moon [82]

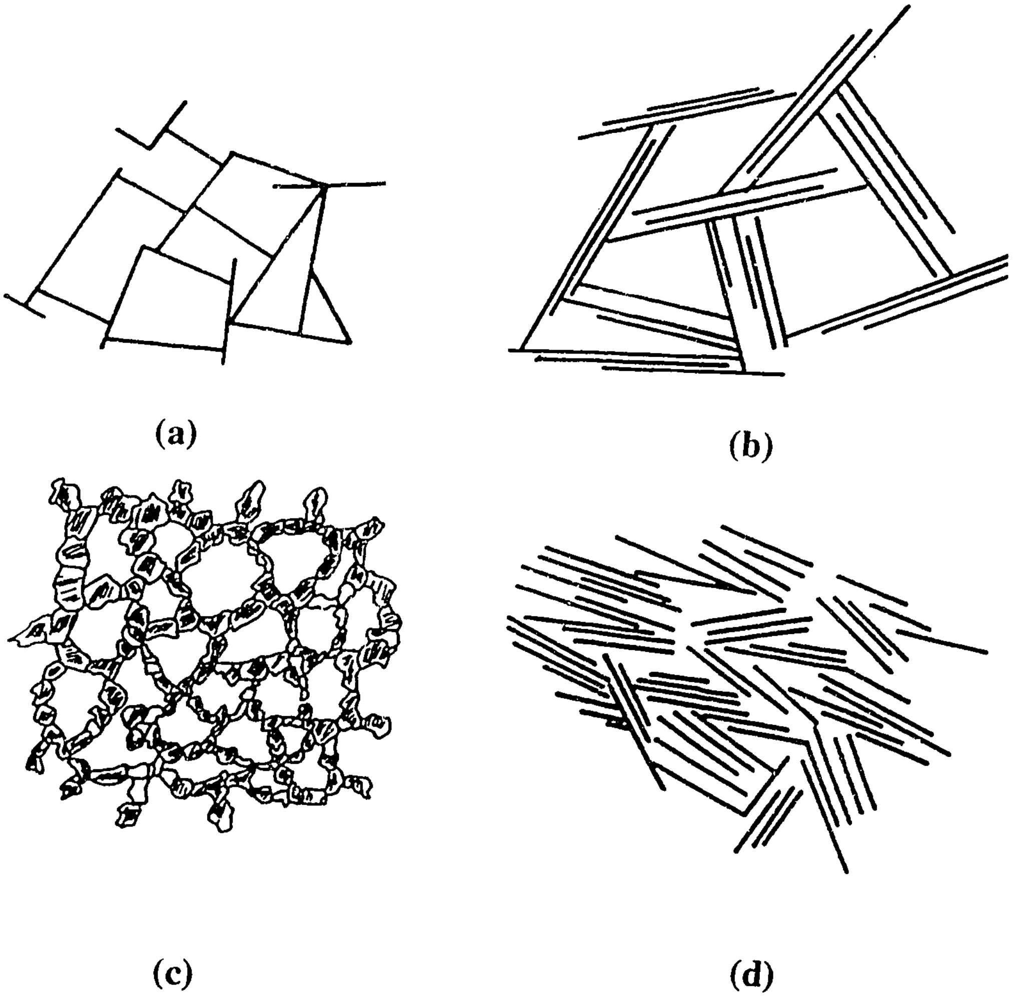

Fig. 2.4-3 - Models for the fabric of clay sediments: (a) Cardhouse structure, form Lambe [83]; (b) Bookhouse structure, from Sloan et al. [80]; (c) Honeycomb structure, from Terzaghi [84] and Casagrande [85]; (d) Turbostratic structure, from Aylmore and Quik [86].

In the honeycomb model (Fig. 2.4-3c), the basic units are single platelike particles which are associated in the EE or the EF modes, to form rings [84].

The turbostratic structure (Fig. 2.4-3d), proposed by Aylmore and Quirk [86], consists of groups of domains which form a random packed array. Such a structure appears as being isotropic on a macroscale, although it is locally anisotropic on a microscale. This structure is termed a stack structure, by Sides and Barden [87] when the domains are large.

In 1971, O'Brien [88] proposed stair-step models based on microscope observations (Fig. 2.4-4 a and b). These models are comprised of platelike particles connected in a stair-step manner. Platelike particles can make cells comprised of stair-step, such as illustrated in Fig. 2.4-4a for kaolinite [88]. In illite sediments , the particles are curved so that the cells take the form of rings, as illustrated in Fig. 2.4-4b [88]. In a tactoid structure (Fig. 2.4-4c), the domains are associated in the EE mode so as to form the walls of cells. The thicker domains ensure a network interconnection [89]. The structure termed "link chain" or "flake" is illustrated in Fig. 2.4-4d. It is somewhat related to the 3 previous structures. However it involves links between particles with a more realistic shape and size distribution.

Some models based on the EE association, either of individual platelike particles, or of domains of particles, were proposed by van Olphen [11]. The models proposed by van Olphen are illustrated in Fig. 2.4-5.

2.4.2 - Preparation of electron microscope samples, by drying

To observe the microstructure of clay sediments in a scanning electron microscope (SEM) or in a transmission electron microscope (TEM), it is necessary to dry sediment samples.

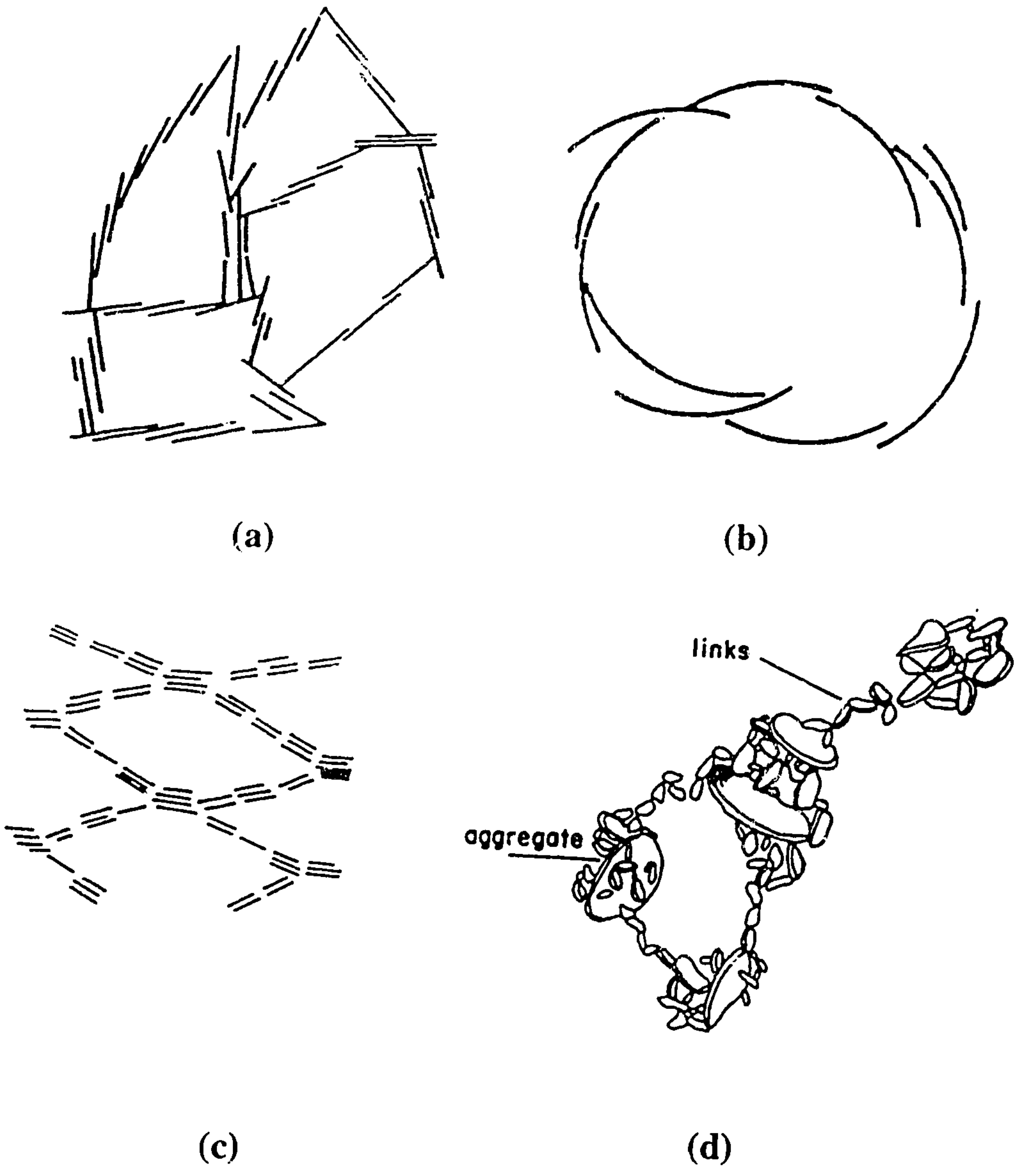
(a)
(b)
links
aggregate
(c)
(d)

Fig. 2.4-4 - Structure models for clay sediments: (a) and (b) Stair-step structure. From O'Brien [88]. (c) Tactoid structure. From Ingles [89]; (d) Aggregates and links structure. From Pusch [90].

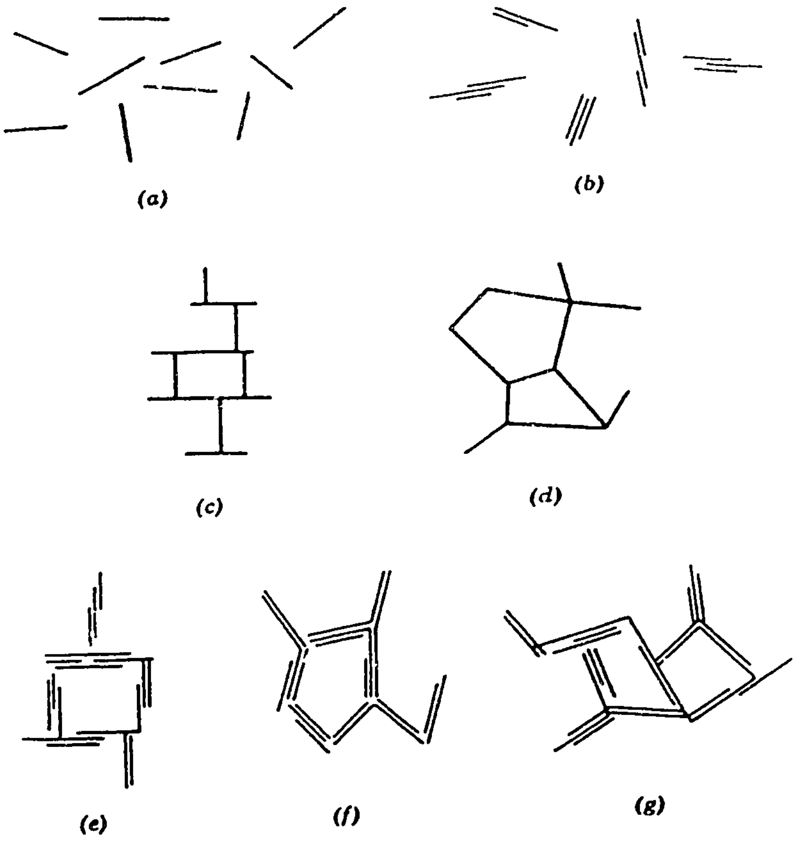

Fig. 2.4-5 - Possible association modes of clay particles according to van Olphen [11]: (a) dispersed particles; (b) Dispersed domains; (c) EF flocculation of particles (cardhouse); (d) EE flocculation of particles; (e) EF flocculation of domains (bookhouse); (f) EE flocculation of domains; (g) mixed EE and EF flocculation of domains.

However, it is necessary to select a drying procedure which minimizes any alteration of the sediment's microstructure. Three drying methods can mainly be used to prepared sediment samples: (1) simple evaporation; (2) freeze-drying, which includes cryogenic SEM; and (3) supercritical-drying. These three techniques are analyzed in the next sections.

2.4.2.1 - Drying by evaporation

The drying by evaporation of a wet sediment can be carried out in the laboratory air, in the dry air of a dessicator, under a controlled humidity, under vacuum, or in an oven. All these techniques are simple and cheap, hence they are used. However, with all these techniques, a sediment shrinks during drying. Hence, the sediment structure is modified. As an example, O'Brien [91] used evaporation to dry illite sediments, and the sediment volume shrunk in a ratio of 26 to 7.

The shrinkage depends on the nature of a clay. For example, the shrinkage is usually large with a fully swollen montmorillonite while it can be negligible for some naturally un-swollen clays [92]. In general, a greater shrinkage extent and a greater degree of reorientation of the particles occurs when the evaporation is done slowly, than when it is rapidly done. However, a fast evaporation often induces cracks in a sample. Also, heating a sample may occasionally cause some mineralogical alterations [93]. On the whole, a slow drying process was generally favored, although a fast drying method might be better to study the actual orientation of the particles in a sediment [92].

In substitution evaporation, a liquid with low surface tension is exchanged for the pore fluid which has a higher surface tension. This operation attenuates the shrinkage effect due to surface tension and the original microstructure of a clay sediment is less altered. The liquids used to exchange for water are acetone[94,95], alcohol [96], and other organic liquids with a low surface tension [92]. However, the substitution process may itself induce a rearrangement of the clay particles. For example, the microstructure may be changed when the exchange process of alcohol or acetone for water is too fast. Some clay-water-organic complexes may also form but this problem can be neglected when acetone or alcohol is used [51, 96].

2.4.2.2 - Freeze-drying

Freeze-drying is used to alleviate the shrinkage due to surface tension. A sample is quenched to a low temperature where its liquid is frozen. Ideally, water can be quenched to a vitreous state, so that the particles of a clay sediment are immobilized in such a way that the sediment fabric is not altered. Next, the vitreous ice matrix of the sediment is evacuated by sublimation. Hence, the receding liquid-vapor meniscus which is formed during evaporation is replaced by a solid-vapor interface, while the pores are filled with an incompressible solid. This significantly attenuates any reorganization of the fabric structure during drying.

This technique was extensively used to unravel the microstructure of sediments made with kaolinite, montmorillonite or illite. Better results were obtained by freeze-drying than by evaporation. However, this technique is not devoid of artifacts. The most common of these artifacts is related to the cooling rate which is achieved during the freezing operation. If the cooling rate is slow, the aqueous medium freezes near 273K by a nucleation and growth process. The clay particles are rejected at the grain boundaries of the growing ice crystals, as in any semiconductor melting-zone process, and the sediment structure which is observed really represents the crystallization pattern of the liquid [51,97,98]. This defect must be avoided [98,99,100]. If the cooling rate is too fast, thermal shock cracking can occur in the sediment, especially when the sample is too big [92]. Also, impurities may be responsible for some complications. For instance, the metallic salts may form eutectics, or they may be precipitated and rejected at the moving boundaries of the growing ice crystals [92].

In many cases, it was reported that the shape of a sample did not change during freeze-drying [92]. In other cases, a powder was left after freeze-drying [101]. Such a disintegration easily occurs when quenching in liquid nitrogen, which boils on contact with the sample [92]. As for the sample volume, a report indicated that it did not change for K-kaolinite, while it decreased by 20 % with Ca-Kaolinite. Rosenqvist [102] reported that a marine clay sample, mainly comprised of illite, showed a 3 % volume increase on freezing, while no further change occurred after sublimation.

In a good sample preparation procedure by freeze-drying, the cooling rate must be sufficiently fast to create ice crystals which are smaller than the resolution of the microscope to be used. One method consists of quenching the sample in a nitrogen slush as described by Mikula et al. in his cryogenic SEM technique [103].

2.4.2.3 - Supercritical-drying

Supercritical-drying is a concurrent technique to freeze-drying. However, this technique was not extensively used to study clay sediments until now. Some authors, such as Naymik [104] argued that supercritical-drying is a technique far superior to freeze-drying. Gillott [97] applied the supercritical drying technique to clay sediments, with alcohol and with CO_2 as the fluids. He found that the aspect of the clay fabric was identical in both cases.

The supercritical drying technique was invented by Kistler [105]. He found that water was not a suitable supercritical fluid for silica gel because of its high critical temperature, 374°C and high critical pressure 22.1 MPa. At this temperature, the samples distorted. Bhasin [106] also used water as the supercritical fluid to dry natural and commercial clay soils. Contrary to silica, X-ray diffraction and infrared spectral analysis showed that no change occurred in the basic characteristics of the clay minerals after supercritical drying. In particular, the total porosity remained unchanged, except in the case of some bentonite samples.

However, possible changes in the mineral structure and in the morphology always are a concern, when a material is heated in an aqueous medium at such high temperatures. Also, the safety hazards are important when working with an autoclave at the critical temperature and the critical pressure of water. Hence, it is desirable to work with a supercritical fluid which has a low critical temperature and a low critical pressure. Tovey suggested using nitrous oxide [94]. Freon 13 can also be used. However, this is an expensive fluid. Some other organic liquids react chemically with clays to form organic complexes.

A favored supercritical fluid is carbon dioxide [96]. Its critical point is low, at a temperature of 31°C and a pressure of 7.433 MPa. Unfortunately, water is not soluble in liquid carbon dioxide. Hence, water must first be exchanged for another liquid which is both miscible with water and with liquid CO_2, such as acetone or ethanol. A list of other possible liquids is reported in Table 2.4-1 from McHugh [107].

Table 2.4-1. List of liquids miscible with carbon dioxide. From McHugh [107].

Compounds	Compounds
Esters	Formic acid
Butyl oxalate	Isocaproic acid
Ethyl acetate	
Ethyl acetoacetate	*Amines and Heterocyclics*
Ethyl benzoate	*N, N* - Dimethylaniline
Ethyl chloroformate	Pyridine
Ethyl maleate	
Ethyl oxalate	*Phenols*
	o - Chlorophenol
Alcohols	*o* - Nitrophenol
t - Amyl alcohol	β - Methoxyethanol
Methyl alcohol	
Ethyl alcohol	*Nitriles and Amides*
	Acetonitrile
Carboxylic Acids	Acrylonitrile
Acetic acid	Tolunitriles (mixed)
Caproic acid	*N, N* - Diethylacetamide
Caprylic acid	*N, N* - Dimethylacetamide

For clays, the most popular sequences of liquid exchange are water-alcohol-amyl acetate-liquid CO_2, water-ethanol-liquid CO_2 and water-methanol-liquid CO_2 [66, 92, 94, 96, 97, 108]. Tovey et al. [109] and Zou and Pierre [66] used the sequence water-acetone - liquid CO_2. Any liquid exchange can be accomplished by dialysis. The dialysis operation should be done very slowly, to avoid the shrinkage of a clay sample when the osmotic pressure difference between the two fluids is too high. Usually, several steps are required to progressively increase the concentration of a new fluid in the clay sample, so as to avoid shrinkage [66].

In the process of supercritical drying, the autoclave chamber which contains the clay sample can be partially filled with liquid CO_2 before increasing the temperature. Hence an interface between the liquid CO_2 and the CO_2 gas exists. As the temperature rises, this boundary first recedes, then it becomes ill-defined and finally it disappears. One must be careful to let a sufficient quantity a liquid CO_2 inside the chamber, so that the transient receding liquid-vapor interface does not contact and distort the sample. On the other hand, if the autoclave chamber is completely filled of liquid CO_2, the pressure and the temperature may not reach their critical point values at the same time during heating. Instead, the pressure first can go above its critical point value, which may activate the safety valve of the autoclave. Once both the temperature and the pressure are above their critical point values, the autoclave chamber is full of supercritical CO_2. No liquid-vapor interface is formed during the evacuation sequence, and the sample can be completely dried without shrinking [110].

2.4.3 - Electron Microscopy observations

The clay sediments which have been observed by electron microscopy can be classified as natural soil sediments or as artificial sediments made in material processing operations. The latter type of sediments are directly related to the present research and the structures, which were observed by electron microscopy are summarized in the following paragraphs.

Sides et al. [87] studied the microstructure of unflocculated and flocculated sediments of kaolinite made by evaporation in air. The unflocculated kaolinite sediments showed a highly oriented structure with very large domains and few macrovoids or cavities, while the flocculated sediments were comprised of small domains with a much more random turbostratic orientation. In both cases, most particles were associated according to the FF mode.

The technique of freeze-drying was applied to study the microstructure of kaolinite sediments by several authors. The kaolinite sediment illustrated in Fig. 2.4-6a was frozen in liquid propane at 113K and dried below 193K [111]. This micrograph show almost single-plate flocs of kaolinite which the author termed cardhouse. O'Brien [88] found that both FF and EF particle associations occurred in flocculated kaolinite sediments. The formation of FF domains in aqueous suspensions was favored either by a high clay content, or by the presence of an electrolyte, as shown in Fig. 2.4-6b and c. In the case where these domains had the shape of big distorted platelike aggregates or chains, they were associated according to a "twisted" EF mode, very close to the FF mode. Hence, these domains could build a stair-step structure, characterized by a high void ratio. Stawinski et al. [112] found similar results. These authors observed that the EF association dominated in kaolinite sediments without any added electrolyte, while both the EF and the FF association modes occurred in the sediments with Na and Ca salt electrolytes. With both types of salts, the sediment structure was of the honeycomb type. By applying the technique of freeze drying, Smart and Tovey [113] observed that the FF association developed more extensively during the consolidation of kaolinite samples, as illustrated in Fig. 2.4.7. Contrary to these observations, Mikula et al. [103] used a special freeze-drying technique, and he found that the structure of flocculated kaolinite sediments was comprised of a very regular EF bookhouse structure inside large flocs (Fig. 2.4-8).

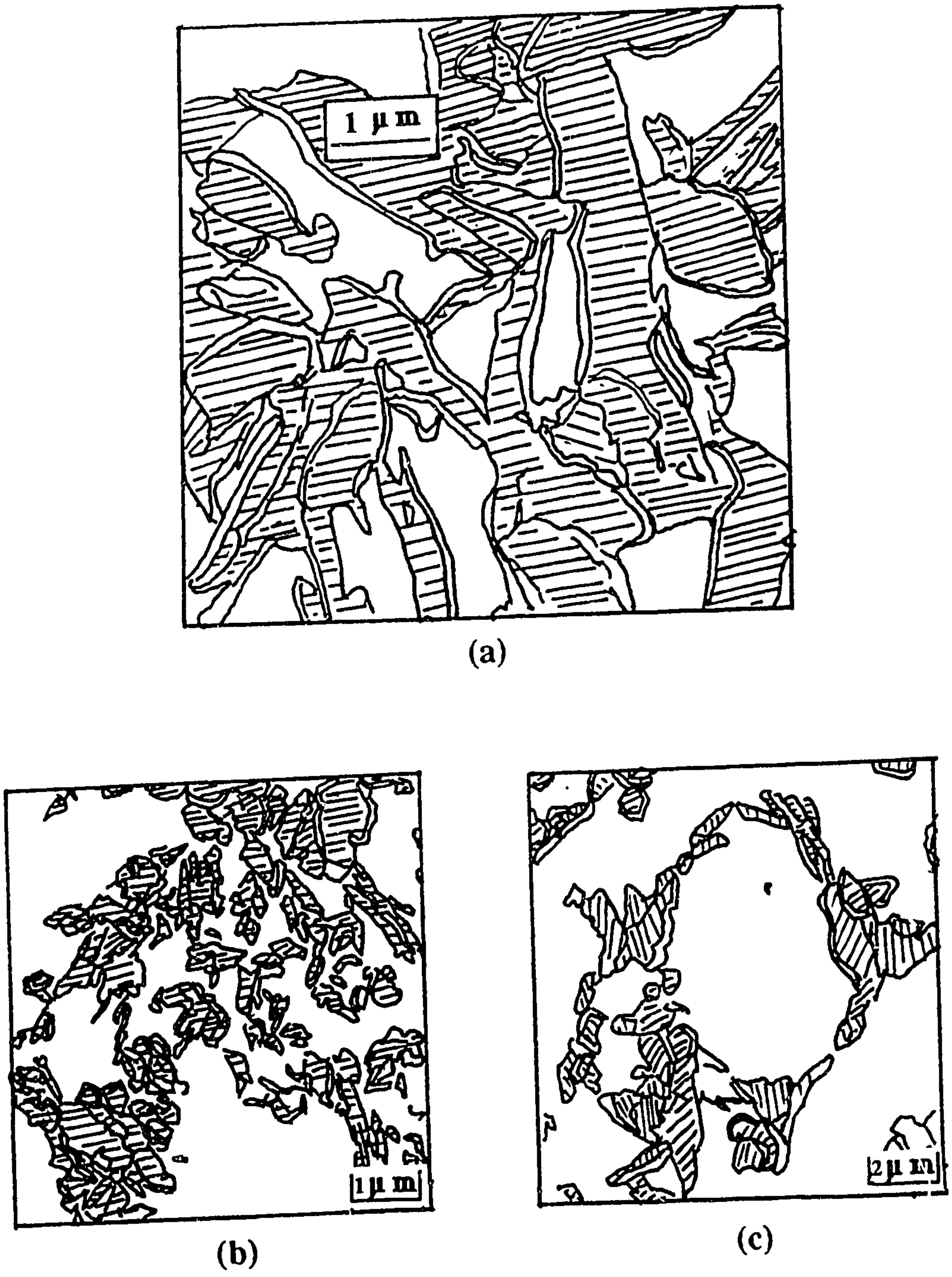

(a)

(b)

(c)

Fig. 2.4-6 - Schematic drawing of SEM micrographs of flocculated kaolinite sediments dried by freeze-drying: (a) from Mattiat [111] (no scale was provided); (b) from O'Brien [88] with 100g/L of clay in distilled water; or (c) with 10g/L of clay concentration in a 1 g/L NaCl solution.

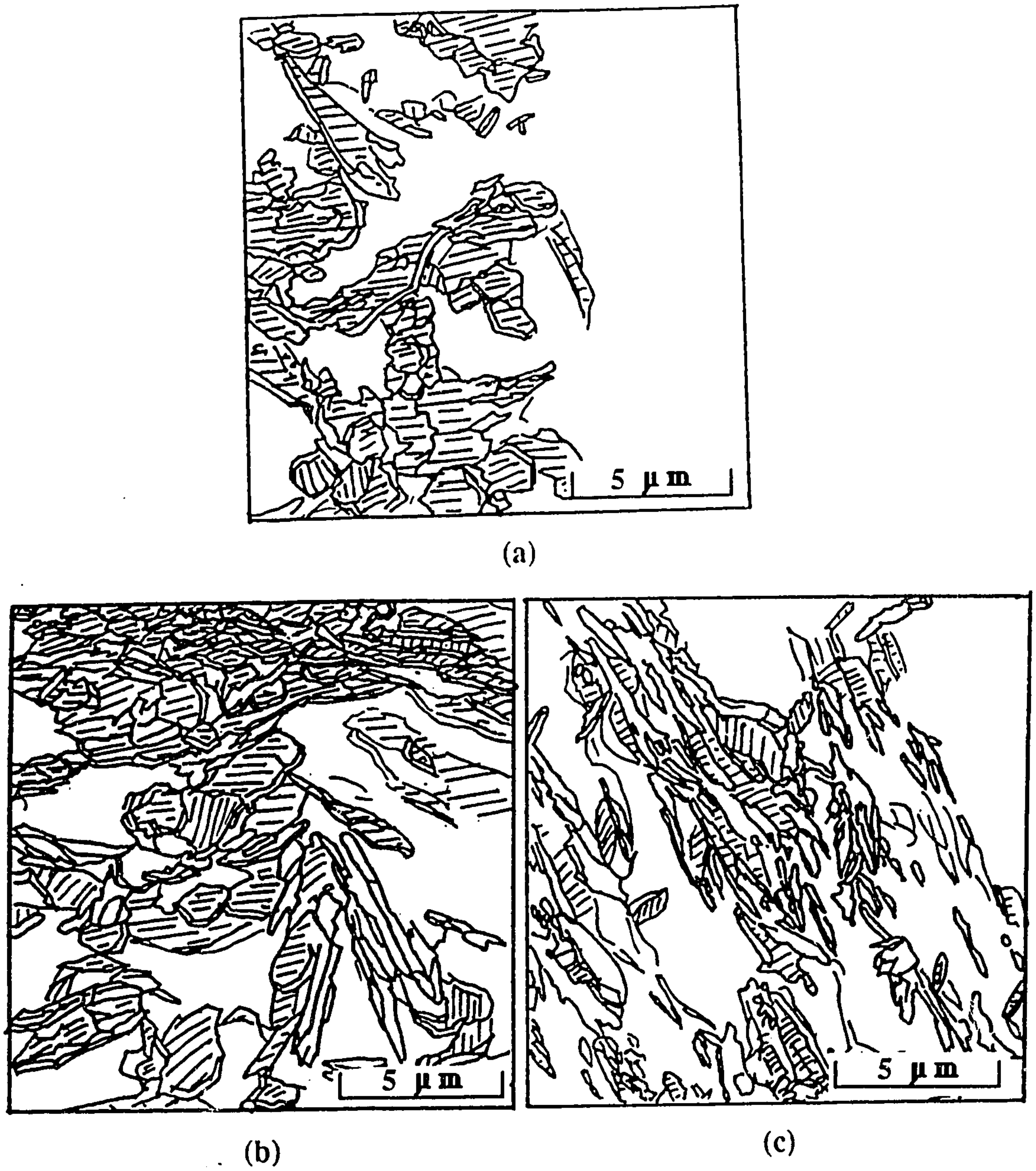

(a)

(b)

(c)

Fig. 2.4-7 - Schematic drawing of SEM micrographs of kaolinite sediments dried by the freeze-drying technique, after uniaxial consolidation at: (a) 0 kPa; (b) 200 kPa; (c) 500 kPa. Drawn after Smart and Tovey [113].

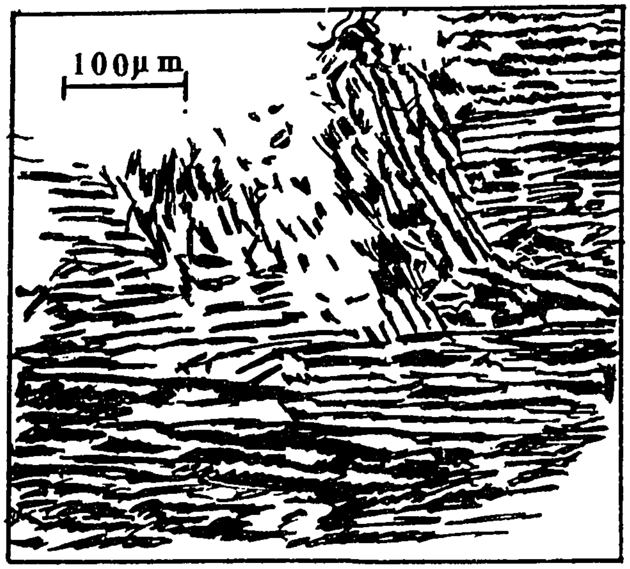

Fig. 2.4-8 - Schematic drawing of SEM micrographs of a regular EF bookhouse structure in a kaolinite based "sludge" sediment, such as made after the extraction of oil from Alberta oil sands. Drawn after Mikula et al. [103].

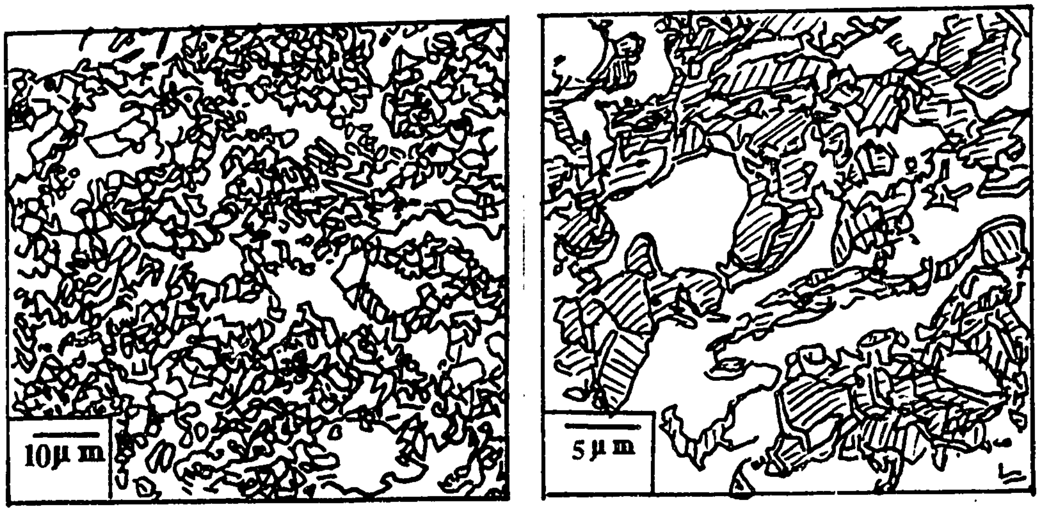

(a) (b)

Fig. 2.4-9 - Schematic drawing of SEM micrographs of kaolinite sediments dried by the supercritical drying technique, and made : (a) in distilled water; (b) in a 3% NaCl solution. Drawn after Lanier et al. [114].

The kaolinite sediments dried by a supercritical-drying technique by Lanier et al. [114], essentially showed some structures consistent with most structures observed by freeze-drying, with the exception of the observations by Mikula. Lanier et al. claimed that in distilled water or in a slightly saline solution (1% NaCl) FF domains comprised of 4 to 6 particles were formed (Fig. 2.4.9a). As the NaCl concentration increased, the domains increased in size (Fig. 2.4.9b) and these domains linked according to the EF mode to create a more open honeycomb structure. The main difference between Lanier's and Mikula's observations is that Mikula showed micrographs where clay particle FF aggregates had built a very regular EF bookhouse structure, in large domains. Such observations were made in oil sands tailing sludge after extraction of the oil from Alberta's oil sands deposits, as well as in kaolnite sediments.

The major difference between the kaolinite and the illite flocculated sediments comes from the particle shapes which are different in the two minerals. While the kaolinite particles are highly crystalline plates with a hexagonal shape, the illite particles are often curved, with an irregular outline, and their crystallinity is less developed [88, 115].

The illite sediments prepared by air drying from dispersed suspensions, after consolidation under a slight pressure by Sides et al. [87], showed a structure similar to the sediments derived from dispersed kaolinite, but there were more macrovoids or cavities. These sediments had a closed-packed structure with strong preferred orientation of the domains. The sediments made from flocculated illite were more open, with a turbostratic structure [87] or a random packed structure [91], although the EF associations were still scarce.

The microstructures which were observed in freeze-dried illite included dispersed particles, such as in the model by van Olphen in Fig. 2.4-5a [11], and domains of particles made by FF association with a strong preferred orientation. In distilled water and in aqueous solutions with a low NaCl content, the structure of illite sediments observed by freeze-drying was similar to the kaolinite sediments. This structure consisted of a random packing of domains. As the NaCl concentration increased, an increasing proportion of individual illite particles were associated according to the EF mode. However, this might only be an apparent association due to the curvature of the illite platelets. The major part of the network still consisted of a stair-step association of domains [88,91]. Hence, the flocculated illite sediments had a honeycomb microstructure similar to the microstructures observed in flocculated kaolinite sediments.

Montmorillonite particles are small and thin, so that the microstructure of sediments is easily destroyed when drying by evaporation. Special care is required to dry such sediments. In particular, montmorillonite particles tend to curl when they are dried by evaporation in air [113].

The freeze-drying technique made it possible to avoid curling [92]. SEM micrographs of flocculated montmorillonite dried by this technique showed that the sediments consisted of platelike particles associated according to the EE and the EF mode (Fig. 2.4-10a).

The supercritical-drying technique was also applied to montmorillonite. SEM micrographs of supercritically dried flocculated montmorillonite sediments, after replacement of the pore water by acetone then by liquid CO_2, are shown in Fig. 2.4-10b [92]. This montmorillonite was flocculated exactly under the same condition as that shown in Fig. 2.4-10a. However, the supercritically dried sediment had a more open microstructure than the freeze-dried sediment. Contradictory observations were made by Jernigan et al. [116]. These authors worked on mixed organic -montmorillonite sediments dried by the supercritical method. They found that the degree of curling of the montmorillonite particles was larger after supercritical-drying than after air-drying. Hence, they concluded that curling was part of the natural morphology of montmorillonite sediments, contrary to the conclusion by Smart and Tovey [92]. Also, they found that supercritical-drying led to a less extensive aggregation of the particles.

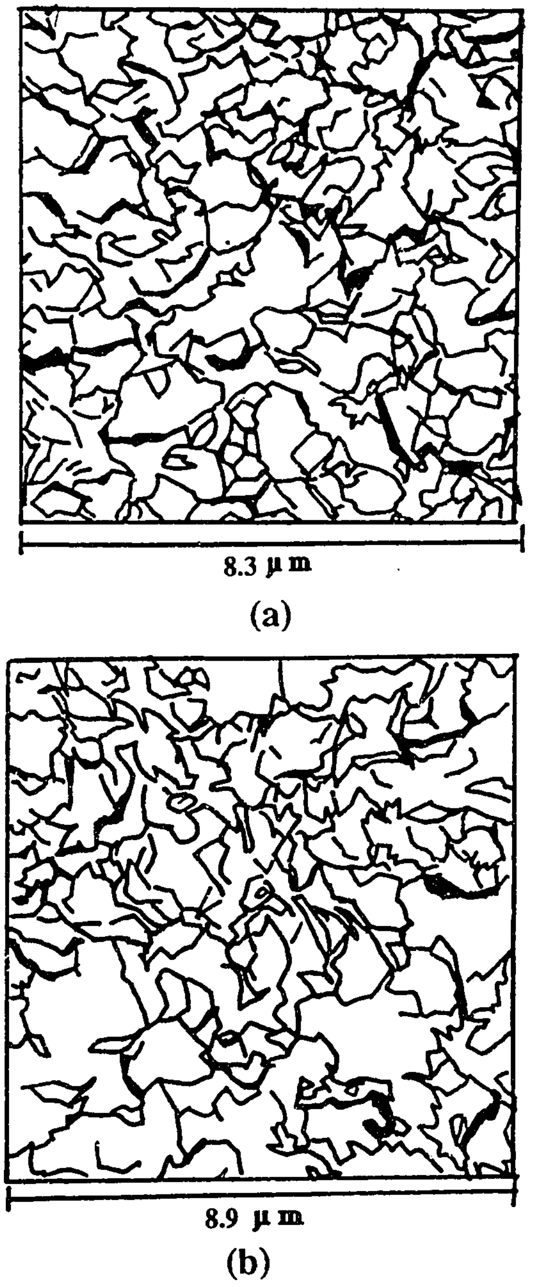

Fig. 2.4-10 - Schematic drawing of SEM micrographs of montmorillonite sediments made by: (a) freeze drying in propane; and (b) supercritical drying. Drawn after Smart and Tovey [92].

Recently, Zou and Pierre [1,66] studied the microstructure of montmorillonite sediments made with the addition of Fe electrolytes. The montmorillonite particles were mainly connected according to the EE mode. The main difference between sediments without Fe electrolyte and the sediments with Fe electrolyte was related to the particle network architecture. The SEM micrographs of sediments made with Fe electrolyte showed a network comprised of fractal branches. The resulting flocs were assembled in a loose fashion. The overall microstructure was roughly consistent with the hierarchical-diffusion-limited-aggregation model (DLA). On the other hand, SEM micrographs of sediments made without Fe electrolyte did not show such fractal branches. The branching, which consisted in the sharing of an edge by three plates, was very frequent in the sediments without Fe.

CHAPTER 3 - DETAILED RESEARCH PLAN

3.1 - RESEARCH ORGANIZATION

As stated in Chapter 1, the main objective of the present study is to determine the microstructure of the clay sediments by SEM, after drying by the supercritical method with CO_2. The clay which we chose to investigate the most extensively was kaolinite, since this is the most abundant mineral in oil sands sludge. However, quite extensive work was also done on montmorillonite.

The microstructure of a kaolinite sediment depends on the conditions in which it was formed, such as the pH and the concentration of metal salt electrolytes. Hence, it was first necessary to classify the type of sediments which were formed according to general characteristics, such as the sediment volume or the sedimentation kinetics. The results of this experimental kinetics part are presented in Chapter 4.

The parameters which we modified were: (1) the nature of the electrical charges on the edges and faces of the clay particles; (2) the pH; (3) the nature of metallic salt electrolyte additives and their concentration; (4) the clay content of the suspensions; (5) the size of the clay particles.

With respect to the electrical charges on the clay particles, two different cases had to be considered: (1) the edges and faces having opposite charges, positive and negative respectively; (2) all charges on both the edges and the faces being negative. Concerning the metallic salt additives, the effect of Fe and Al electrolytes were studied. This choice is due to the fact that these additives are considered to play an important role in the behavior of Alberta oil sands tailing sludge. With both cations, the effects of unaged electrolyte versus aged electrolyte were compared. In the case of Fe, the effect of solid amorphous iron oxide was also studied. This amorphous iron oxide was termed hydroxoferric particles in this thesis, as explained in a later section.

Chapter 5 gives the experimental results on various physical-chemical characterizations of the clay particles or sediments, in the aqueous conditions of this thesis. The data include: (1) some measurements by atomic absorption spectroscopy or by flame photometry, of the Fe and Al precipitated with the clay in the wet sediments; (2) some observations by transmission electron microscopy (TEM) of the Fe compounds which were precipitated with the clay particles; (3) some limited measurement of the sediment viscosities; (4) some measurements of the zeta potential of clay particles, in the electrolyte conditions which were studied in this thesis; and (5) some SEM observations of mixed clay-colloidal SiO_2 particles. The latter investigation was an attempt at gathering some evidence on the opposite sign of the electric charges on the edges and the faces of clay particles, in the conditions when this is supposed to occur. A similar work on mixed kaolinite-colloidal gold particles was done by Thiessen [57]. However, this author did not interpret his results in terms of different signs on the edges and the faces of the clay particles.

The SEM observations of the previous sediments, after supercritical drying with CO_2, are presented in Chapter 6.

As mentioned in Chapter 2, some computations on the clay particles interactions, according to the DLVO theory, have been done by many authors. However, it was necessary to compare the type of particles association which could be computed according to the DLVO theory, in the typical conditions where different sediments were formed in this thesis. The results of these computations are presented in Chapter 7. The zeta potentials used in these computations was selected according to the measurements which are presented Chapter 5.

The results presented in Chapters 4 to 7, are discussed in Chapter 8. The presentation of a comprehensive model for the flocculation and the sedimentation of clay suspensions, is attempted.

3.2 - MATERIALS

3.2.1- Kaolinite

3.2.1.1 - Raw kaolinite

Two different kinds of kaolinites were used in the present study and they were provided by the Georgia Kaolin Company Inc. These kaolinites were Hydrite UF (HUF) and Hydrite R (HR). The chemical analysis, as reported by the supplier, is the same for these two Hydrite kaolinites [117]. In % by mass, this composition is SiO_2 (combined), 45.30 %; Al_2O_3, 38.38 %; H_2O (combined, by ignition), 13.97 %; Fe_2O_3, 0.30 %; TiO_2, 1.44 %; MgO, 0.25 %; Na_2O, 0.27 %; K_2O, 0.04 %. These two kaolinites had a different particle size. Their median sizes according to the supplier were 0.20μm and 0.77μm respectively for the HUF and HR. Some characteristics of these kaolinites are summarized in Table 3.2-1

Table 3.2-1 -Typical physical characteristics of HUF and HR kaolinites. From Georgia Kaolin Company [117].

Grade	Median Particle Size (μm)	pH (1)	Typical Aqueous Viscosity kg/m.s	Specific Surface Area (m^2/g) (4)
Hydrite UF	0.20	4.2-5.2	0.4 (2)	21
Hydrite R	0.77	4.2-4.5	0.29 (3)	10

(1) pH of a 20% aqueous slurry.

(2) Viscosity of a 58% by mass kaolinite slurry with 0.5 % sodium hexametaphosphate, measured at 10 R.P.M. on a Brookfield Viscometer.

(3) Viscosity of a 71% by mass kaolinite slurry with 0.3 % sodium hexametaphosphate, measured at 10 R.P.M. on a Brookfield Viscometer.

(4) Specific surface area measured by the Brunauer, Emmett and Teller (BET) method.

3.2.1.2 - Kaolinite with negatively charged faces and positively charged edges

Both kaolinites (HUF and HR) were converted to the sodium form according to the method of Schofield and Samson [59]. This method consists of replacing the exchangeable cations with Na^+, in a 1M NaCl solution adjusted at pH 3 with HCl. Then, the treated kaolinites were washed with distilled water until there was no evidence of Cl^- in the supernatant liquid tested with $AgNO_3$. The washing step was very carefully made in order to avoid loosing out clay particles from the vessel. The washed kaolinite was not dried. This washed kaolinite suspension had a high solid content (10 % by mass) and it was stored in the vessel where it was washed. Usually, a washed kaolinite stock was used no later than 10 days after washing, in order to avoid any change in the crystal structure of kaolinite in water.

The dependence of the zeta potential on the pH, for the Na-kaolinite which was treated as indicated before, was reported in Fig. 2.3-2. As stated by Schofield and Samson [59], such a dependence is consistent with the existence of positive electric charges on the edges and negative charges on the faces of the kaolinte particles, with a global z.p.c at pH = 4.2.

3.2.1.3 - Kaolinite with negative charges on both the faces and the edges

To obtain kaolinite particles with only negative charges both on the edges and the faces, the kaolintes were first converted to the Na-form, as described in 3.2.1.2. Then they were treated with a sodium phosphate solution, according to a method by van Olphen [5] and by Yaalon [118]. The proportions of each component in this treatment were 50g distilled water for 1mL of 0.125M $Na_4P_2O_7$ and 0.5 g Na-kaolinite. After this treatment, the pH of a kaolinite suspension was ≈ 9.5. As a consequence, the Na-kaolinite particles were dispersed and they slowly settled. The dispersion is due to the adsorption of phosphate anions on the edges of the broken Al-O atomic layers. In this way, the kaolinite particles only carry negative charges, and their zeta potential is negative at all pH, as is shown in Fig. 3.2-1. This figure also reports the data for Na-kaolinite from Yong et al. [54], as this was shown in Fig. 2.3-2. Moreover, the phosphate anions do not easily desorb [5].

With the proportion of $Na_4P_2O_7$ which we used, a Na-kaolinite suspension would slowly settle in about half an hour, which was a very reasonable time scale for the present experimental research.

3.2.2 - Montmorillonite

The Na-montmorillonite used in this study was the SWy-1 montmorillonite from the Clay Minerals Repository of the Clay Minerals Society at the University of Missouri. This montmorillonite was directly used in the as received state, as this was done in the MSc study by Zou [1]. The cation exchange capacity of this clay is 76meq/100g and its specific surface area is 32 m^2/g [1].

Directly after dispersion in distilled water, the pH of a SWy-1 montmorillonite suspension was 9.5. The zeta potentials of such montmorillonite particles are known to be negative at most pH values, as our own data in Fig. 3.2-1c show. However, van Olphen [5] considers that such a montmorillonite still carries negative charges on the particles faces and positive charges on the edges at low pH.

3.2.3 - Fe Additives

3.2.3.1 - Unaged Fe electrolyte solutions

$FeCl_3$ and $Fe_2(SO_4)_3$ or $FeSO_4$ were dissolved in distilled water at room temperature. Each dissolution was performed just prior to a clay sedimentation experiment. Other authors have termed such Fe solutions as "fresh solutions".

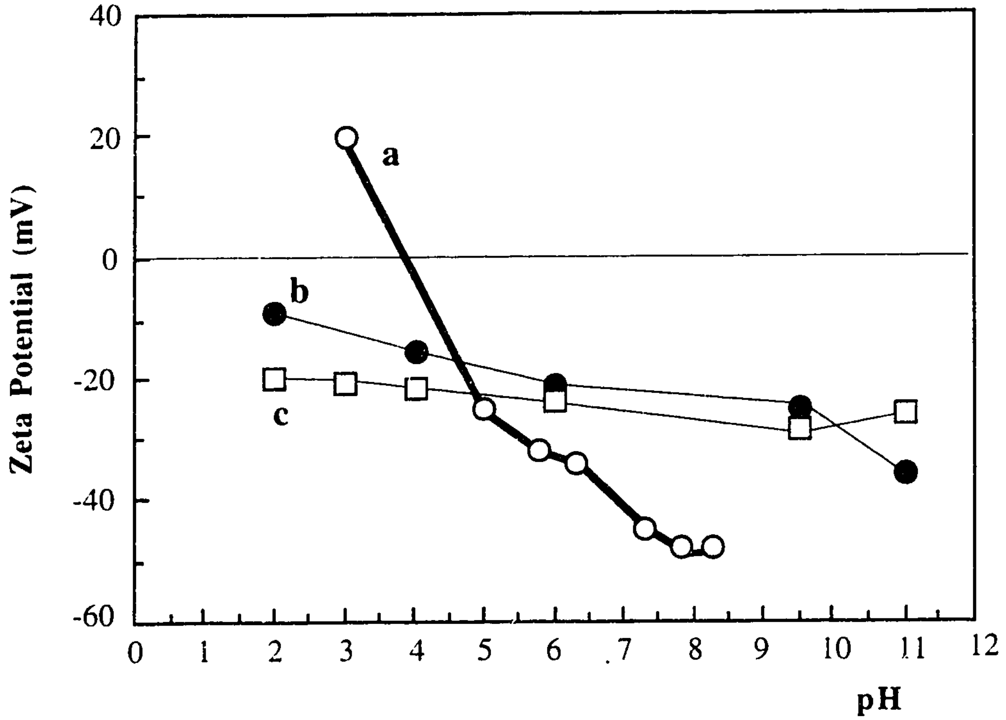

Fig. 3.2-1 - Relationship between the pH and the zeta potential, in an aqueous clay suspensions: (a) Na-kaolinite (Hydrite PX) after Yong et al. [54], compared with the present measurements on: (b) HUF Na-kaolinite treated with $Na_4P_2O_7$; and (c) untreated Na-montmorillonite.

3.2.3.2 - Aged Fe electrolyte solutions

Beakers containing 500 mL of a 0.5M solution of $FeCl_3$ in distilled water, were prepared. These solutions were allowed to age for a month. With time, a precipitate formed at the bottom of the beakers, while the supernatant solution remained brown and translucent. The precipitate was separated from the brown solution by centrifugation. By using the technique of atomic analysis, we found that the Fe concentration in the brown solution had decreased to a value of 0.33 M.

The precipitate was dried in a dessicator. Then, it was analyzed by X-ray diffraction and the recorded data is shown in Fig. 3.2-2. These X-ray diffraction patterns indicate a mixture of ferric compounds. The particles in this precipitate had either a needle-like or a platelike shape, as illustrated in the SEM micrographs of Fig. 3.2-4. The EDX analysis of these particles is reported in Table 3.2-2.

Table 3.2-2- Semiquantitative EDX analysis of the precipitates from aged $FeCl_3$ solutions.

	Needle-like particle		Platelike particle	
Element	% wt	% Atom	% wt	% Atom
Fe	48.3	36	47	36
Cl	49.3	58	52	61
O	2.4	6	1	3

3.2.3.3 - Hydroxoferric particles

Hydroxoferric particles were made by the method of Ohtsubo et al. [45]. This method consists in adding drop by drop a saturated sodium bicarbonate ($NaHCO_3$) solution to a solution of 48.66g $FeCl_3$ in 300mL distilled water, until the pH reaches the value of 1.5. Precipitation occurs, and the precipitate was termed amorphous iron hydroxide, ferrihydrite or hydroxoferric particles, depending on the authors.

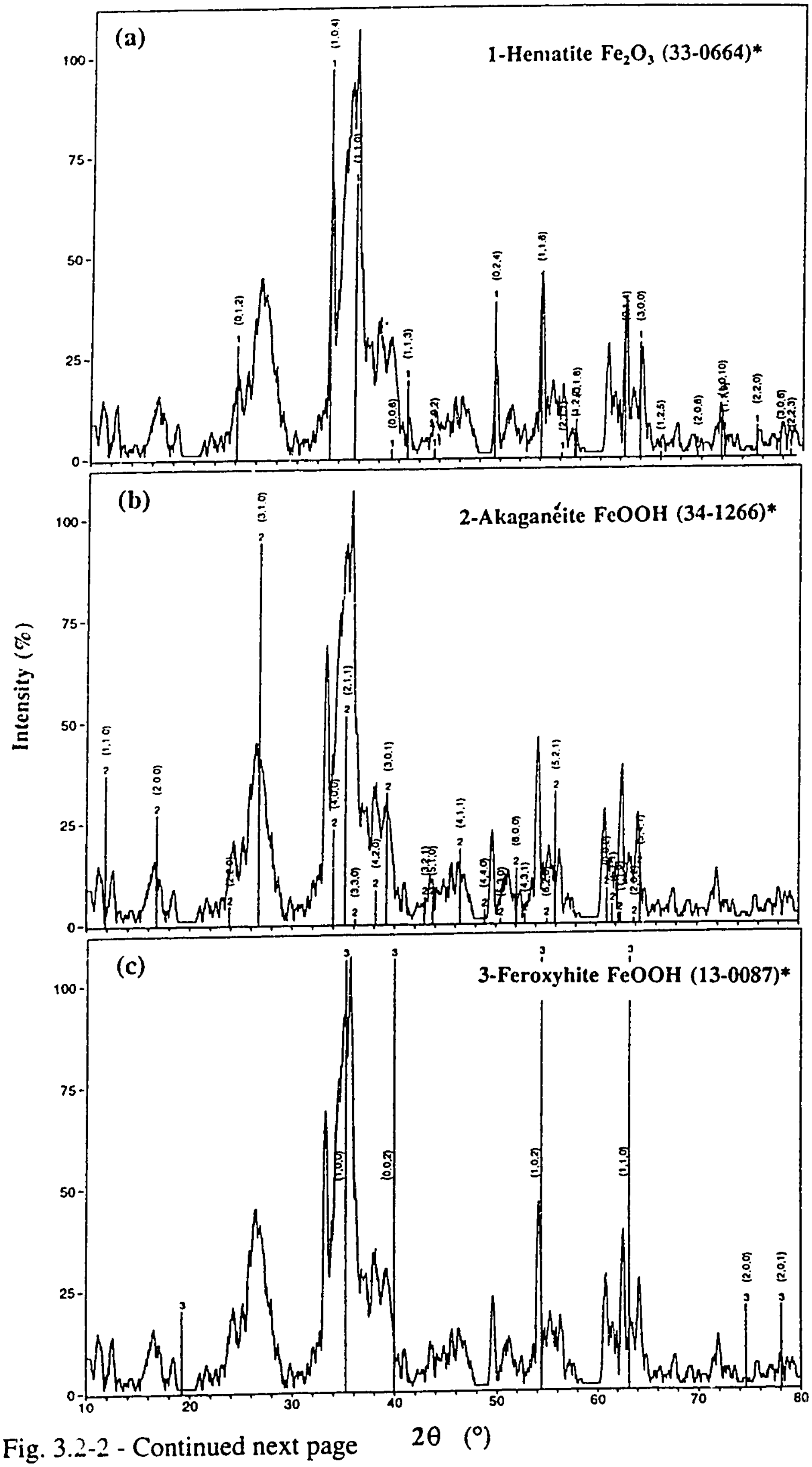

Fig. 3.2-2 - Continued next page

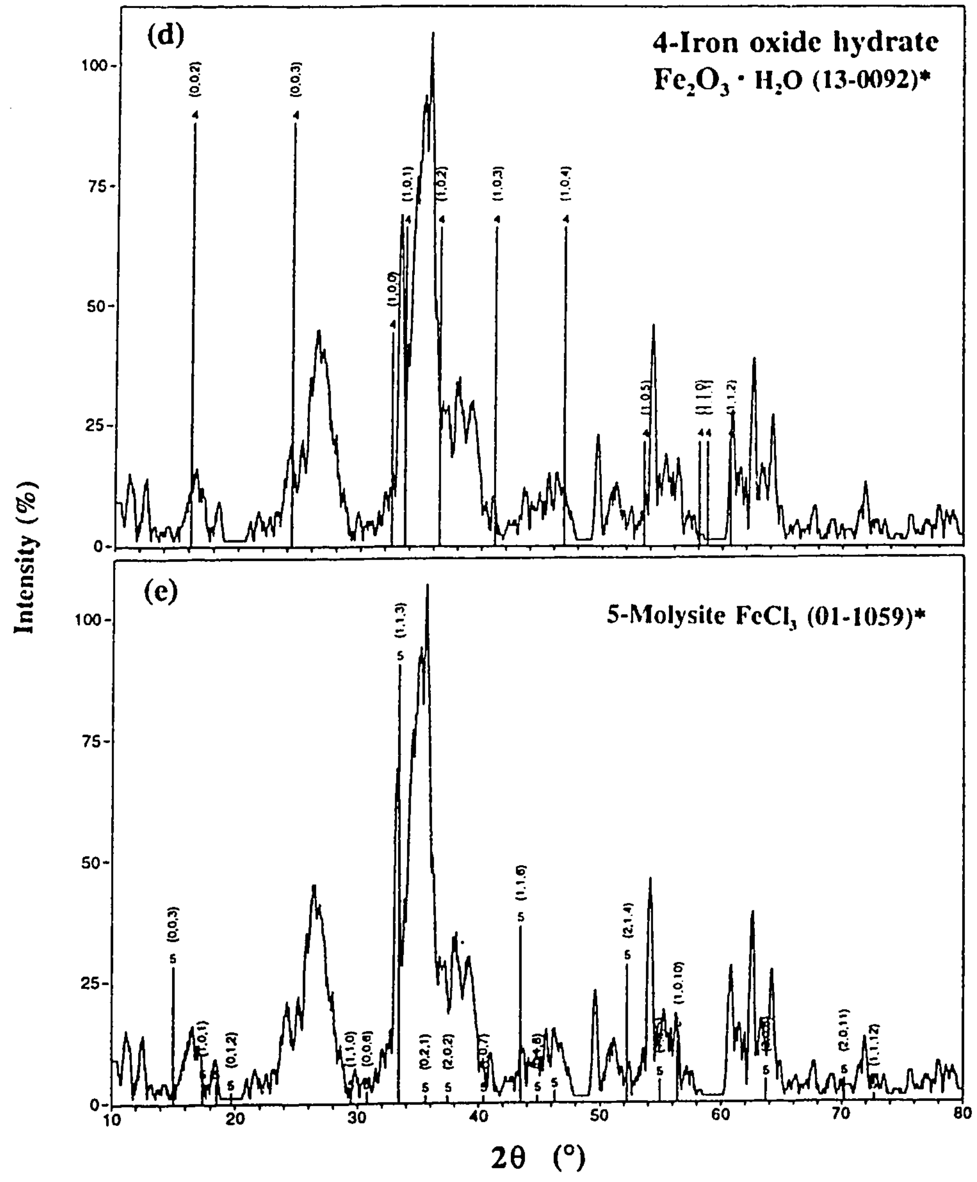

* - X-ray file number

Fig. 3.2-2 - X-ray diffraction patterns (Cu Kα, Ni filtered) of the precipitates from aged $FeCl_3$ solution with the X-ray diffractometer (Rigaku Rotating Anode XRD). The precipitates include phases: (a) Hematite Fe_2O_3; (b) Akaganéite FeOOH; (c) Feroxyhite FeOOH; (d) Iron oxide hydrate $Fe_2O_3.H_2O$; (e) Molysite $FeCl_3$.

In the present work, the term of hydroxoferric particles from Blackmore [74], is used. The excess salt was removed from this precipitate by dialysis in distilled water. The distilled water was renewed until the pH of the suspension was in the range 3.8 to 4.2. The solid content in the suspension was 2.5g/100mL.

A part of this precipitate was dried and it was analyzed by the technique of powder X-ray powder diffraction, with Ni filtered Cu K_α radiation. The X-ray pattern showed that akaganéite β-FeOOH was the main crystalline phase (Fig. 3.2-3), in agreement with the reports in the bibliography. The hydroxoferric particles examined by TEM had an aspect which was termed "pepper-like" by Ohtsubo et al. [61] (Fig. 3.2-4c). Also, the selected area diffraction pattern proved that these particles were akaganéite β-FeOOH (Fig. 3.2-4d).

3.2.4 - Al additives

3.2.4.1 - Unaged Al electrolytes

$AlCl_3$, $Al_2(SO_4)_3$, and $Al(NO_3)_3$ were used. They were dissolved in distilled water at room temperature, just before adding them into the clay suspensions. These Al-containing electrolyte aqueous solutions were transparent.

3.2.4.2 - Aged Al electrolyte

Beakers containing 500 mL of a 0.5M $AlCl_3$ solution in distilled water, were prepared These solutions were allowed to age for a month. No obvious precipitation occurred during this aging process.

3.2.5 - SiO_2 additives

Monodispersed SiO_2 colloidal particles were prepared according to the method developed by Stöber et al. [119]. This method consist of hydrolyzing the tetraethoxysilane

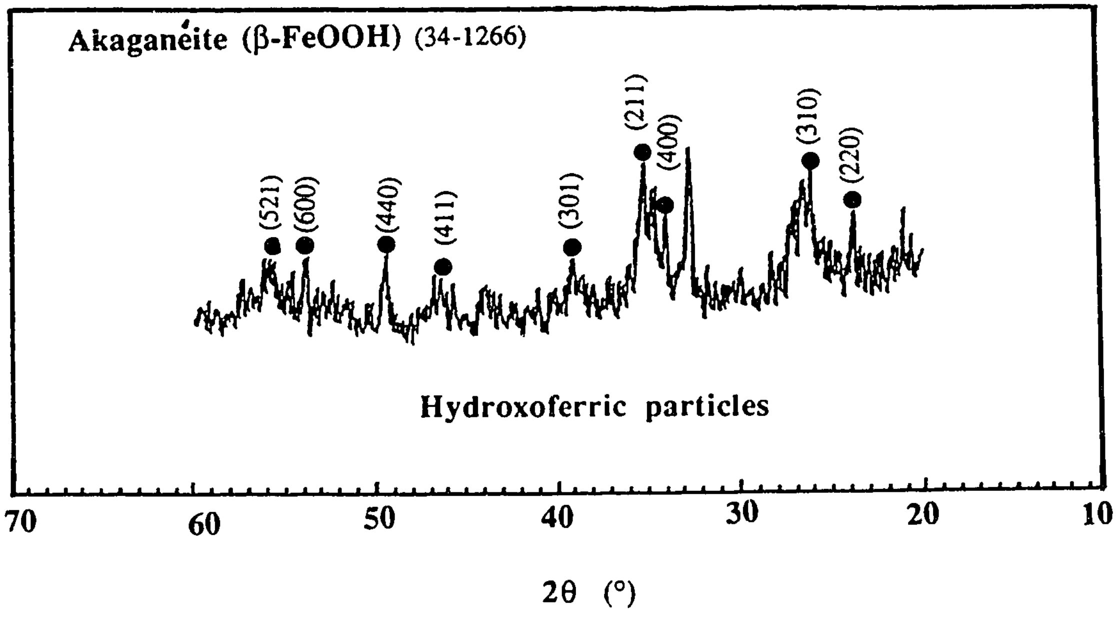

Fig. 3.2-3 - X-ray diffraction patterns (CuKa, Ni filtered) of hydroxoferric particles with the X-ray diffractometer (Rigaku-Denki XRD).

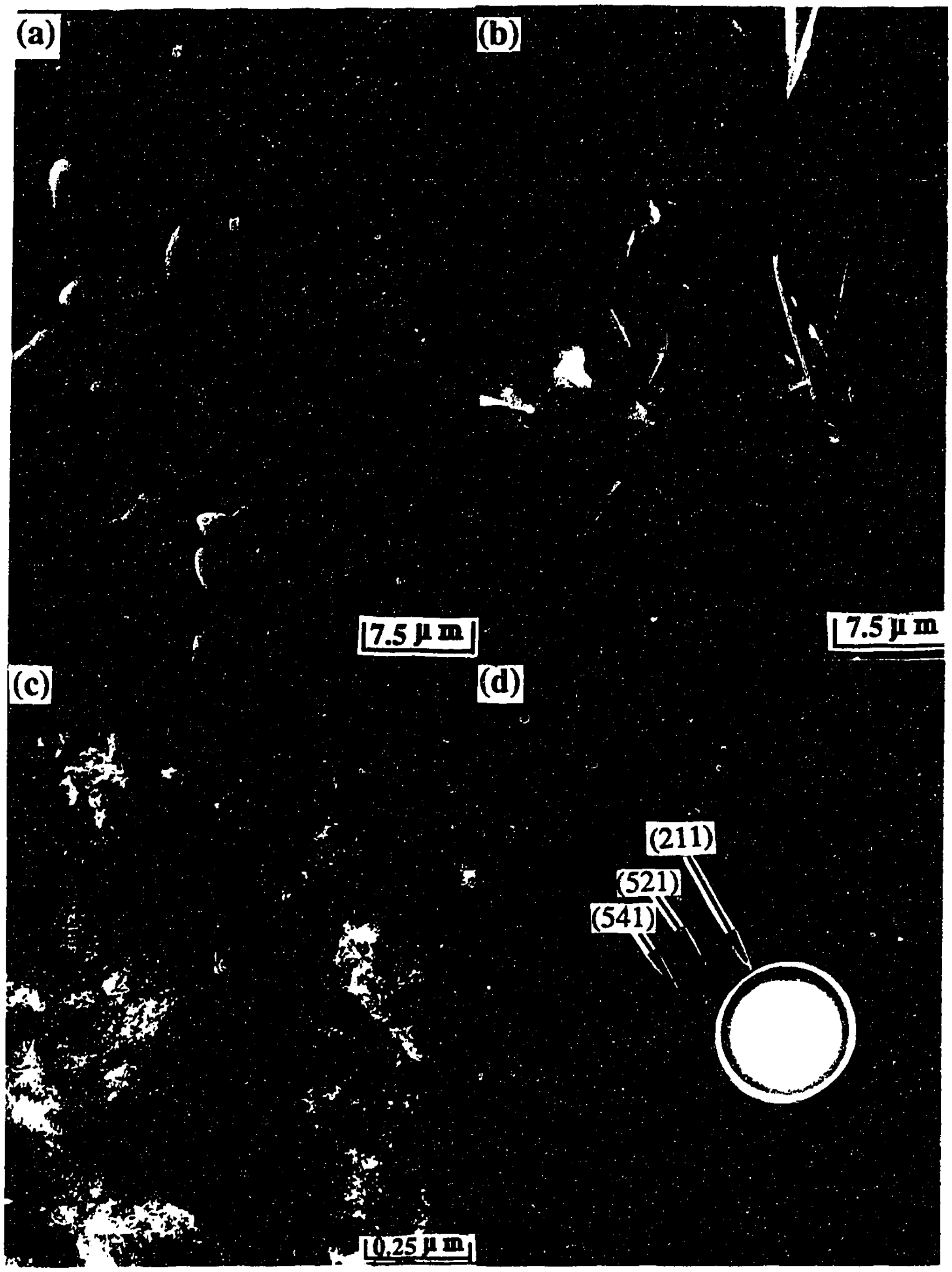
(a)
(b)
7.5 μm
7.5 μm
(c)
(d)
(211)
(521)
(541)
0.25 μm

Fig. 3.2-4 - SEM micrographs of the precipitates from aged $FeCl_3$ solutions: (a) needle-like particles; (b) platelike particles. (c) TEM micrograph of hydroxoferric particles; (d) Pattern of the selected area diffraction in the center of (c). The rings correspond to β-FeOOH.

(TEOS) in the presence of ammonia. The SiO_2 particle size depends on the molar ratio of the reagents.

In the present thesis, the reagents' molar ratios used are reported in Table 3.2-3. The total volume of the liquid mixture was 100mL, and the reagents were mixed with a magnetic bar in a beaker at room temperature. After an induction time, SiO_2 particles started to form. This process was allowed to proceed for 24 hours. Then the suspension was centrifuged and washed 3 times in distilled water, in order to remove the residual chemical reactants. Next, 2 grams of SiO_2 particles were dispersed to make a sol, in 100mL of distilled water. The pH value of the suspensions was 7.5. Three different types of SiO_2 sols, with a different particle diameter, were prepared in this way, as indicated in Table 3.2-3. Fig. 3.2-5 shows the SEM micrographs of these particles.

Table 3.2-3. Molar ratio of the reagents used to prepare monodispersed SiO_2 particles, and size of the particles which were obtained by the Stöber method [119]

Sample Number	1	2	3
TEOS	0.28	0.28	0.28
H_2O	7.5	7.5	7.5
NH_4OH	0.2	1.0	3.0
Average Particle Diameter (μm)	0.2	0.35	0.65

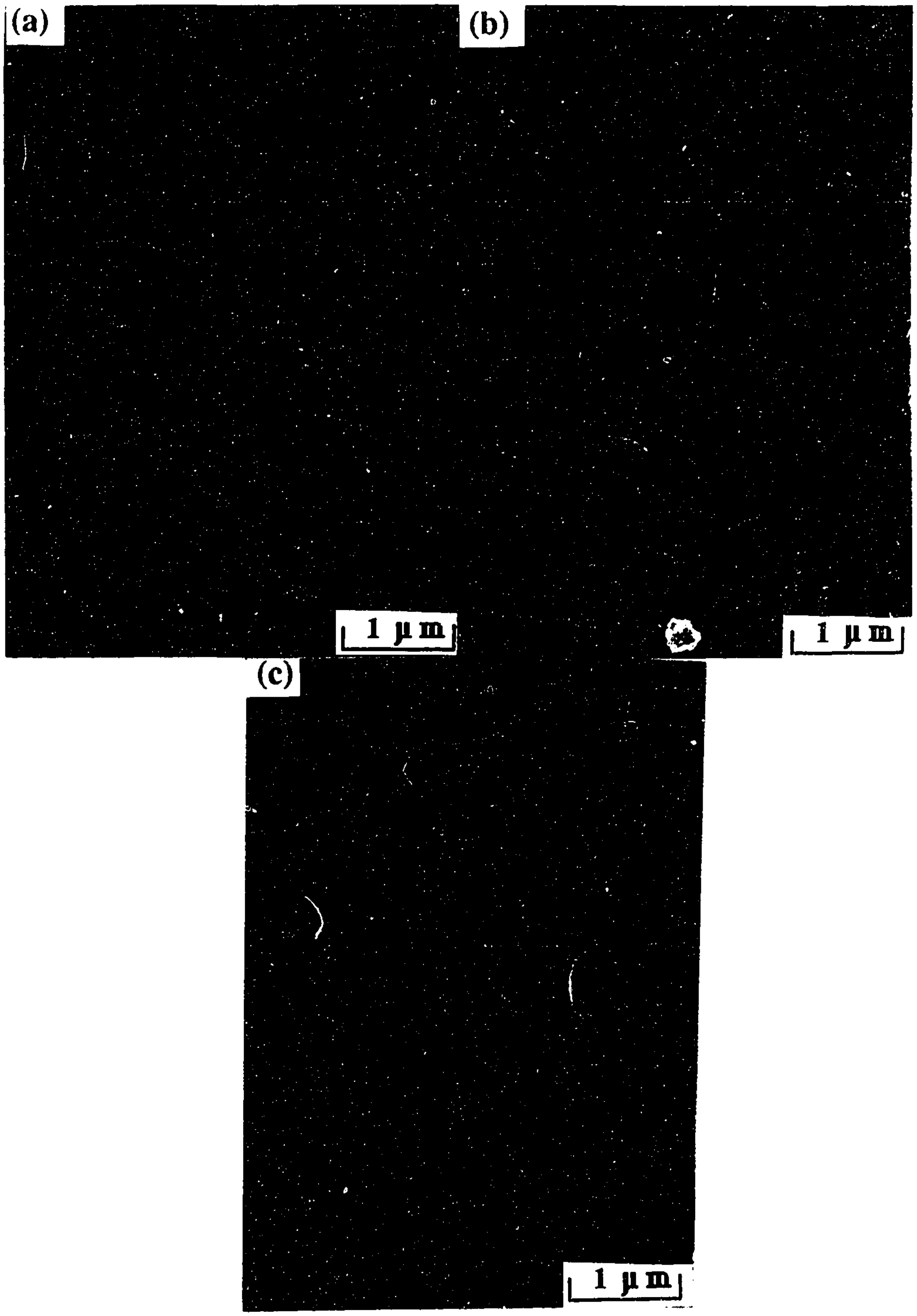

Fig. 3.2-5 - SEM micrographs of the SiO_2 particles prepared by the Stöber method [119] in the conditions listed in Table.3.2-3: (a) Sample 1; (b) Sample 2; (c) Sample 3.

3.3 SEDIMENTATION PROCEDURE

3.3.1 - Kaolinite suspensions

3.3.1.1 - Kaolinite with negatively charged faces and positively charged edges

In all these experiments, the HUF Kaolinite was treated according to the method of Schofield and Samson [59], as indicated in Section 3.2.1.2. A suspension containing 1% kaolinite by mass, was made in distilled water, and the measured pH was 6.9. Two groups of suspension samples, each containing 0.5 % (by mass) of kaolinite, were made from the previous suspension. Each of these samples had a total volume of 100 mL, and was contained in a graduated cylinder.

The first group was comprised of samples where the pH values were respectively adjusted to 2, 4 and 6 with HCl, and to 9.5 with NaOH. No other electrolyte was added to these samples. The second group was also comprised of samples where the pH were respectively adjusted to 2, 4, 6 and 9.5. However, each of these samples also contained a concentration of 0.67mM unaged $FeCl_3$.

After preparation, each cylinder which contained a kaolinite suspension was covered with a piece of parafilm to prevent water evaporation. Each cylinder was turned upside down 20 times to uniformly distribute the components inside the suspension. The sedimentation tests were performed at room temperature.

In each sedimentation cylinder where a sharp interface between 2 different layers was observed, the height of this interface was recorded. Readings were recorded every 5 or 10 minutes, depending on the settling rate, during the first hour. Then, this interface position was read every hour for the next two hours. At the end of a sedimentation experiment, this height was measured every 24 hours, until 360 hours. The settling rate was defined as the derivative of the sediment thickness with respect to the time and it was measured in cm/hour. The final sediment thickness was defined as the thickness after 360 hours. A height of 1 cm corresponded to a volume of 6.16 mL in a graduated cylinder.

3.3.1.2 - Kaolinite with negative charges on both the faces and the edges

In all these experiments, the HUF Kaolinite was treated with phosphate as indicated in Section 3.2.1.3.

Unless stated differently, suspension samples containing 0.5 g of kaolinite in 50 mL distilled water were prepared in graduated cylinders. To these samples, different concentration of unaged or aged Fe electrolyte solutions were added. The pH of each suspension sample was adjusted to a different value by adding some NaOH, HCl or H_2SO_4. These acids and this base were selected to avoid any undesirable ion exchange with the clay. HCl was used when the Fe electrolyte was $FeCl_3$, while H_2SO_4 was used with $Fe_2(SO_4)_3$. The total volume of each suspension was finally adjusted to 100mL before beginning the sedimentation test, so that the kaolinite concentration was 0.5 %.

The behavior of such HUF kaolinite suspensions in the presence of unaged Fe electrolyte was investigated at the pH values of 2, 4, 6, 8, 9.5, 10, and 11, respectively. At each pH, the unaged $FeCl_3$ concentrations studied were 0.17, 0.33, 0.67, 1.67, and 3.3mM while the concentrations of unaged $Fe_2(SO_4)_3$ were 0.08, 0.17, 0.33, 0.83, 1.67mM. In order to better understand the role of Fe^{3+} hydrolysis on the flocculation behavior, the effect of aged $FeCl_3$ concentrations of 0.17, 0.33, 0.67, 1.67, 3.3, 5, and 10mM were examined at the pH values of 2, 4, 6, 9.5, and 11.

Also, to assess the role of different cations and anions on the sedimentation behavior, supplementary experiments were carried out on the HUF kaolinite with the electrolytes $FeSO_4$ (unaged) and NaCl, at pH 2.

Furthermore, to assess the effect of the kaolinite particles size and of the clay content in a suspension, the behavior of two kinds of kaolinite, hydrite (HUF) and hydrite (HR), were compared in a few typical cases. As mentioned previously, these two types of kaolinite have a different particle size. These clays were prepared according to the treatment summarized in 3.2.1.3. Four different pH values were selected: 2, 4, 6 and 9.5. At each pH value, four different clay contents were selected; 0.5, 1, 2, and 5 % (by mass). At each pH and for each clay content, four different unaged $FeCl_3$ concentrations were selected: 0, 1, 5, 10mM, respectively.

As this was done with the Fe electrolytes, the sedimentation of HUF kaolinite suspensions in the presence of Al electrolytes was studied. The kaolinite content was 0.5 % (by mass). The pH studied with $AlCl_3$ was 2, 4, 6, 8, 9.5 and 12, while the pH studied with $Al_2(SO_4)_3$ and $Al(NO_3)_3$ was 2, 6, 9.5 and 12. These pH values were achieved by addition of HCl, H_2SO_4, HNO_3 or NaOH, respectively, depending on the nature of anions in the Al electrolyte. The concentrations of unaged $AlCl_3$, $Al_2(SO_4)_3$, $Al(NO_3)_3$ which were investigated were 1, 2, 5, 10, and 50 mM, respectively, for each pH. Similar studies were made with aged $AlCl_3$ at concentrations of 1, 2, 5, 10, and 10mM, and at the pH of 2, 4, 6, 9.5 and 12.

The sedimentation experiments themselves were performed according to the same procedure as indicated in the previous section.

3.3.2 - Montmorillonite suspensions

The aqueous system montmorillonite-unaged $FeCl_3$ was investigated in detail by Zou [1]. In order to address the effect of Fe^{3+} hydrolysis on the stability of montmorillonite suspensions and the microstructure of the sediment, the sedimentation of montmorillonite with aged $FeCl_3$ was studied in the present thesis. Each cylinder contained 100 mL of a suspension with 1 % Na montmorillonite. Before adding any electrolyte, the suspension pH was about pH=9.5. The pH values investigated in the present study were 2, 4, 6, 9.5 and 12 and they were realized by adding HCl or NaOH to the suspension, depending on the pH. The aged $FeCl_3$ concentrations studied at each pH were 0.33, 1, 2, 3.3, 5 and 10mM. Another series of sedimentation was performed by mixing hydroxoferric particles with the montmorillonite suspensions. The pH were the same as previously and the hydroxoferric particles contents were 0.025, 0.125, 0.25 and 0.50 % (by mass) at each pH.

As with kaolinite, the sedimentation of montmorillonite in the presence of unaged or of aged $AlCl_3$ was studied. The pH investigated were the same as previously, and the concentrations of unaged or aged $AlCl_3$ were 0.17, 0.33, 1, 2, 3.3, 5, 10, and 20 mM at each pH.

3.3.3 Mixed kaolinite - colloidal SiO_2 samples

3.3.3.1 - Kaolinite with negatively charged faces and positively charged edges

The kaolinite used in this study was the hydrite HR, because it is comprised of bigger particles than the HUF kaolinite. This HR kaolinite was converted to the sodium form by the exchange procedure described in Section 3.2.1.2. A suspension containing 1% kaolinite by mass in distilled water, was made. The pH of this suspension was ≈7.6. Next, this suspension was divided in six identical 20 mL samples. In three of these samples, the pH was adjusted to 2 with HCl, while in the three other samples the pH was adjusted to 4 with HCl. At these two pH values, kaolinite particles are expected to carry negative charges on their faces and positive charges on their edges. However, pH 4 is close to the global z.p.c of Na-kaolinite particles. To one of the pH 2 kaolinite samples, and to one the pH 4 kaolinite samples, 1mL of the SiO_2 sol sample # 1 described in Section 3.2.5, was added. The mixed samples were stirred for 10 minutes with a magnetic stirrer. Similar mixed systems were made by adding 1 mL of the SiO_2 sols # 2 and # 3 to the four remaining kaolinite suspension samples. The addition of the SiO_2 sols did not significantly modify the pH of the original kaolinite samples made at pH 2, while it increased the pH to a value between 4.1 and 4.2 for the original kaolinite samples prepared at pH 4. Also, the SiO_2

particles are expected to be charged positively at pH 2, while they are charged negatively near pH 4. Drops of each mixed system were placed on SEM sample holder where they were dried, for examination.

3.3.3.2 - Kaolinite with negative charges on both the faces and the edges

Three samples containing 20 mL of a 1% HR kaolinite were prepared as previously described in Section 3.3.3.1. In two of these samples, the pH was adjusted to 10 with NaOH. Next, 1mL of the SiO_2 sols # 1 and # 3 were added, each to one of these two kaolinite samples. The third HR kaolinite sample was adjusted to pH 10 with a 0.125M $Na_4P_2O_7$ solution. Then, 1mL of the SiO_2 sol # 2 was added. In these three kaolinite samples, the pH was not significantly modified by adding the SiO_2 sols, the kaolinite particles were expected to carry negative charges on both their faces and their faces, and the SiO_2 particles should also be negatively charged. Drops of these 3 mixed systems were dried and examined under a SEM.

3.3.4 - Supercritical drying of sediments

In order to dehydrate the samples for SEM observation, the aqueous medium of a suspension was exchanged for ethanol by dialysis, in a tube from the SPECTRUM Company. First, the sedimentation experiment was directly performed in the dialysis tube, with one end of the tube being closed. Then, after sedimentation was complete, the supernatant liquid above the sediment was removed. Finally the tube was closed and it was placed in a beaker where 99% pure ethanol was gradually added. The ethanol diffused into the sediment and it slowly replaced water. This liquid exchange had to be done very slowly, to avoid any shrinkage of the sediment. This step was repeated at least 10 times, until practically all the water was replaced with alcohol. The dialysis tube was then moved to a supercritical point dryer (BIO-RAD E3000 SERIES). The alcohol was replaced with liquid CO_2 by flowing this liquid inside the dryer, and a supercritical drying route was applied to the dryer and its content. This only requires heating the dryer with a hot water circulation since the critical point is low as was previously mentioned (T_c = 31°C and P_c = 7433kPa [92]). The warm supercritical CO_2 fluid could be evacuated as a gas without creating a liquid-gas meniscus. The dried sediment samples were gold-coated or carbon-coated, for SEM observation.

3.4 CHARACTERIZATION TECHNIQUES

3.4.1 - Rheological Properties

In this study, the rheological properties of a limited number of suspensions were determined with a cylindrical rotor viscometer, of the type CONTRAVE RHEOMAT 115. Flow curves were first recorded by increasing, then by decreasing the shear rate, and waiting for equilibrium at each shear rate. In order to compare the samples in a consistent manner, the Bingham yield stress which was recorded for a suspension was determined form the increasing shear rate data.

The rheology of two different groups of samples was studied. A first series of suspensions was comprised of kaolinite particles treated according to the method in Section 3.3.3.1, with opposite electric charges on the edges and on the faces. This series was the same as in the sedimentation experiments detailed in Section 3.3.1.1, except that the kaolinite content in the suspensions was 10 % by mass. The pH values were 2, 4, 6, 9.5 and 12, without any other additive, or with an unaged $FeCl_3$ concentration of 0.67 mM.

The second series of samples which were examined by this technique were from the montmorillonite-hydroxoferric particles system. The montmorillonite content in the suspensions was 1% by mass. The pH values investigated were 2, 4, 6, 8, 9.5 and 12, while the hydroxoferric contents of the suspensions were 0, 0.025, 0.125, 0.25 and 0.5 % (by mass) at each pH.

3.4.2 - Determination of the zeta potential (ζ)

The electrophoresis equipment used was the particle micro-electrophoresis MARK II apparatus from the RANK BROTHERS company. This piece of equipment had a flat and rectangular cell. The measurements were performed for one of the stationary level conditions inside the cell. The electrophoretic mobility of a minimum of five particles were successively measured, first when applying the electric field in one direction, then after reversing the polarity of the applied electric field. The average value was recorded. For the equipment being used, the zeta potential could be calculated from the following formula [120]:

$$\zeta = \frac{4\pi\eta u}{\varepsilon E} \times (300)^2 \qquad (3.4\text{-}1)$$

In this formula, ζ is the zeta potential in Volt, η is the liquid viscosity in Poise (as an approximation, the viscosity of water was used in this formula), ε is the relative dielectric constant of the liquid (the dielectric constant of water was used in this study), u is the electrophoretic mobility in cm/s, E is the electric field in V/cm. For the cell being used, $E = \frac{\Delta V}{3.27}$ in which ΔV was the applied voltage.

Because the 0.5 % (by mass) kaolinite and the 1 % (by mass) montmorillonite suspensions were too dense to directly measure their zeta potential, these clay suspensions were first diluted to 0.05% and to 0.01%, respectively, in distilled water. In each case, and just before measuring the zeta potential, the pH was adjusted to the value the suspension had before dilution, with addition of HCl or NaOH depending on this pH. In the same way, some Fe or Al electrolyte was added to each clay suspension so as to maintain the initial concentration of these electrolytes before dilution.

In the present study, two types of kaolinite suspensions systems were treated according to the method in 3.2.1.2 and they were investigated. They included: kaolinite suspensions at the pH values 2, 4, 6 and 9.5, without any Fe or Al additives; and kaolinite-unaged $FeCl_3$ samples at the pH values 2, 4, 6 and 9.5, with an unaged $FeCl_3$ concentration of 0.67 mM.

Three other types of kaolinite suspensions systems, treated with the phosphate according to the method in 3.2.1.3, were investigated. They included: kaolinite-unaged $FeCl_3$ at the pH values 2, 4, 6, 9.5, 10 and 11, and the unaged $FeCl_3$ concentrations 0.17, 0.33, 0.67, 1.67 and 3.3 mM; kaolinite-aged $FeCl_3$ at the pH values 2, 4, 6, 9.5, 10 and 11, and the aged $FeCl_3$ concentrations 0.17, 0.33, 0.67, 1.67, 3.3, 5 and 10 mM; and kaolinite-unaged $AlCl_3$ at the pH values 2, 4, 6, 9.5, and 12, and the unaged $AlCl_3$ concentrations 1, 2, 5, and 10 mM.

Two more types of samples with montmorillonite were studied, namely: montmorillonite-hydroxoferric particles at the pH values of 2, 4, 6, 9.5 and 12, and the hydroxoferric particles concentrations of 0.025, 0.125, 0.25, and 0.5 % (by mass); and montmorillonite-unaged $AlCl_3$ at the pH values of 2, 4, 6, 9.5 and 11, and the unaged $AlCl_3$ concentrations 0.5, 1, 3.5, and 10 mM.

3.4.3 - Scanning Electron Microscope (SEM) Observations

The sediment samples dried by the supercritical drying method described in Section 3.3.4, were examined with a Hitachi S-2700 SEM equipped with a LINK-eXL Energy Dispersion X-ray (EDX) system. These observations were mostly done at 10 kV, sometimes at 15 or 20 kV, depending on the sample. When a sample had an oriented microstructure, it was observed in a horizontal and in a vertical cross-section, as shown in Fig. 3.4-1.

All the types of clay sediments made in this thesis were examined by this technique.

3.4.4 - Transmission Electron Microscope (TEM) Observations

For the TEM observations, a diluted suspension was dropped on a carbon coated copper grid supplied by the SPI company. Two different TEM were used in this study. Most samples were examined in a PHILIPS EM 300 TEM. In order to obtain some composition analysis of the TEM samples, a JEOL-2010 Analytical Transmission Electron Microscope (ATEM) was also used. The latter microscope was connected with a X-ray

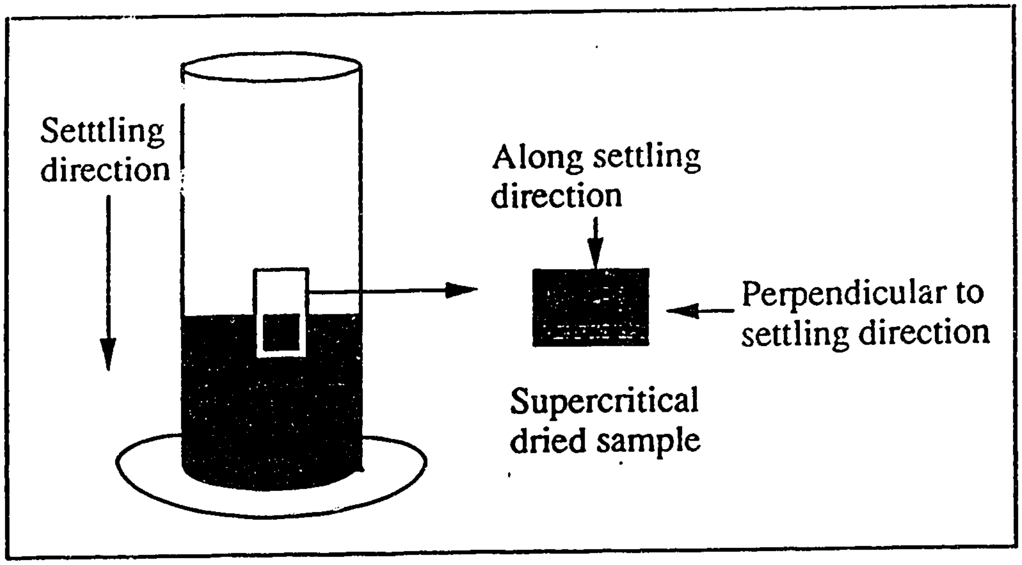
Setttling direction
Along settling direction
Perpendicular to settling direction
Supercritical dried sample

Fig. 3.4-1 - Directions in which supercritical-dried clay sediment samples were observed.

detector, so that Energy Dispersed X-Ray Spectrum (EDX) could be obtained besides TEM micrographs.

The samples which were examined by TEM included: a 0.5 % (by mass) kaolinite suspension treated with the phosphate as in 3.3.1.2, and comprised of a 10 mM unaged $FeCl_3$ concentration at pH 9.5; a 1 % (by mass) montmorillonite suspension comprised of a 10 mM unaged $FeCl_3$ concentration at pH 9.5; and a series of suspensions containing 1 % (by mass) montmorillonite, mixed with hydroxoferric particles at the concentrations of 0.125 % (by mass) at pH 2, 6 and 9.5 and 0.5% at pH 2, 9.5 and 12.

3.4.5 - Atomic Absorption Spectroscopy and Flame Photometry

Kaolinite and montmorillonite suspensions were prepared in the same way as described in detail in Sections 3.3-1 and 3.3-2. The kaolinite concentration was 0.5 % (by mass) and the concentration of montmorillonite was 1 % (by mass). These suspensions were prepared in 100mL graduated cylinders. Both with the kaolinite and with the montmorillonite, the pH values investigated were 2, 4, 6, 9.5 and 11. The concentrations of aged or of unaged $FeCl_3$ electrolyte investigated were 0.33, 1.67, 3.3, and 10mM.

In samples where a clear supernatant liquid formed naturally after 12 hours, the Fe or the Al content in the supernatant liquid was directly analyzed directly analyzed by atomic absorption spectroscopy. In clay suspension where flocculation did not occur, the suspension was centrifuged until a clear supernatant liquid separated from the suspension. These clear liquid was used for chemical analysis.

The chemical analysis focused on determining the Fe and the Al which remained in solution. From these results, the amount of Fe or of Al adsorbed on the clay particles could be determined. The main equipment used was a PERKIN-ELMER 4000 AAS atomic absorption spectrophotometer. In some samples, Na was also analyzed in a flame photometer from BUCK SCIENTIFIC , Inc.

3.4.6 - Phase Identification and X-Ray Diffractometer

Two kinds of X-Ray diffractometer were used in this study. One of them was a Rigaku Denki X-Ray diffractometer with a Philips goniometer used to identify the phase of the hydroxoferric particles. The other was a Rigaku Denki rotating anode X-Ray diffractometer used to analyze the precipitates from aged $FeCl_3$ solutions. The X-ray data from the second diffractometer was analyzed with Jade Search/Match software available from MDI, Inc. A Cu target with a Ni filter was used in both equipments.

CHAPTER 4 - SEDIMENTATION BEHAVIOR

The detailed research plan of this thesis, concerning sedimentation, was presented in Section 3.3. The present chapter addresses the results on sedimentation behavior of clay suspensions. The sedimentation data which are presented concern: (1) kaolinite suspensions where kaolinite particles were charged negatively on their faces and positively on their edges; (2) kaolinite suspensions where kaolinite particles were charged negatively on both their faces and their edges; (3) montmorillonite suspensions. The preparation procedures of these clays were detailed in Chapter 3. For these three systems, the sedimentation data which are reported concern clay mixed with unaged and aged Fe electrolytes, then with unaged and aged Al electrolytes.

4.1 - KAOLINITE WITH NEGATIVELY CHARGED FACES AND POSITIVELY CHARGED EDGES

In the two groups of kaolinite suspensions listed in Section 3.3.1.1, that is to say with or without unaged $FeCl_3$, the sedimentation behavior followed the same pattern which is illustrated in Fig. 4.1-1. In all cases the sedimentation was fast, since it was over in about one hour.

At pH 9.5, both with 0.67 mM unaged $FeCl_3$ and without $FeCl_3$, the sedimentation kinetics were characterized by an induction period of the order of 10 minutes. During this induction period, flocs were being formed. At one moment, these flocs joined to each other and constituted an apparently uniform sediment, separated by a sharp interface from the clear supernatant liquid. The settling of the flocculated sediment started at a relatively fast initial settling rate. Then this settling progressively slowed down.

At pH 2, both with 0.67 mM unaged $FeCl_3$ and without $FeCl_3$, the sedimentation kinetics were characterized during the 5 first minutes by the accumulation of a thin sediment

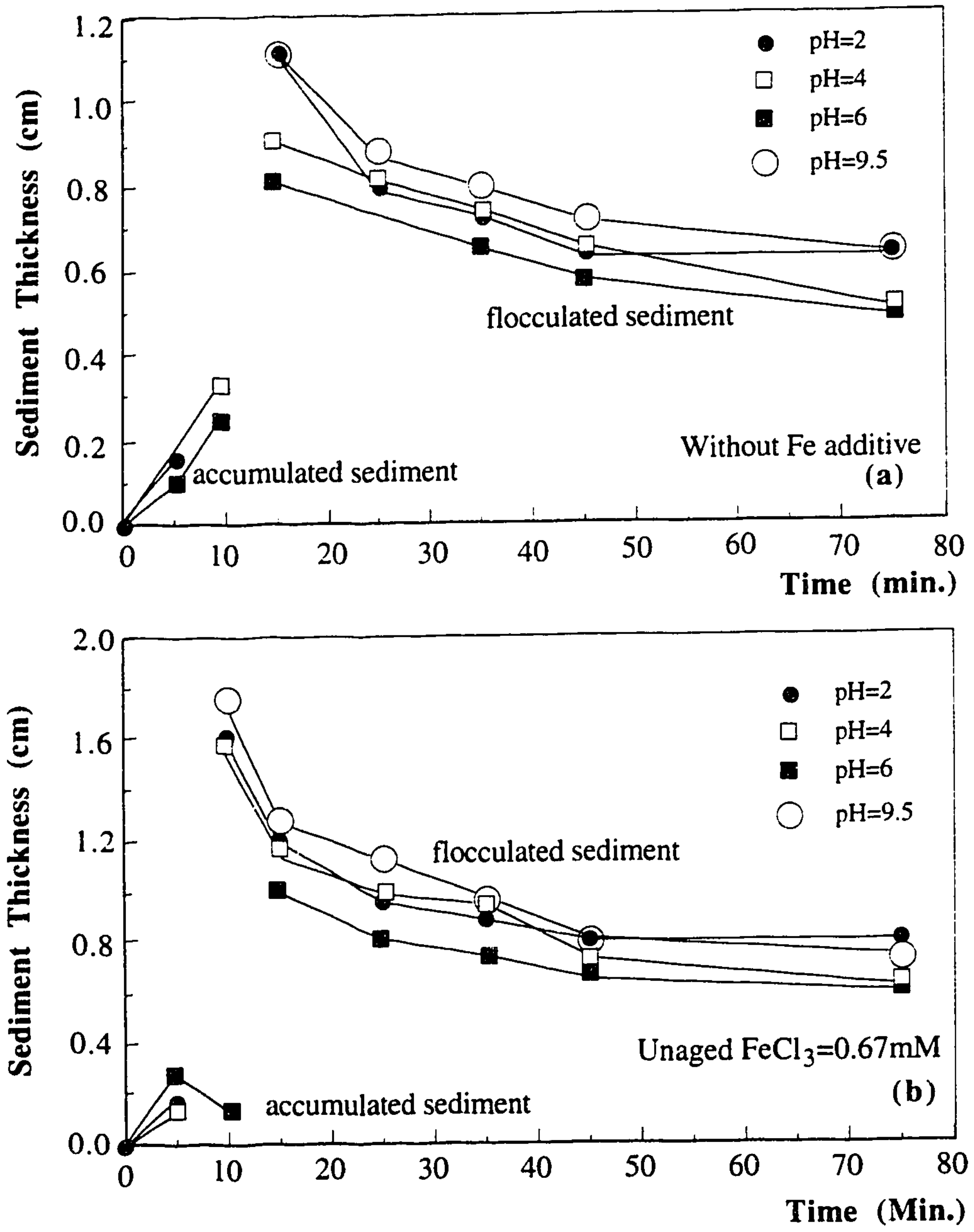

Fig. 4.1-1 - Kinetics of sedimentation of 0.5% Na-kaolinite suspensions treated by the method of Schofield and Samson [59]: (a) without Fe electrolyte; (b) with 0.67 mM unaged $FeCl_3$.

at the bottom of the cylinder. This accumulated sediment was separated by a sharp interface from the remaining suspension which was progressively less dense at distance increasingly closer from the top of the cylinder. The accumulated sediment thickness increased with time. However, after 5 minutes, the sharp interface separating this sediment from the remaining suspension could no longer be observed, for lack of contrast. Then, after an induction time of 10 minutes, the remaining suspension had formed a flocculated sediment, separated by a sharp interface from an upper clear supernatant liquid, as this was described at pH 9.5. The settling of this flocculated sediment proceeded as described previously at pH 9.5. Hence the sedimentation behavior at pH 2 was a mixed accumulation-flocculation behavior.

The final thickness of the kaolinite sediments made in these conditions is shown in Fig. 4.1-2. Both with unaged $FeCl_3$ and without this electrolyte, the final sediment thickness shows a minimum near pH 5. The final thickness of the kaolinite sediments made without $FeCl_3$ electrolyte was lower than that of the kaolinite sediments made with $FeCl_3$.

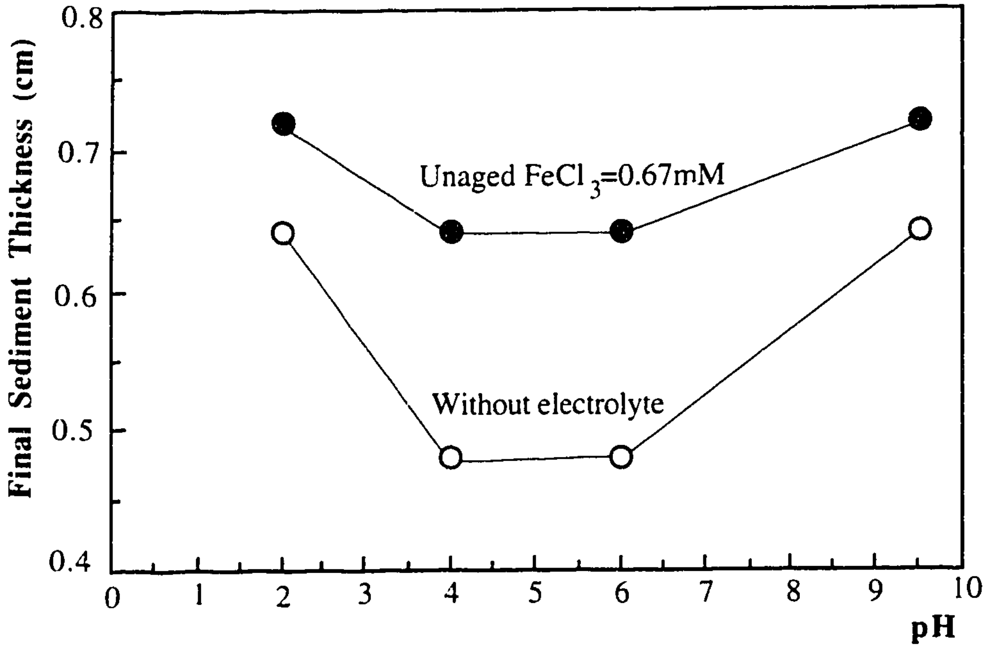

Fig. 4.1-2 - Final thickness of the sediments made from 0.5% Na-kaolinite suspensions treated by the method of Schofield and Samson [59], as a function of the pH.

4.2 - KAOLINITE WITH NEGATIVE CHARGES ON BOTH THE EDGES AND THE FACES

4.2.1 - Kaolinite suspensions with unaged Fe electrolytes

The sedimentation behavior of kaolinite suspensions depended largely on the Fe electrolyte concentration, the nature of the cations and the anions in the electrolyte, and the pH. Three types of sedimentation behavior were observed with $FeCl_3$: (1) accumulation sedimentation; (2) flocculation sedimentation; and (3) mixed flocculation-accumulation sedimentation. These three types of behavior are illustrated in Fig. 4.2-1.

4.2.1.1 - Accumulation sedimentation with unaged $FeCl_3$

Accumulation sedimentation was already described in Section 4.1, for kaolinite particles with opposite charges on their edges and their faces. In the present case, the main difference is that accumulation sedimentation could proceed from the beginning to the end of the settling process, instead of just at the beginning of the settling process.

Accumulation-sedimentation data with $FeCl_3$ concentrations 0.0 and 3.3mM at pH 4.0 are reported in Fig. 4.2-2b. This type of sedimentation occurred when a relatively stable suspension was achieved. The heaviest clay particles settled the fastest to the bottom of the graduated cylinder. A sharp interface between the sediment at the bottom and the remaining suspension was observed. The bottom sediment initial volume was zero and it increased slowly by the accumulation of new particles. The interface position was recorded as a function of time.

On top of the accumulated layer, the remaining suspension was comprised of smaller clay particles which had not yet settled. As time elapsed, the interface between the sediment at the bottom and the remaining suspension could still be observed. However, the solid content in this remaining suspension, decreased with an increasing height in the cylinder. Eventually, the upper part of the remaining suspension slowly transformed to a

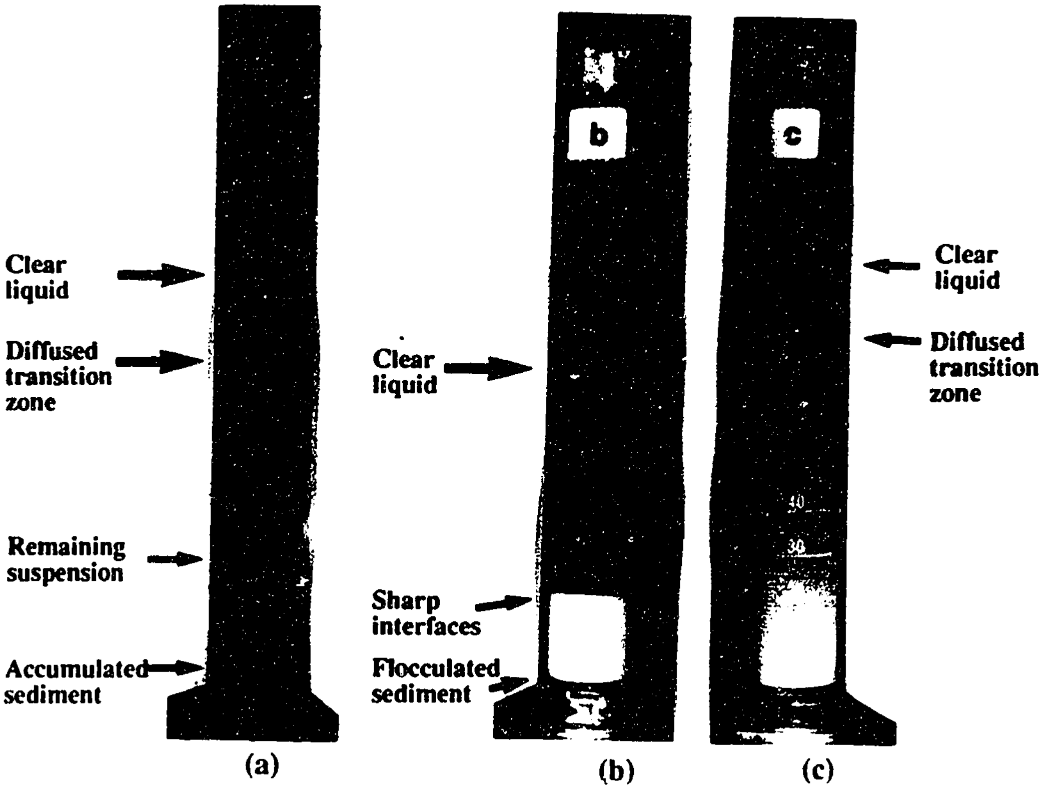
Clear liquid
Diffused transition zone
Remaining suspension
Accumulated sediment
b
Clear liquid
Sharp interfaces
Flocculated sediment
c
Clear liquid
Diffused transition zone
40
30
(a)
(b)
(c)

Fig. 4.2-1 -Types of sedimentation behavior of 0.5% Na-kaolinite suspensions treated with $Na_4P_2O_7$, at pH = 4.0 and after 3 days settling: (a) accumulation-sedimentation with a concentration [$FeCl_3$]=3.3mM; (b) flocculation-sedimentation with [$FeCl_3$]=0.33mM; (c) mixed accumulation-flocculation sedimentation with [$FeCl_3$]=1.67 mM.

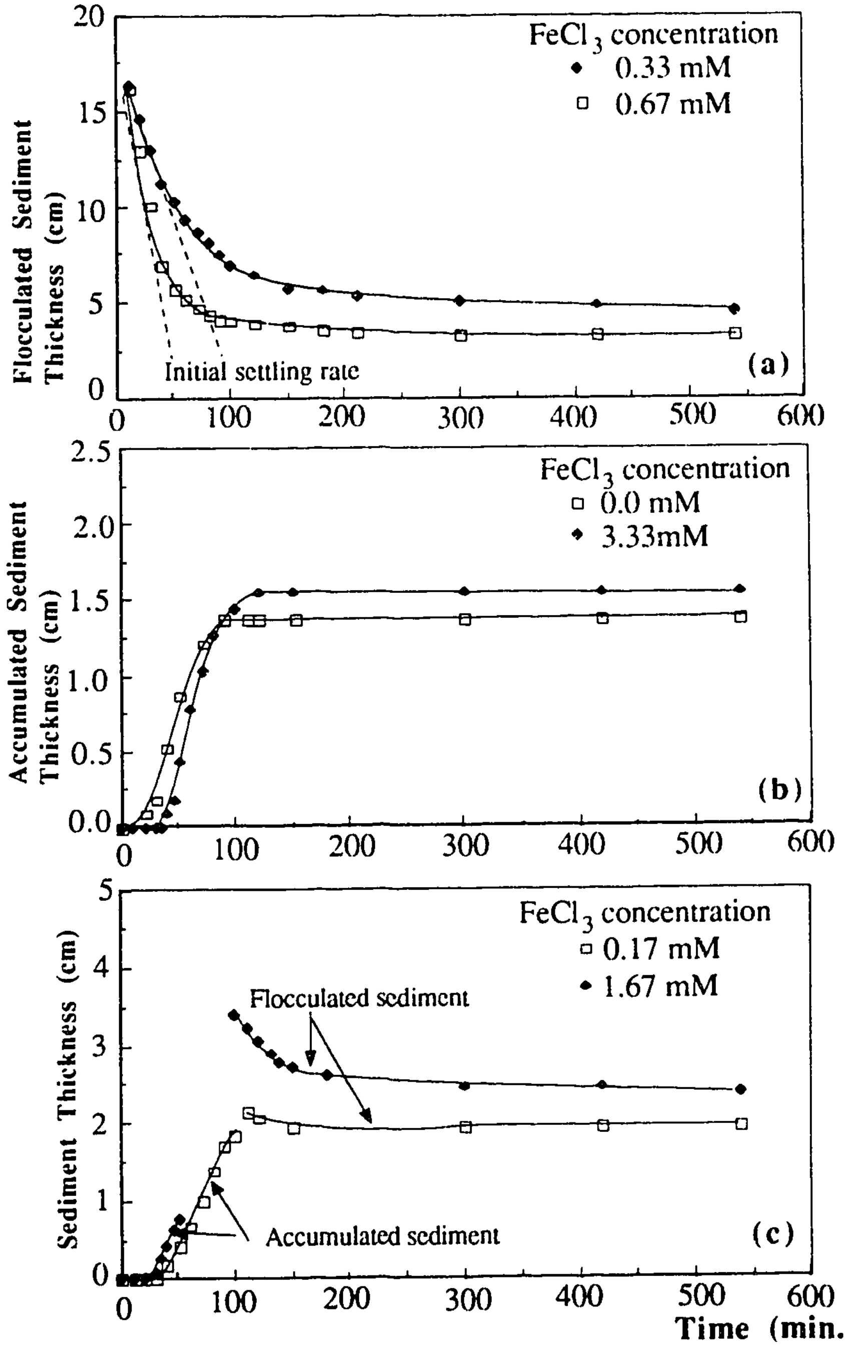

Fig. 4.2-2 - Sediment kinetics, as measured by the displacement of sharp interfaces, in 0.5% Na-Kaolinite suspensions treated with $Na_4P_2O_7$ at pH = 4.0: (a) interface between the flocculated sediment and the supernatant liquid in flocculation sedimentation with $[FeCl_3]$ = 0.33 and 0.67mM; (b) interface between the accumulated sediment and the remaining suspension in accumulation sedimentation with $[FeCl_3]$ = 0.0 and 3.33 mM ; (c) interfaces accumulated sediment-remaining suspension and flocculated sediment-supernatant liquid in mixed sedimentation with $[FeCl_3]$ = 0.17 and 1.67 mM.

clear liquid which seemed to contain no clay particles. This clear liquid is termed a supernatant liquid in the present study. Stated differently, the interface between this remaining suspension and the supernatant liquid was not sharp, but diffuse.

In the remaining suspension, no flocculation occurred during the entire sedimentation study. Flocculation would consist in a sudden transformation of the entire remaining suspension to a sediment with uniform visual characteristics. This flocculated sediment would be separated from the supernatant liquid by a sharp interface. Its thickness would decreas with time, instead of increasing as in accumulation.

If the sedimentation was observed for a sufficiently long time, the process according to which the larger particles first settled to the bottom of the cylinder while the smaller particles remain in the upper part of the cylinder, kept proceeding. In the end, all kaolinite particles had settled down to form the accumulated sediment. In practice, the final sediment volume was defined as the sediment volume after 360 hours sedimentation, for all sedimentation experiments performed in the present study. The final accumulated sediments were the most densely packed of all final sediments. Their volume did not undertake any observable change during further aging. Also, the accumulated sediments did not flow easily.

4.2.1.2 - Flocculation sedimentation with unaged $FeCl_3$

Flocculation sedimentation was also described in Section 4.1. Flocculation-sedimentation kinetics are reported for $FeCl_3$ concentrations of 0.33 and 0.67mM at pH 4 in Fig. 4.2-2a. It was characterized by an induction period of the order of 10 minutes. During this induction period, flocs were being formed. At one moment, these flocs joined to each other and they constituted an apparently uniform sediment, separated by a sharp interface from the clear supernatant liquid. Then, the flocculated sediment started to settle. That is to say its thickness decreased. The initial settling rate was relatively fast . However, it progressively decreased until it reached an aging period when the sediment thickness decreased very slowly. This shrinking during aging process is known as syneresis in sol-gel science.

Flocculated sediments have a higher final volume than accumulated sediments. Moreover they easily flow, when a cylinder is tilted.

4.2.1.3 - Mixed accumulation-flocculation sedimentation with unaged $FeCl_3$

Depending on the Fe electrolyte concentration, the transition from a complete accumulation behavior to a complete flocculation behavior was progressive, and a mixed flocculation-accumulation sedimentation behavior was observed. This type of behavior was already described in Section 4.4. In the first stage, a sediment layer built up by accumulation. This accumulated sediment was separated by a clear interface from the remaining suspension, until this interface could no longer be observed due to a lack of contrast. However, at a later time, the remaining suspension flocculated, and the settling behavior eventually looked like flocculation sedimentation.

In this study, mixed accumulation-flocculation sedimentation was observed at pH 4 for $FeCl_3$ concentrations of 0.17 mM and 1.67mM and the data are reported in Fig. 4.2-2c. These data show in a first stage the increasing thickness of the accumulated sediment, at the bottom of the cylinder, as long as it could be followed. In a second stage, the data show the shrinking thickness of the flocculated-sediment on top of the accumulated sediment, starting from the moment when a sharp interface with the supernatant liquid could be observed. For 0.17 mM $FeCl_3$, the data points of these two periods seem to make a single curve showing a maximum in the sediment volume. However, two interfaces were involved: one resulting from the accumulation sedimentation and the other from the flocculation. This mixed sedimentation behavior occurred when flocculation was slow. The biggest clay particles settled without contributing significantly to flocculation, while the smallest particles remained a sufficiently long time in the suspension to achieve substantial flocculation.

4.2.1.4 - Diagram of the sedimentation behavior with unaged $FeCl_3$

A diagram which summarizes the sedimentation behavior of the negatively charged kaolinite suspensions with unaged $FeCl_3$ is shown in Fig. 4.2-3a. The dotted lines were tentatively drawn to outline the ranges of conditions where each type of sedimentation occurred.

4.2.1.5 - Sedimentation behavior with unaged $Fe_2(SO_4)_3$

The sedimentation behavior not only depended on the pH and the Fe^{3+} electrolyte concentration, but also on the nature of the anions. With $Fe_2(SO_4)_3$, accumulation-sedimentation occurred in a smaller field of conditions than with $FeCl_3$, and the mixed sedimentation regime occurred in a much reduced field of conditions, as this is shown in Fig. 4.2-3b.

Concerning flocculation sedimentation, Figs. 4.2-4a and b, respectively, show the initial settling rate and the final volume of the flocculated sediment. In Fig. 4.2-4b, the final sediment volume when accumulation-sedimentation occurred, is also reported. This corresponds to the dotted lines. A small concentration of 0.33 mM $Fe_2(SO_4)_3$ drastically increased the final sediment volume. However, a further increase in the concentration of this electrolyte did not affect much this final sediment volume.

By comparing Fig. 4.2-4a and Fig. 4.2-4b, it appears that the final sediment volume tended to increase as the initial settling rate decreased.

4.2.1.6 - Comparison of the influence of the cation and the anion from the Fe electrolyte

The initial settling rate and the final sediment volume for unaged $FeCl_3$, $Fe_2(SO_4)_3$, $FeSO_4$ and NaCl are compared in Fig. 4.2-5. From these data of the three Fe electrolytes, it appears that the nature of the anion has a significant influence on the sedimentation results. From the data of NaCl and $FeCl_3$, it appears that the cation also has a great influence. Hence, the combination of the anion and the cation is important.

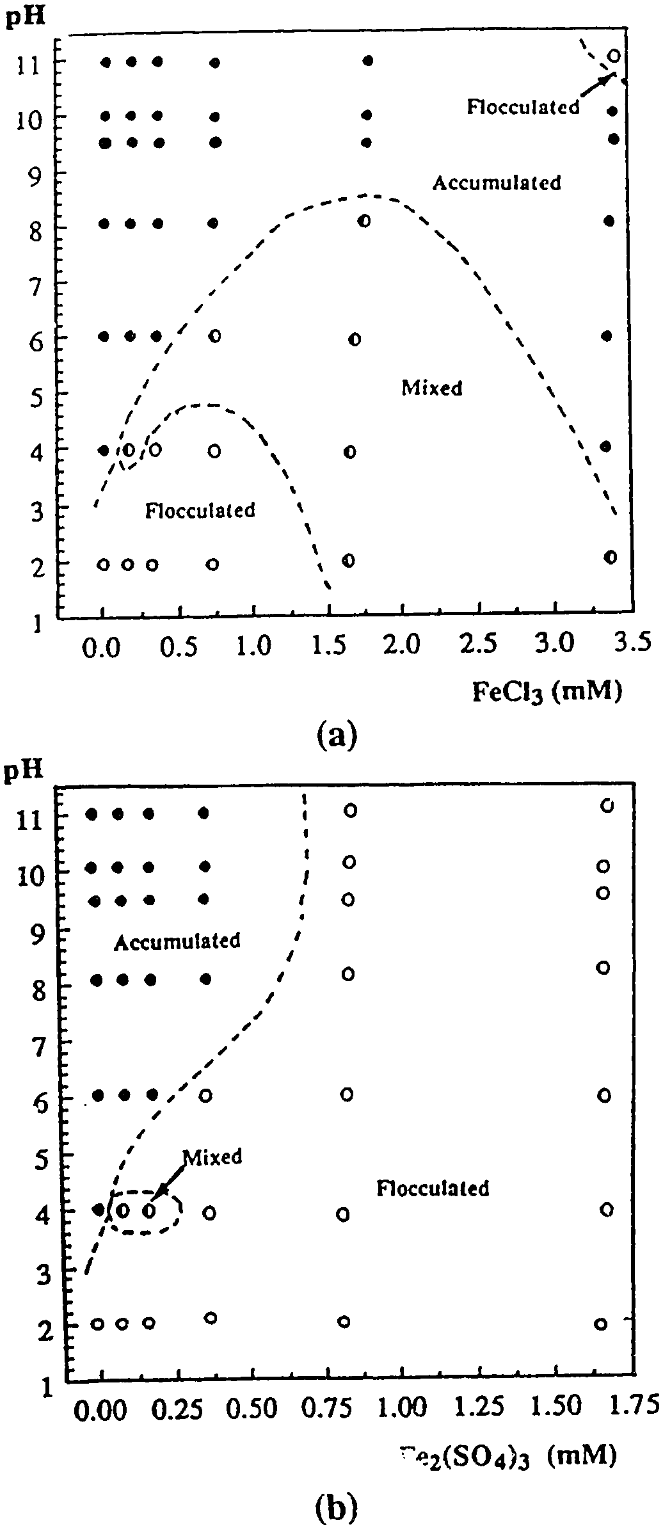

Fig. 4.2-3 - Diagrams of the sedimentation behavior of 0.5% Na-kaolinite suspensions treated with $Na_4P_2O_7$ and mixed with: (a) unaged $FeCl_3$; (b) unaged $Fe_2(SO_4)_3$. The solid, open, and semi-open dots respectively indicate accumulation, flocculation, and mixed behavior.

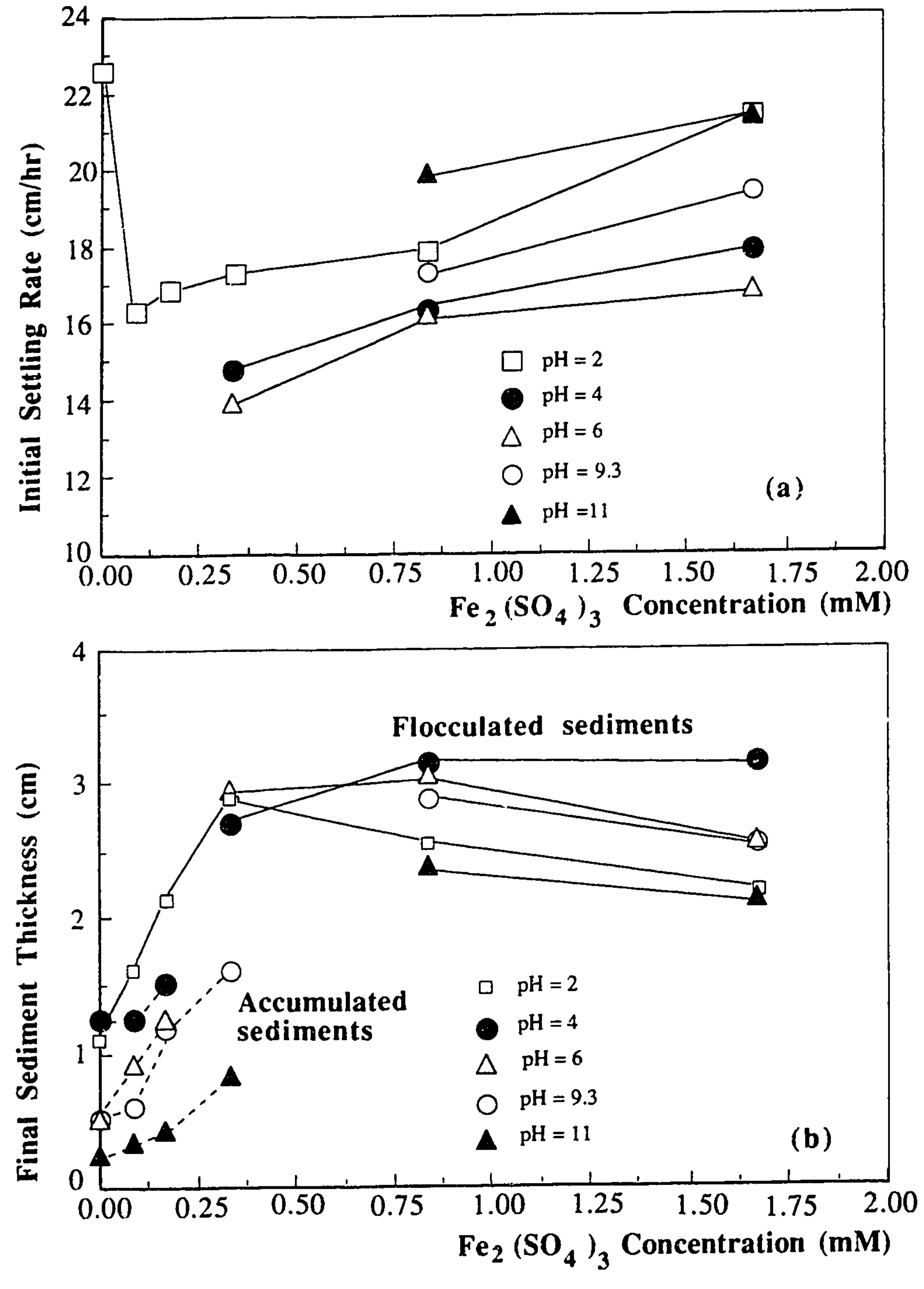

Fig. 4.2-4 - Sedimentation of 0.5% Na-kaolinite suspensions treated with $Na_4P_2O_7$ as a function of the $Fe_2(SO_4)_3$ concentration: (a) Initial settling rate; (b) Final sediment thickness.

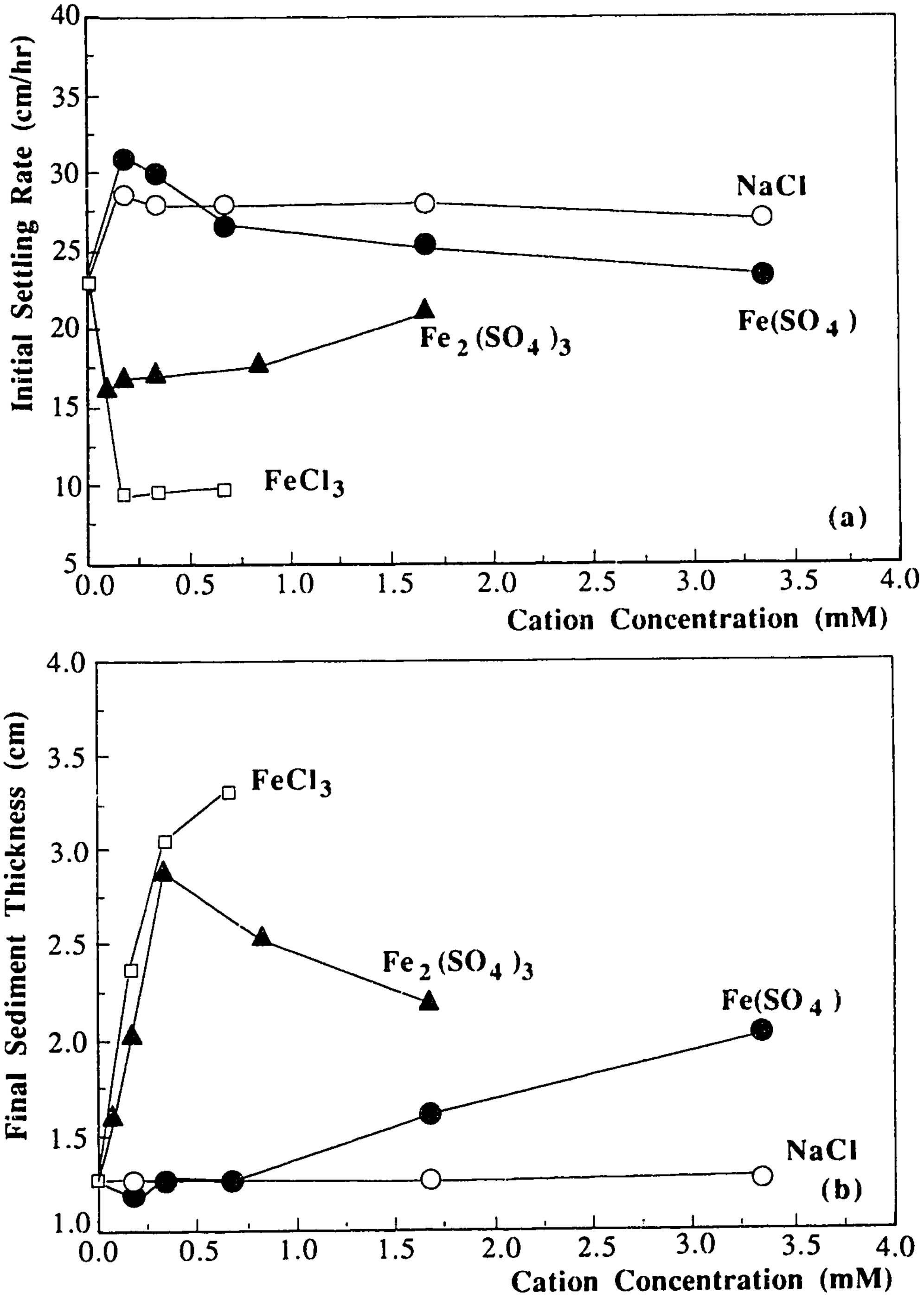

Fig. 4.2-5 - Comparison of sedimentation data for 0.5% Na-kaolinite suspensions treated with $Na_4P_2O_7$, at pH = 2, when mixed with different electrolytes: (a) Initial settling rate; (b) Final sediment thickness.

4.2.2 - Kaolinite suspensions with aged Fe electrolytes

In these experiments, the three types of sedimentation which were found to occur with unaged Fe electrolytes, also occurred with aged $FeCl_3$. These three types are accumulation, flocculation, and mixed accumulation-flocculation sedimentation.

Fig. 4.2-6a and b show the sediments of 0.5% Na-kaolinite made with different concentrations of aged $FeCl_3$, after one week at pH=4.0 and after twenty days at pH 9.5. Flocculation occurred in only two samples, with an aged $FeCl_3$ concentration of 1.67mM at pH = 4 , and 3.3 mM at pH=9.5. These pictures illustrate that the flocculated sediments have a larger final thickness.

The sedimentation data in Fig. 4.2-7 are for the same $FeCl_3$ concentrations as in Fig. 4.2-2. However, in the present section these data are for aged $FeCl_3$, instead of unaged $FeCl_3$ as in Fig. 4.2-2. The data in Fig. 4.2-7a correspond to a flocculation sedimentation and to a mixed accumulation-flocculation sedimentation. Fig. 4.2-7b shows a rapid accumulation sedimentation while slow accumulation sedimentation is shown in Fig. 4.2-7c.

Fig. 4.2-8 is a diagram which summarizes the sedimentation behavior of kaolinite suspensions with aged $FeCl_3$, depending on the conditions.

The initial settling rate and the final sediment thickness dependence on the concentration of unaged or of aged $FeCl_3$ at pH=2.0, are compared in Fig. 4.2-9a and b. This figure shows that aging $FeCl_3$ significantly increased the initial settling rate and it decreased the final sediment thickness, compared with unaged $FeCl_3$.

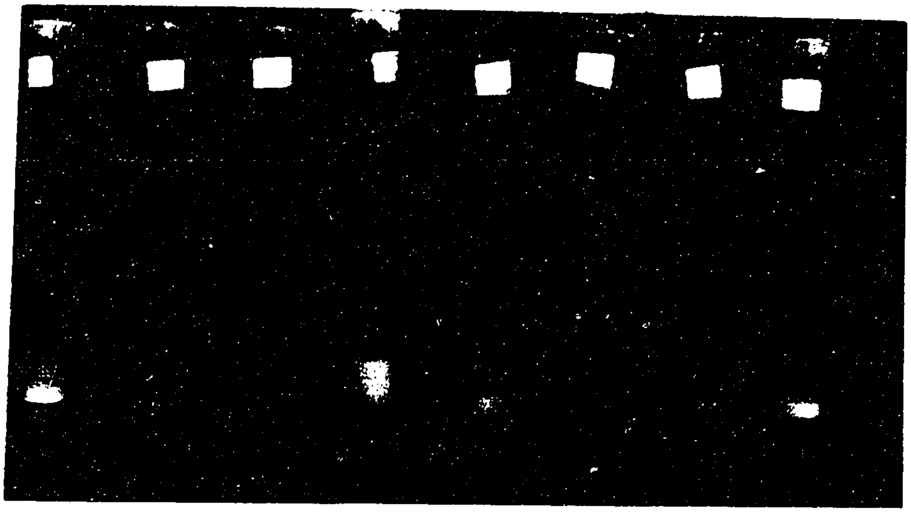

(a)

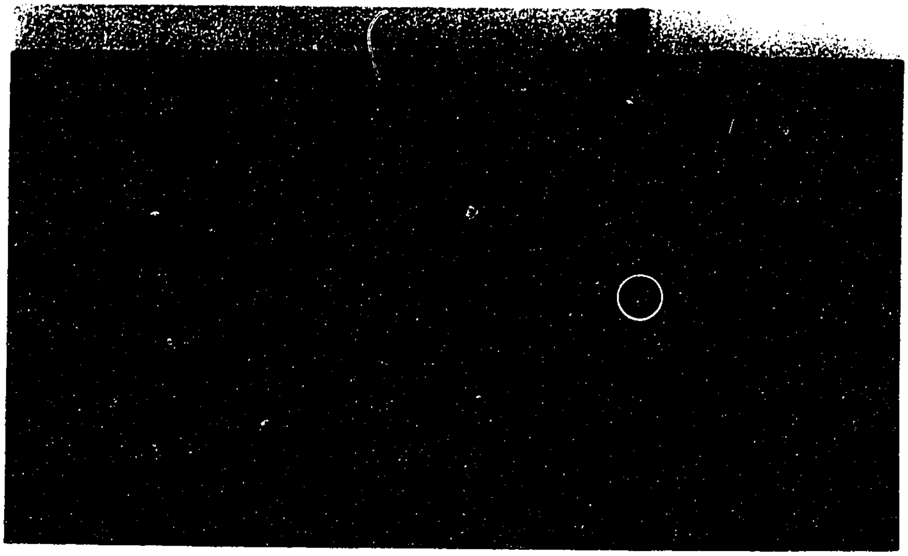

(b)

Fig. 4.2-6 - Sediments of 0.5% Na-kaolinite as a function of the aged $FeCl_3$ concentration: (a) at pH = 4 after a week; (b) at pH=9.5 after 20 days. From left to right, the aged $FeCl_3$ concentration was 0.17, 0.33, 0.67, 1.67, 3.33, 5, 10, 20 mM.

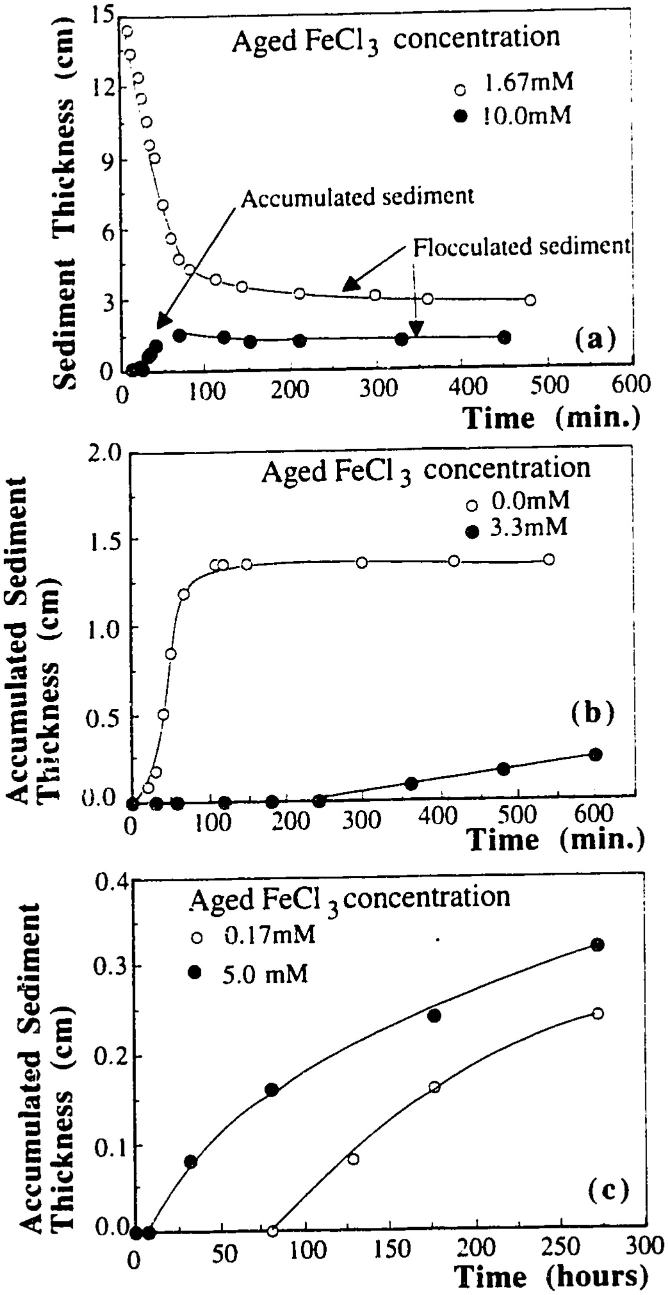

Fig. 4.2-7 - Sediment kinetics, as measured by the displacement of sharp interfaces, in 0.5% Na-Kaolinite suspensions treated with $Na_4P_2O_7$ at pH = 4.0: (a) with aged $FeCl_3$ concentrations of 1.67mM and 10.0 mM; (b) with aged $FeCl_3$ concentrations of 0.0 and 3.3 mM; (c) with aged $FeCl_3$ concentrations of 0.17 and 5.0 mM.

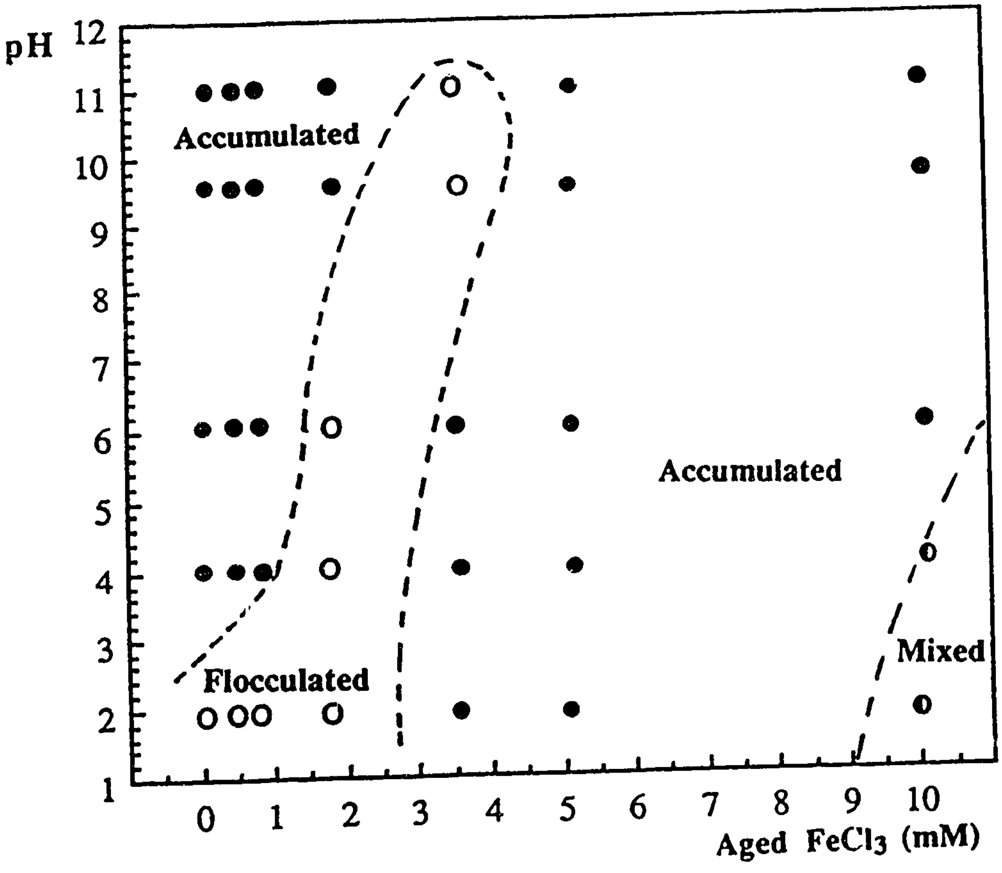

Fig. 4.2-8 - Diagram of the sedimentation behavior in 0.5% Na-kaolinite suspensions treated with $Na_4P_2O_7$, mixed with aged $FeCl_3$. The solid, open, and semi-open dots respectively indicate accumulation, flocculation, and mixed behavior.

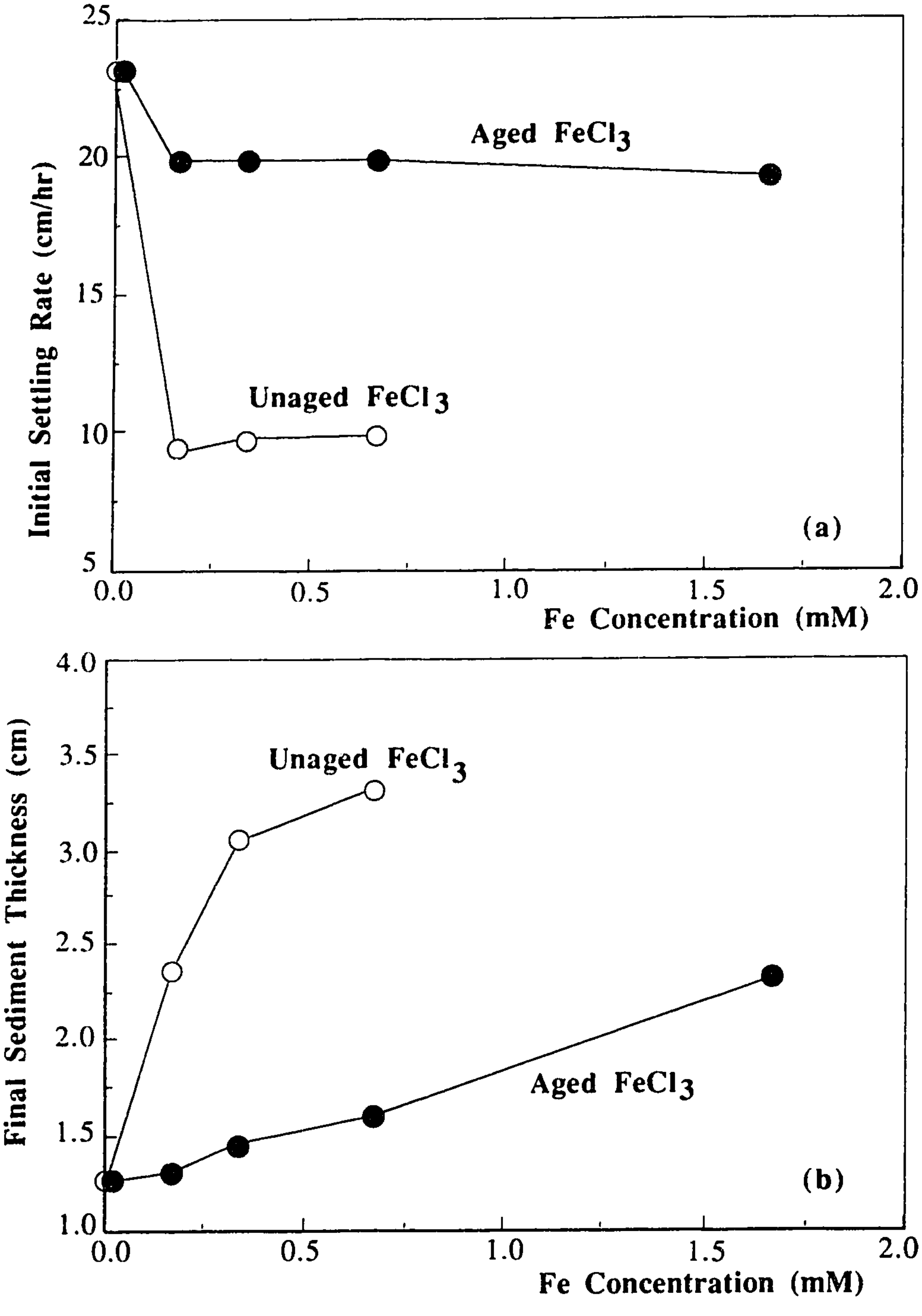

Fig. 4.2-9 - Comparison of sedimentation behavior for 0.5% Na-kaolinite suspensions treated with $Na_4P_2O_7$, as a function of the concentration of unaged or aged $FeCl_3$ at pH=2: (a) Initial settling rate; (b) Final sediment thickness.

4.2.3 - Effect of the kaolinite particle size on the sedimentation behavior with unaged $FeCl_3$

Fig. 4.2-10 shows the initial settling rate of HR kaolinite suspensions and HUF kaolinite suspensions, at different pH, different unaged $FeCl_3$ concentrations, and different clay concentrations. In particular, the data on 1% suspensions by mass at pH=2 are reported in Fig. 4.2-10a for the HR kaolinite, and in Fig. 4.2-10b for the HUF kaolinite. Both kaolinites were treated with $Na_4P_2O_7$. The HR kaolinite has a bigger particle size than the HUF kaolinite and the initial settling rate was higher with the bigger particles of the HR kaolinite.

Similarly, the initial settling rates of 2 % (by mass) HR kaolinite suspensions and of 2 % (by mass) HUF kaolinite suspensions, as a function of the unaged $FeCl_3$ concentration at different pH, are reported in Fig. 4.2-11. These data also indicate that the kaolinite with the bigger particles, that is to say the HR kaolinite, settled faster. The data on the initial settling rate for 5 % (by mass) kaolinite are reported in Fig. 4.2-12. With this % (by mass) of kaolinite, the influence of the size of the particles became marginal.

Fig. 4.2-13a and b show the final sediment thickness of 2% HR kaolinite suspensions and of 1% HUF kaolinite suspensions, as a function of the concentration of unaged $FeCl_3$, at different pH.

By comparing the data at pH 2 and at pH 4, for instance, it appears that the final sediment thickness with 2 % by mass of HR kaolinite, is hardly larger than with 1 % HUF kaolinite. This again indicates that the bigger HR kaolinite particles packed more tightly than the smaller HUF particles. This tendency was confirmed by the final sediment thickness of 5% HR and 5% HUF kaolinite suspensions, which are reported in Fig. 4.2-14, for several pH and several unaged $FeCl_3$ concentrations. However, with both kaolinites, the final sediment thickness went through a maximum for a $FeCl_3$ concentration of 5 mM.

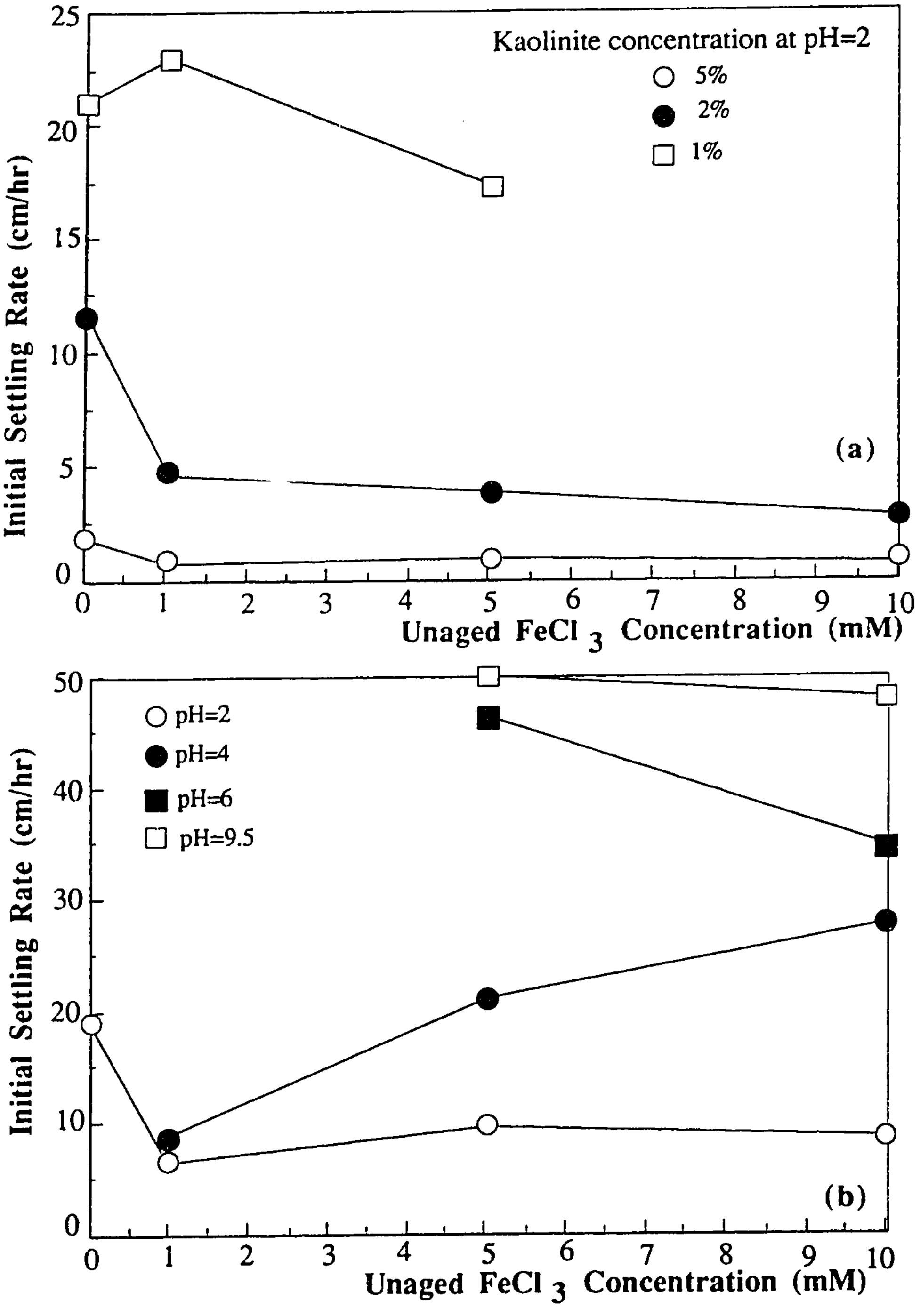

Fig. 4.2-10 - Initial settling rate of Na kaolinite suspensions treated with $Na_4P_2O_7$ and flocculated with unaged $FeCl_3$: (a) Na-HR kaolinite at concentrations of 1%, 2% and 5% by mass; (b) Na-HUF kaolinite at the concentration of 1 %.

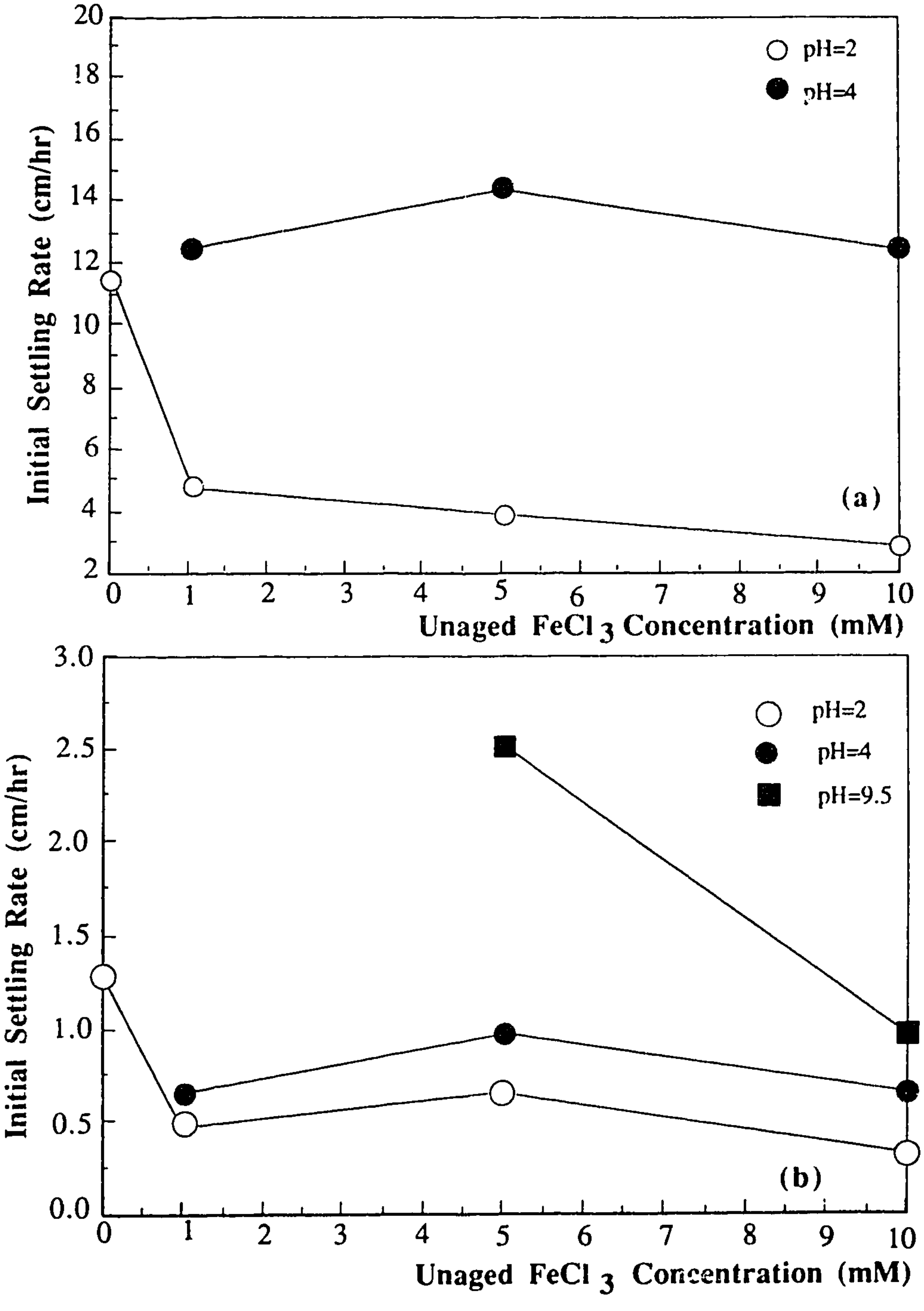

Fig. 4.2-11 - Initial settling rate of 2% Na-kaolinite suspensions treated with $Na_4P_2O_7$ and flocculated with unaged $FeCl_3$: (a) Na-HR kaolinite; (b) Na-HUF kaolinite.

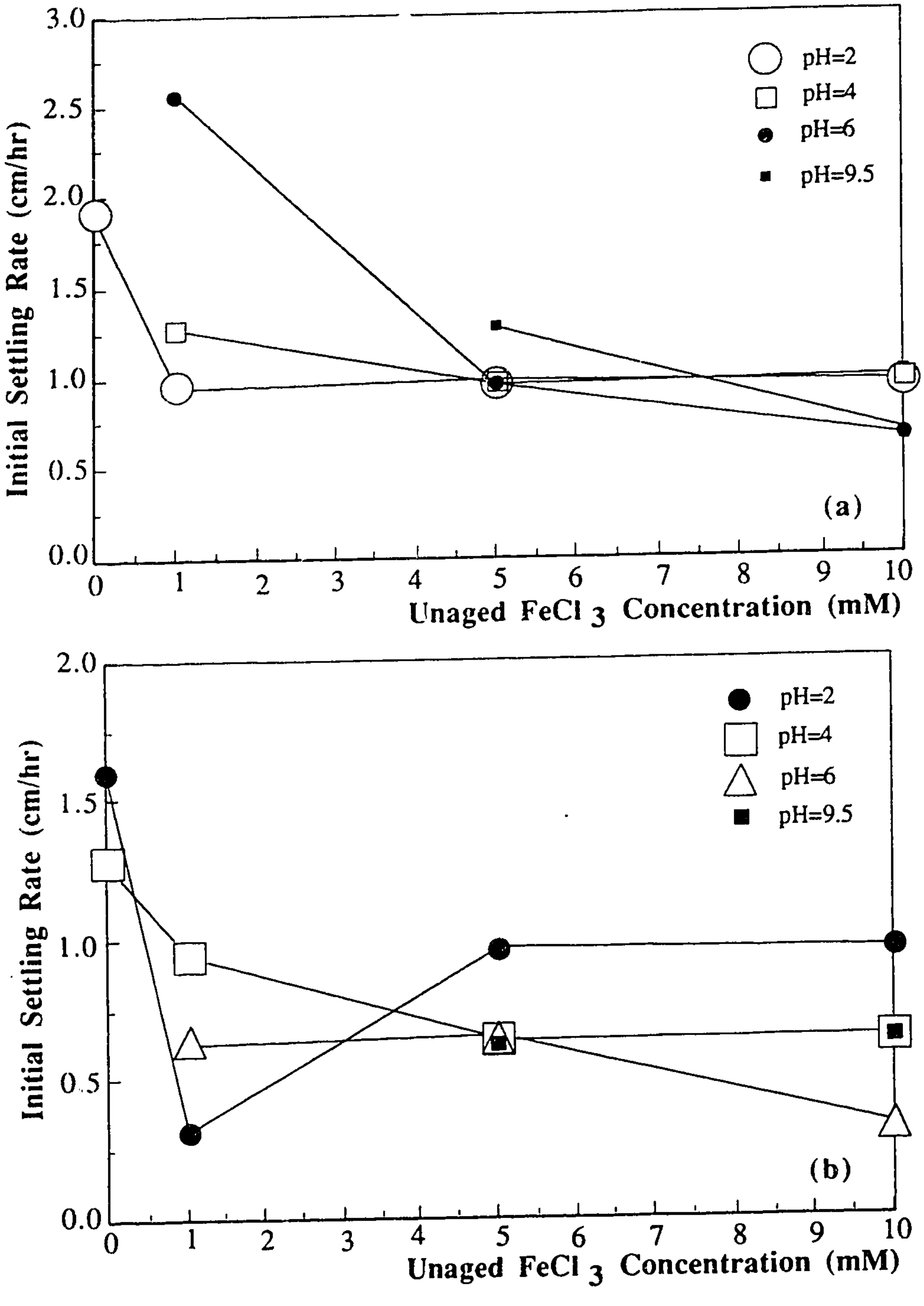

Fig. 4.2-12 - Initial settling rate of 5% kaolinite suspensions treated with $Na_4P_2O_7$ and flocculated with unaged $FeCl_3$; (a) Na-HR kaolinite; (b) Na-HUF kaolinite.

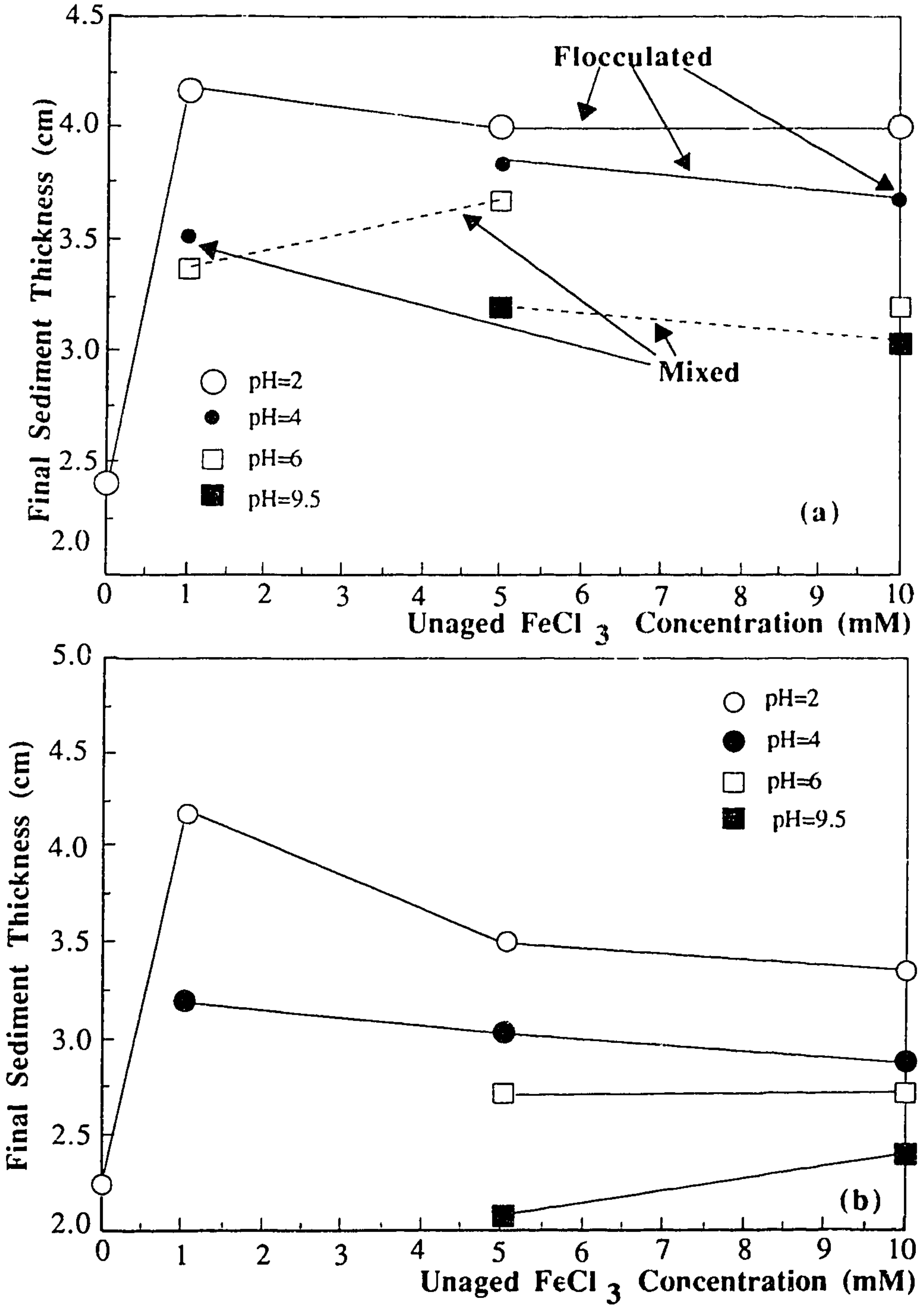

Fig. 4.2-13 - Final sediment thickness of kaolinite suspensions treated with $Na_4P_2O_7$, as a function of the concentration of unaged $FeCl_3$ and at different pH: (a) 2% Na-HR kaolinite; (b) 1% Na-HUF kaolinite. The solid lines indicate flocculated sediments while the dashed lines indicate mixed accumulated-flocculated sediments.

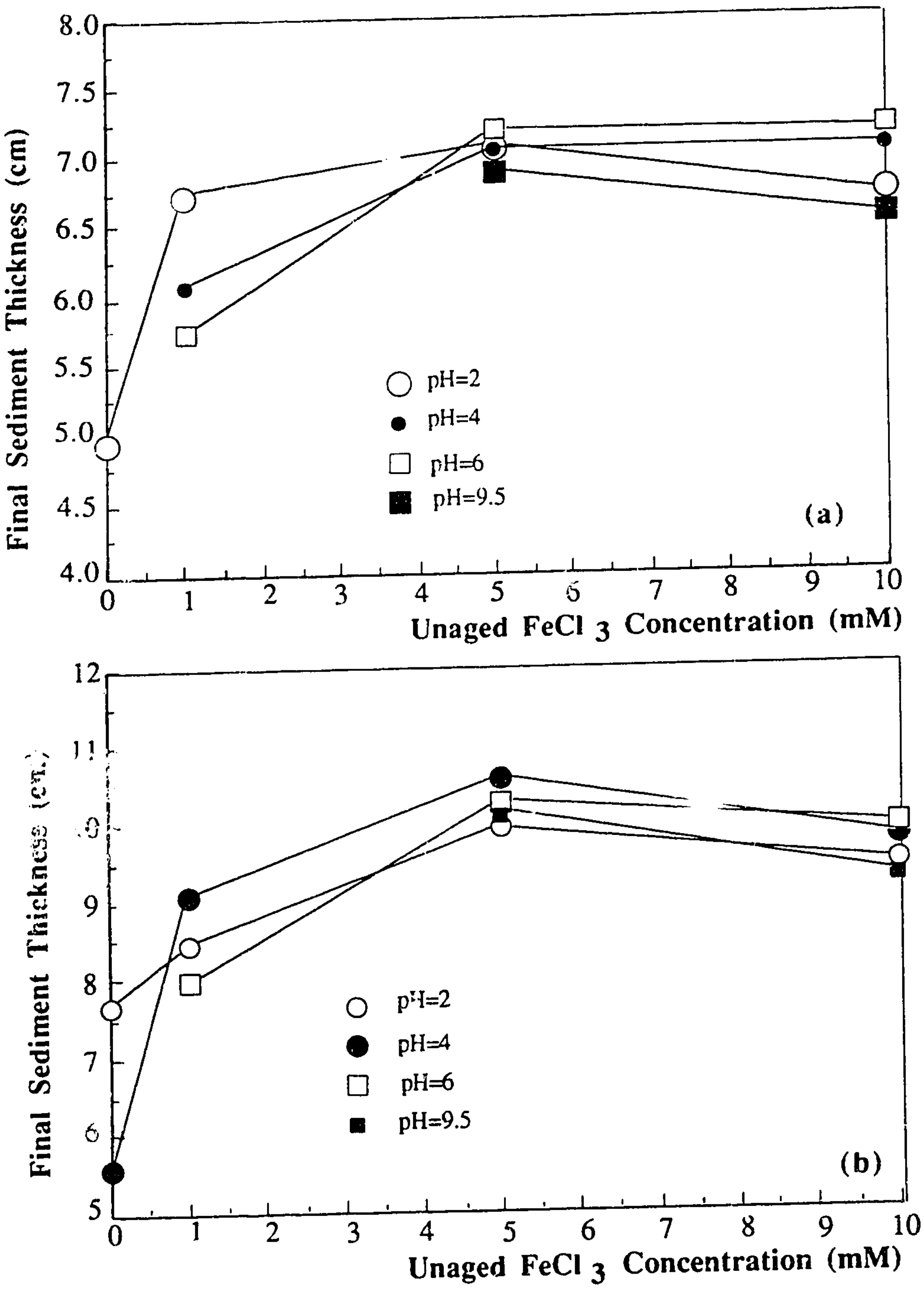

Fig. 4.2-14 - Final sediment thickness of 5% kaolinite suspensions treated with $Na_4P_2O_7$, as a function of the concentration of unaged $FeCl_3$ concentration: (a) Na-HR kaolinite; (b) Na-HUF kaolinite.

4.2.4 - Effect of the kaolinite proportion on the sedimentation behavior with unaged $FeCl_3$

From the analysis of Michaels and Bolger [42], which is summarized in Section 2.2.4.2, it is possible to estimate the ratio C_{Ap} between the volume fraction occupied by the flocs (or aggregate) Φ_A and the volume fraction occupied by the primary kaolinite particle Φ_p . After reporting the final sediment volumes V_{F1} and V_{F2} when the initial primary kaolinite particles volume fractions are Φ_{p1} and Φ_{p2}, in equation (2.2-47), we could derive the following formula for C_{Ap} [42, 60]:

$$C_{Ap} = \frac{0.62}{V_o} \left(\frac{V_{F1} - V_{F2}}{\Phi_{p1} - \Phi_{p2}} \right) \tag{4.2-1}$$

In this equation, V_0 is the initial volume of the suspension. C_{Ap} can be used as a characteristic of the kaolinite aggregate (or floc) pores.

From the data on the final sediment thickness of 2% and of 5% HUF Na-kaolinite suspensions, the value of C_{Ap} could be calculated for the HUF kaolinite, as a function of the unaged $FeCl_3$ concentration and on the pH. The results are reported in Fig. 4.2-15. They show that the flocs were the most porous, hence probably the biggest, for a $FeCl_3$ concentration of 5 mM, at all pH. The highest porosity was at pH=4.

The diagrams for the sedimentation behaviors of HUF kaolinite suspensions containing 1, 2, and 5% by mass of clay, as a function of pH and concentration of unaged $FeCl_3$, are gathered in Fig. 4.2-16. These three diagrams are similar to each other. However the field where accumulation sedimentation occurred decreased as the clay content increased. This field was very large with a 0.5 % kaolinite content (Fig. 4.2-3). The diagrams which summarize the sedimentation behavior of HR kaolinite suspensions with 0.5, 1, 2, and 5% clay concentrations, are gathered in Fig. 4.2-17. With this type of kaolinite, the occurrence of accumulation-flocculation sedimentation was frequent. However, in the cases where this occurred, it often took about a day for the remaining

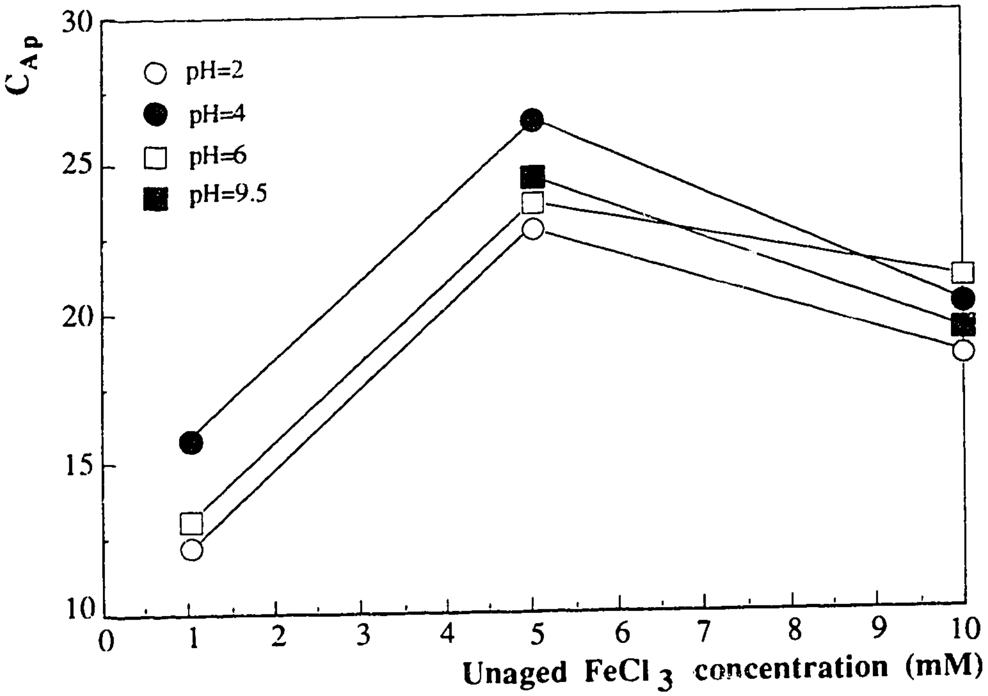

Fig. 4.2-15 - Ratio C_{Ap} between the volume occupied by the flocs and the volume occupied by the primary particles, in HUF kaolinite suspensions treated with $Na_4P_2O_7$, as a function of the concentration of unaged $FeCl_3$.

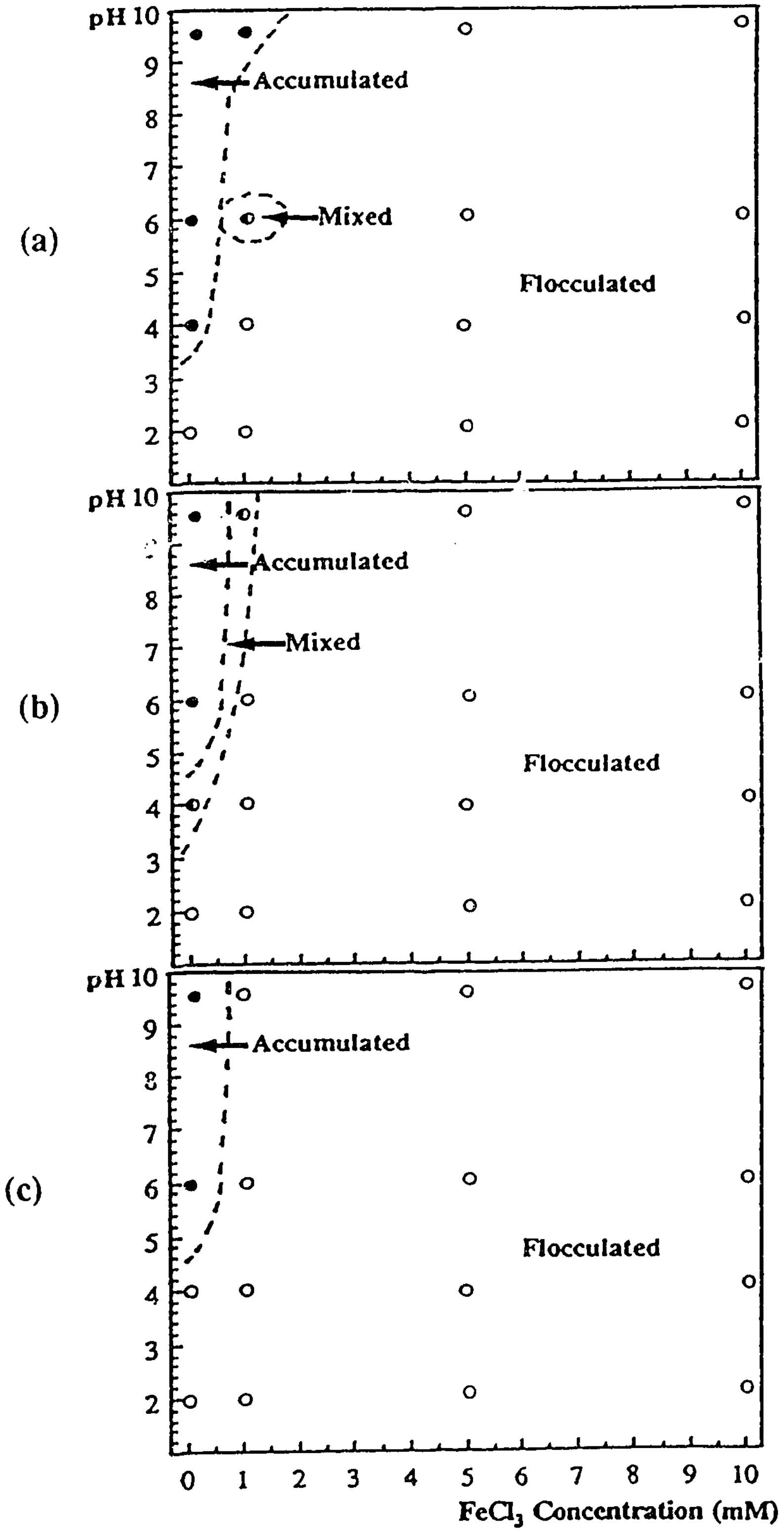

Fig. 4.2-16 - Diagrams of the sedimentation behavior of Na-HUF kaolinite suspensions with unaged $FeCl_3$: (a) 1% kaolinite; (b) 2% kaolinite; (c) 5% kaolinite. The solid, open, and semi-open dots respectively represent accumulation, flocculation, and mixed behavior.

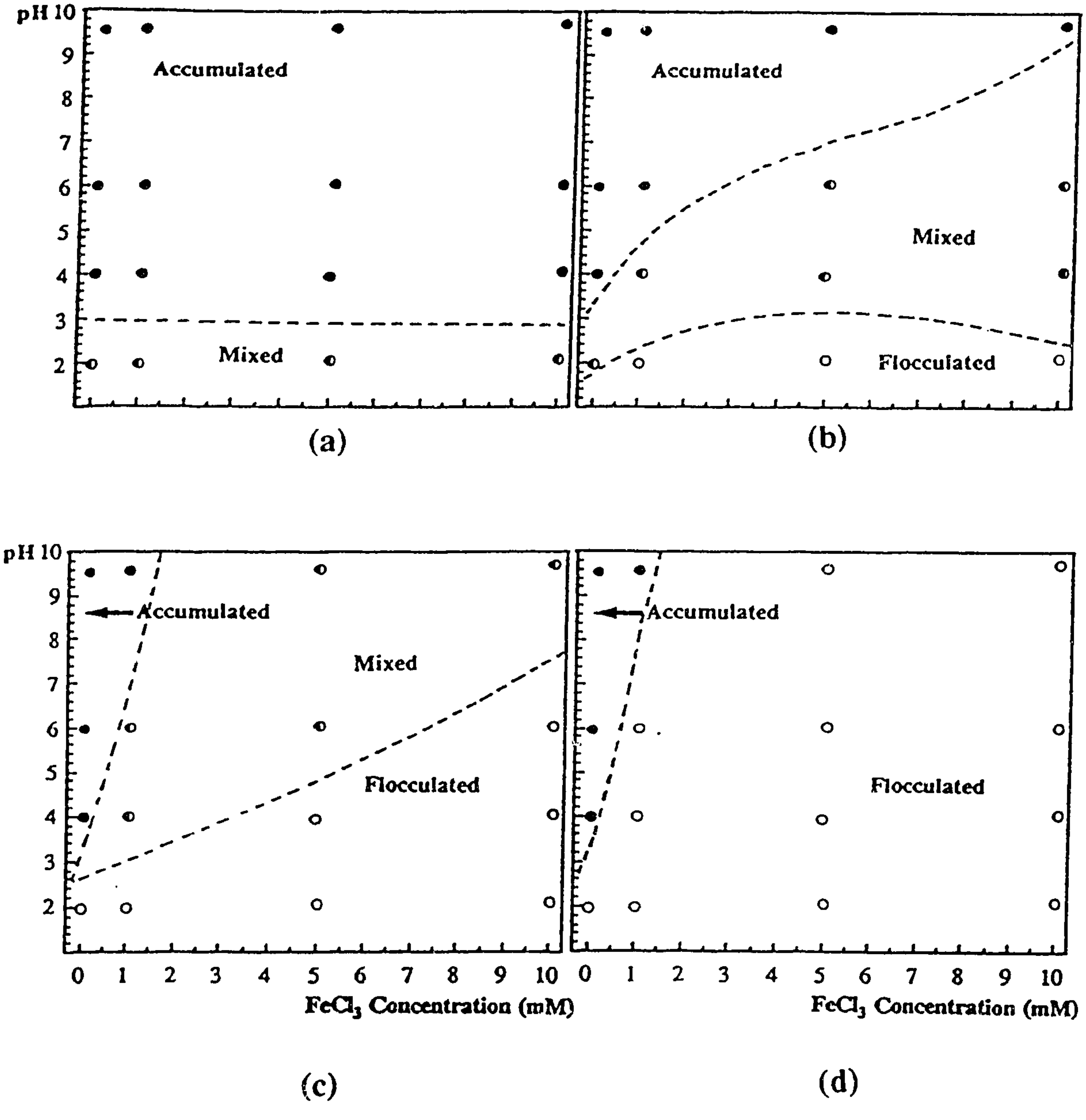

Fig. 4.2-17 - Diagrams of the sedimentation behavior of Na-HR kaolinite suspensions with unaged $FeCl_3$: (a) 0.5% kaolinite; (b) 1% kaolinite; (c) 2% kaolinite; (d) 5% kaolinite. The solid, open, and semi-open dots respectively indicate accumulation, flocculation, and mixed behavior.

suspension to form flocculated sediment, on top of the accumulated sediment. By comparing the HR kaolinite and the HUF kaolinite, it appears the bigger size of the clay particles in the HR kaolinite the more frequent the occurrence of accumulation or of mixed accumulation-flocculation sedimentation with this clay.

4.2.5 - Kaolinite suspensions with unaged Al electrolytes

The sedimentation behaviors of 0.5 % (by mass) Na-kaolinite HUF suspensions, treated with $Na_4P_2O_7$, were studied with three types of unaged Al electrolytes: $AlCl_3$, $Al(NO_3)_3$, and $Al_2(SO_4)_3$. The three types of sedimentation behavior which were reported with the Fe electrolytes also ocurred with these Al elecrolytes. These behavior are flocculation, accumulation or mixed accumulation-flocculation. They are illustrated in Fig. 4.2-18. Typical sedimentation data for 0.5% HUF kaolinite-$AlCl_3$ and $Al(NO_3)_3$ are reported in Fig. 4.2-19. This figure shows flocculation-sedimentation kinetics with the unaged $Al(NO_3)_3$ concentrations of 5 and 10 mM at pH = 2 (Fig. 4.2-19a), and with the unaged $AlCl_3$ concentrations of 2 and 10 mM at pH 6 (Fig. 4.2-19d). No induction time could be noticed.

Accumulation sedimentation occurred for a concentration of 5 mM of unaged $Al(NO_3)_3$ at pH = 12 (Fig. 4.2-19b), or without any Al electrolyte (Fig. 4.2-19e). This accumulation was very slow. Mixed flocculation-accumulation sedimentation occurred for instance at pH = 9.4 with unaged $Al(NO_3)_3$ concentrations of 5 mM and 10 mM (Fig. 4.2-19c), and at pH=6 with the unaged $AlCl_3$ concentrations of 2 and 10 mM (Fig. 4.2-19f).

The diagrams which summarize the sedimentation behavior of 0.5 % (by mass) Na-HUF kaolinite suspensions, treated with $Na_4P_2O_7$, when they are mixed with unaged $AlCl_3$, $Al(NO_3)_3$, or $Al_2(SO_4)_3$, are gathered in Fig. 4.2-20. The three diagrams in this figure are similar to each other. Accumulation sedimentation had a tendency to occur at a high pH and a low Al electrolyte concentration.

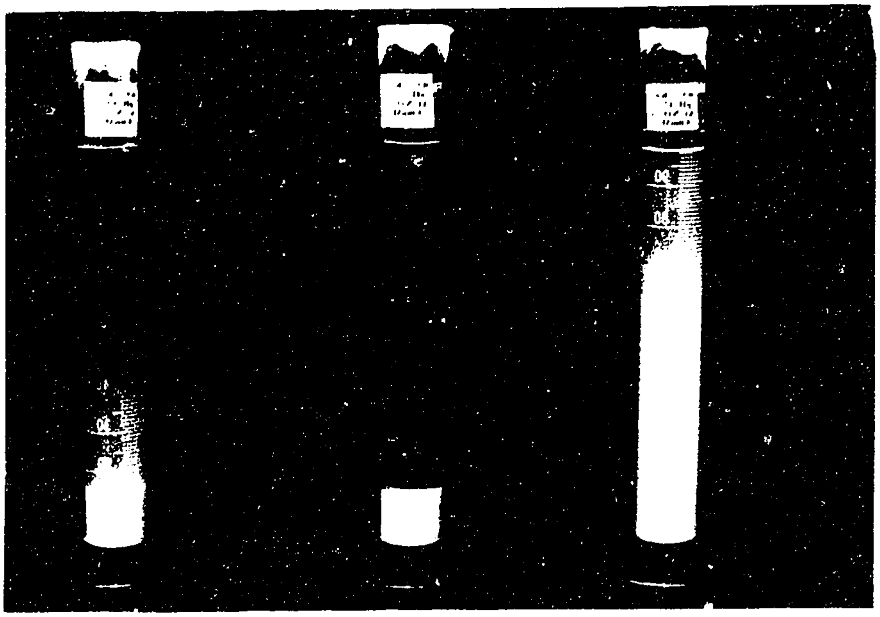

Fig. 4.2-18 - Sedimentation of 0.5% Na-HUF kaolinite suspensions with a concentration of unaged $Al(NO_3)_3$ of 5.0mM: (a) accumulation sedimentation at pH=12; (b) flocculation sedimentation at pH=2; (c) mixed sedimentation at pH=9.5.

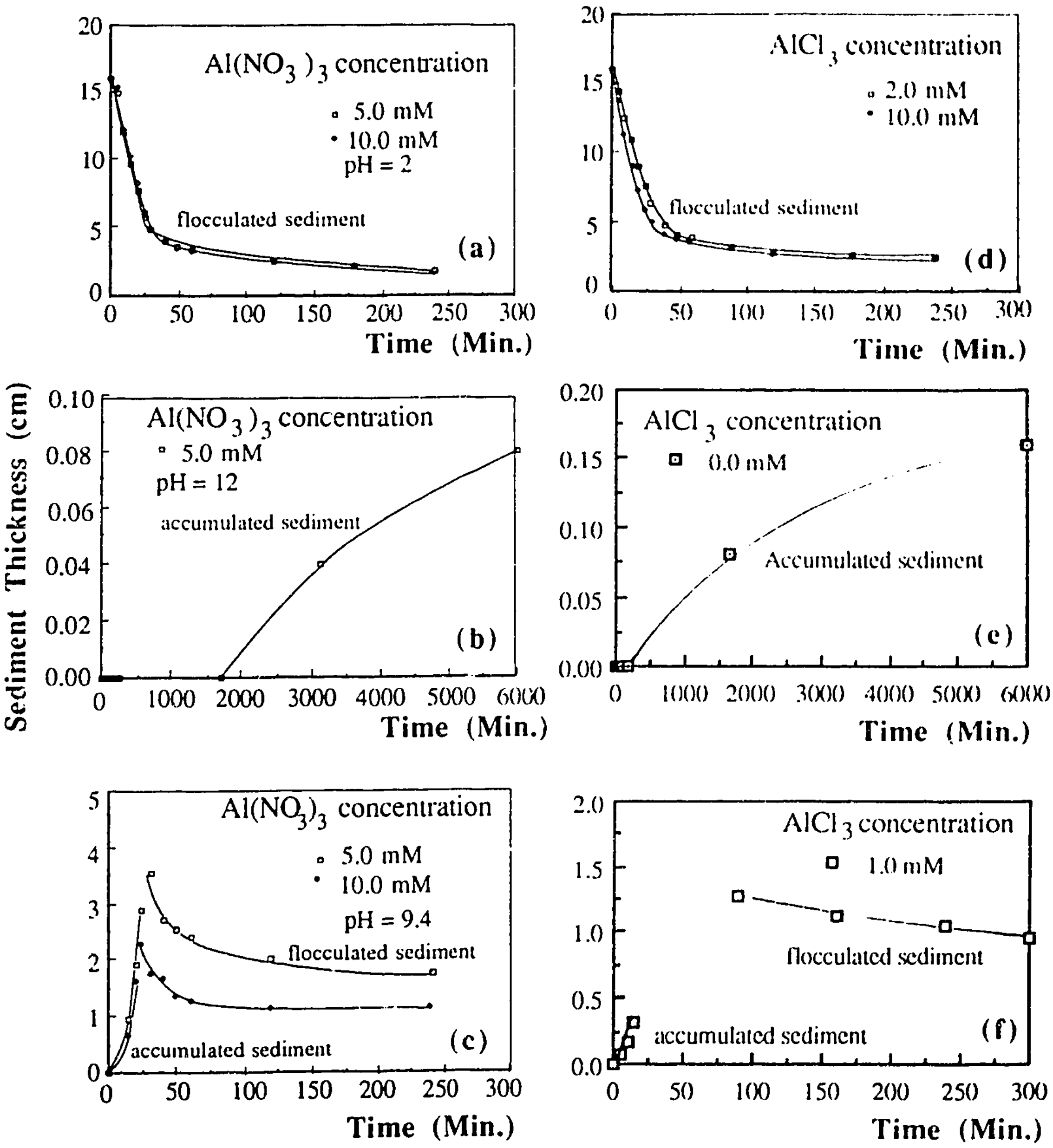

Fig. 4.2-19 - Sedimentation kinetics of 0.5% Na-HUF Kaolinite suspensions with unaged Al electrolytes: (a) Concentration [Al(NO3)3] = 5 and 10 mM at pH=2; (b) [Al(NO3)3] =5 mM at pH=12 ; (c) [Al(NO3)3] = 5 and 10 mM at pH=9.4; (d)[AlCl3] = 2 and 10 mM at pH= 6; (e) [AlCl3] = 0 mM at pH= 6; (f)[AlCl3] =1 mM at pH= 6.

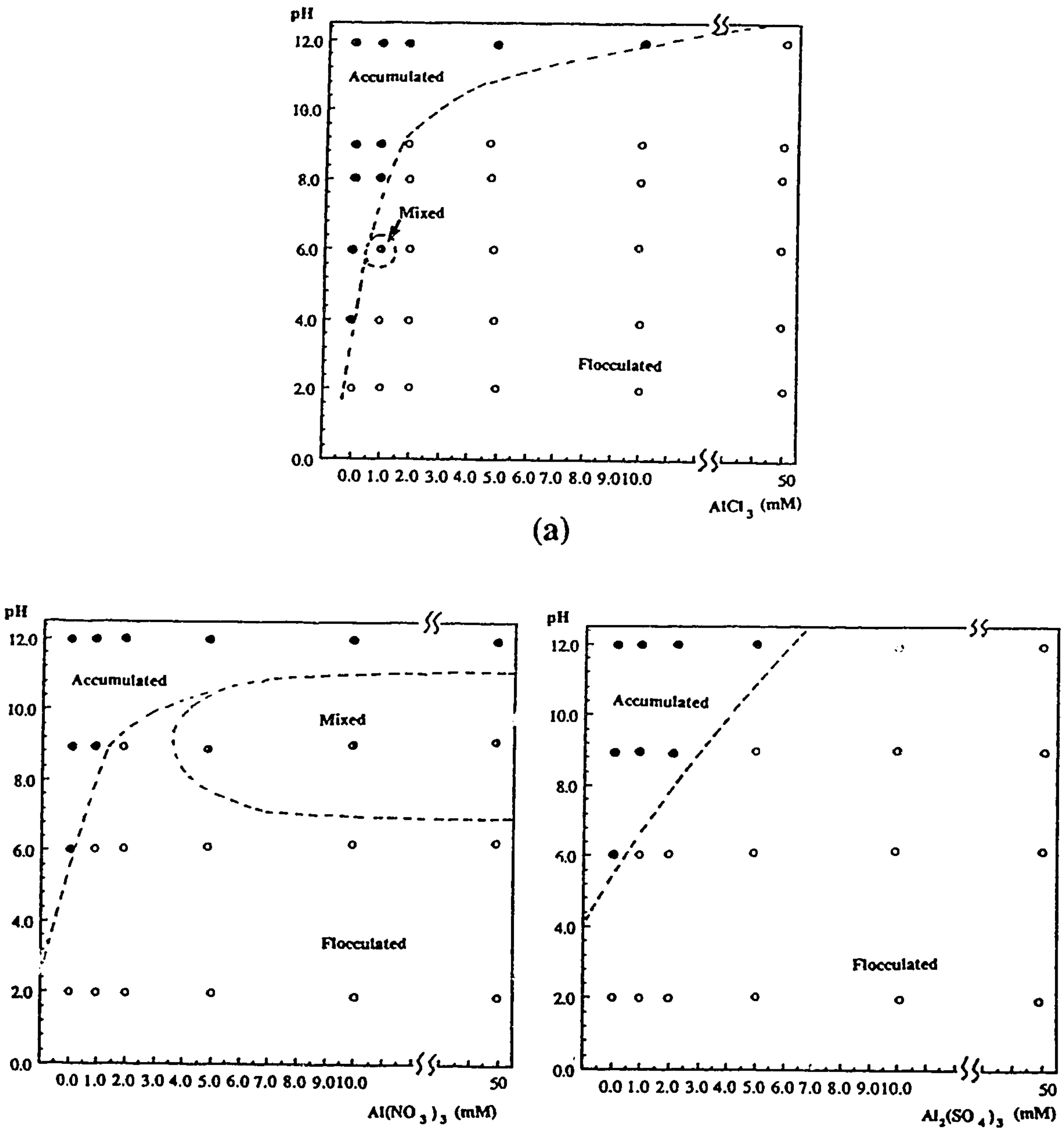

(a)

(b)

(c)

Fig. 4.2-20 - Diagrams of the sedimentation behavior of 0.5 % (by mass) Na-HUF kaolinite suspensions with unaged Al electrolytes: (a) $AlCl_3$; (b) $Al(NO_3)_3$; (c) $Al_2(SO_4)_3$. The solid, open, and semi-open dots respectively indicate accumulation, flocculation, and mixed behavior.

Mixed accumulation-flocculation sedimentation was more developed with unaged $Al_2(SO_4)_3$ than with unaged $AlCl_3$ and $Al(NO_3)_3$. This indicated that the sedimentation behavior not only depends on the pH value and the Al^{3+} concentration but also on the nature of the anions.

The initial settling rates of 0.5% Na-kaolinite suspensions, as a function of the Al electrolyte concentration, are reported in Fig. 4.2-21 for pH 2 and 6. At both pH values, the initial settling rate increased in the order $Al(NO_3)_3 < Al_2(SO_4)_3 < AlCl_3$, for a given Al electrolyte concentration. The data on the final sediment thickness, which correspond to the previous samples, are reported in Fig. 4.2-22. The nature of the anions has an influence. However, the trend as a function of the Al electrolyte concentration is the same as the three electrolytes.

More extensive data for the initial settling rate and the final sediment thickness, in the case of unaged $AlCl_3$, are reported in Fig. 4.2-23, respectively. Except at pH=2, the initial settling rate went through a maximum for a concentration $[AlCl_3] = 5mM$. In this figure, the solid lines correspond to the flocculated sediments while the dashed lines correspond to the accumulated sediments. In the case of the flocculated sediments, the final sediment thickness shows a maximum for a $AlCl_3$ concentration of 2 mM.

4.2.6 - Kaolinite suspensions with aged $AlCl_3$

The visual appearance of 0.5 % (by mass) Na-kaolinite suspensions, treated with $Na_4P_2O_7$ and mixed with different concentrations of aged $AlCl_3$ at pH 4 and 9.5, after three days of sedimentation, are shown in Fig. 4.2-24. Some typical sedimentation kinetics are shown in Fig. 4.2-25. These data include two cases of sedimentation by flocculation sedimentation with the aged $AlCl_3$ concentrations of 1 and 10 mM at pH=6. They also include two examples of sedimentation by accumulation with the $AlCl_3$ concentrations of 1 and 10 mM at pH =11.

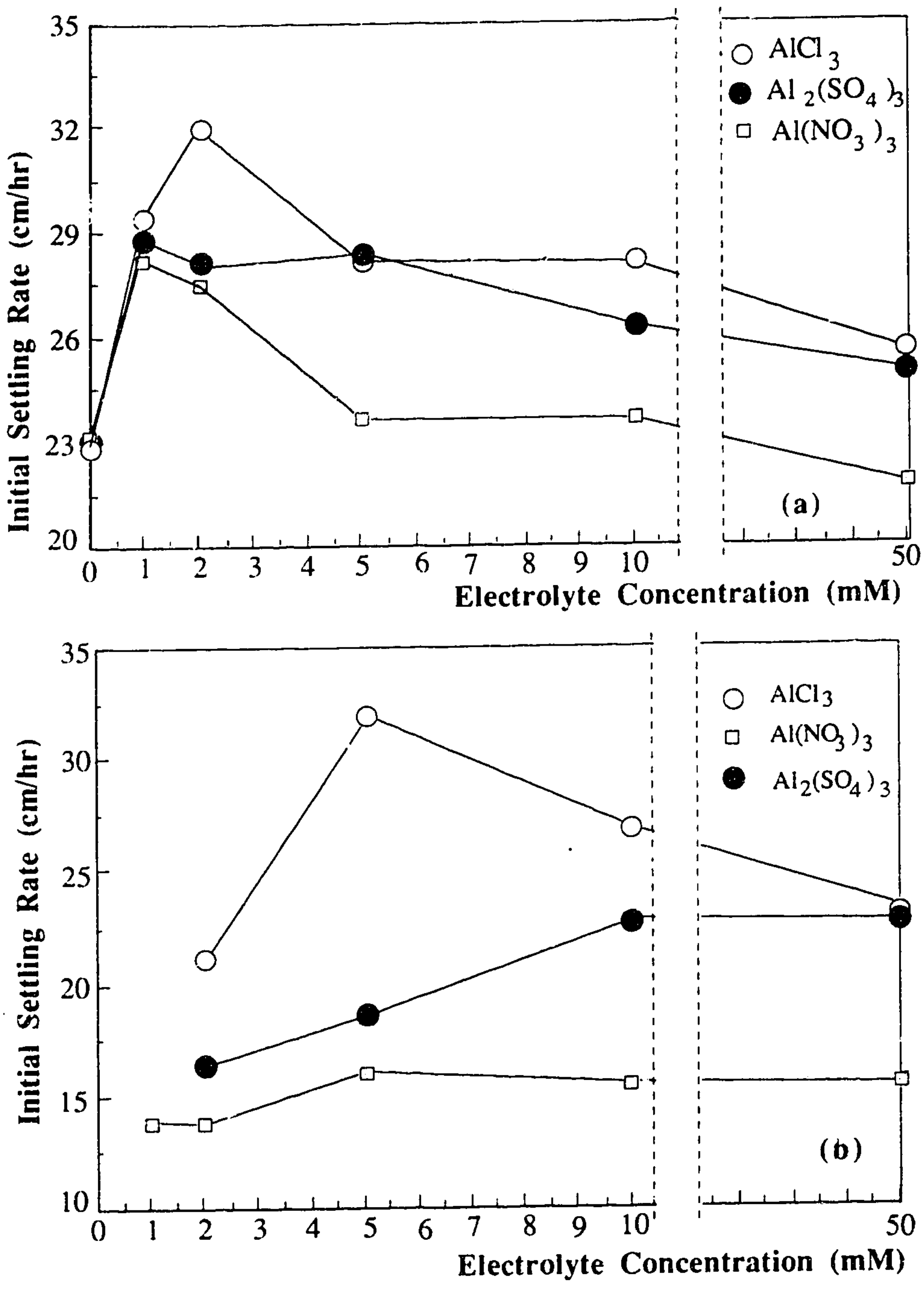

Fig. 4.2-21 - Initial settling rate of 0.5% Na-kaolinite suspensions treated with $Na_4P_2O_7$ suspensions, when flocculated with three different unaged Al electrolytes: (a) at pH = 2 ; (b) at pH = 6.

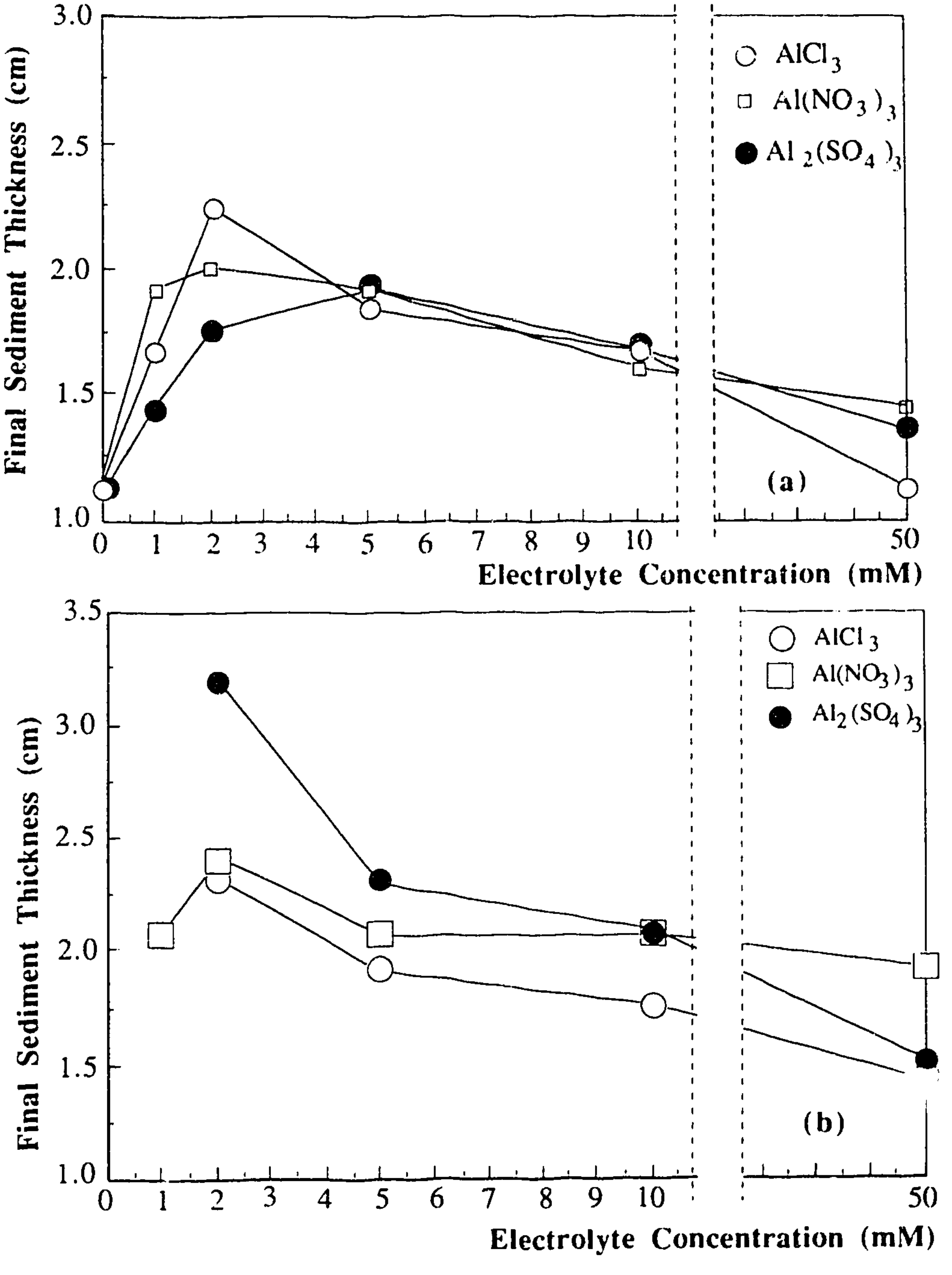

Fig. 4.2-22 - Final sediment thickness of 0.5% Na-kaolinite suspensions treated with $Na_4P_2O_7$ and flocculated with three different unaged Al electrolytes: (a) at pH = 2; (b) at pH = 6.

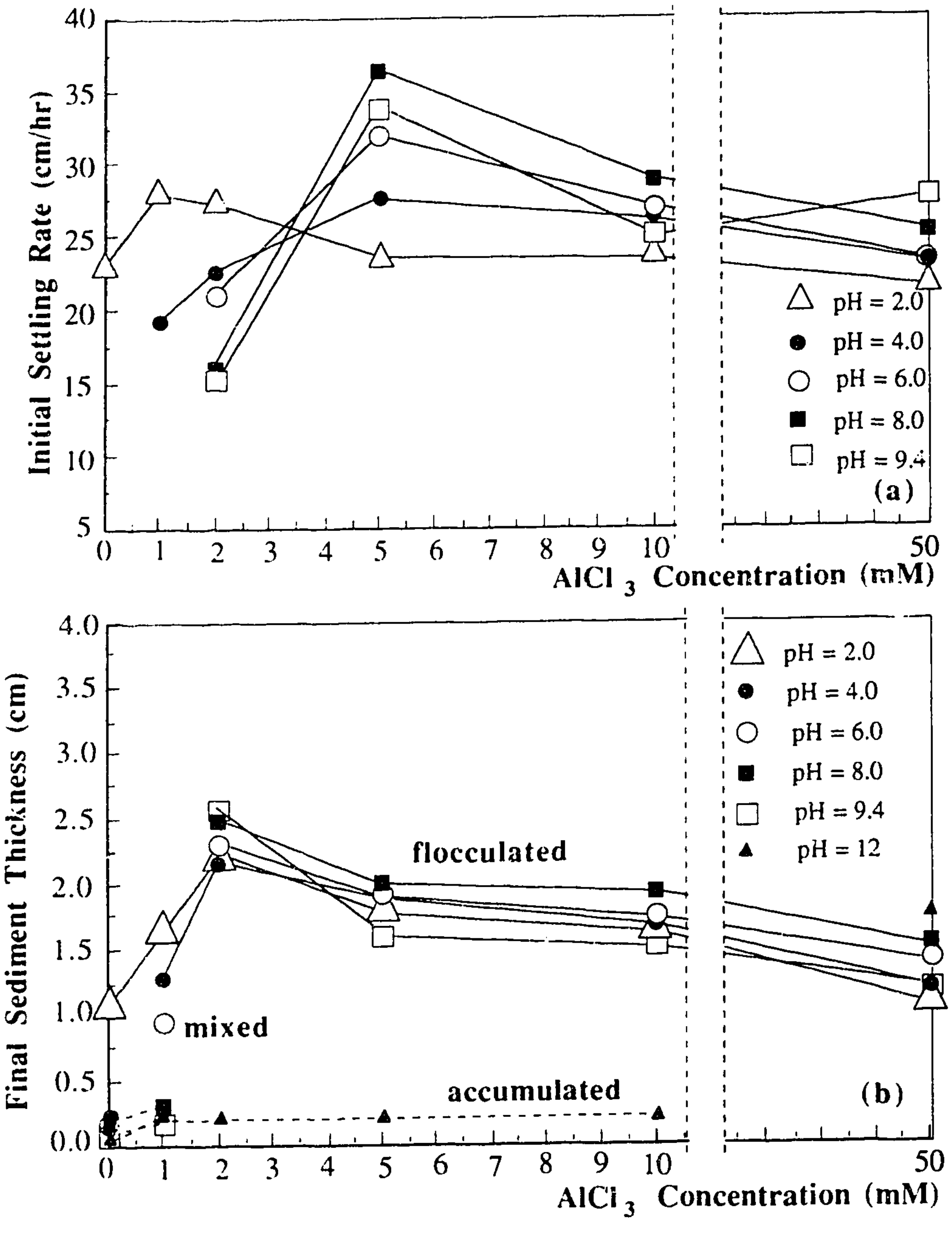

Fig. 4.2-23- Sedimentation behavior of 0.5% Na-Kaolinite suspensions treated with $Na_4P_2O_7$, as a function of the concentration of unaged $AlCl_3$, at different pH: (a) Initial settling rate; (b) Final sediment thickness.

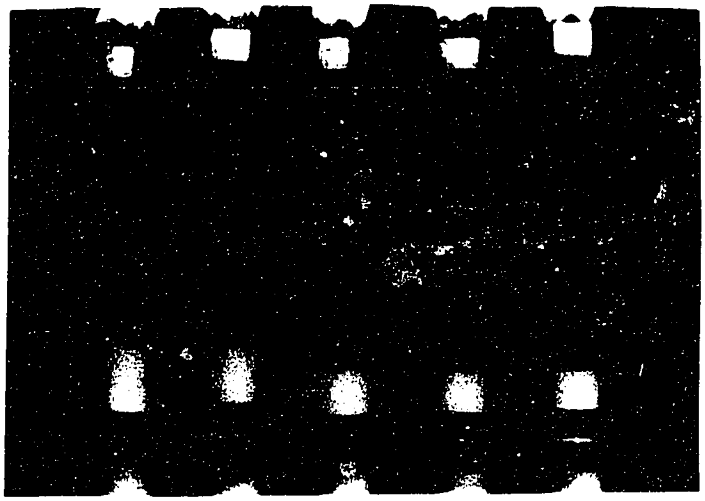

(a)

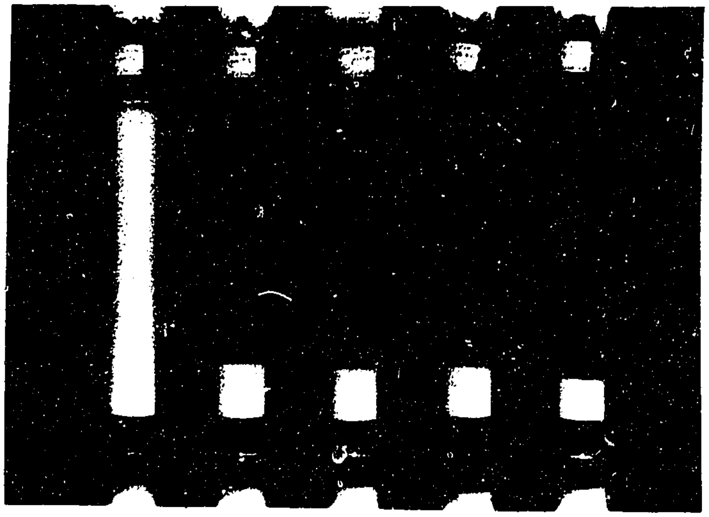

(b)

Fig. 4.2-24 - Characteristics of 0.5% Na-kaolinite suspensions, treated with $Na_4P_2O_7$ and mixed with aged $AlCl_3$ concentrations of 1, 2, 5, 10 and 50 mM from the left to the right, after three days of sedimentation: (a) at pH=4 ; (b) at pH=9.5.

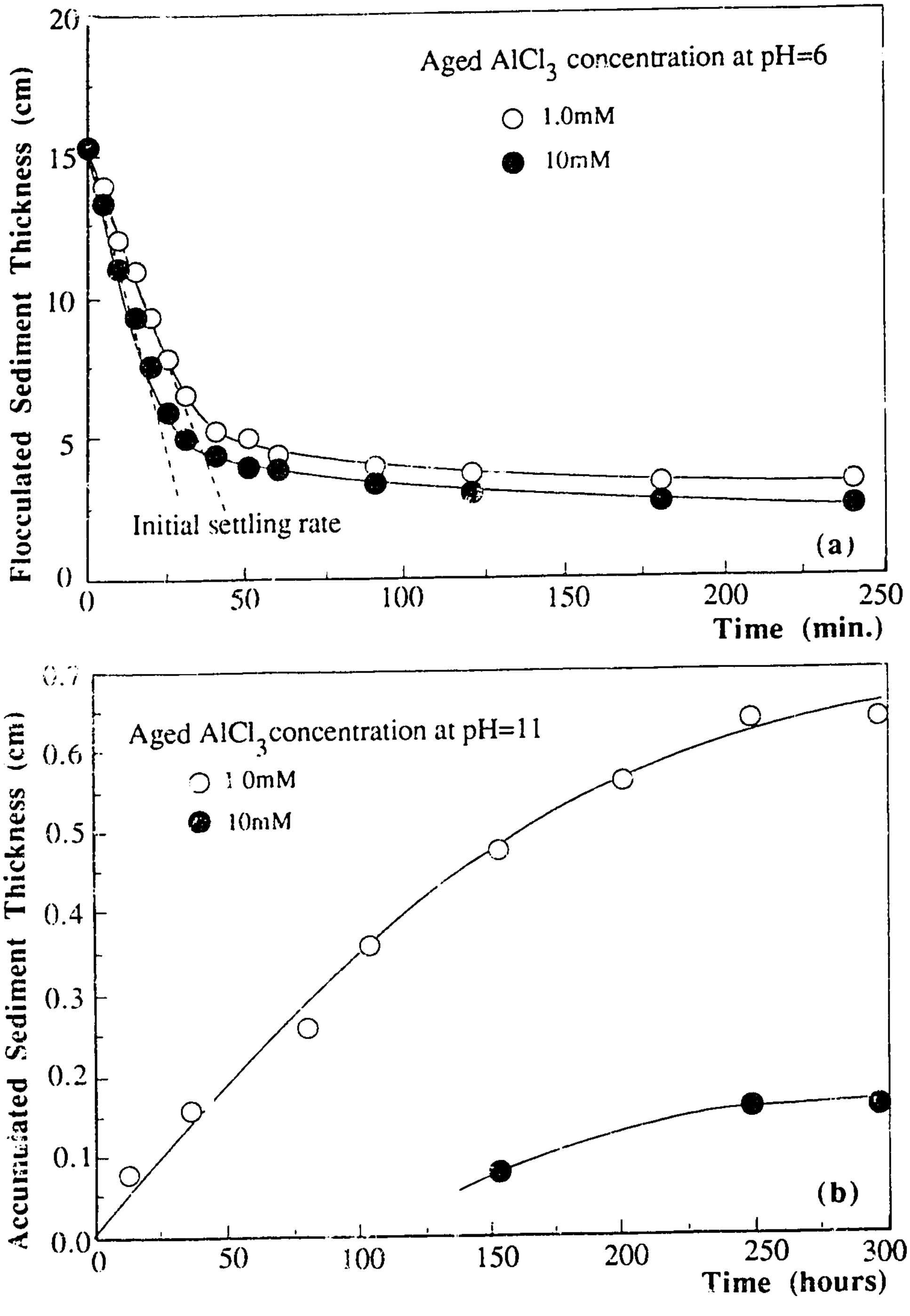

Fig. 4.2-25 - Displacement kinetics of sharp interfaces in 0.5 % (by mass) Na-kaolinite suspensions: (a) flocculated sediment-supernatant liquid interface with aged $AlCl_3$ concentrations of 1mM and 10mM at pH=6. (b) accumulated sediment-diffuse suspension interface with aged $AlCl_3$ concentrations of 1 and 10mM at pH=11.

The diagram which summarizes the sedimentation behavior of 0.5 % by mass HUF Na-kaolinite treated with $Na_4P_2O_7$ and mixed with aged $AlCl_3$, is reported in the Fig. 4.2-26. This diagram is not very different from the diagram reported for unaged $AlCl_3$. The initial settling rates for the suspensions made with aged $AlCl_3$, both when flocculation or when sedimentation occurred, are gathered in Fig. 4.2-27a, while the final sediment thicknesses are gathered in Fig. 4.2-27b.

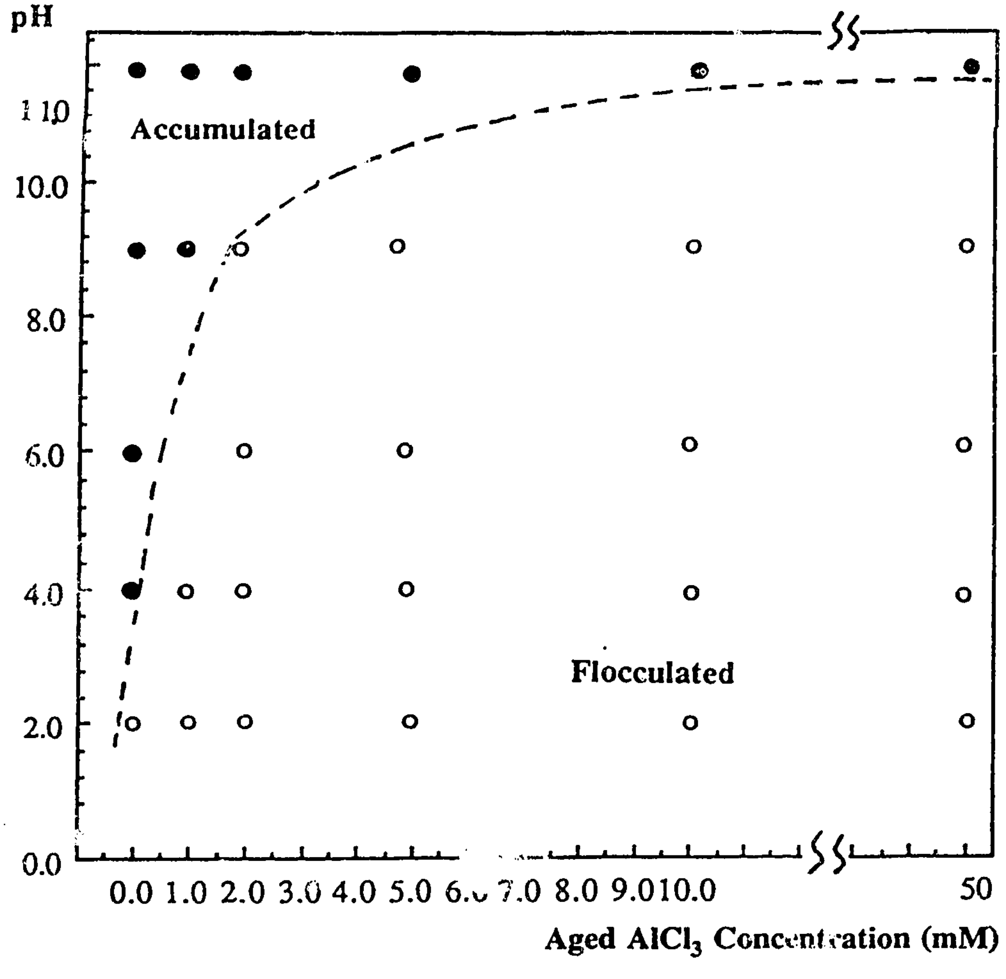

Fig. 4.2-26 - Diagram of the sedimentation behavior in 0.5% HUF Na-kaolinite suspensions treated with $Na_4P_2O_7$ and mixed with aged $AlCl_3$. The solid, open, and semi-open dots respectively indicate accumulation and flocculation behavior.

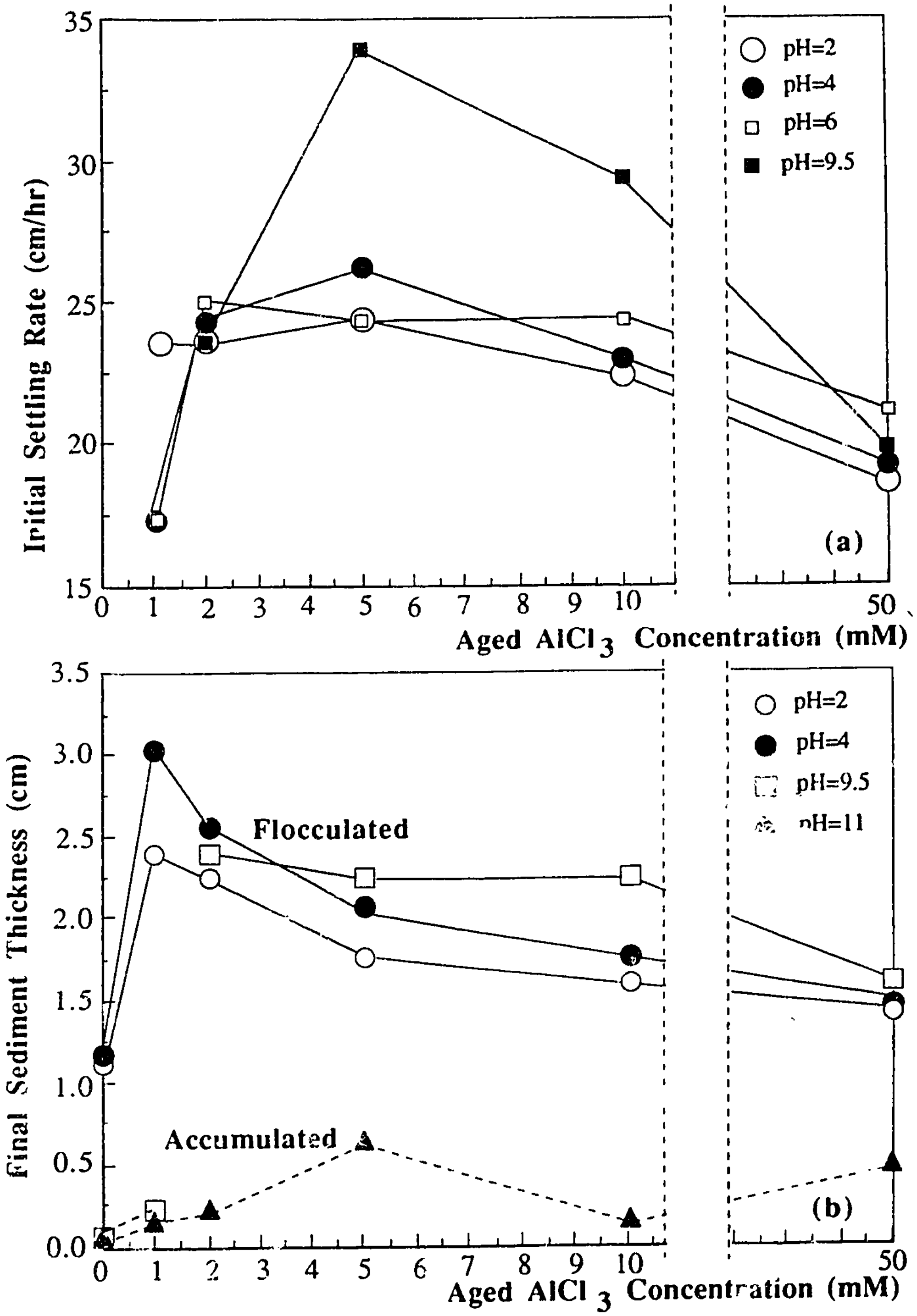

Fig. 4.2-27 - Sedimentation data of 0.5% HUF Na-kaolinite suspensions flocculated with aged $AlCl_3$ at different pH values: (a) Initial settling rate; (b) Final sediment thickness.

4.3 - MONTMORILLONITE SUSPENSIONS

4.3.1 - Montmorillonite-unaged $FeCl_3$ suspensions

This system was investigated in detail by Zou [1] for a clay solid content of 0.5 % by mass. The types of sedimentation behavior which Zou found included accumulation sedimentation and flocculation sedimentation. However, no mixed accumulation-flocculation behavior was reported. As an illustration, some data from Zou on 0.5 % by mass montmorillonite are reported in Fig. 4.3-1, on the same graphs as some sedimentation data which were obtained as part of the present thesis. The latter data are on 1 % by mass Na-montmorillonite suspensions with the unaged $FeCl_3$ concentration 1.67mM and 16.7mM, and with the hydroxoferric particles contents of 0.025 % (by mass) and 0.25 % (by mass). As these data show, the settling rate of the montmorillonite-unaged $FeCl_3$ suspensions was faster than for the montmorillonite-hydroxoferric particles mixed suspensions, for a low concentration of the Fe additives (Fig. 4.3-1a). However these rates were similar for a higher concentration of Fe additives (Fig. 4.3-1b).

4.3.2 - Montmorillonite-aged $FeCl_3$ suspensions

The visual characteristics of 1% montmorillonite sediments made with different concentrations of aged $FeCl_3$ at pH=4.0 and 9.5, are shown in Fig. 4.3-2. The data on typical sedimentation kinetics corresponding to different types of sedimentation behaviors at pH=9.5, are gathered in Fig. 4.3-3. These data include flocculation sedimentation with aged $FeCl_3$ concentrations of 1mM and 3.3mM which do not show any significant induction time, flocculation sedimentation with 10mM aged $FeCl_3$ where a significant induction time can be noticed (Fig. 4.3-3a), and accumulation sedimentation with aged $FeCl_3$ concentration of 0.33mM (Fig. 4.3-3b).

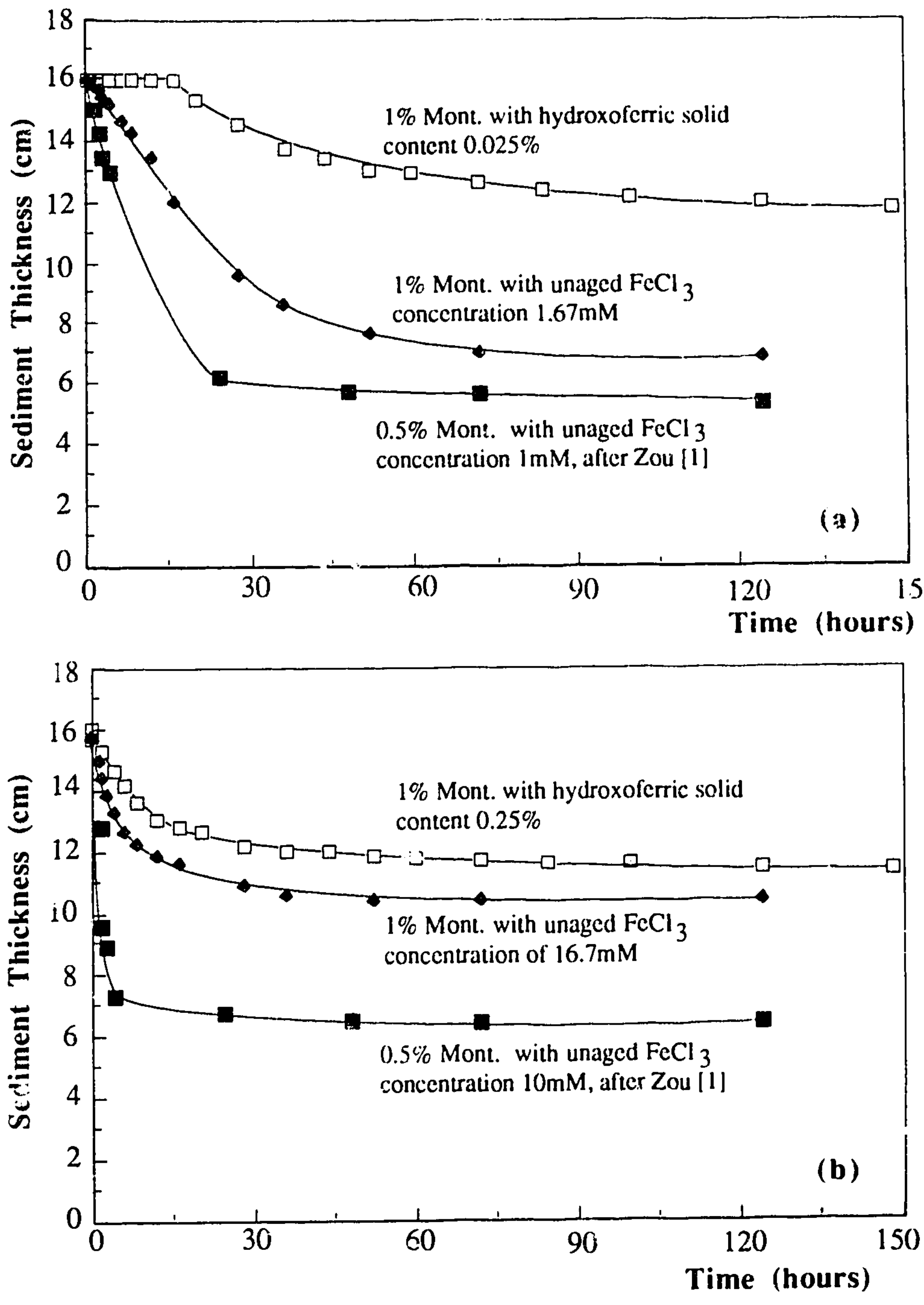

Fig. 4.3-1 - Displacement rates of the sharp interfaces in Na-montmorillonite suspensions at pH=9.5 with: (a) a low content of Fe additives; (b) a higher content of Fe additives.

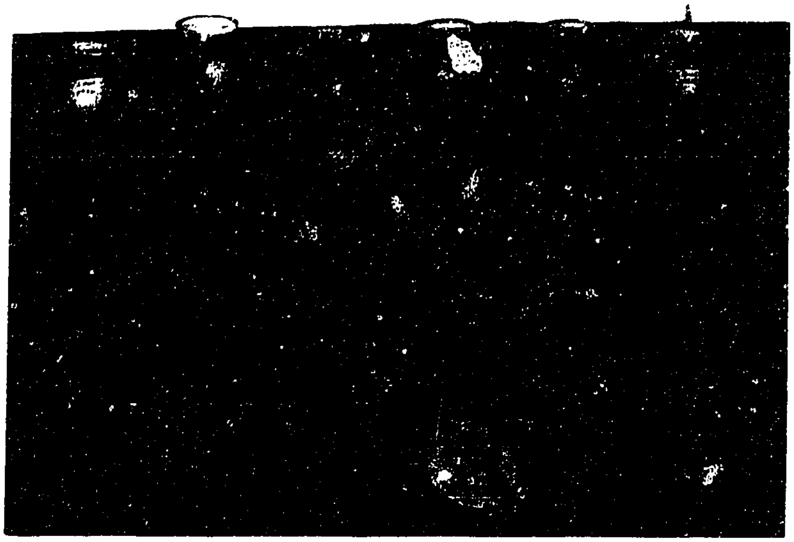

(a)

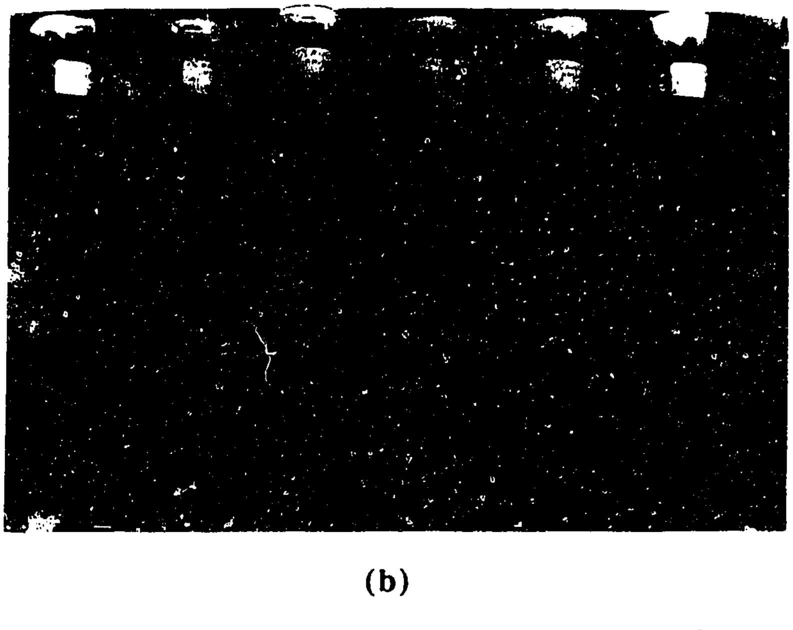

(b)

Fig. 4.3-2 - Characteristics of the sediments made from 1% by mass Na-montmorillonite suspensions, with aged $FeCl_3$ concentrations of 0.33, 1, 2, 3.3, 5 and 10mM, from left to right, after 10 days sedimentation: (a) at pH = 4; (b) at pH = 9.5.

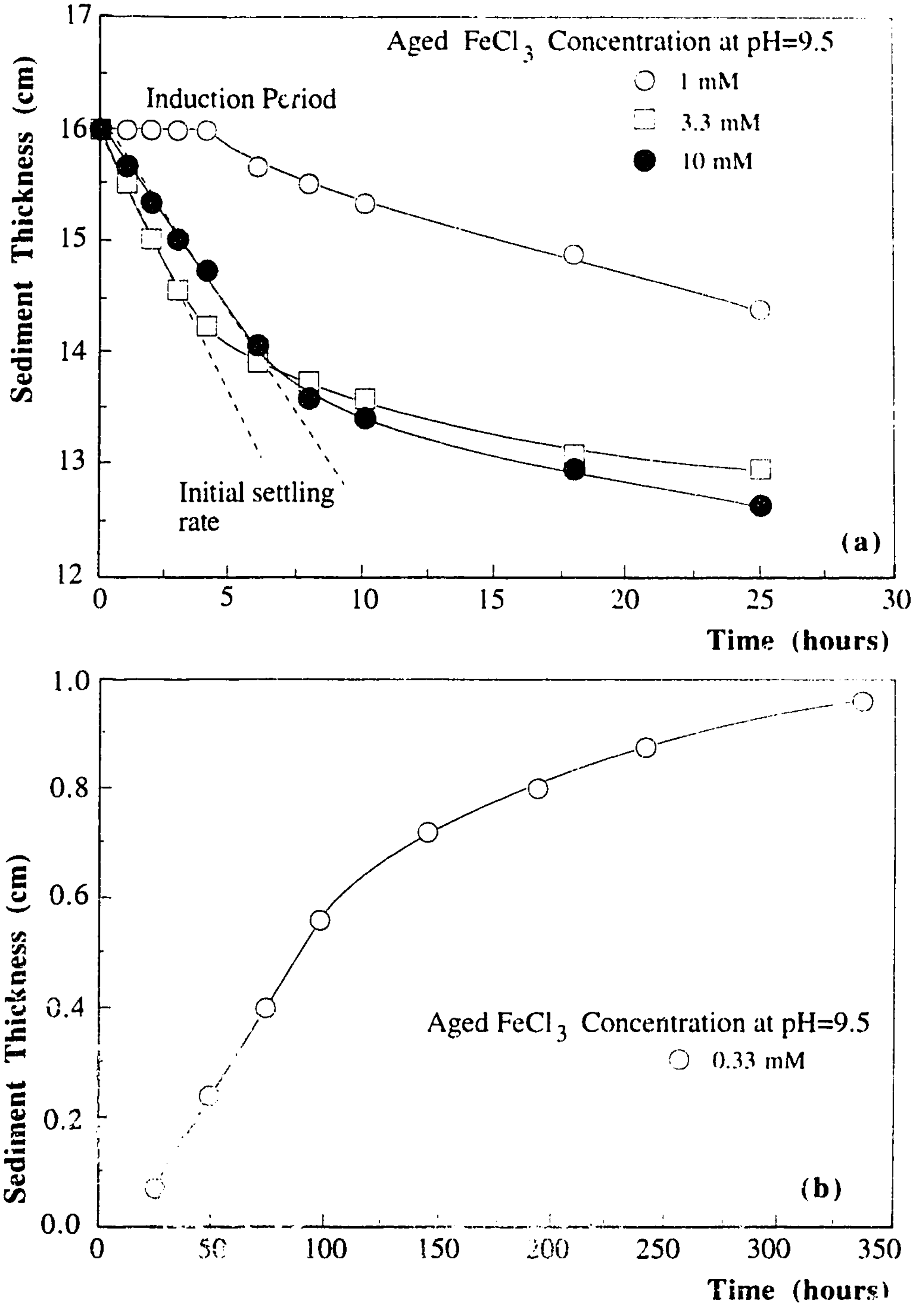

Fig. 4.3-3 - Displacement kinetics of the sharp interfaces in 1% Na-montmorillonite suspensions at pH=9.5, with different aged FeCl$_3$ concentrations: (a) flocculated sediment-supernatant liquid interface with aged FeCl$_3$ = 1mM, 3.3mM and 10mM; (b) accumulated sediment-diffuse suspension interface with aged FeCl$_3$ = 0.33 mM.

The sedimentation behavior of 1% Na-montmorillonite suspensions mixed with aged $FeCl_3$ electrolyte is reported in Fig. 4.3-4a. Accumulation sedimentation occurred in a limited field of conditions, in basic conditions and for a low aged $FeCl_3$ concentration. Flocculation sedimentation occurred for all other conditions. The data on the sedimentation kinetics for these suspensions, with respect to the initial settling rate and the final sediment thickness, are reported in Fig. 4.3-5.

4.3.3 - Montmorillonite - Hydroxoferric Particles

Typical sedimentation kinetics for the flocculation of 1% Na-montmorillonite with 0.25% by mass of hydroxoferric particles are reported in Fig. 4.3-6 for a few pH values. The diagram on the sedimentation behavior of 1% Na-montmorillonite suspensions with hydroxoferric particles is reported in Fig. 4.3-4b, where it can easily be compared with the diagram obtained with aged $FeCl_3$. The two diagrams are not much different.

The initial settling rate and the final sediment thickness of these suspensions, as a function of the hydroxoferric % (by mass), are reported in Fig. 4.3-7 for several pH values. The initial settling rate increased with the hydroxoferric % (by mass) (Fig. 4.3-7a). As for the final sediment thickness, it was higher with hydroxoferric particles than without them. A slight maximum could be observed in a range from 0.15 to 0.30 % (by mass) of particles (Fig. 4.3-7b), from pH 2 to 9.5.

4.3.4 - Montmorillonite-unaged $AlCl_3$ suspensions

Some aspects of the sediments from 1% (by mass) Na-montmorillonite with different concentrations of unaged $AlCl_3$ are shown in Fig. 4.3-8, at pH=4.0 and 9.5. Typical flocculation kinetics are reported in Fig. 4.3-9, at pH=9.5 for three unaged $AlCl_3$ concentrations of 10mM, 3.3mM and 0.33mM.

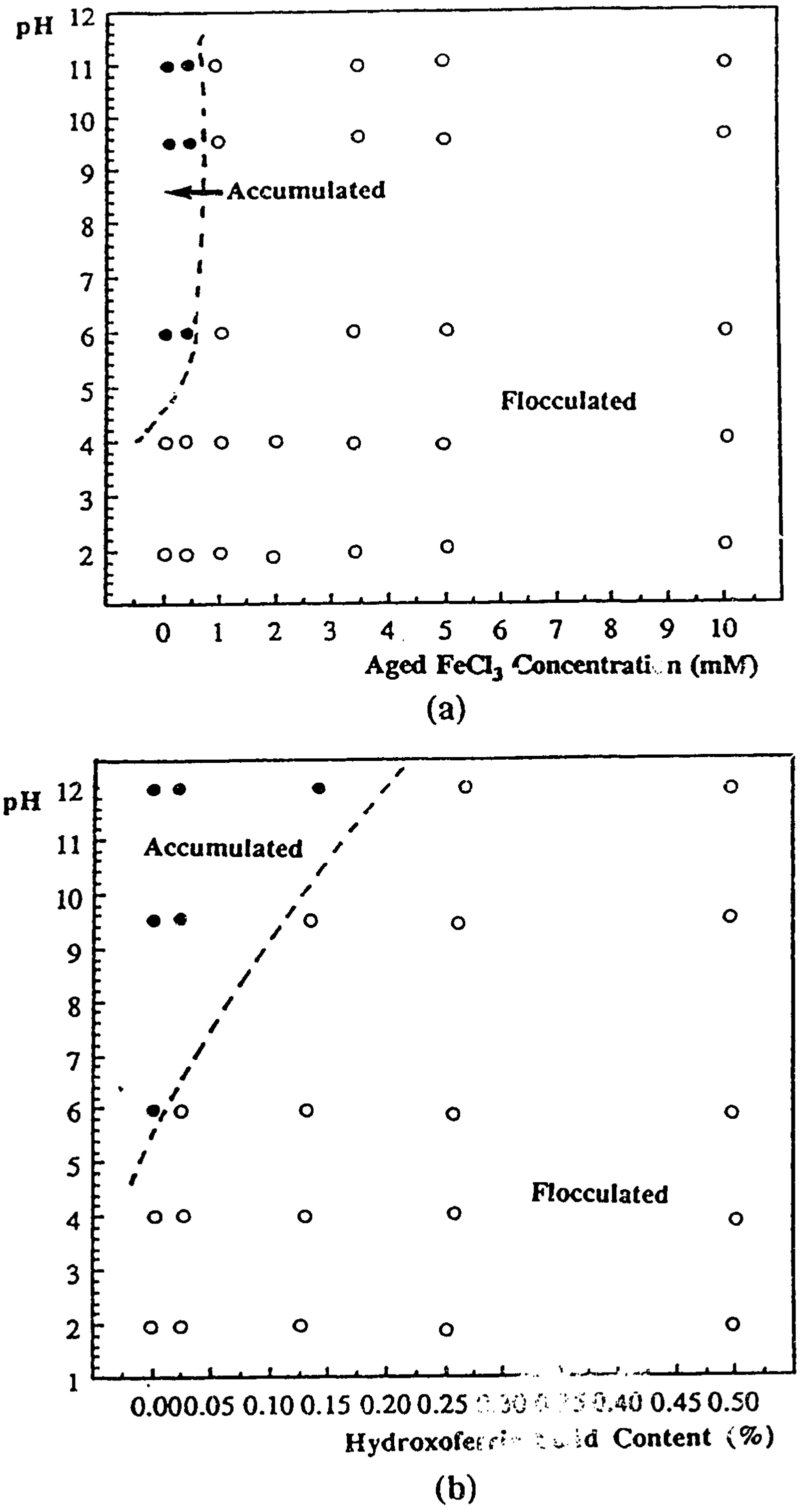

Fig. 4.3-4 - Diagrams of the sedimentation behavior in 1% Na-montmorillonite suspensions: (a) with aged $FeCl_3$; (b) with hydroxoferric particles. The solid, open, and semi-open dots respectively indicate accumulation and flocculation sedimentation.

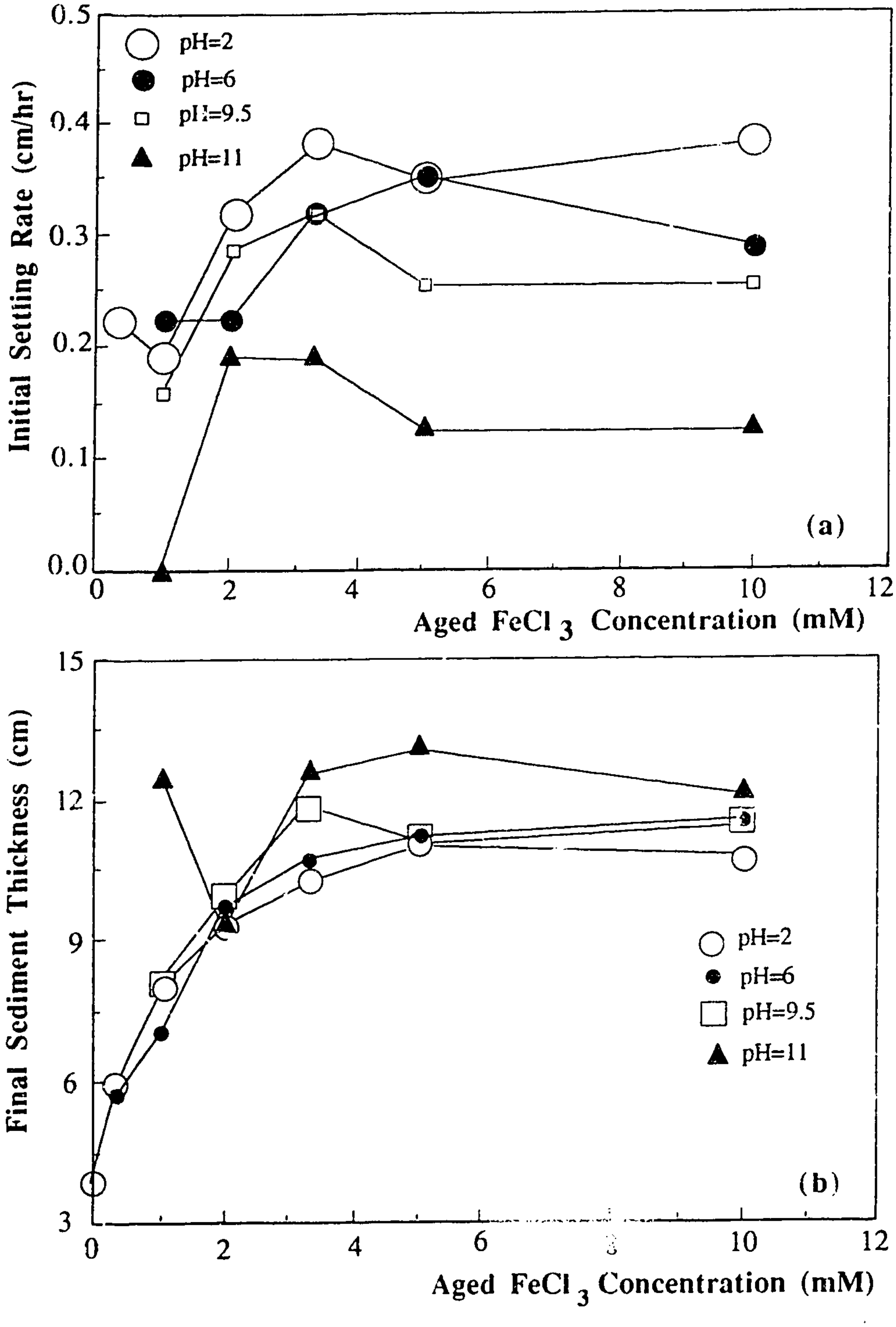

Fig. 4.3-5 - Sedimentation kinetics of 1% Na-montmorillonite suspensions flocculated with aged $FeCl_3$ at different pH: (a) Initial settling rate; (b) Final sediment thickness.

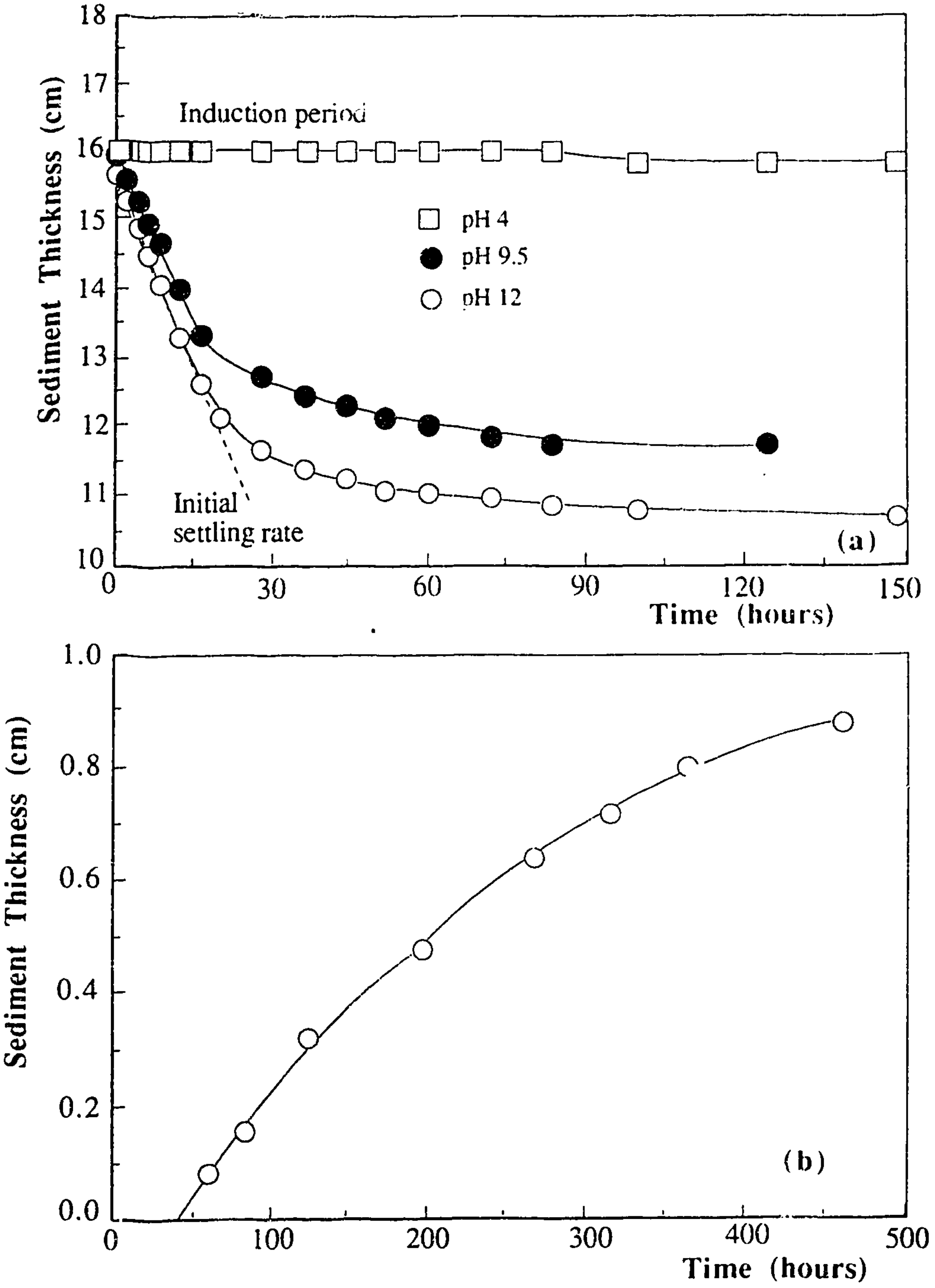

Fig. 4.3-6 - Displacement rate of sharp interface between the flocculated sediment and the supernatant liquid, in 1 % (by mass) Na-montmorillonite suspensions flocculated with 0.25% (by mass) of hydroxoferric particles at pH=12, 9.5 and 4.

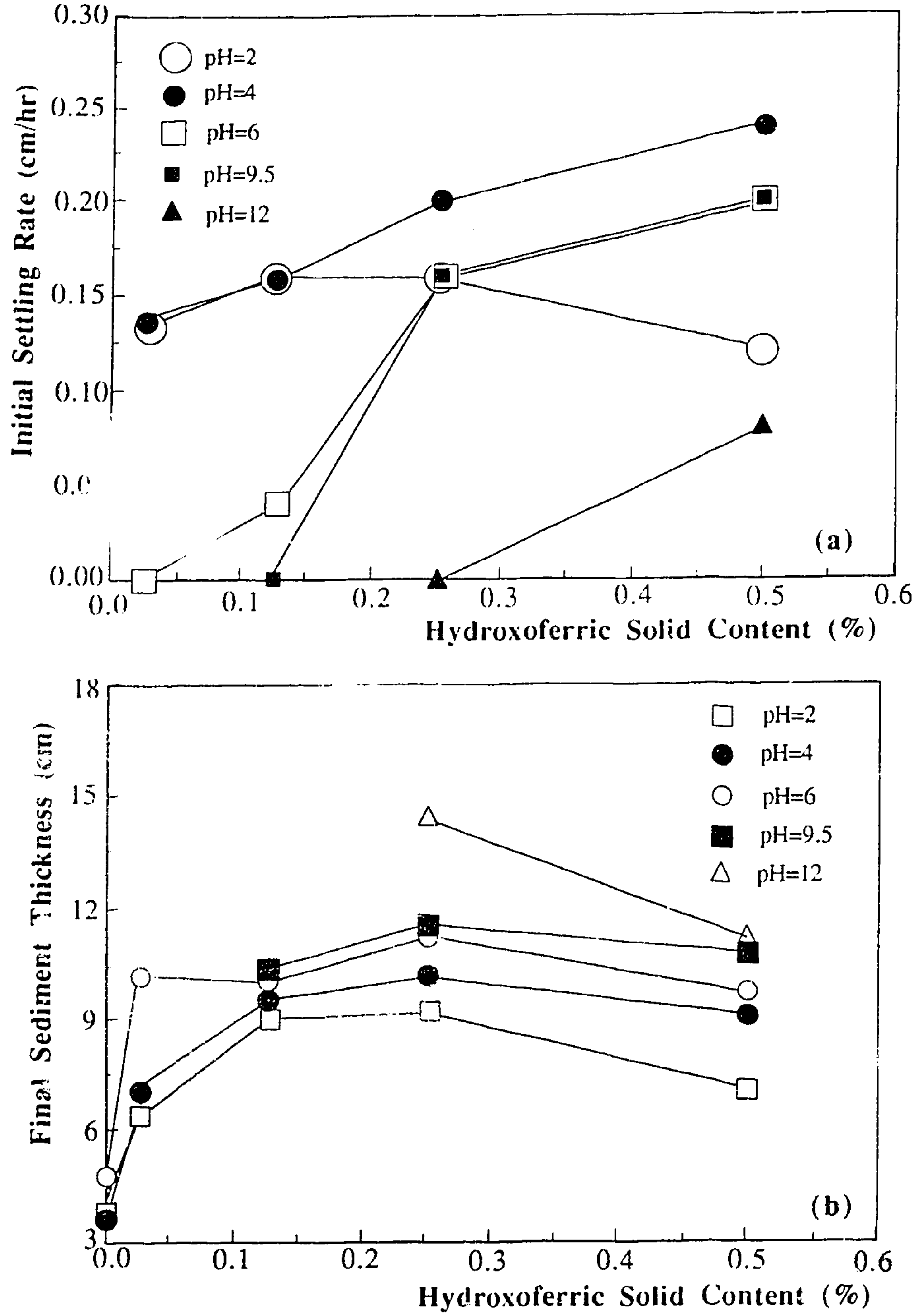

Fig. 4.3-7 - Sedimentation of 1 % (by mass) montmorillonite suspensions with hydroxoferric particles at different pH values: (a) Initial settling rate; (b) Final sediment thickness

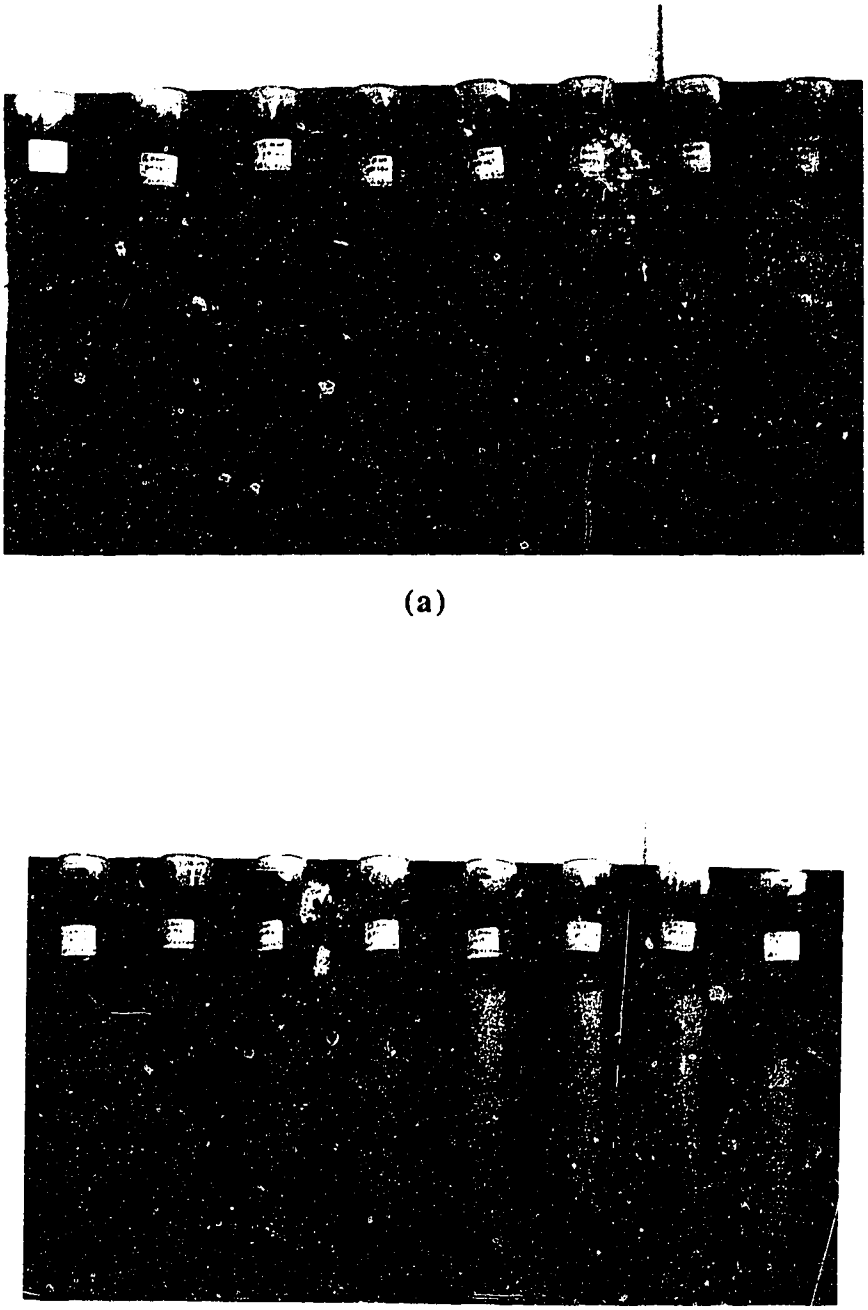

(a)

(b)

Fig. 4.3-8 - Sedimentation of 1% (by mass) Na-montmorillonite suspensions after 10 days, for the unaged $AlCl_3$ concentrations of 0.17, 0.33, 1, 2, 3.3, 5, 10 and 20mM, from the left to the right: (a) pH = 4.0; (b) at pH = 9.5.

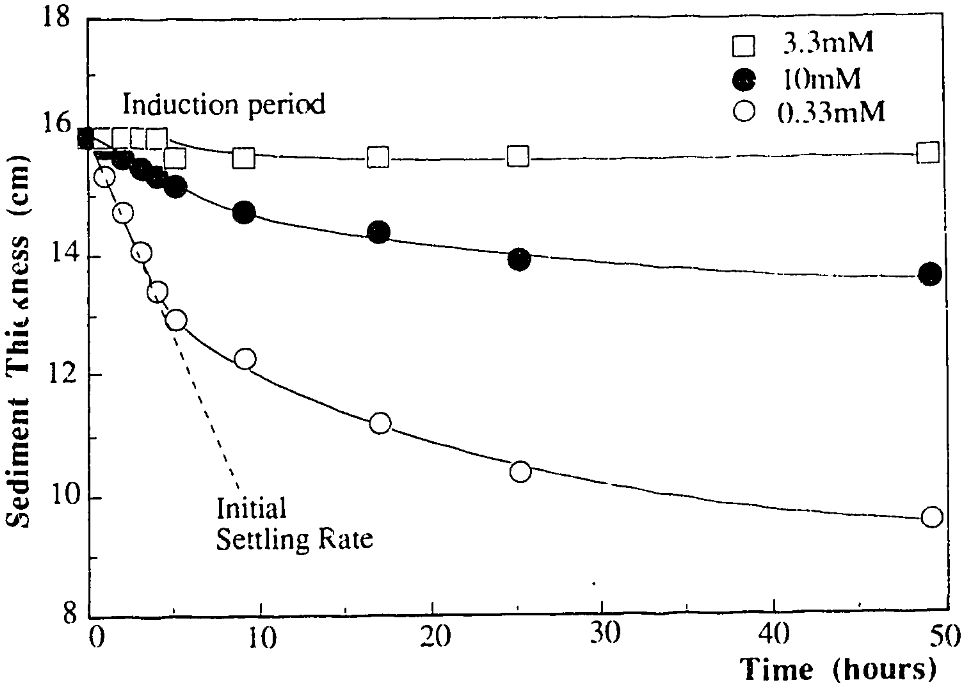

Fig. 4.3-9 - Displacement rate of the sharp interface between the flocculated sediment and the supernatant liquid, in 1% Na-montmorillonite suspensions at pH=9.5, for the unaged $AlCl_3$ concentrations of 0.33mM, 3.3mM and 10mM.

The diagram for the sedimentation behavior of 1% Na-montmorillonite suspensions mixed with unaged $AlCl_3$ is reported in Fig. 4.3-10. As with aged $FeCl_3$, accumulation sedimentation occurs in a limited field in rather basic conditions and at low $AlCl_3$ content. In the case where flocculation occurs, the initial settling rate and the final sediment thickness are reported in Fig. 4.3-11. Generally, the initial settling rate decreased as the $AlCl_3$ concentration increased, except at pH 4. Also, the final sediment thickness increased with a small concentration of unaged $AlCl_3$, then it remained relatively constant above 2 mM $AlCl_3$.

4.3.5 - Montmorillonite-aged $AlCl_3$ Suspensions

The data for typical sedimentation kinetics of 1% Na-montmorillc ith aged $AlCl_3$ are reported in Fig. 4.3-12a. These are for aged $AlCl_3$ concentrations of 2mM and 5mM, at pH=9.5. Fig. 4.3-12b concerns the sedimentation kinetics of the accumulated sediment at pH 9.5 with 0.33 mM aged $AlCl_3$. The diagram on the sedimentation behavior is reported in Fig. 4.3-10b. It is not very different from the diagram with unaged $AlCl_3$ (Fig. 4.3-10a).

The initial settling rate and the final sediment thickness of these suspensions, as a function of the aged $AlCl_3$ concentration at different pH values, are reported in Fig. 4.3-13. The general trend is that the initial settling rate increased with aged $AlCl_3$ concentration up to 3.3mM, where it reached a maximum. For higher $AlCl_3$ concentrations, the initial settling stabilized to a intermediate value. As for the final sediment thickness of flocculated sedimentation, it was roughly independent of the aged $AlCl_3$ concentration, above a concentration of about 2 mM.

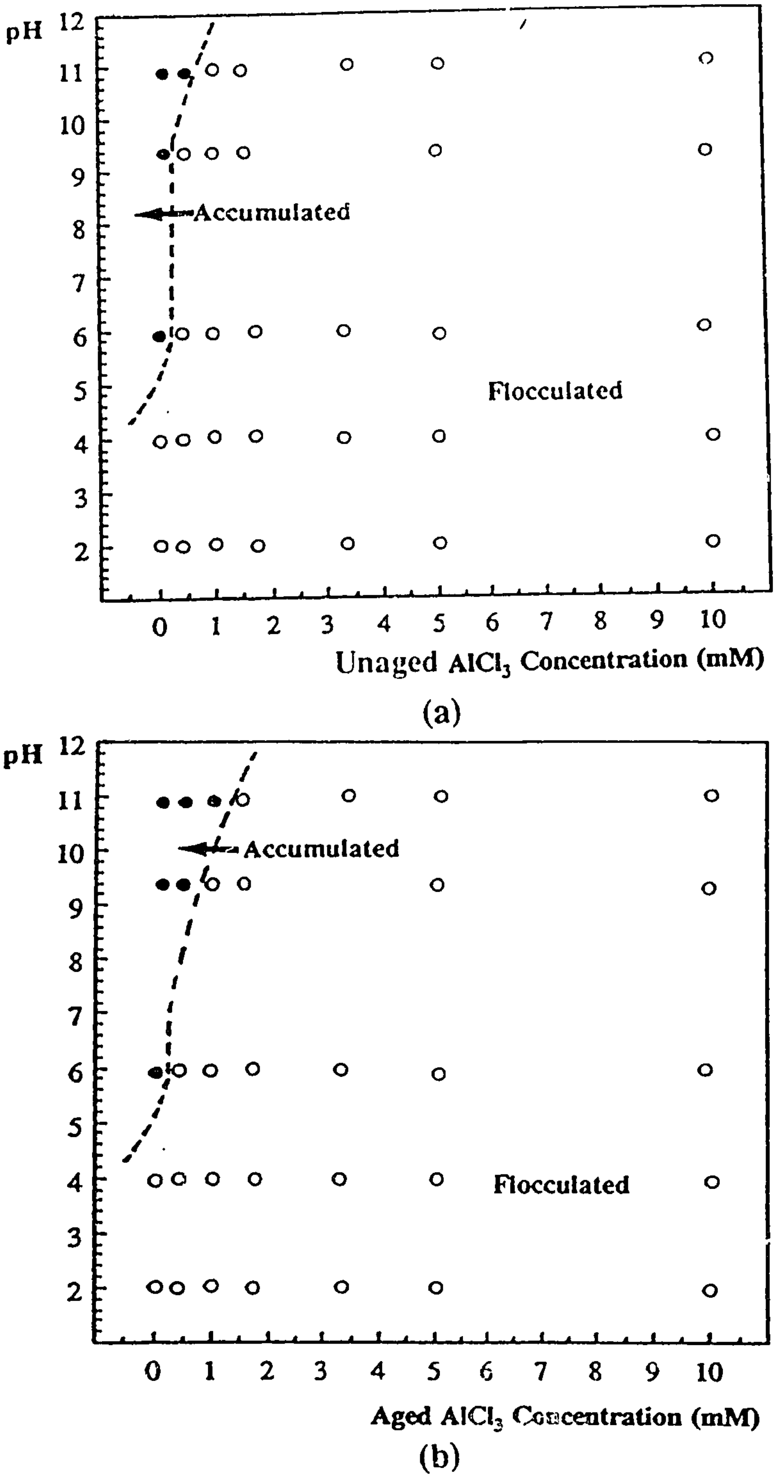

Fig. 4.3-10 - Diagram of the sedimentation behavior of 1% Na-montmorillonite suspensions: (a) with unaged $AlCl_3$; (b) with aged $AlCl_3$. The solid, open, and semi-open dots respectively indicate accumulation and flocculation.

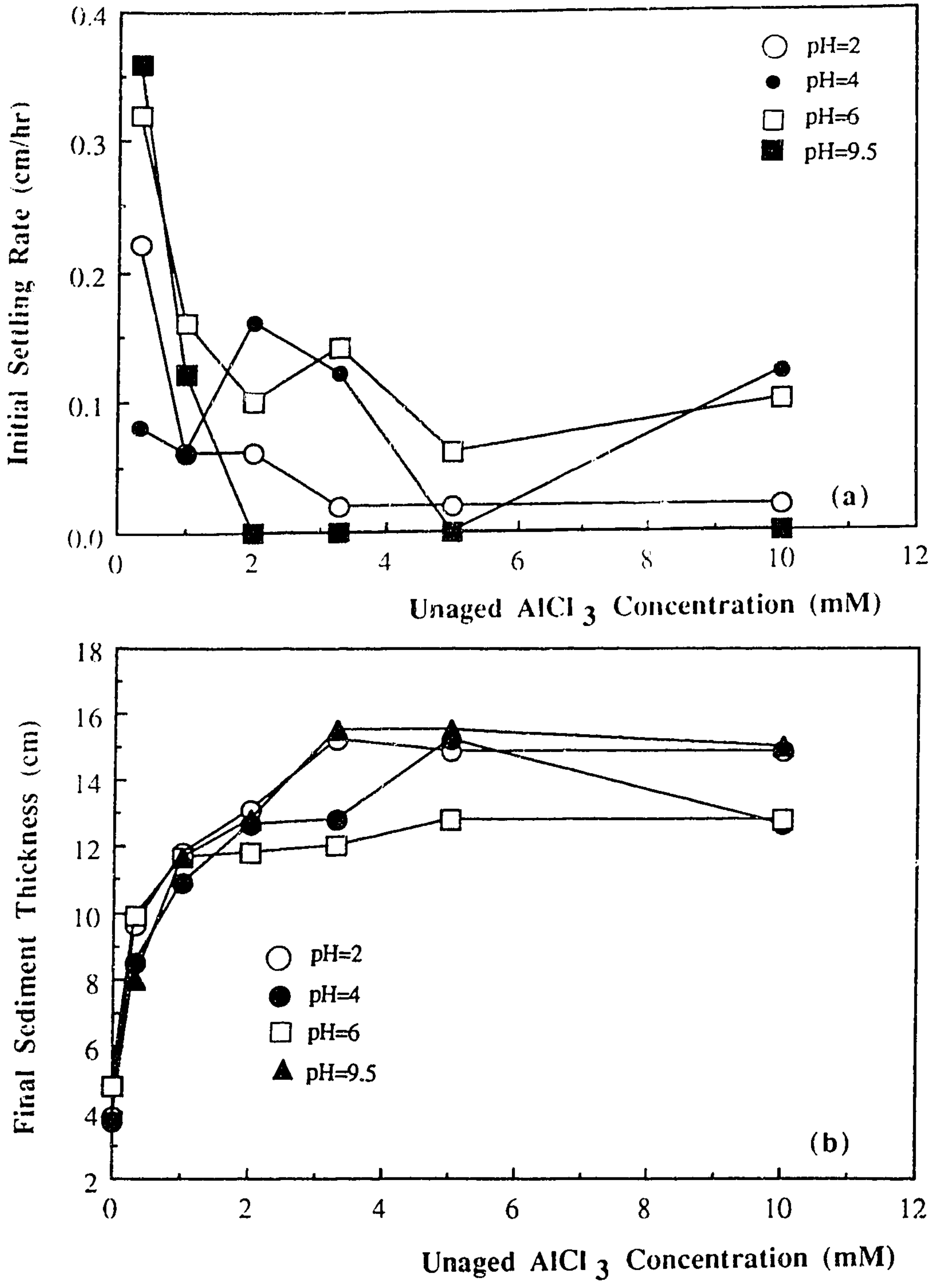

Fig. 4.3-11 - Sedimentation characteristics of 1% Na-montmorillonite suspensions flocculated with unaged $AlCl_3$ at different pH: (a) Initial settling rate; (b) Final sediment thickness.

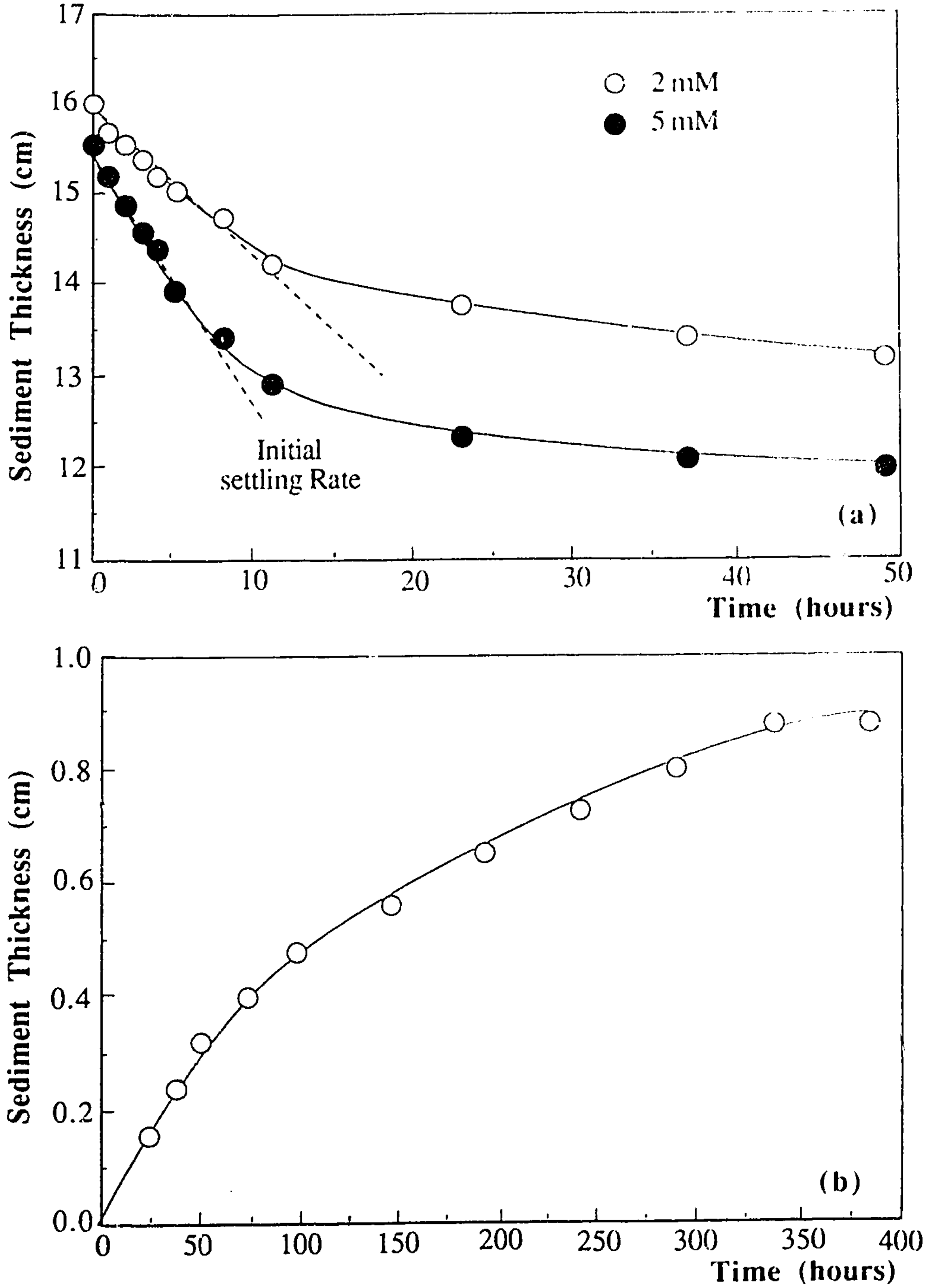

Fig. 4.3-12 - Displacement kinetics of sharp interfaces in 1% Na-montmorillonite suspensions at pH=9.5: (a) interface between the flocculated sediment and the supernatant liquid with the aged $AlCl_3$ concentrations of 5mM and 2mM; (b) interface between the accumulated sediment and the diffuse suspension with an aged $AlCl_3$ concentration of 0.33 mM.

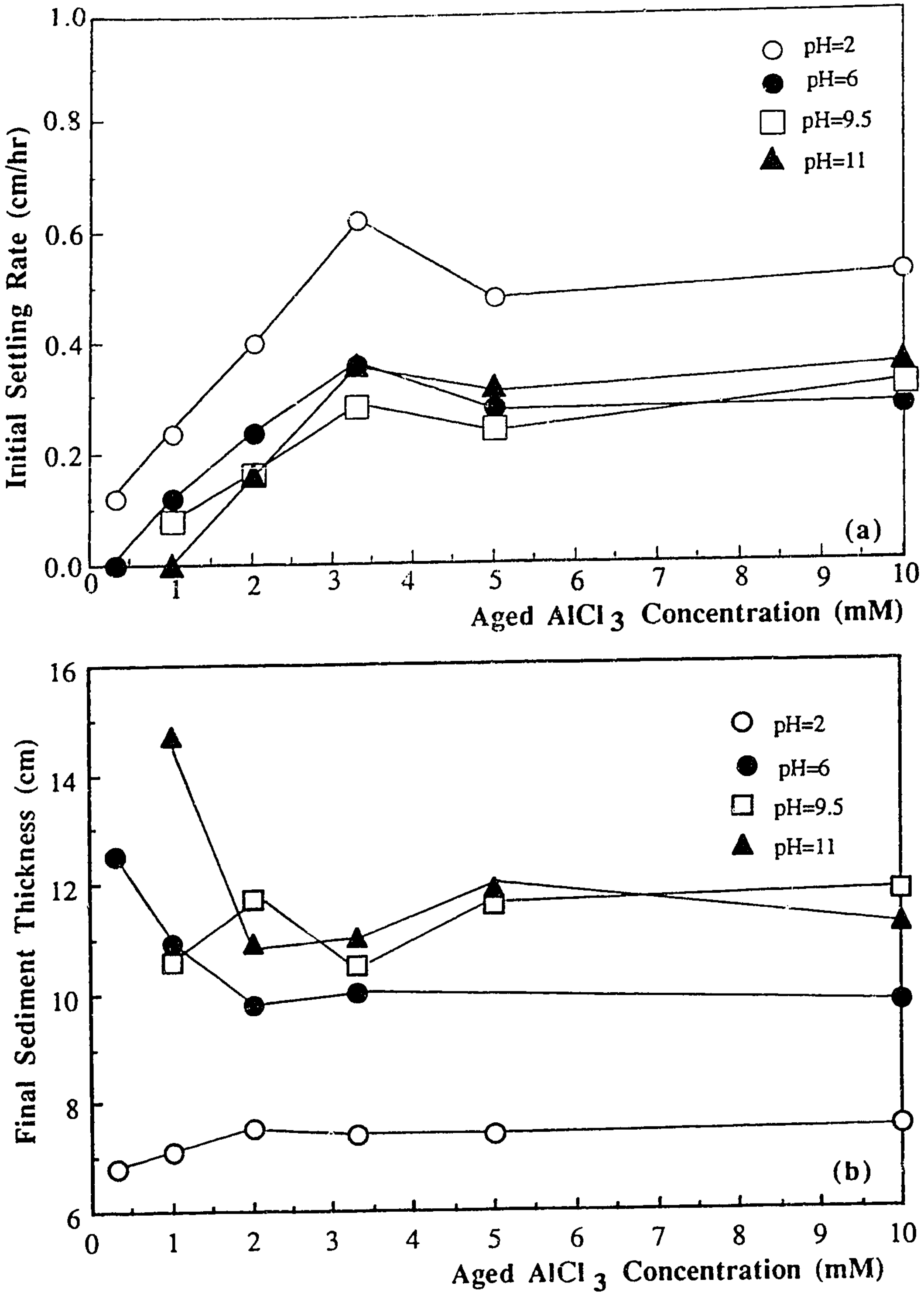

Fig. 4.3-13 - Sedimentation characteristics of 1% (by mass) Na-montmorillonite suspensions flocculated with aged $AlCl_3$ at different pH: (a) Initial settling rate; (b) Final sediment thickness.

CHAPTER 5 - PHYSICAL-CHEMICAL CHARACTERIZATIONS

The detailed research plan of this thesis, concerning physical-chemical characterization, was presented in Chapter 3. The present chapter addresses the results on physical-chemical characterizations of clay suspensions. These results are intended to provide some information on the interaction of clay particles with additives such as unaged $FeCl_3$ or $AlCl_3$, particularly on the electrical properties of the surface of clay particles as they are modified by these additives. For this purpose, chemical analyses data on the Fe and Al elements adsorbed by clay particles are first reported. Next, TEM observations of Fe products adsorbed on the surface of clay particles, are shown. Then, zeta potential data provide some direct evidence of the electrical properties of the surface of clay particles. Finally, SEM observations of kaolinite particles mixed with SiO_2 particles at different pH are reported. These observations address the existence of electrical charges with a different sign on the edges and the faces of clay particles

5.1 - DETERMINATION OF Al OR Fe ADSORBED ON THE CLAY PARTICLES BY ATOMIC ABSORPTION SPECTROPHOTOMETRY

5.1.1 - Kaolinite suspensions

5.1.1.1 - Fe or Al in the supernatant liquid after sedimentation

The concentration of Fe or Al which remained in the liquid of the kaolinite suspensions after 24 hours sedimentation, are gathered in Tables 5.1-1 to 5.1-4.

Table 5.1-1. Concentration of Fe (in mM) in the liquid of 0.5 % (by mass) kaolinite suspensions mixed with unaged $FeCl_3$, after 24 hours sedimentation, as determined by Atomic Absorption (AA) method.

Initial unaged $FeCl_3$ concentration	0.33mM	1.67mM	3.33mM	10.0mM
pH	Fe(mM)	Fe(mM)	Fe(mM)	Fe(mM)
2	0.23	0.44	2.05	8.32
4	0.21	0.41	1.80	8.04
6	0.26	0.44	1.43	7.77
9.5	0.26	0.21	1.15	6.98
11	0.19	0.20	1.09	6.93

Table 5.1-2. Concentration of Fe (in mM) in the liquid of 0.5 % (by mass) kaolinite suspensions mixed with aged $FeCl_3$, after 24 hours sedimentation, as determined by AA.

Initial aged $FeCl_3$ concentration	0.33mM	1.67mM	3.33mM	10.0mM
pH	Fe(mM)	Fe(mM)	Fe(mM)	Fe(mM)
2	0.09	0.16	0.45	5.63
4	0.09	0.19	0.27	5.39
6	0.10	0.28	0.25	5.39
9.5	0.13	0.19	0.03	4.50

Table 5.1-3. Concentration of Al (in mM) in the liquid of 0.5 % (by mass) kaolinite suspensions mixed with unaged $AlCl_3$, after 24 hours sedimentation, as determined by AA.

Initial unaged $AlCl_3$ concentration	1.0mM	2.0mM	5.0mM	10.0mM
pH	Al(mM)	Al(mM)	Al(mM)	Al(mM)
2	1.37	2.15	4.89	9.01
6	1.22	2.11	4.85	8.71
9.5	0.44	1.85	4.85	8.71
12	0.15	1.48	2.63	7.48

Table 5.1-4. Concentration of Al (in mM) in the liquid of 0.5 % (by mass) kaolinite suspensions mixed with aged $AlCl_3$, after 24 hours sedimentation, as determined by AA.

Initial aged $AlCl_3$ concentration	1.0mM	2.0mM	5.0mM	10.0mM
pH	Al(mM)	Al(mM)	Al(mM)	Al(mM)
2	1.00	2.25	5.29	9.37
4	0.48	1.89	4.52	7.81
6	0.41	2.00	4.53	7.81
9.5	0.48	1.52	4.37	7.81

5.1.1.2 - Fe or Al adsorbed on the kaolinite particles

From the data in the preceding section, it was possible to calculate the amounts of Fe or Al which were adsorbed on the kaolinite particles. The results of these calculations are presented as graphs.

The amount of Fe adsorbed on the kaolinite particles, as a function of the pH and on the concentration of unaged or aged $FeCl_3$, is reported in Fig. 5.1-1. It appears that the amount of Fe adsorbed on kaolinite particles, from unaged $FeCl_3$, increased with the initial Fe concentration and with the pH (Fig. 5.1-1a). On the contrary, the amount of adsorbed Fe from aged $FeCl_3$ was almost independent of the pH (Fig. 5.1-1b).

The graphs which correspond to the adsorption of Al are reported in Fig. 5.1-2. It must be noticed that at low pH, some Al from the kaolinite particles dissolved in the supernatant liquid (negative adsorption).

5.1.2 - Montmorillonite suspensions

5.1.2.1 - Al and Na in the supernatant liquid after sedimentation.

The concentration of Al which remained in the liquid of the montmorillonite suspensions after 24 hours sedimentation from $AlCl_3$, are gathered in Tables 5.1-5 and 5.1-6. The amount of Na is also reported in the case of aged $AlCl_3$, in Table 5.1-7.

Table 5.1-5. Concentration of Al (in mM) in the liquid of 1 % (by mass) montmorillonite suspensions mixed with unaged $AlCl_3$, after 24 hours sedimentation, as determined by AA.

Initial unaged $AlCl_3$ concentration	0.33mM	2.0mM	3.33mM	10mM
pH	Al(mM)	Al(mM)	Al(mM)	Al(mM)
2	0.24	0.27	0.71	6.33
4	<0.04	<0.04	0.41	6.22
6	<0.04	<0.04	0.51	5.49
9.5	<0.04	<0.04	0.28	5.44
11	<0.04	<0.04	0.34	5.15

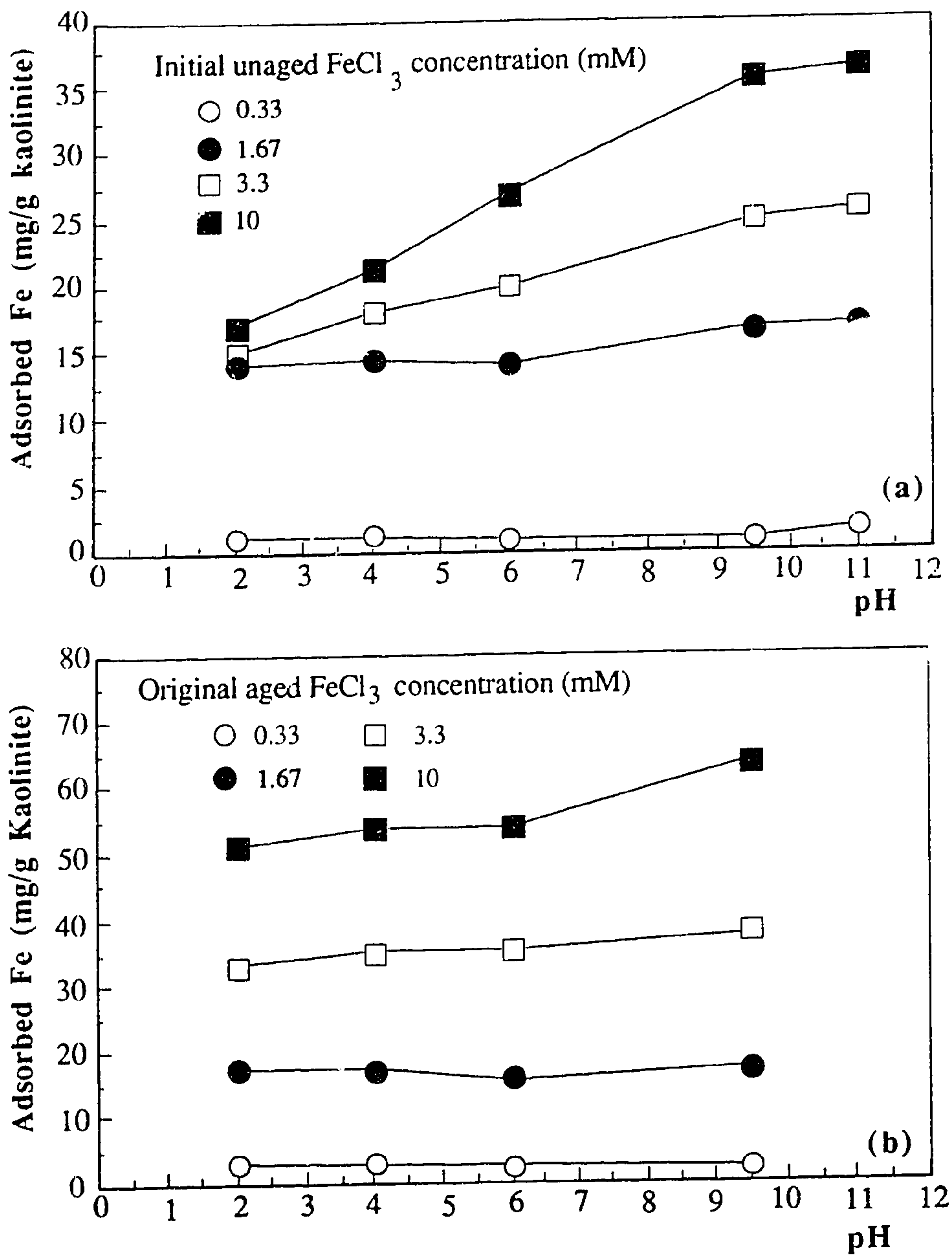

Fig. 5.1-1 - Amount of Fe adsorbed on the kaolinite particles from $FeCl_3$, at different pH: (a) from unaged $FeCl_3$; (b) from aged $FeCl_3$.

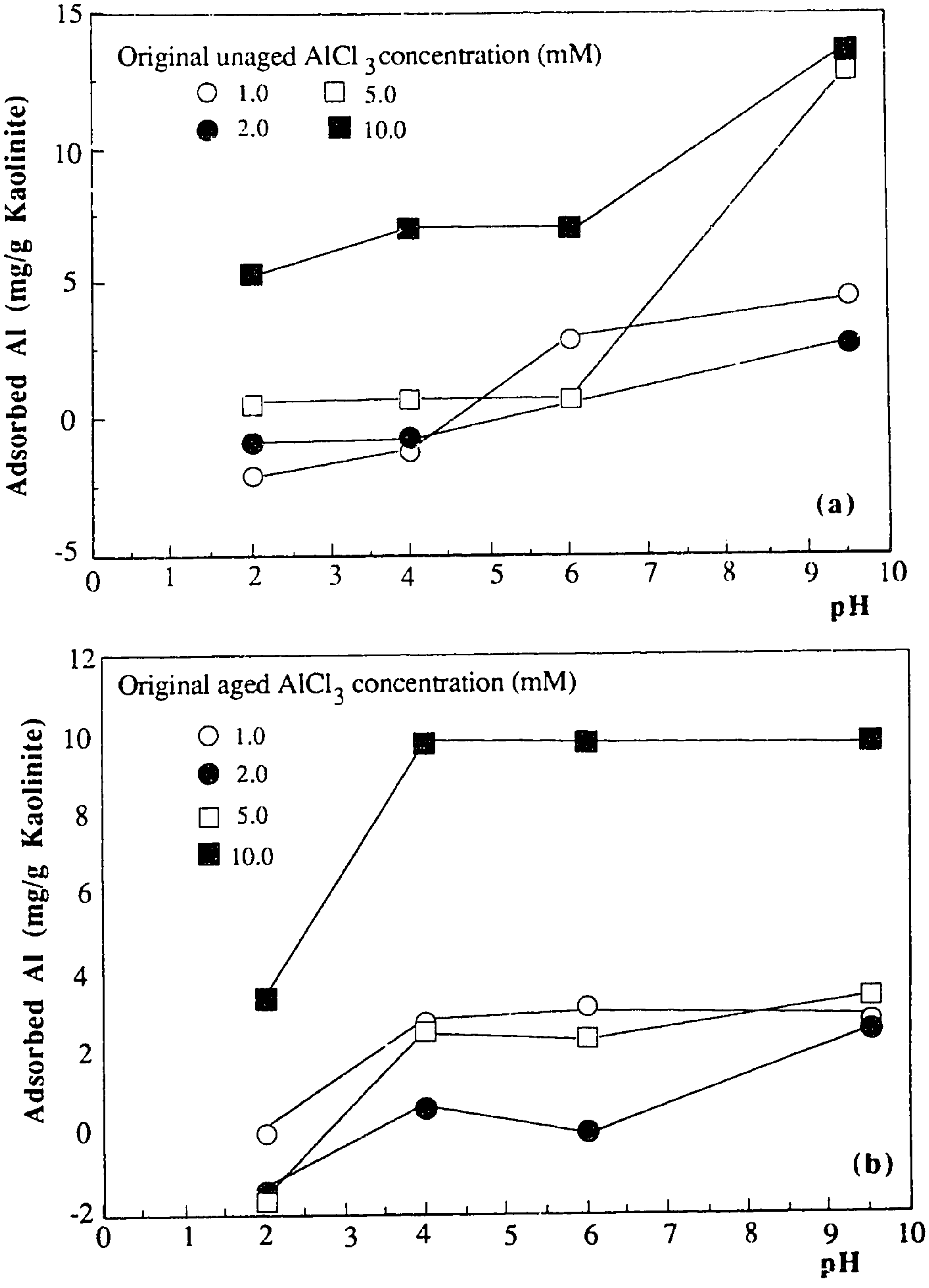

Fig. 5.1-2 - Amount of Al adsorbed on the kaolinite particles from $AlCl_3$, as a function of the pH: (a) unaged $AlCl_3$; (b) aged $AlCl_3$.

Table 5.1-6 - Concentration of Al (in mM) in the liquid of 1 % (by mass) montmorillonite suspensions mixed with aged $AlCl_3$, after 24 hours sedimentation, as determined by AA.

Initial aged $AlCl_3$ concentration	0.33mM	1.0mM	5.0mM	10.0mM
pH	Al(mM)	Al(mM)	Al(mM)	Al(mM)
2	<0.07	<0.07	2.89	7.33
4				
6	<0.07	<0.07	2.30	6.41
9.5	<0.07	<0.07	1.70	5.59

Table 5.1-7. Concentration of Na (in mM) in the liquid of 1 % (by mass) montmorillonite suspensions mixed with aged $AlCl_3$, after 24 hours sedimentation, as determined by flame photometry

Initial unaged $AlCl_3$ concentration	0 mM	0.33mM	1.0mM	5.0mM	10.0mM
pH	Na(mM)	Na(mM)	Na(mM)	Na(mM)	Na(mM)
2	0.40	0.38		0.39	
4			0.39		0.25
6	0.10	0.38		0.44	
9.5	<0.04	0.09		0.40	

As Table 5.1-7 shows, the Na ion concentration in the supernatant liquid depended largely on the pH at low Al electrolyte concentration. However, this Na concentration was progressively stabilized at a relatively high value independent of the pH, as the Al elecrolyte concentration increased up to 5mM.

5.1.2.2 - Al adsorbed on the montmorillonite particles

From Tables in the previous section, the amount of Al adsorbed on the montmorillonite particles could be derived, and the results are plotted as a function of the pH in Fig. 5.1-3.

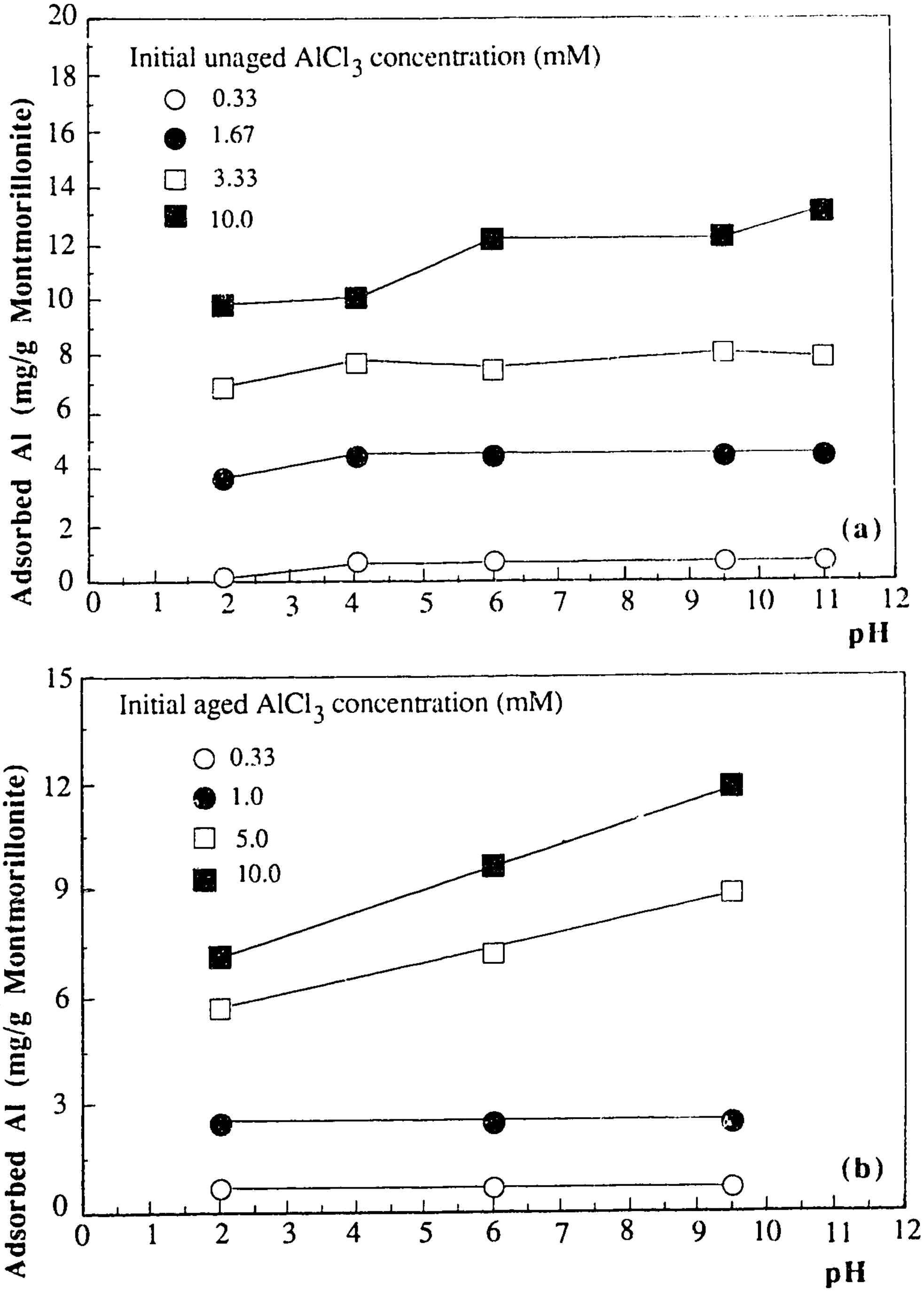

Fig. 5.1-3 - Amount of Al adsorbed on the montmorillonite particles from AlCl3, as a function of the pH: (a) unaged AlCl3; (b) aged AlCl3.

5.2 - TEM OBSERVATIONS OF THE Fe DEPOSITS ON THE CLAY PARTICLES

5.2.1 - Deposits from unaged $FeCl_3$

5.2.1.1 - Deposits on kaolinite particles

The TEM observations of the material which was deposited on the kaolinite particles from unaged $FeCl_3$ are shown in Fig. 5.2-1. The EDX analysis of selected areas, represented by small circles on the previous micrographs, are reported in Fig. 5.2-2. This EDX analysis indicate that the deposits consisted of Fe compounds. The structure of these deposited materials included: (1) some relatively large particles with a rodlike or platelike shape (Fig. 5.2-1a); (2) some smaller particles with a spherical shape (Fig. 5.2-1c); (3) thin films made from the previous spherical particles (Fig. 5.2-1b).

5.2.1.2 - Deposits on montmorillonite particles

TEM micrographs of the Fe compounds which were deposited on the montmorillonite particles, in the sediments made with unaged $FeCl_3$, are shown in Fig. 5.2-3. EDX analysis of selected area of these montmorillonite particles are reported in Fig. 5.2-4. These deposits had the characteristics of thin films (Fig. 5.2-3a) or of rod-like precipitates (Fig. 5.2-3b).

5.2.2 - Deposits from the hydroxoferric particles

These deposits were observed in the case of montmorillonite. The TEM micrographs in Figs. 5.2-5 and 5.2-6 are from the montmorillonite sediments made at pH=2, and the hydroxoferric particles have the appearance of a "pepper" spray on the clay particles.

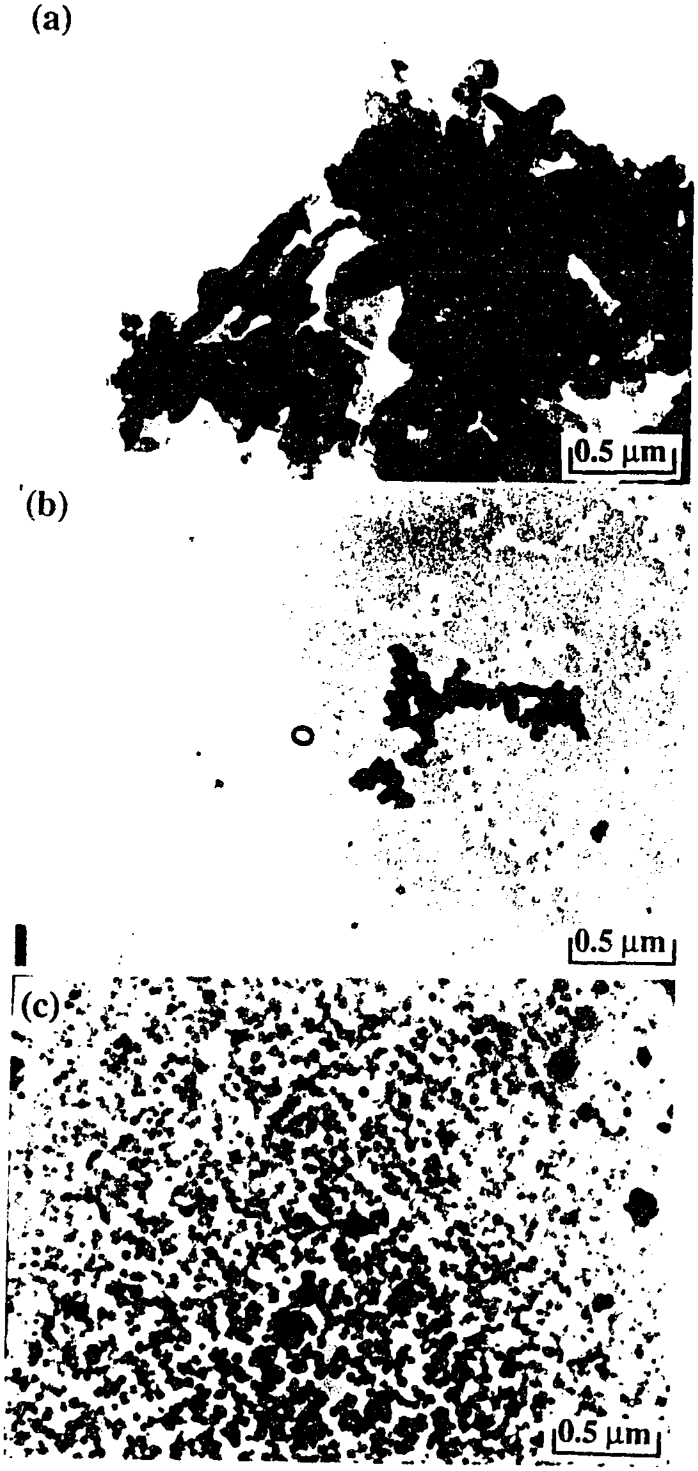

Fig. 5.2-1 - TEM micrographs of the Fe materials deposited on the kaolinite particles, in sediments made with 10mM $FeCl_3$ at pH 9.5: (a) rodlike and platelike particles; (b) thin film; (c) small spherical particles.

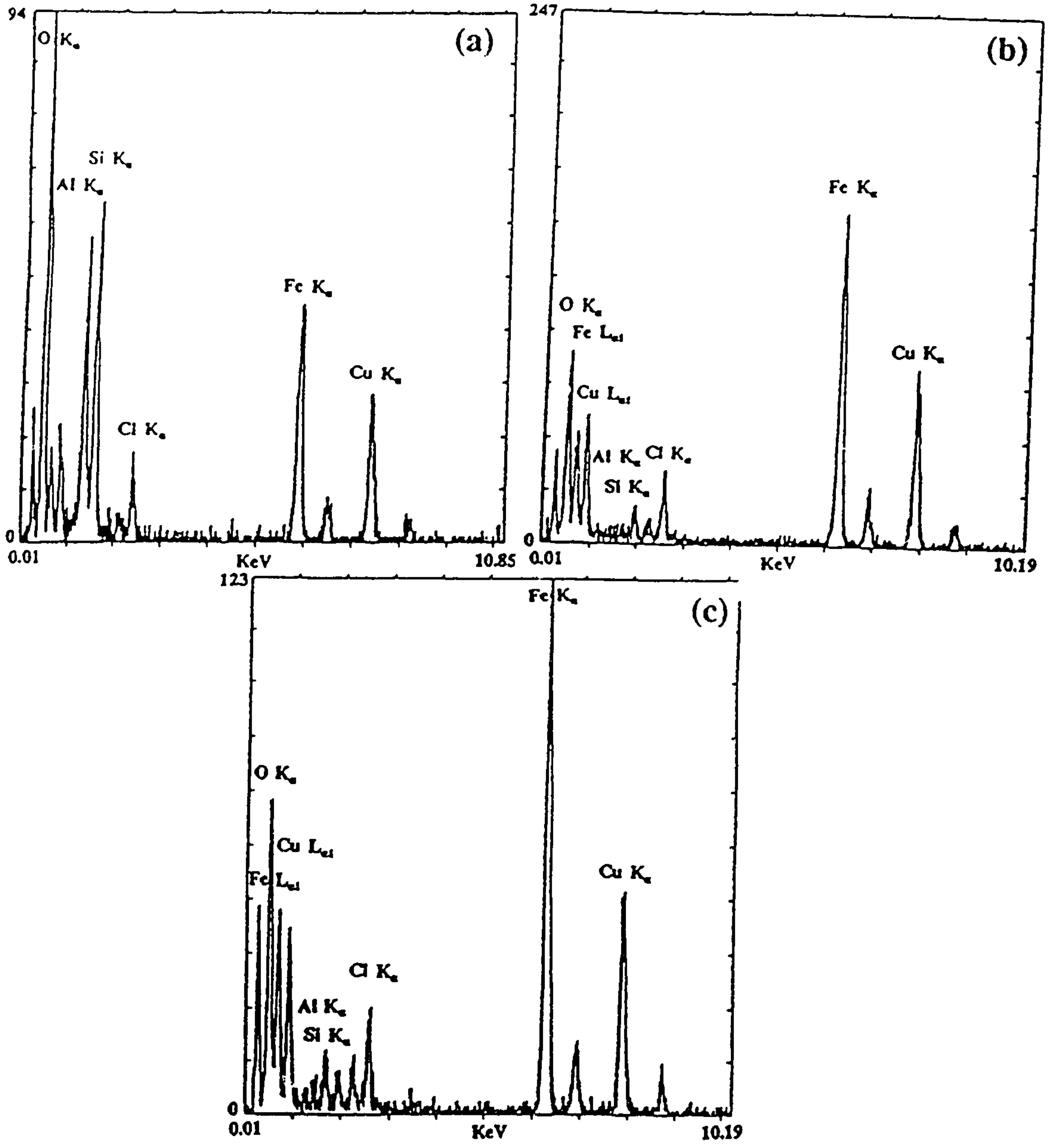

Fig. 5.2-2 - EDX spectrum of the surface of the kaolinite particles shown in Fig. 5.2-1: (a), (b), and (c) respectively correspond to each circle in the (a), (b), and (c) micrographs in Fig. 5.2-1.

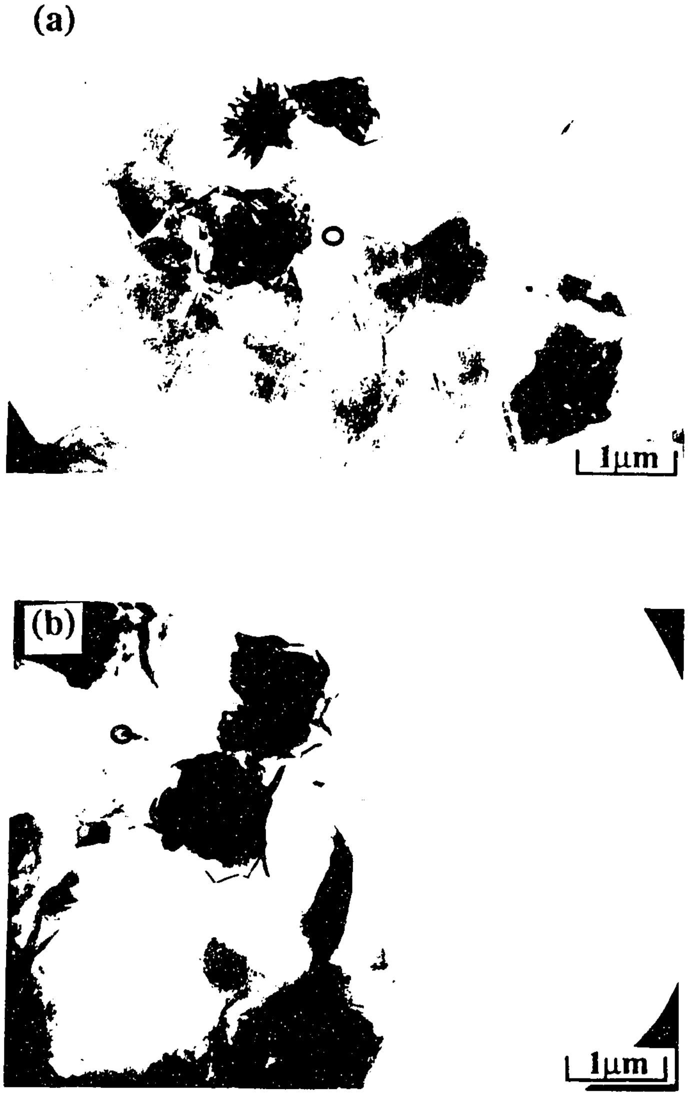

Fig. 5.2-3 - TEM micrographs of the Fe compound deposited on montmorillonite particles in sediments made with 10mM $FeCl_3$ at pH=9.5: (a) thin films; (b) rod-like particles.

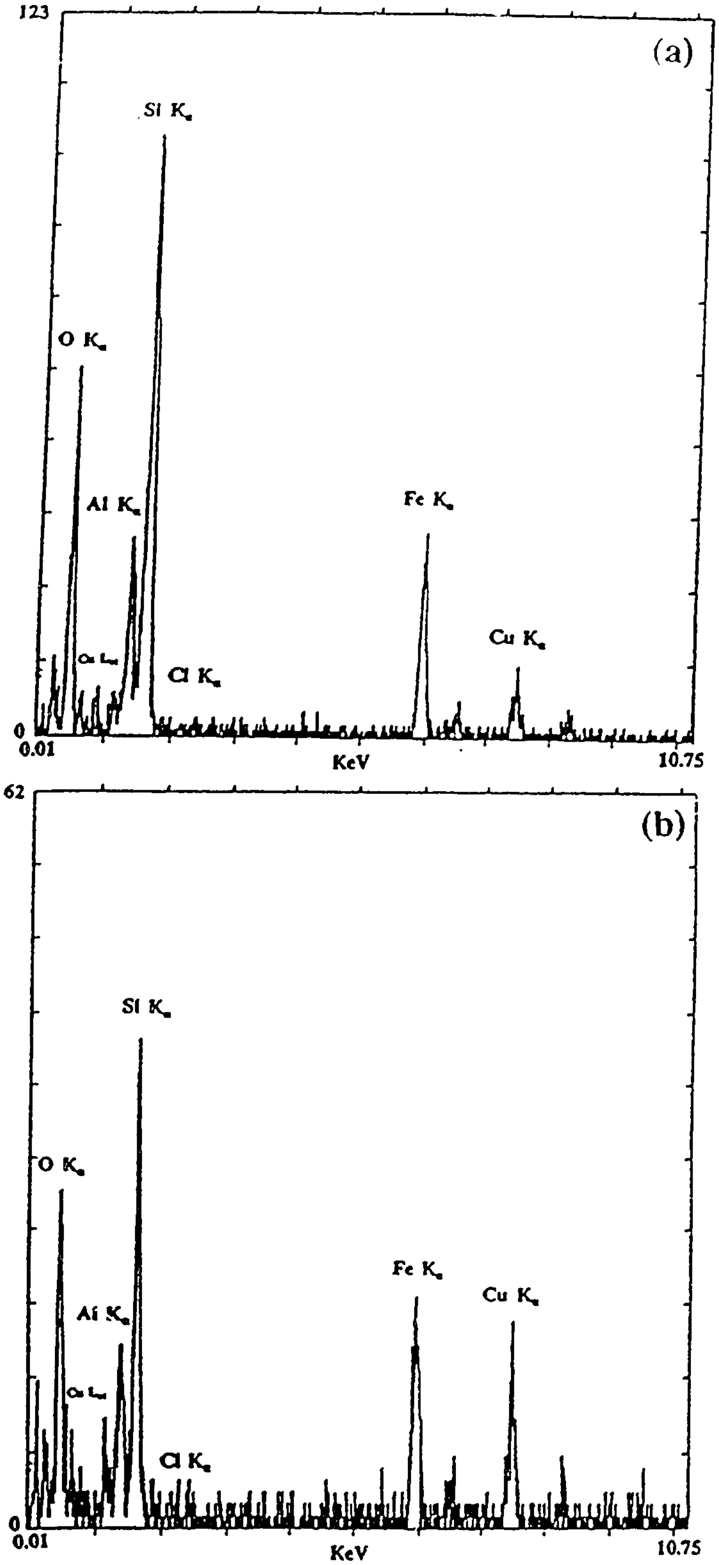

Fig. 5.2-4 - EDX spectrum of selected areas on the surface of the montmorillonite particles shown in Fig. 5.2-3: (a) and (b) respectively correspond to the circled areas in the (a) and (b) micrographs in Fig. 5.2-3.

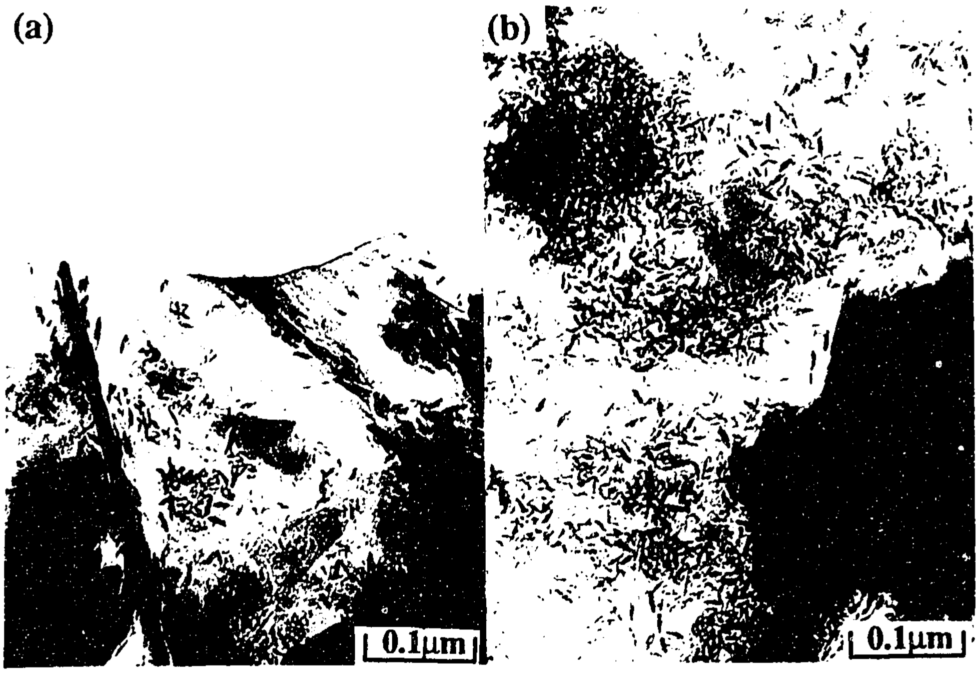

Fig. 5.2-5 - TEM micrographs of the hydroxoferric particles deposited on montmorillonite particles, in a sediment made from a 1% Na-montmorillonite suspension mixed with 0.125% (by mass) of hydroxoferric particles, at pH=2: (a) near the edge of a montmorillonite particle; (b) far from the edges of a montmorillonte particle.

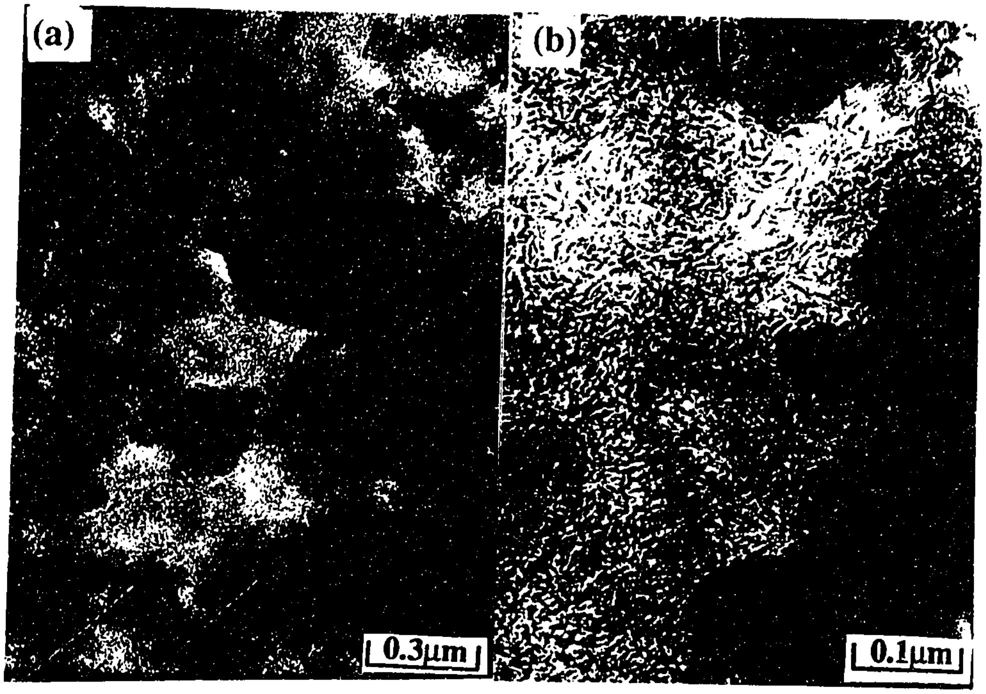

Fig. 5.2-6 - TEM micrographs of the hydroxoferric particles deposited on montmorillonite particles, in a sediment made from a 1% Na-montmorillonite suspension mixed with 0.5% (by mass) of hydroxoferric particles, at pH=2 and at 2 different scales.

When the hydroxoferric particles content was 0.125% (by mass), these particles gathered in loose clusters on the faces of the montmorillonite particles (Fig. 5.2-5a), while they were rather scarce near the edges of the montmorillonite plates (Fig. 5.2-5b). However, when the hydroxoferric particle content was 0.5% (by mass), the hydroxoferric pepper was more uniformly distributed on the faces the montmorillonite plates (Fig. 5.2-6). These observations were consistent with an electrostatic attraction between the negative charges on the faces of the montmorillonite particles and the positive charges on the hydroxoferric particles.

When the pH value of the montmorillonite suspension was 6 and the hydroxoferric solid content was 0.125% (by mass), the hydroxoferric particle clusters on the faces of the montmorillonite particles were less uniformy dispersed than at pH 2 (Fig. 5.2-7). It seemed that the hydroxoferric particles had first built some clusters, before being deposited on the faces of the clay particles. This was consistent with the fact that the z.p.c of the hydroxoferric particles has values between pH 7 and 9, depending on the exact mineral form [121].

The hydroxoferric particles deposited on the faces of montmorillonite particles at pH 9.5 are reported in Fig. 5.2-8 and 5.2-9, respectively for the hydroxoferric contents of 0.125% and of 0.5% (by mass). Even with a hydroxoferric content of 0.125 %, some hydroxoferric clusters could be observed near the edges, as well as anywhere on the faces, of the montmorillonite particles. A pH value of 9.5 was very close to the z.p.c of the hydroxoferric particles. Hence these particles could make dense clusters which were deposited at random on the montmorillonite plates.

At pH = 12, both the hydroxoferric particles and the montmorillonite particles were supposed to be negatively charged. However, the hydroxoferric particles were densely flocculated and very few hydroxoferric particles were separately deposited on the montmorillonite particles (Fig. 5.2-10). Considering that the hydroxoferric flocs had a tendency to remain for a longer time in the suspension, as shown by a more brown color of the final upper half sediment, it appears that the montmorillonite flocs and of the hydroxoferric flocs settled independently and concurrently.

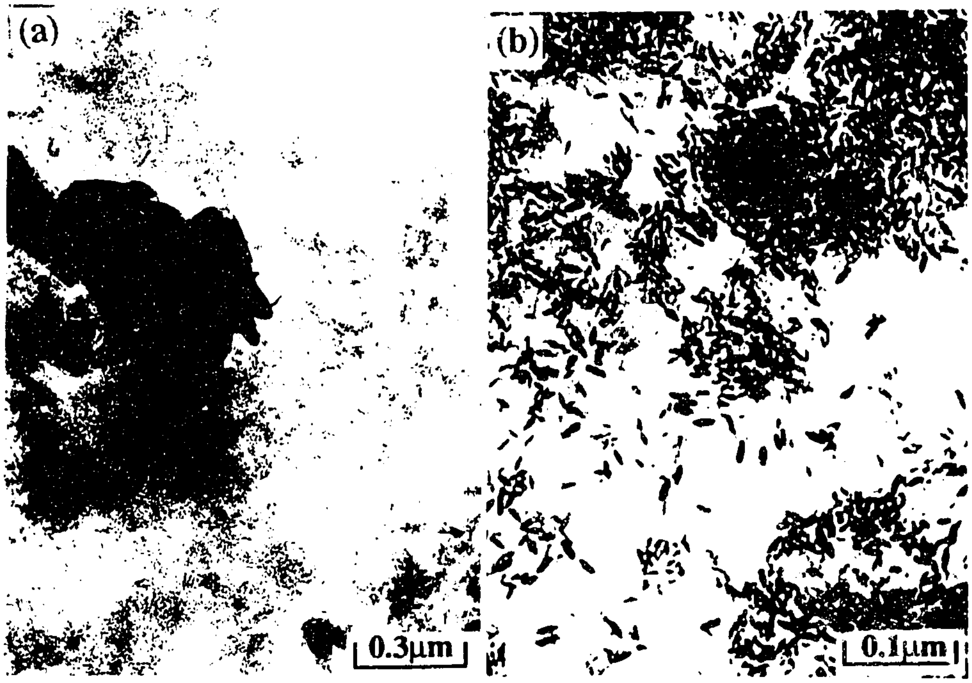

Fig. 5.2-7 - TEM micrographs of the hydroxoferric particles deposited on the faces of montmorillonite particles, in a sediment made from a 1% (by mass) Na-montmorillonite suspension mixed with 0.125% (by mass) of hydroxoferric particles, at pH=6 and at 2 different scales.

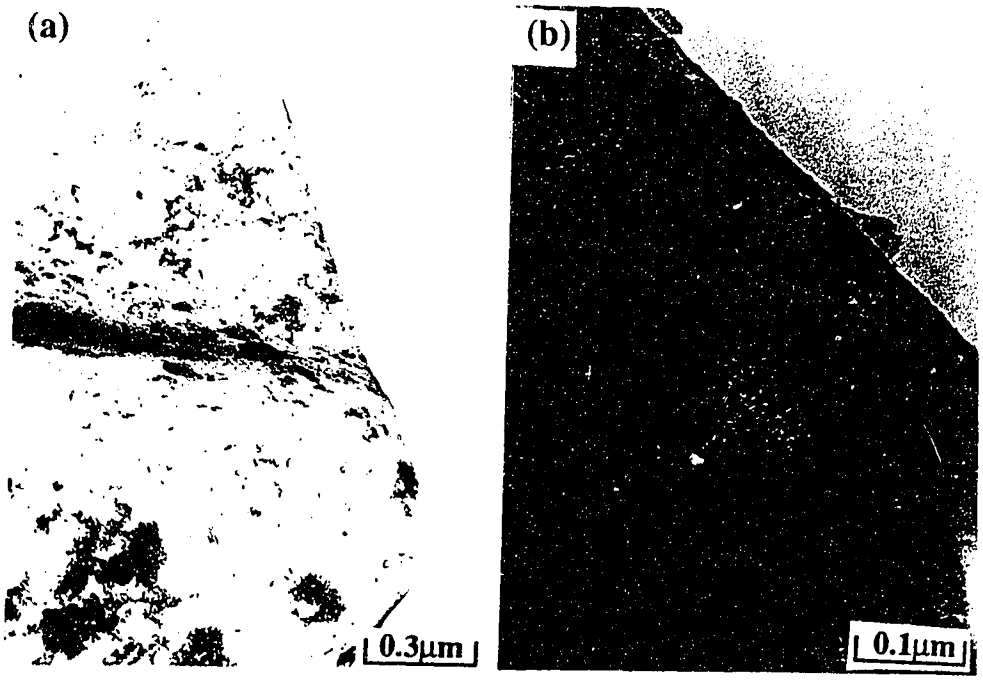

Fig. 5.2-8 - TEM micrographs of the hydroxoferric particles deposited on montmorillonite particles, in a sediment made from a 1% Na-montmorillonite suspension, mixed with 0.125% by mass of hydroxoferric particles, at pH=9.5 and at 2 different scales.

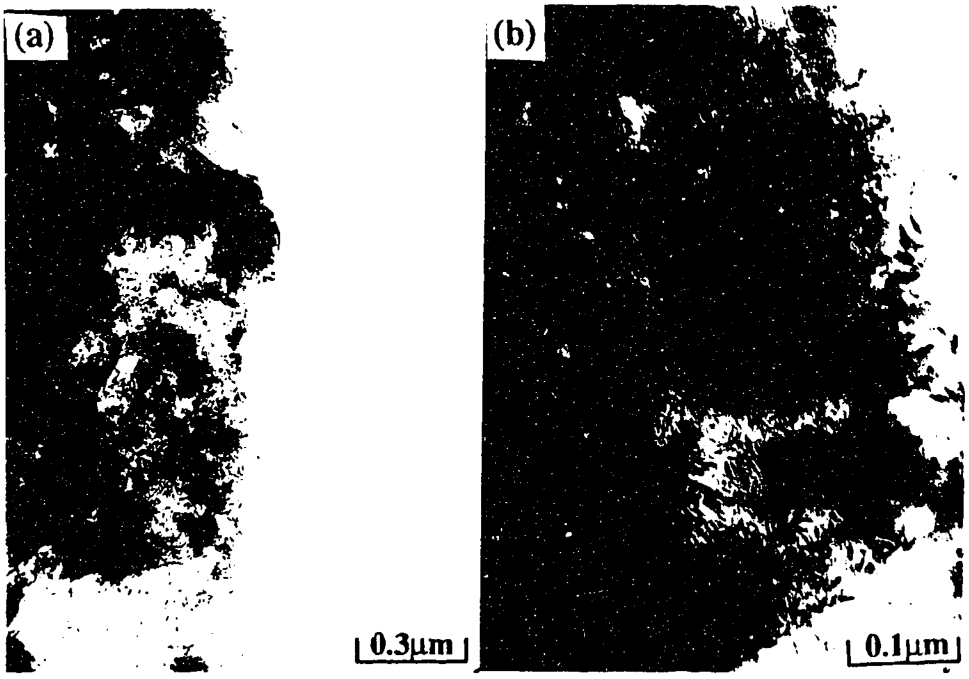

Fig. 5.2-9 - TEM micrographs of the hydroxoferric particles deposited on montmorillonite particles, in a sediment made from a 1% Na-montmorillonite suspension mixed with 0.5% (by mass) of hydroxoferric particles, at pH=9.5 and at 2 different scales.

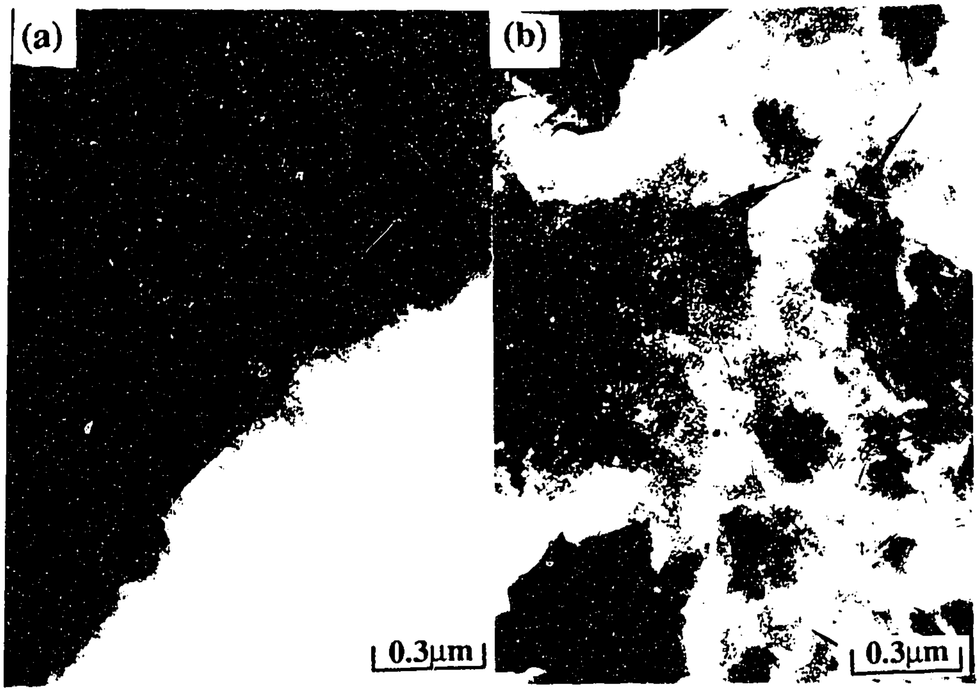

Fig. 5.2-10 - TEM micrographs of the hydroxoferric particles clusters settled with the montmorillonite particles, in a sediment made from a 1% Na-montmorillonite suspension, mixed with 0.5% (by mass) of hydroxoferric particles, at pH=12.

5.3 - RHEOLOGICAL PROPERTIES

5.3.1 - Kaolinite particles with initial negative charges on their faces and positive charges on their edges, mixed with unaged $FeCl_3$

Some HUF kaolinite was treated by the method of Schofield and Samson [59], as indicated in Section 3.2.1.2, and a series of 10% (by mass) suspension samples were prepared, at the pH indicated in Section 3.4.1. An unaged $FeCl_3$ concentration of 0.67 mM was mixed in some suspension samples. The Bingham yield stresses of these suspensions were measured, as a function of the pH, and the data are reported in the Fig. 5.3-1. In some other samples, no Fe compound was added and the Bingham yield stresses, as a function of the pH, are reported in the same figure.

Up to pH=6, the suspensions without any Fe additive had a higher Bingham yield stress than the suspensions including some unaged $FeCl_3$. Also, the latter suspensions had a constant Bingham yield stress up to pH=6. The Bingham yield stress of both types of suspensions decreased with the pH, above pH=6.

5.3.2 - Montmorillonite suspensions mixed with hydroxoferric Particles

Flow curves, which relate the shear rate to the shear stress, were recorded at increasing shear rates, then at decreasing shear rates. The type of flow curves which were obtained as illustrated in Fig. 5.3-2a. Such flow curves are consistent with the Bingham model which was introduced in Section 2.2.5. However, such flow curves also show that some hysteresis was observed. Consequently, the Bingham yield stress was determined for an increasing shear rate, as shown in Fig. 5.3-2b, and in agreement with equation (2.1-35).

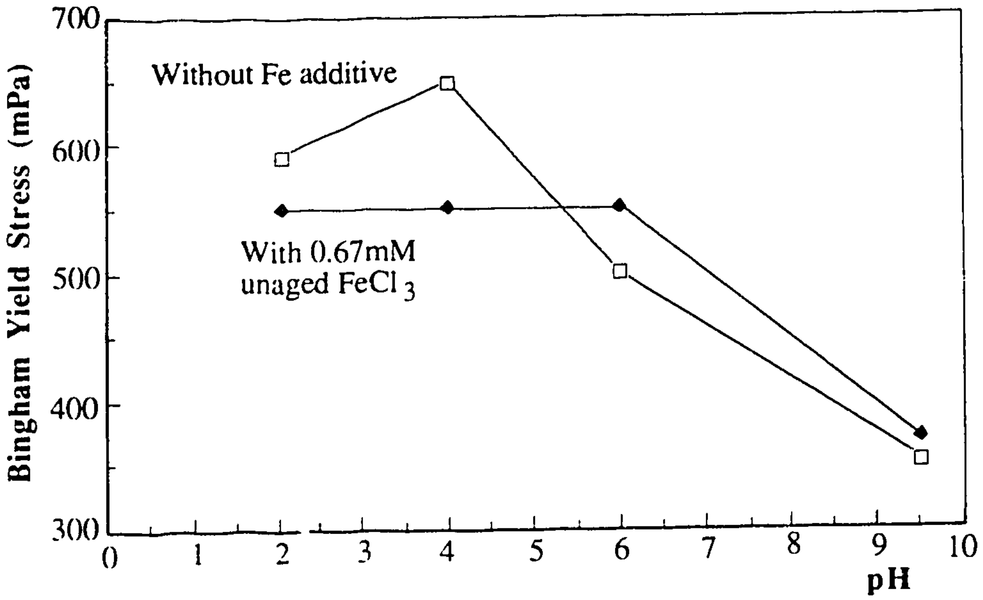

Fig. 5.3-1 - Bingham yield stress of 10% (by mass) kaolinite suspensions with initial negative charges on the particles faces and positive charges on their edges, as a function of the pH.

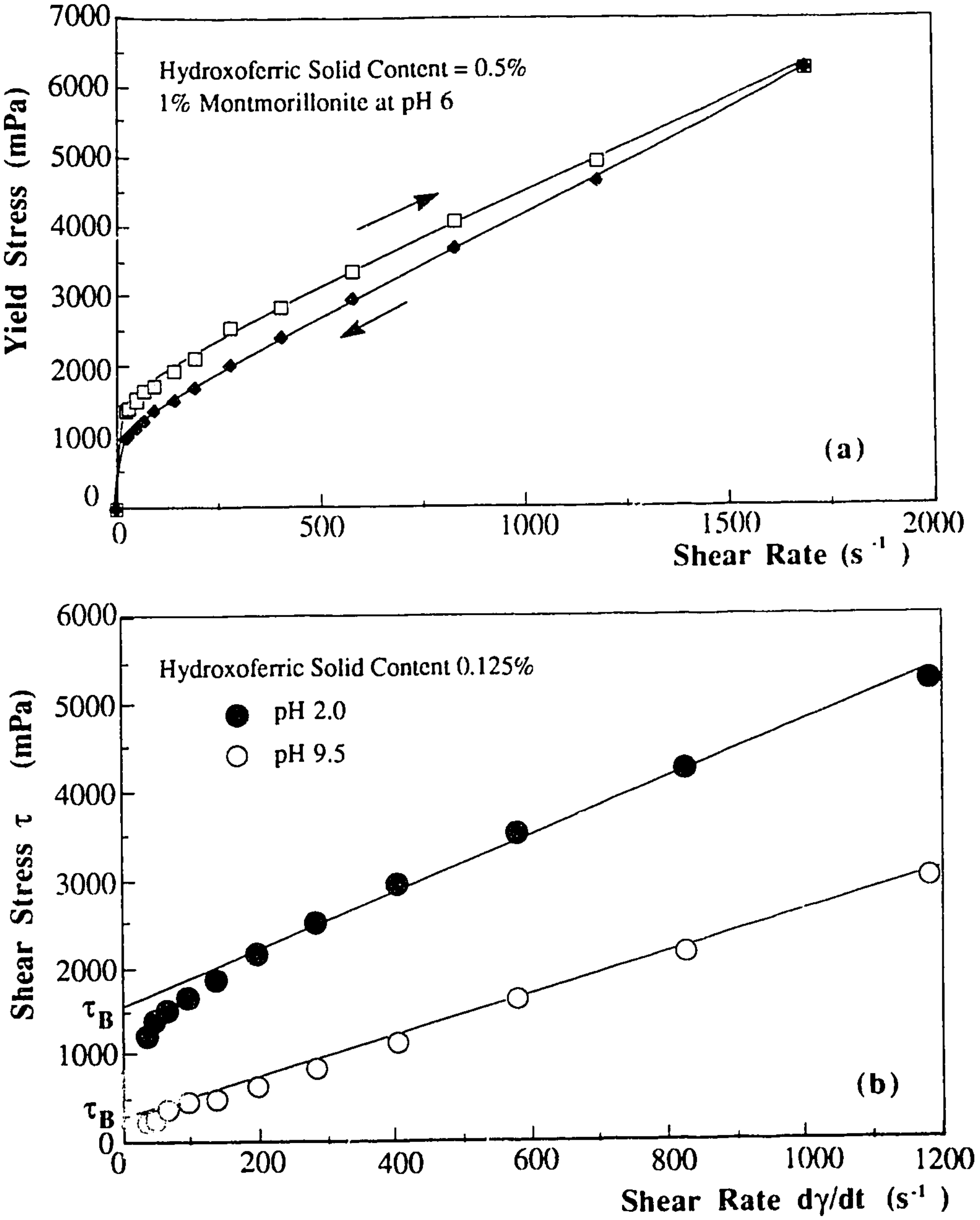

Fig. 5.3-2 - Typical flow data of data 1% (by mass) Na-montmorillonite suspensions mixed with hydroxoferric particles: (a) flow curve for a suspension comprised of 0.500% (by mass) of hydroxoferric particles; (b) Bingham yield stress τ_B for suspensions comprised of 0.125% (by mass) of hydroxoferric particles.

The data for the Bingham yield stress of montmorillonite suspensions mixed with hydroxoferric particles, as a function of the pH, are reported in Fig. 5.3-3. As the hydroxoferric particles content increased up to 0.5% (by mass), a stronger Bingham yield stress developed near pH=6, that is to say close to the z.p.c range for the various hydroxoferric mineral forms [121]. Hydroxoferric particles carried a negative charge at pH < 6 and at such pH they repulsed each other. Also, since the hydroxoferric particles content in the clay suspension was significantly high (0.5 % by mass) the interaction between hydroxoferric particles largely influenced the Bingham yield stress. Consequently, the Bingham yield stress decreased at low pH values (i.e. pH 4 and 2) when the solid content in hydroxoferric particles was high (0.5%) as shown in Fig.5.3-3.

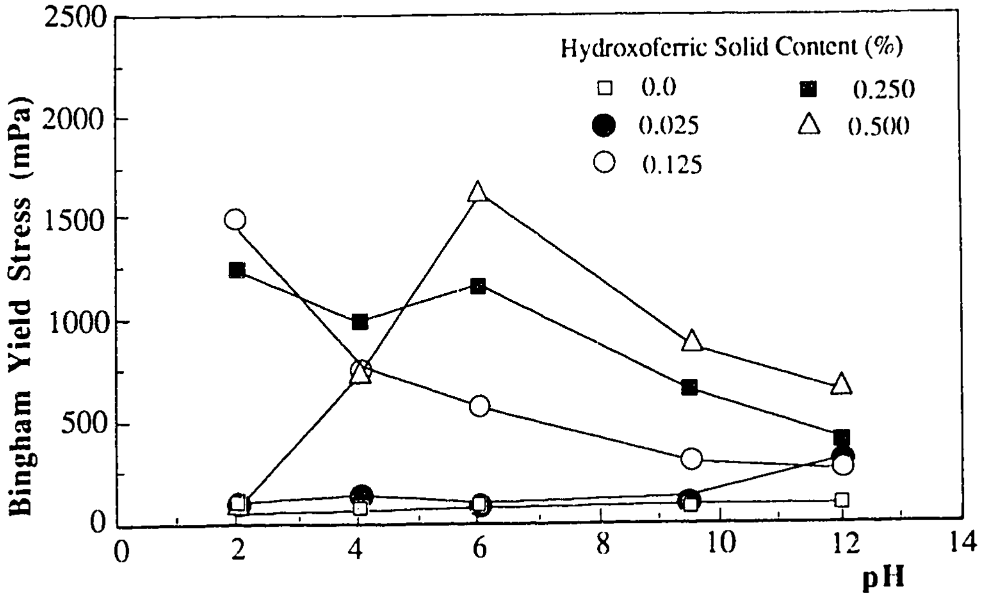

Fig. 5.3-3 - Bingham yield stress τ_B as a function of the pH, for 1% Na-montmorillonite suspensions mixed with different hydroxoferric particles proportions.

5.4 - DETERMINATION OF THE ZETA POTENTIAL (ζ)

5.4.1 - Kaolinite particles initially treated to have negative charges on the faces and positive charges on the edges.

The zeta potential of kaolinite particles initially treated by the method of Schofield and Samson [59], as indicated in Section 3.2.1.2, was measured. The data are reported in Fig. 5.4-1. In this figure, the zeta potential as a function of the pH is plotted for a kaolinite suspension mixed with 0.67 mM unaged $FeCl_3$, and for a kaolinite suspension without any Fe additive. The isoelectric point was at pH = 3.7 without any Fe additive, while it was about pH = 7.2 with 0.67 mM unaged $FeCl_3$.

5.4.2 - Kaolinite initially treated with $Na_4P_2O_7$ to only have negative charges

5.4.2.1- Kaolinite suspensions mixed with unaged $FeCl_3$

The dependence of the zeta potential on the pH, for several unaged $FeCl_3$ concentrations, is reported in Fig. 5.4-2a. This zeta potential increased from a negative to positive value as the concentration of aged $FeCl_3$ increased, in acidic conditions.

From these determined zeta potentials, it is possible to establish a diagram where the variables are the pH and the unaged $FeCl_3$ concentration. Then, this diagram can be divided in 3 fields. The first field corresponds to data points represented by white dots, where the zeta potential absolute value is $|\zeta| < 0.01$ V. A second field corresponds to data points, represented by black dots, where $|\zeta| > 0.015$ V. The third field, represented by mixed dots, corresponds to data points such that $0.01 \text{ V} \leq |\zeta| \leq 0.015$ V. This diagram is reported in Fig. 5.4-3b, and it is compared with the diagram from the experimental sedimentation behavior (Fig. 4.2-3a) which is reproduced in Fig. 5.4-3a.

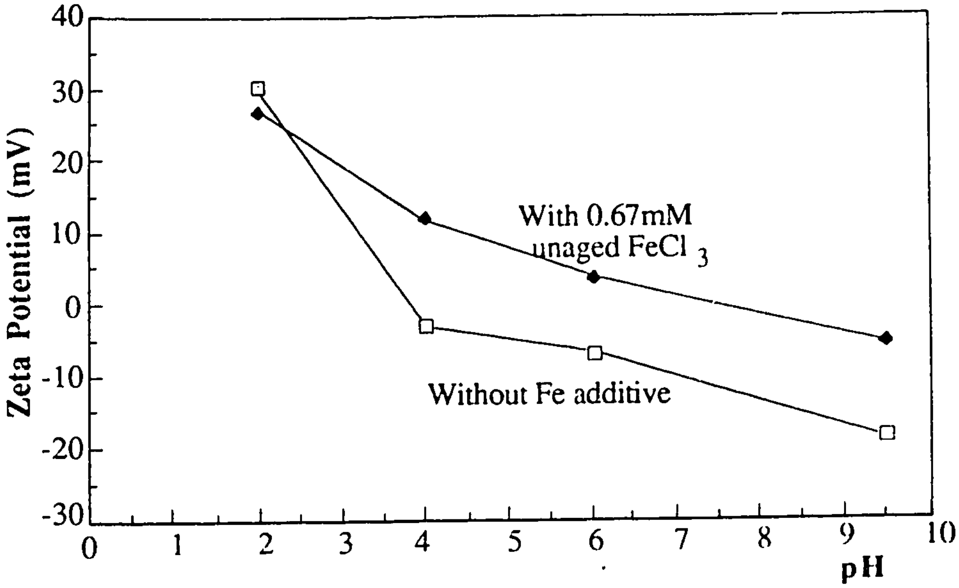

Fig. 5.4-1 - Zeta potential of kaolinite particles only treated by the method of Schofield and Samson [59] (no treatment with $Na_4P_2O_7$).

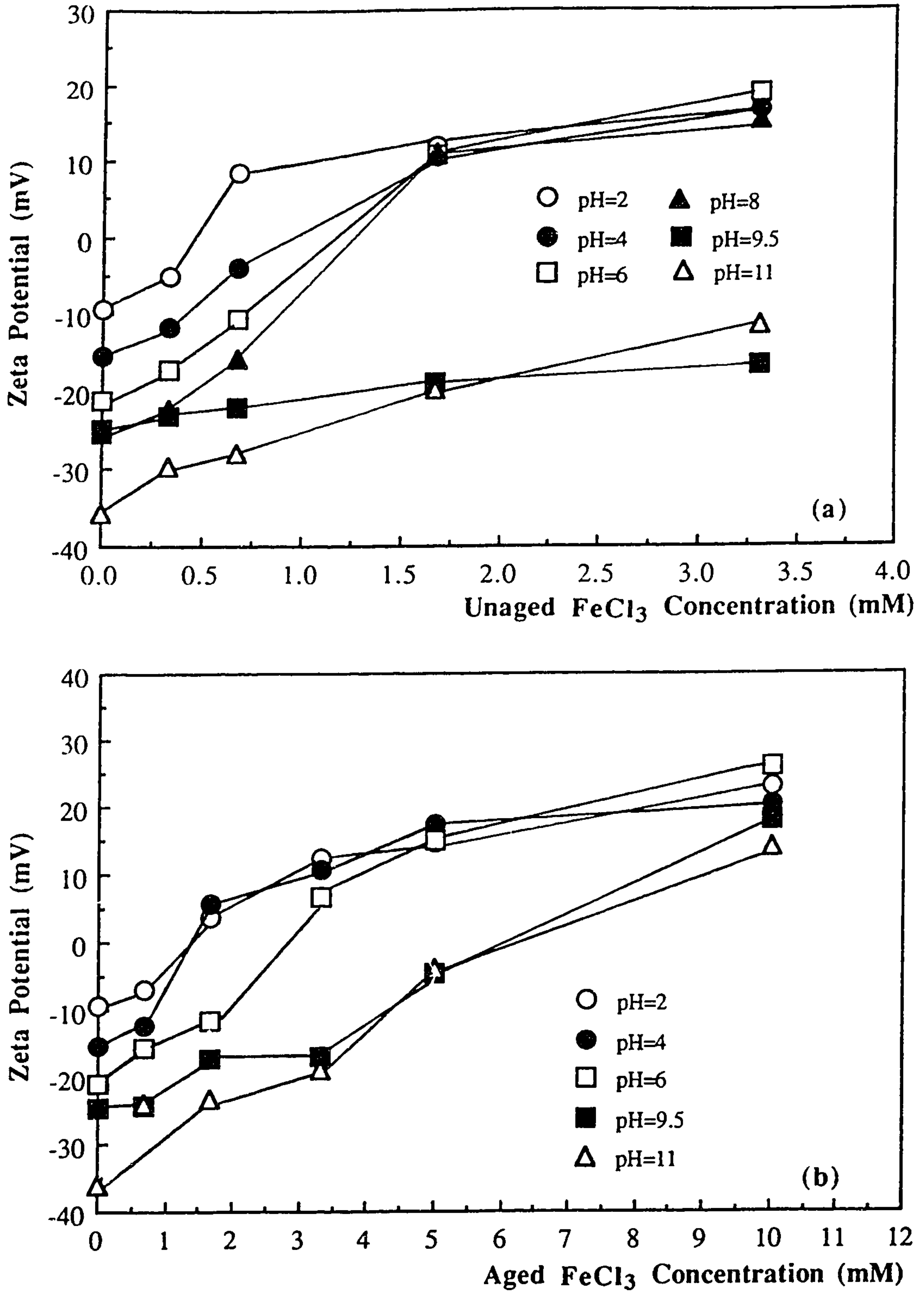

Fig. 5.4-2 - Variation of the zeta potential with the concentration of $FeCl_3$ at different pH values in 0.5% (by mass) kaolinite suspensions treated with $Na_4P_2O_7$: (a) unaged $FeCl_3$; (b) aged $FeCl_3$.

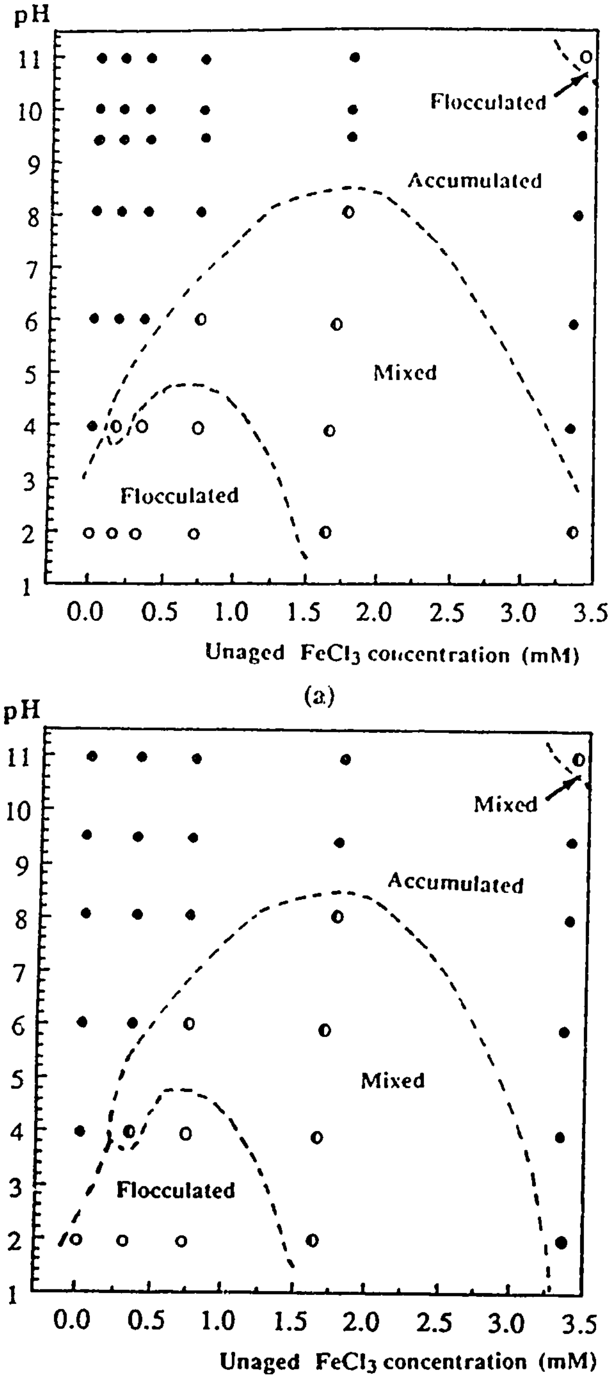

(a)

(b)

Fig. 5.4-3 - Diagram of the sedimentation behavior in 0.5% kaolinite suspensions treated with $Na_4P_2O_7$ and mixed with unaged $FeCl_3$: (a) observed results reproduced from Fig. 4.2-3a; (b) prediction from the measured zeta potential ζ. The solid dots are for $|\zeta| < 0.01$ V, the open dots for $|\zeta| > 0.015$ V, the semi-open dots for $0.0\ 1\ V \leq |\zeta| \leq 0.015$ V.

It clearly appears that the 2 diagrams are identical. Hence the sedimentation behavior can be predicted from the measured zeta potential. In practice, flocculation-sedimentation occurred when $|\zeta| < 10mV$, accumulation-sedimentation occurred when $|\zeta| > 0.015$ V, and mixed flocculation-accumulation sedimentation occurred when $0.01 V \leq |\zeta| \leq 0.015$ V.

5.4.2.2- Kaolinite suspensions mixed with aged $FeCl_3$

The zeta potentials of kaolinite particles mixed with different concentrations of aged $FeCl_3$ and at different pH's, are reported in Fig. 5.4-2b. The zeta potentials increased from negative to positive values as the concentration of aged $FeCl_3$ increased, at all pH values. The zeta potential data were also used to build a diagram to predict the sedimentation behavior of clay suspensions. This diagram is reported in Fig. 5.4-4b and it is compared with the diagram from the experimental sedimentation behavior (Fig. 5.4-4a). The predictions from the zeta potentials are in rough agreement with the experimental observations. However, the agreement between these two diagrams is not as good as for the kaolinite suspensions mixed with unaged $FeCl_3$, as shown in Fig. 5.4-3.

5.4.2.3 - Kaolinite suspensions mixed with unaged $AlCl_3$

The data on the zeta potential of kaolinite particles mixed with unaged $AlCl_3$ are reported in Fig. 5.4-5. At, or below pH 9.5, the addition of unaged $AlCl_3$ at a concentration from 1 mM to 9 mM, increased the zeta potential from a negative to a slightly positive value, independent of the pH and of the $AlCl_3$ concentration.

5.4.3 - Montmorillonite

5.4.3.1 - Montmorillonite suspensions mixed with hydroxoferric particles

The zeta potential of montmorillonite particles in suspensions mixed with different hydroxoferric particles content, at different pH, is reported in Fig. 5.4-6. Generally, the zeta potential was negative. Its absolute value decreased with the pH and with the

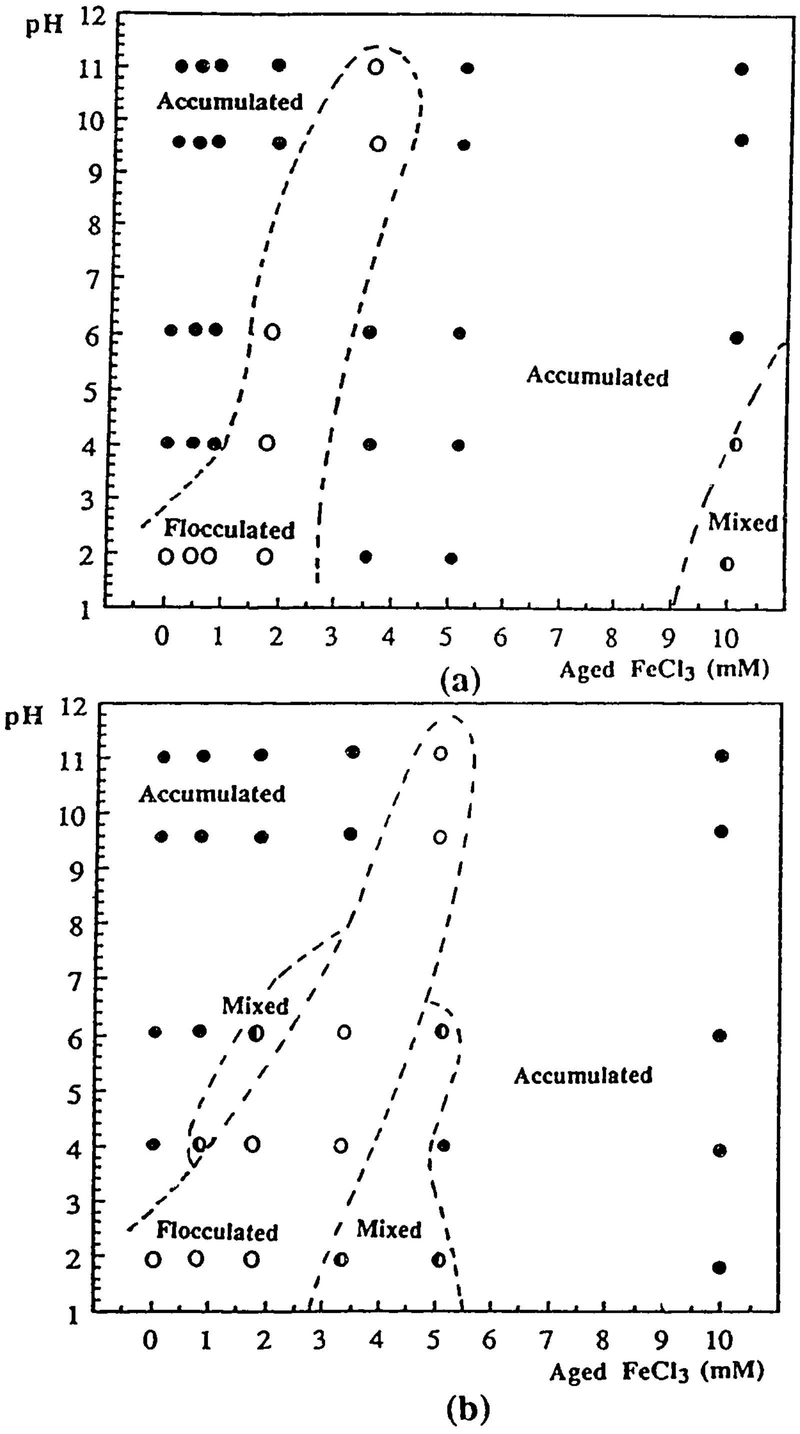

Fig. 5.4-4 - Diagram of the sedimentation behavior in 0.5% kaolinite suspensions treated with $Na_4P_2O_7$ and mixed with aged $FeCl_3$: (a) observed results reproduced from Fig. 4.2-8; (b) prediction from the measured zeta potential ζ. The open dots are for $|\zeta| < 0.01$ V, the solid dots for $|\zeta| > 0.0\ 15$ V, the semi-open dots for $0.0\ 1\ V \leq |\zeta| \leq 0.015V$.

hydroxoferric particles content in the suspension. The sign of this zeta potential was reversed and it became slightly positive for hydroxoferric particle contents of 0.25 % and 0.5% (by mass), respectively at pH = 2 and pH = 6. The data at pH = 2 and 4, with a hydroxoferric solid content of 0.5 % (by mass) could not be obtained, because flocculation of the montmorillonite suspensions occurred rapidly after addition of the hydroxoferric particles. These results indicate that the electrokinetic behavior of the montmorillonite was controlled by the hydroxoferric particles adsorbed on the faces of the montmorillonite particles.

A strong correlation between the value of the zeta potential and the Bingham yield stress could be observed, in the montmorillonite suspensions mixed with hydroxoferric particles. This correlation is obvious from the data as they are plotted in Fig. 5.4-7. The Bingham yield stress increased, as the absolute value of the zeta potential decreased.

A possible explanation is that the absolute value of the zeta potential of montmorillonite particles is likely to approach zero when the edges and faces start to carry opposite charges, instead of carrying charges of the same sign. And, as indicated by van Olphen [11], in these conditions montmorillonite particles should connect in an edge to face mode, so as to build a card-house structure. Hence, the maximum Bingham yield stress can be related to the minimum absolute value of the zeta potential of montmorillonite particles.

5.4.3.2 - Montmorillonite suspensions mixed with unaged $AlCl_3$

The zeta potential of montmorillonite particles in suspensions mixed with unaged $AlCl_3$, as a function of the $AlCl_3$ concentration and at several pH, is reported in Fig. 5.4-8. This zeta potential roughly decreased (negative), then increased (positive) with unaged $AlCl_3$ concentration.

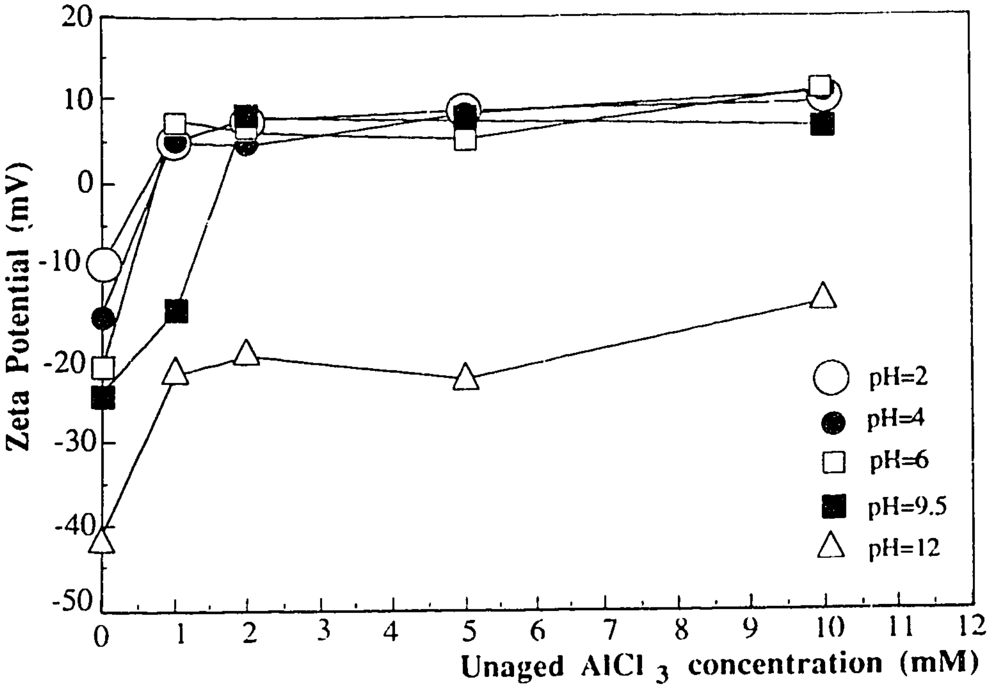

Fig. 5.4-5 - Variation of the zeta potential with the concentration of unaged $AlCl_3$ at different pH values in 0.5% (by mass) kaolinite suspensions treated with $Na_4P_2O_7$.

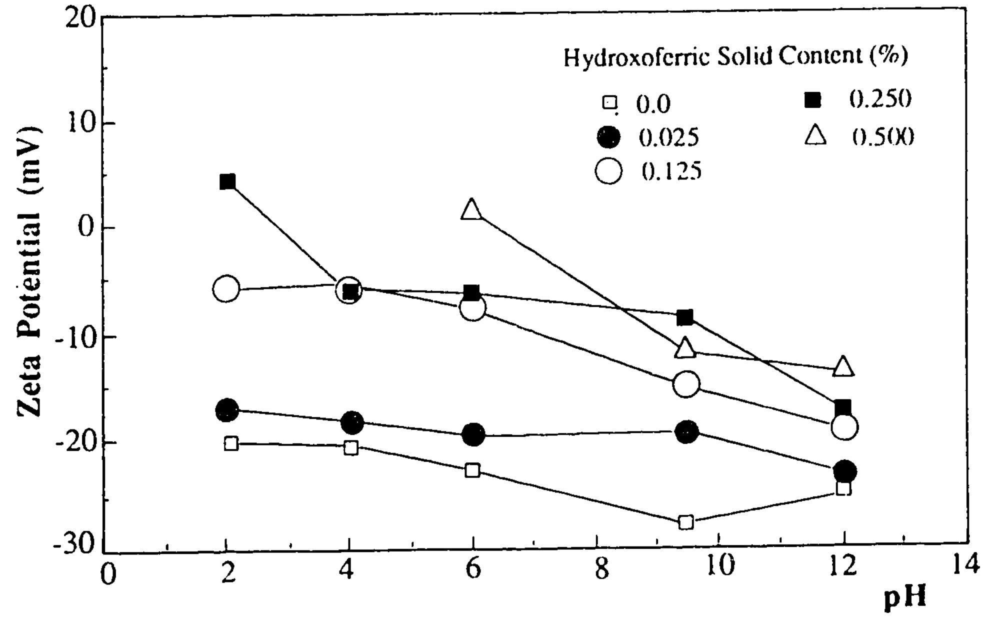

Fig. 5.4-6 - Zeta potential of montmorillonite particles from mixed montmorillonite hydroxoferric suspensions, as a function of the pH.

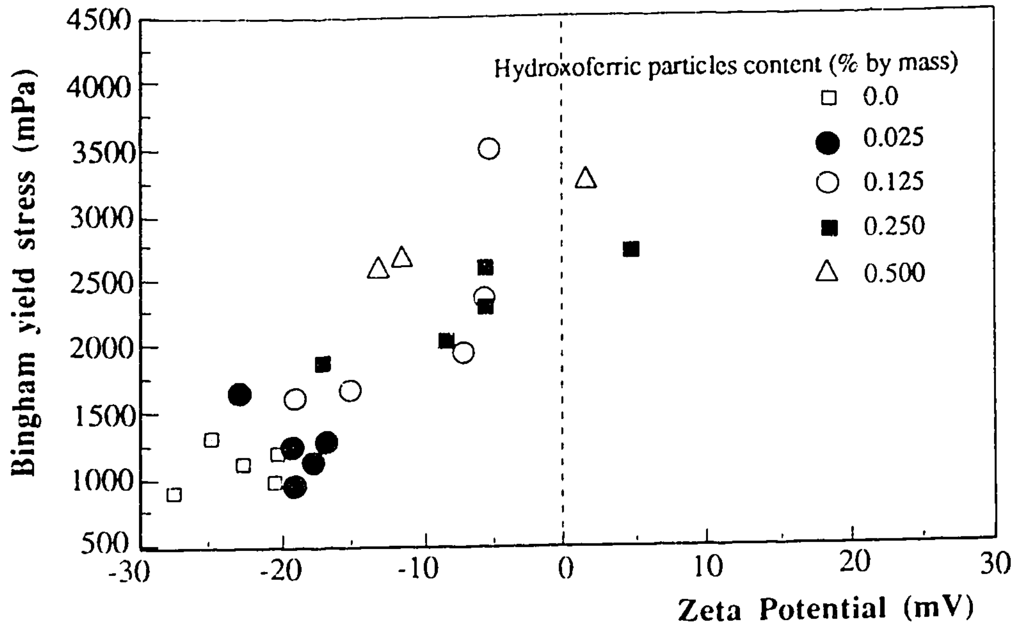

Fig. 5.4-7 - Relationship between the zeta potential and the Bingham yield stress in mixed montmorillonite-hydroxoferric particles suspensions.

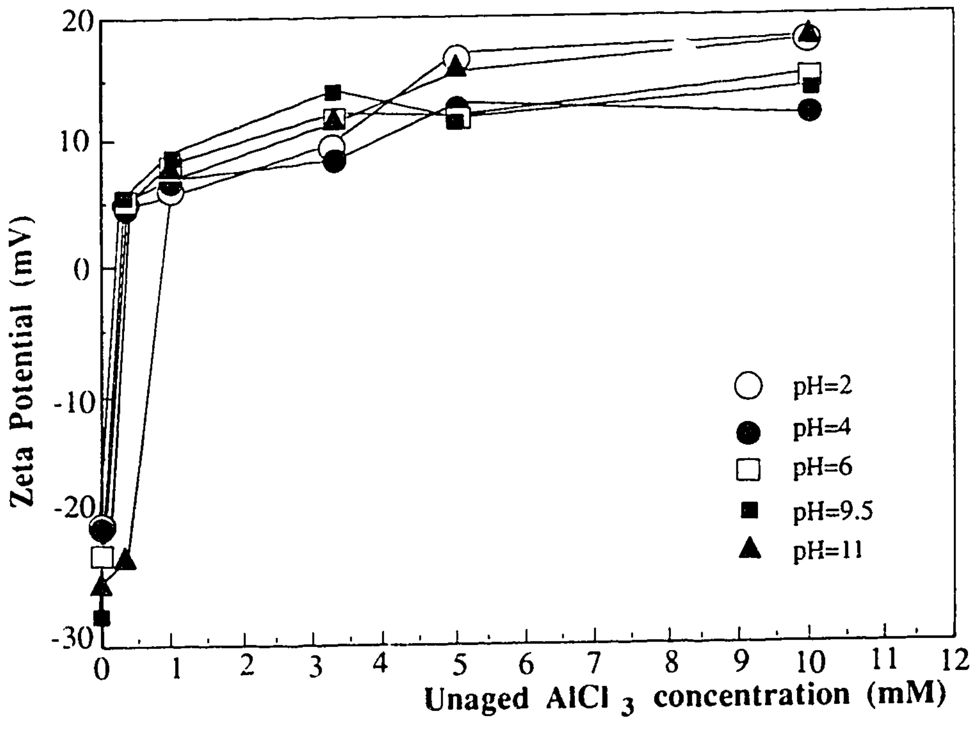

Fig. 5.4-8 - Dependence of the zeta potential of montmorillonite particles on the concentration of unaged $AlCl_3$ in the suspension, at different pH.

5.5 - SEM OBSERVATIONS OF KAOLINITE PARTICLES MIXED WITH COLLOIDAL SiO_2 PARTICLES

These observations were undertaken in an attempt to discriminate between the sign of the electric charges on the edges and on the faces of kaolinite particles. Hence, they must be considered as a complement to the zeta potential determination in Section 5.4.

5.5.1 - Kaolinite with negatively charged faces and positively charged edges.

Some kaolinite was treated by the method of Schofield and Samson [59], as indicated in Section 3.2.1.2, to have opposite charges on the faces and the edges of the platelike particles. Such kaolinite particles were mixed with some colloidal SiO_2 particles prepared by the method of Stöber et al. [119], as indicated in Section 3.2.5. The three different sizes of SiO_2 particles mentioned in Section 3.2.5 were used. SEM micrographs of the mixed kaolinite-SiO_2 system, which were obtained at pH =2 and pH = 4, are reported in Figs. 5.5-1 and 5.5-2, respectively. At pH =2, almost all the SiO_2 particles were located on the faces of the kaolinite particles (Fig. 5.5-1). On the other ghand, at pH=4, some SiO_2 particles were in contact with the edges of the kaolinite particles (Fig. 5.5-2). As summarized in Section 2.3.2, the faces of kaolinite particles were supposed to be negatively charged at all pH [27]. On the other hand, the edges of kaolinite particles have a z.p.c. between pH ≈ 6.5 [56] and pH = 7.5 [53]. The z.p.c of SiO_2 is known to be at pH ≈ 2.5. Hence, at pH = 2, the SiO_2 particles were positively charged and they were expected to be attracted by the negatively charged faces of the kaolinite particles, which is in agreement with the observations.

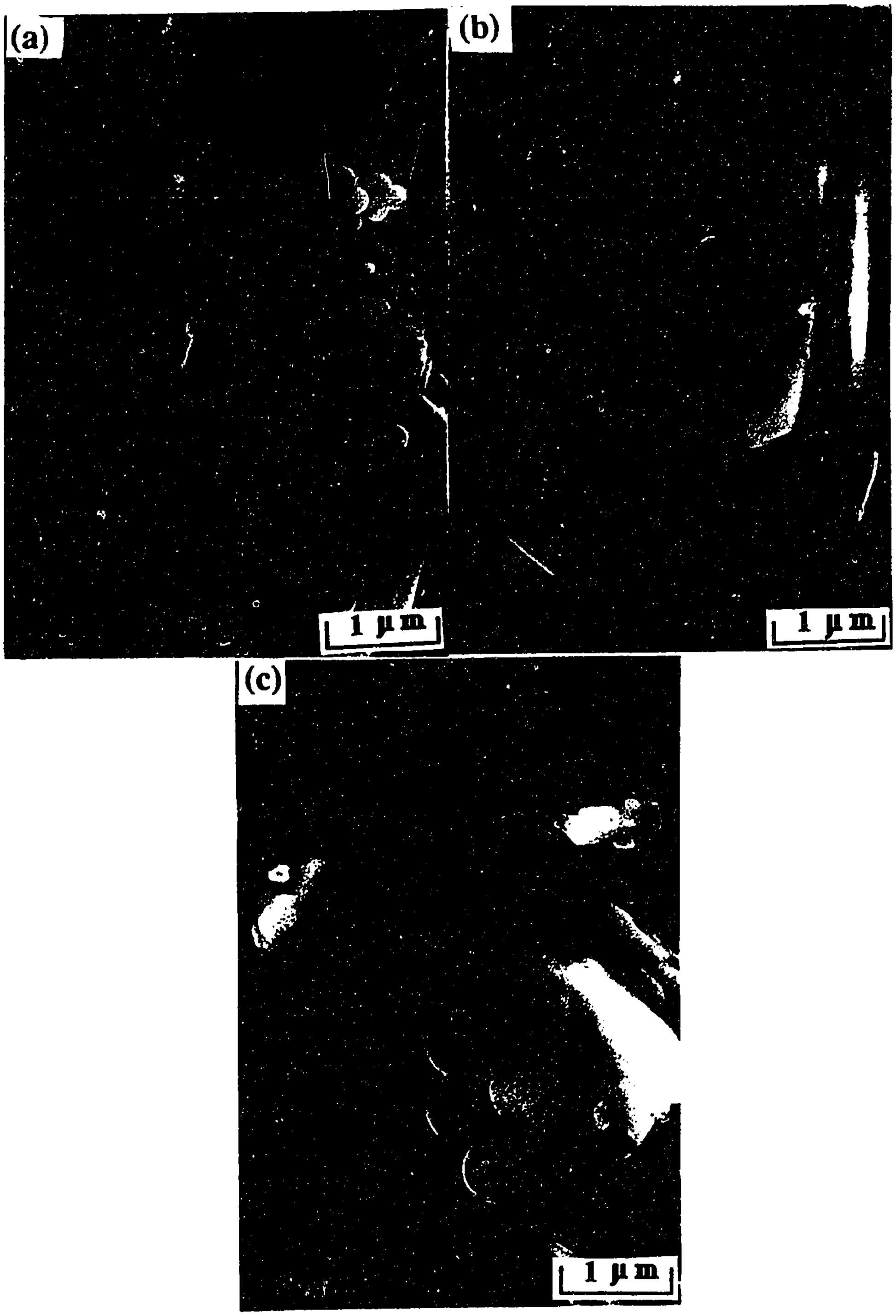

Fig. 5.5-1 - SEM micrographs of kaolinite particles treated by the method of Schofield and Samson [59], and mixed with SiO_2 particles at pH=2. SiO_2 particles size: (a) 0.2μm; (b) 0.35μm; (c) 0.65μm.

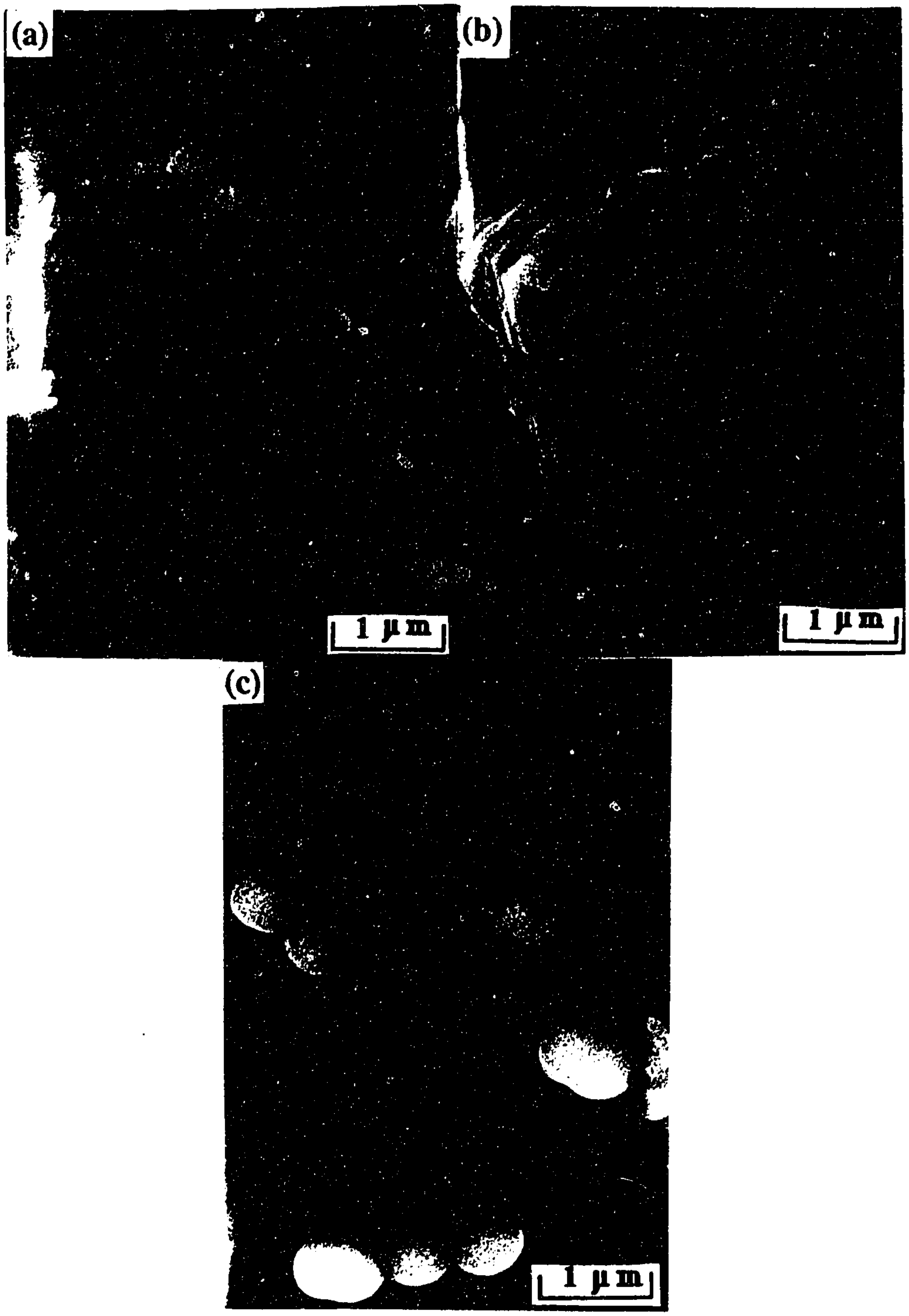

Fig. 5.5-2 - SEM micrographs of kaolinite particles treated by the method of Schofield and Samson [59], and mixed with SiO_2 particles at pH=4. SiO_2 particles size: (a) 0.2μm; (b) 0.35μm; (c) 0.65μm.

On the other hand, at pH = 4, the SiO_2 particles were negatively charged. Hence they were repulsed by the faces and attracted by the edges of the kaolinite particles. The present results were in satisfactory agreement with the expectations.

5.5.2 - Kaolinite with negative charges on both the edges and the faces

Some kaolinite samples were only treated by the method of Schofield and Samson [59], while some other samples were also treated with $Na_4P_2O_7$. Both types of samples were mixed with colloidal SiO_2 particles at pH = 10, and they were observed in a SEM. As the micrographs in Fig. 5.5-3 show, the SiO_2 particles did not really adsorb either on the faces nor on the edges of the kaolinite particles. This was consistent with a repulsion between the SiO_2 particles and the faces as well as the edges of the kaolinite particles, since all the particles only carried negative electric charges at this pH.

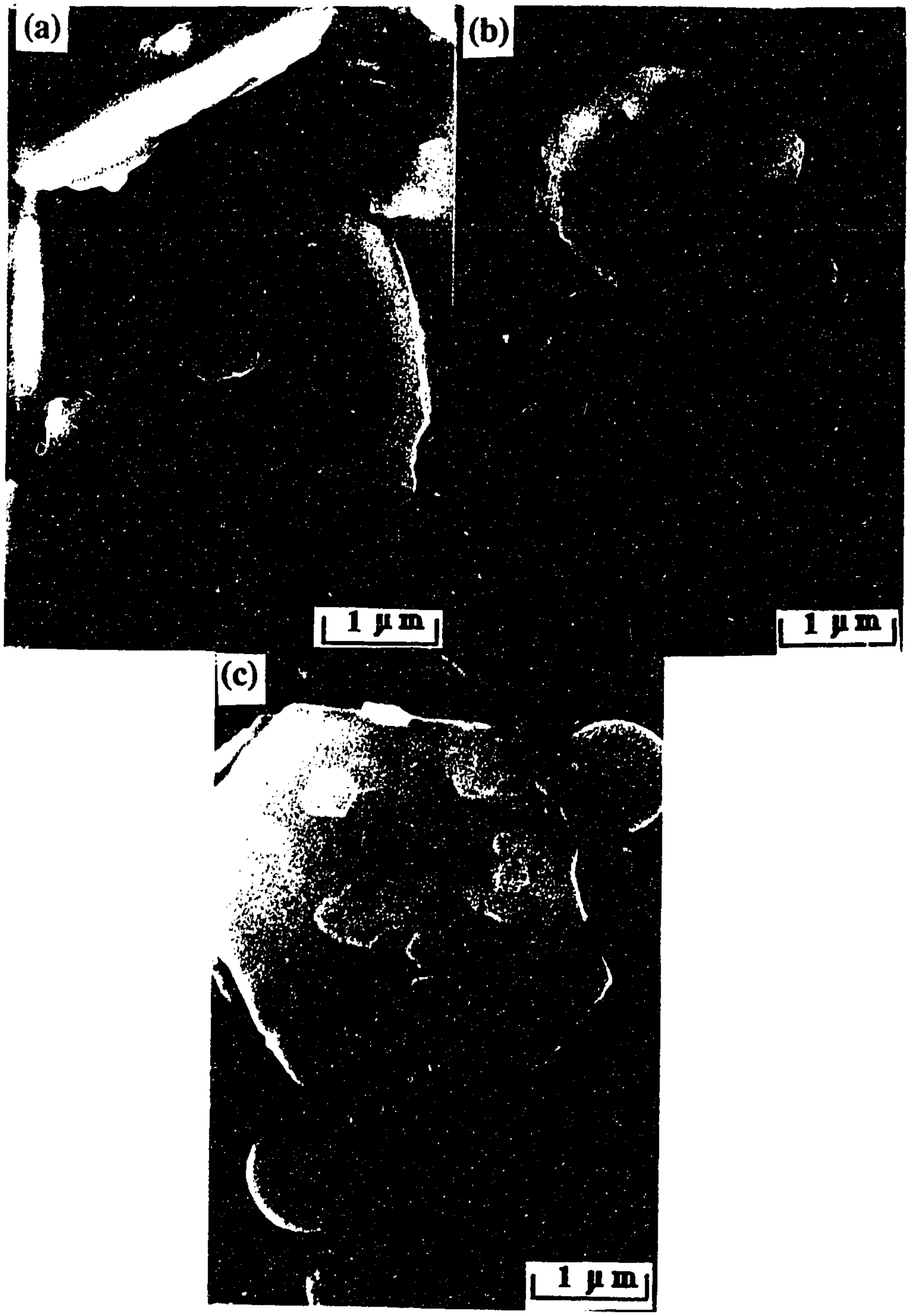

Fig. 5.5-3 - SEM micrographs of kaolinite particles mixed with SiO_2 particles at pH=10. In (a) and (b) the kaolinite was first treated by the method of Schofield and Samson [59], while in (c) it was treated with $Na_4P_2O_7$. The SiO_2 particles size was: (a) 0.2μm; (b) 0.35μm; (c) 0.65μm.

CHAPTER 6 - SEM OBSERVATIONS OF SEDIMENTS DRIED BY THE SUPERCRITICAL METHOD

The detailed research plan of this thesis, concerning SEM observations, was presented in Chapter 3. The present chapter addresses the results on SEM observations of clay suspensions. The SEM experimental procedure was detailed in Section 3.3.4. The SEM microstructures illustrated in the present chapter concern the three following systems: (1) kaolinite sediments comprised of kaolinite particles treated to carry negative charges on their faces and positive charges on their edges; (2) kaolinite sediments comprised of kaolinite particles treated to carry negative charges on both their edges and their faces; (3) montmorillonite sediments. The detailed preparation procedure of the sediments was described in Chapter 3, and the sedimentation data in Chapter 4.

6.1 - KAOLINITE WITH NEGATIVELY CHARGED FACES AND POSITIVELY CHARGED EDGES

6.1.1 - Kaolinite mixed without unaged $FeCl_3$

SEM of sediments made from 0.5 % (by mass) kaolinite suspensions treated by the method of Schofield and Samson [43], that is to say without $Na_4P_2O_7$ and unaged $FeCl_3$ at pH = 2, are reported in Fig. 6.1-1. These micrographs show relatively uniform and dense sediments (Fig. 6.1-1a and b). At the highest magnification (Fig. 6.1-1c), most kaolinite particles are associated in the face-to-face (FF) mode. A few of these particles are associated according to the edge-to-face (EF) mode, as indicated by arrows in Fig. 6.1-1c.

The equivalent micrographs of the sediments made at pH = 4, 6 and 9.5, from the same kaolinite as previously, mixed without unaged $FeCl_3$, are respectively reported in Figs. 6.1-2, 6.1-3 and 6.1-4. The micrographs show microstructures which have a fractal

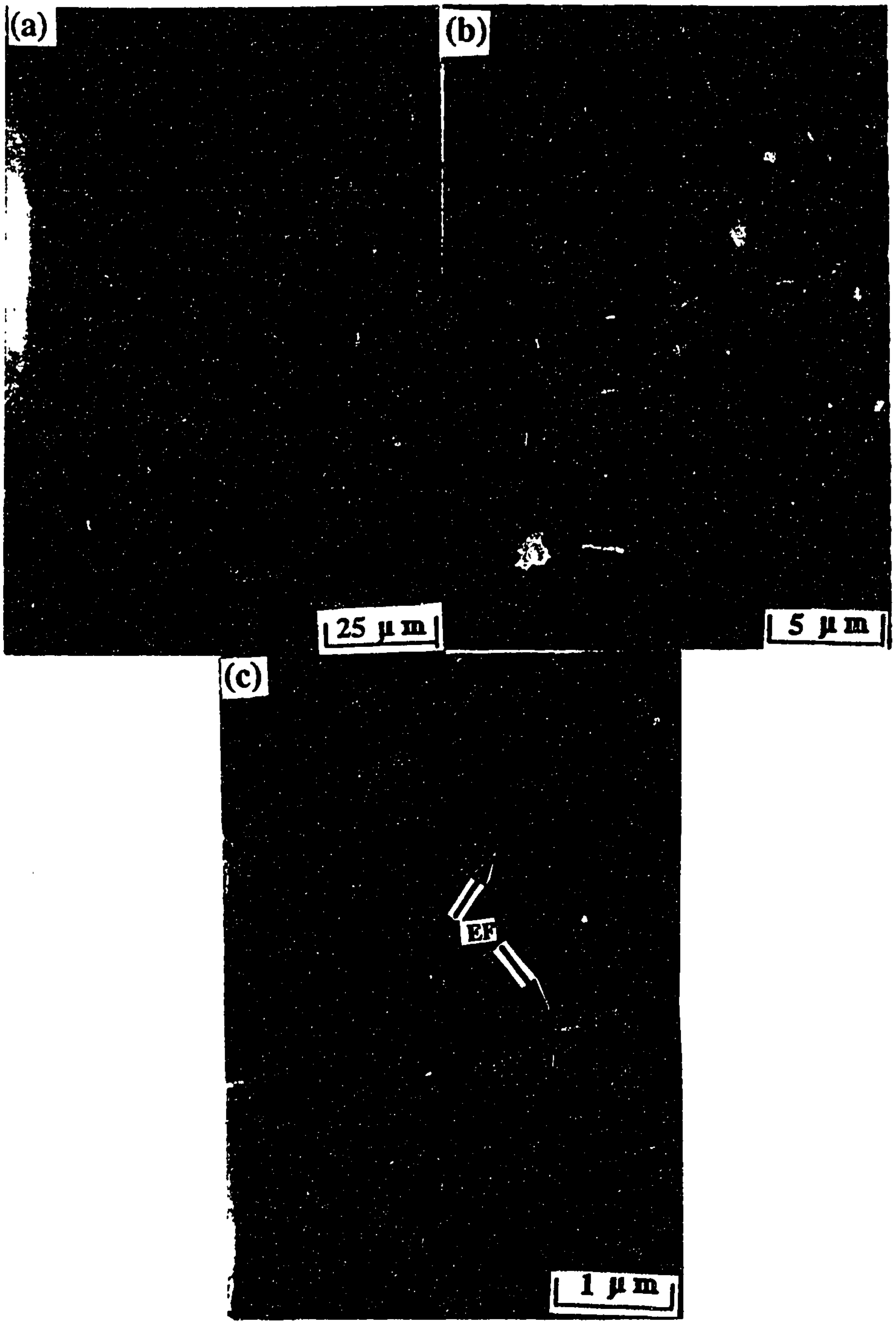

Fig. 6.1-1 - SEM micrographs at 10 kV of the sediments made from 0.5 % (by mass) kaolinite suspensions treated by the method of Schofield and Samson [59], and mixed without unaged $FeCl_3$, at pH 2. (a), (b) and (c) are at increasing magnification.

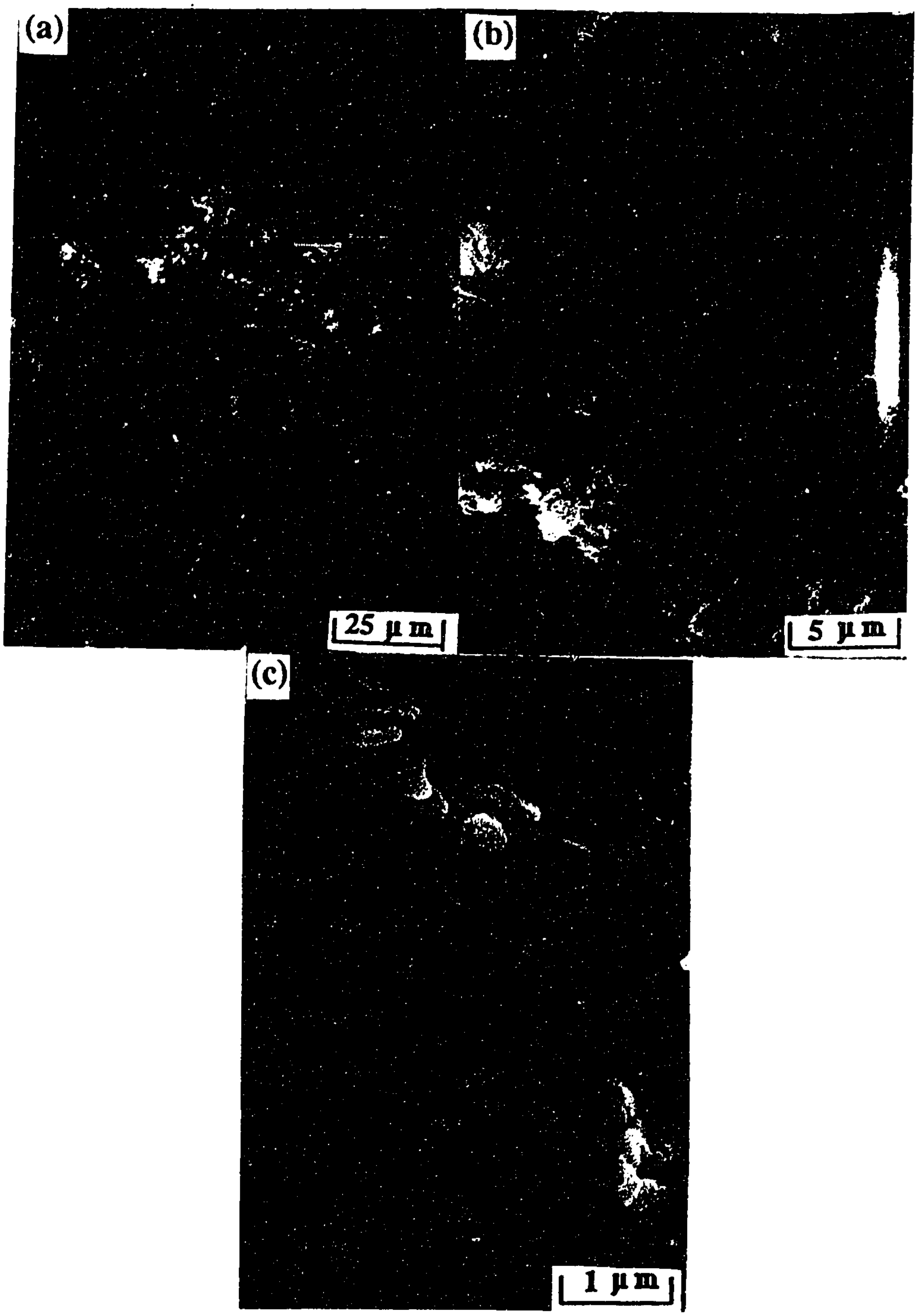

Fig. 6.1-2 - SEM micrographs at 10 kV of the sediments made from 0.5 % (by mass) kaolinite suspensions treated by the method of Schofield and Samson [59], and mixed without unaged $FeCl_3$, at pH 4. (a), (b) and (c) are at increasing magnification.

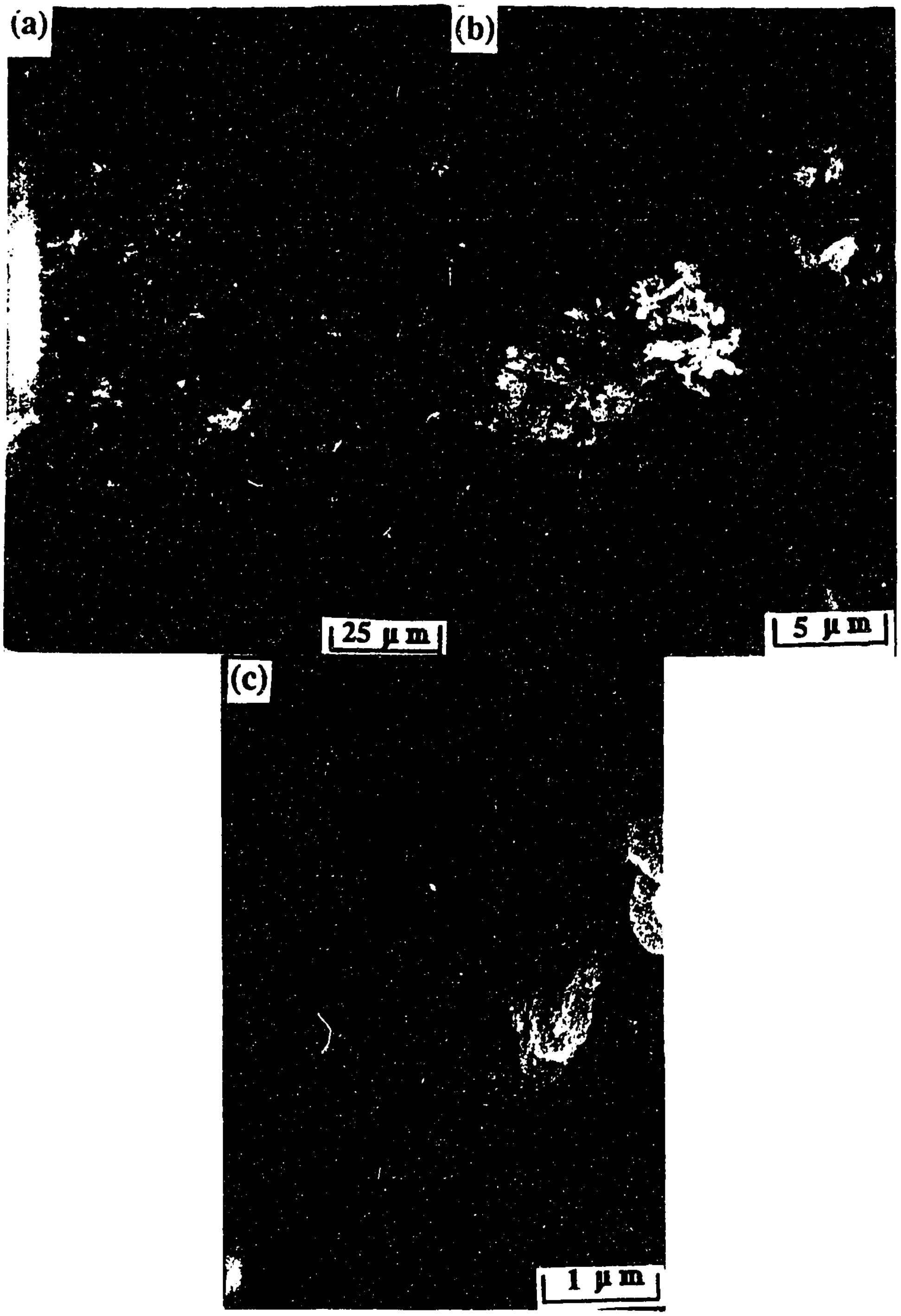

Fig. 6.1-3 - SEM micrographs at 10 kV of the sediments made from 0.5 % (by mass) kaolinite suspensions treated by the method of Schofield and Samson [59], and without Fe additives, at pH 6. (a), (b) and (c) are at increasing magnification.

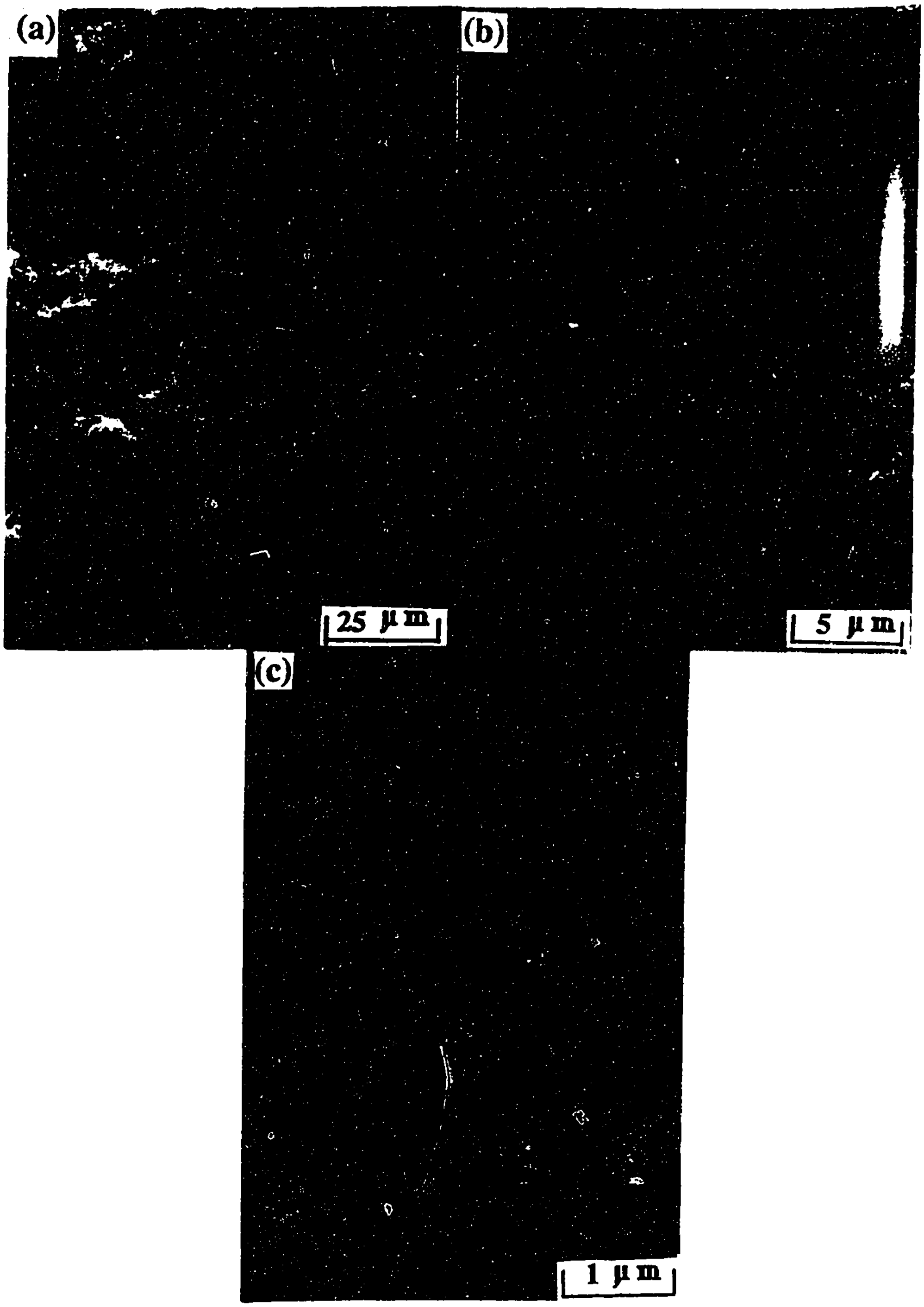

Fig. 6.1-4 - SEM micrographs at 10 kV of the sediments made from 0.5 % (by mass) kaolinite suspensions treated by the method of Schofield and Samson [59], and without Fe additives, at pH 9.5. (a), (b) and (c) are at increasing magnification.

aspect at the lowest magnification (Fig. 6.1-2a&b, Fig. 6.1-3a&b, and Fig. 6.1-4a&b), while this fractal aspect is lost at the highest magnification (Fig. 6.1-2c, Fig. 6.1-3c, and Fig. 6.1-4c). As in Fig. 6.1-1, most kaolinite particles are associated in the FF mode, and only few of them are connected in the EF or the EE modes.

Bookhouse structures, according to the terms introduced in Section 2.4, could be observed, especially at pH 4 and 6 (Fig. 6.1-2c, Fig. 6.1-3c). The sediment network was built by interconnection of these platelike domains. It seems that the bookhouse structure collapsed at pH 2.

6.1.2 - Kaolinite mixed with aged $FeCl_3$

SEM micrographs of sediments made from 0.5 % (by mass) kaolinite suspensions treated as previously, and mixed with 0.67 mM unaged $FeCl_3$ at pH =2 ,4 ,6 and 9.5, are respectively reported in Figs. 6.1-5, to 6.1-8. The microstructures which are shown are similar to those shown in Figs. 6.1-1 to 6.1-4 for the kaolinite sediments made without unaged $FeCl_3$.

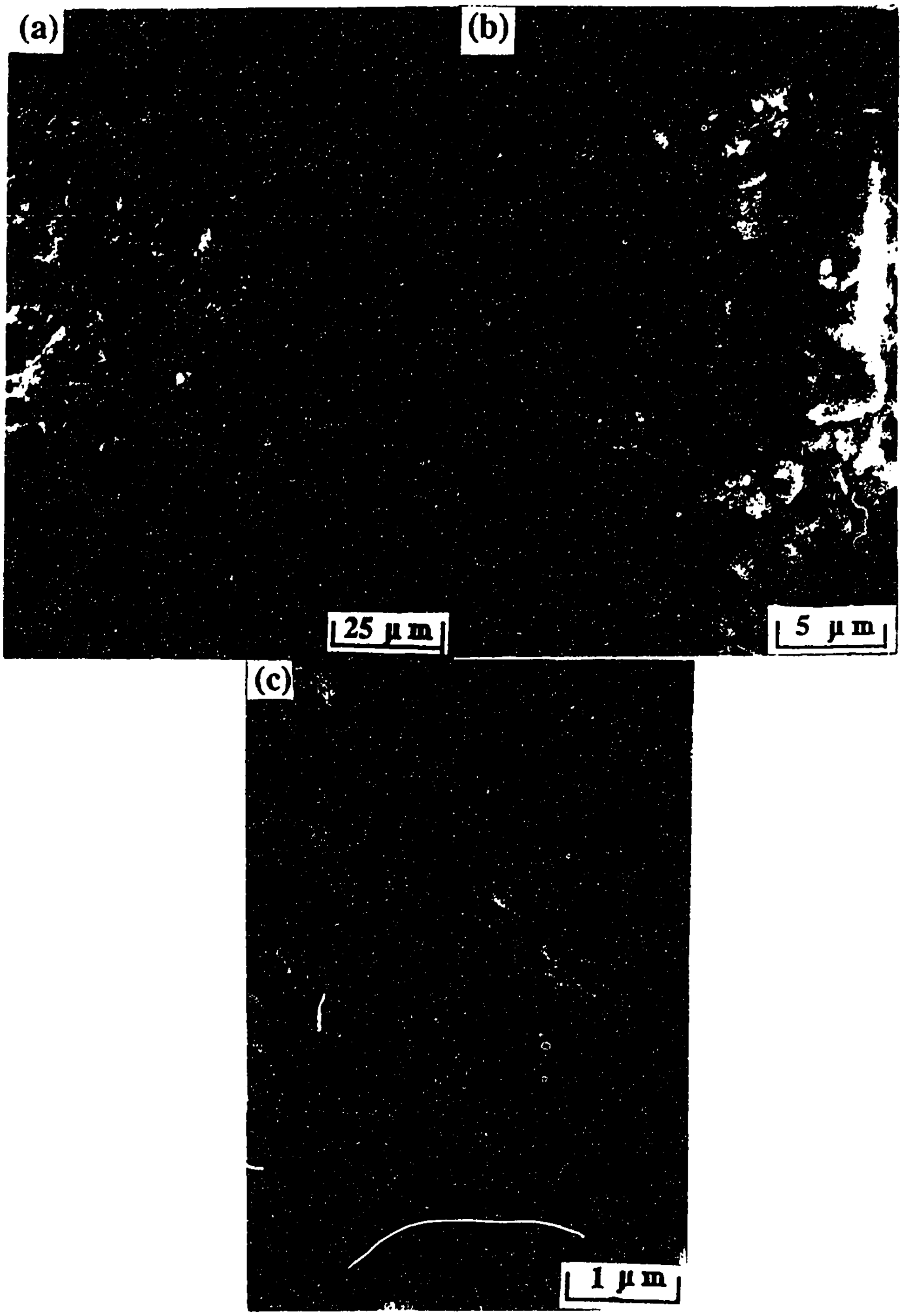

Fig. 6.1-5 - SEM micrographs at 10 kV of the sediments made from 0.5 % (by mass) kaolinite suspensions treated by the method of Schofield and Samson [59], and mixed with 0.67 mM unaged $FeCl_3$, at pH 2. (a), (b) and (c) are at increasing magnification.

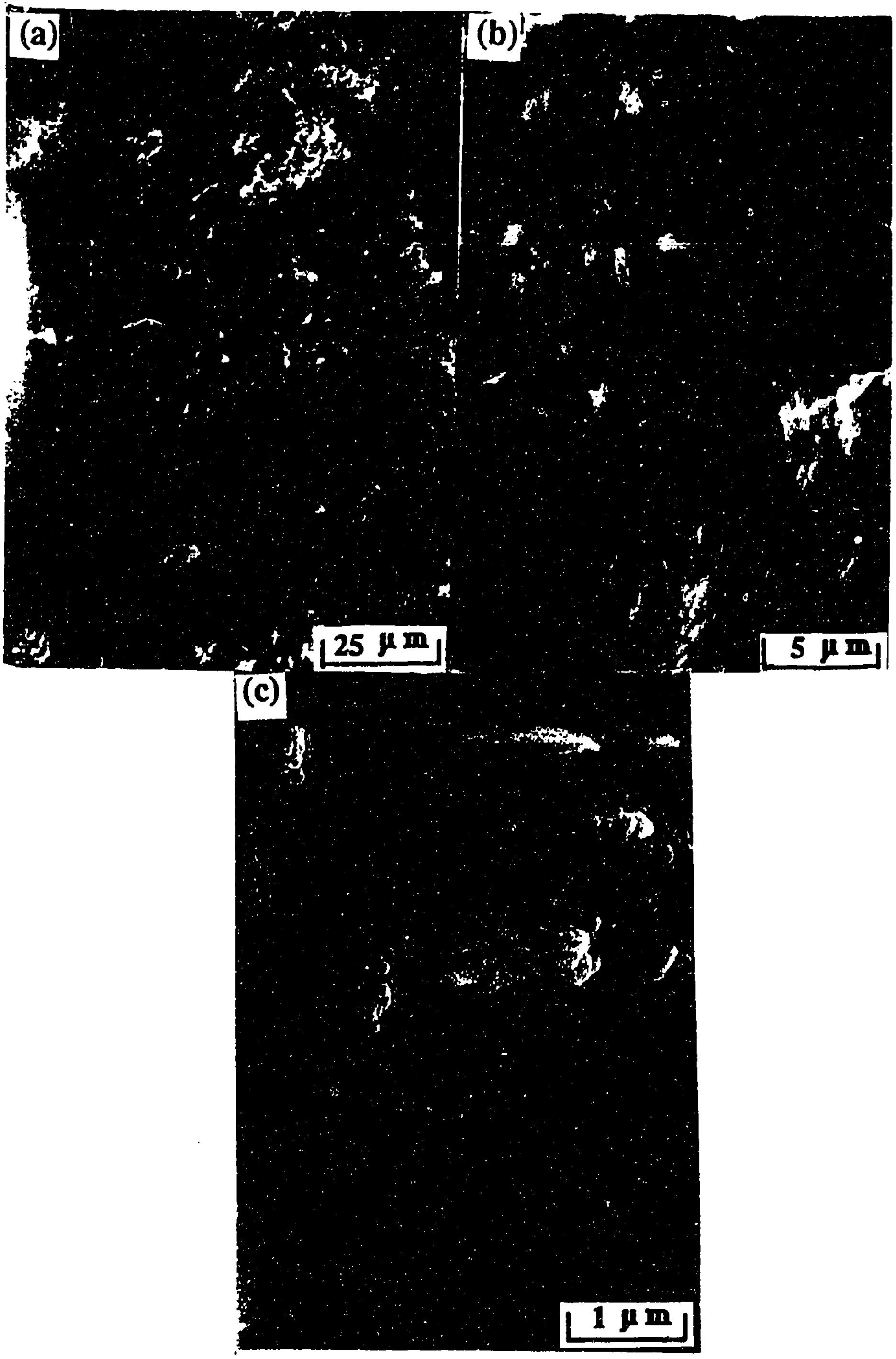

Fig. 6.1-6 - SEM micrographs at 10 kV of the sediments made from 0.5 % (by mass) kaolinite suspensions treated by the method of Schofield and Samson [59], and mixed with 0.67 mM unaged $FeCl_3$, at pH 4. (a), (b) and (c) are at increasing magnification.

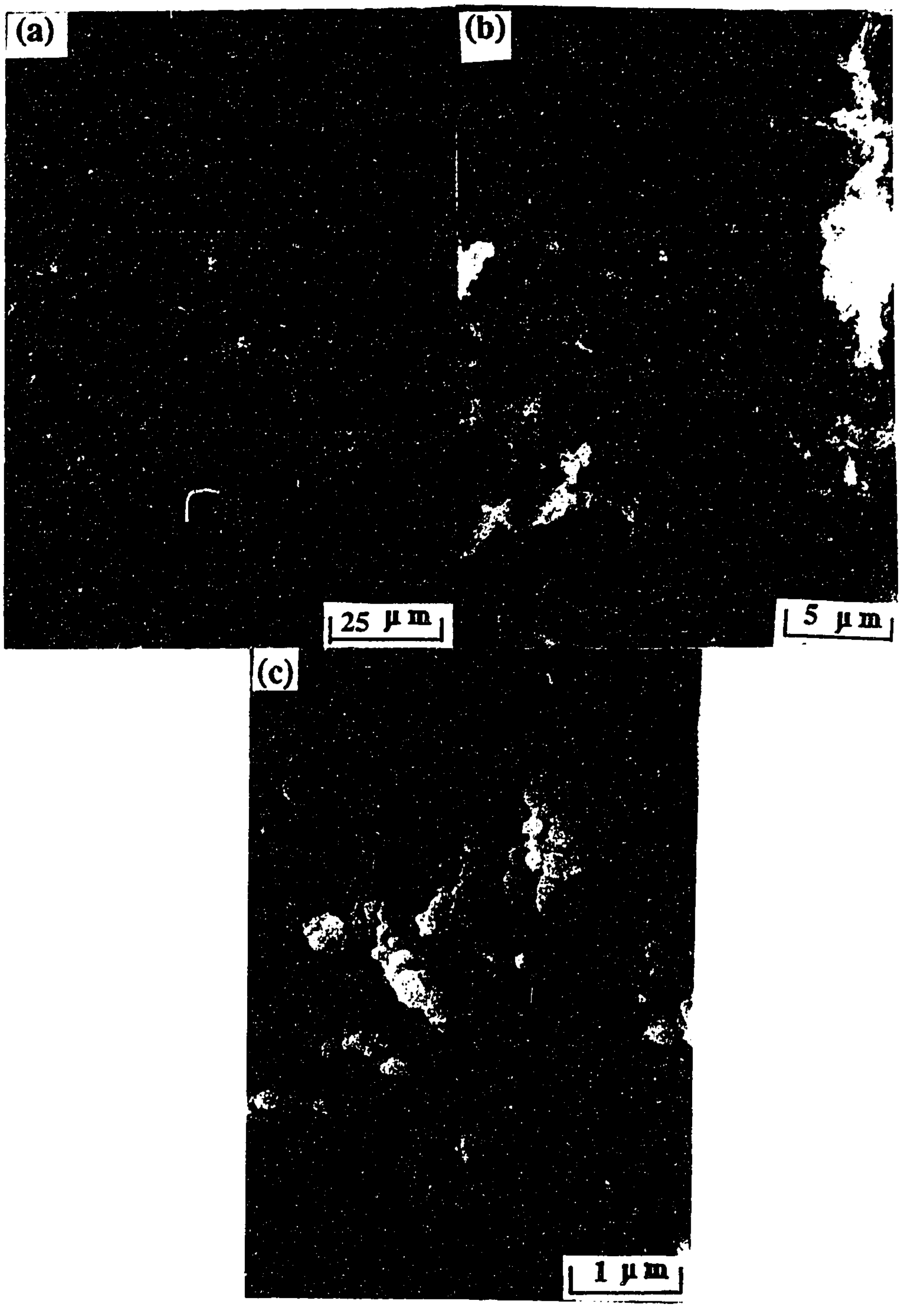

Fig. 6.1-7 - SEM micrographs at 10 kV of the sediments made from 0.5 % (by mass) kaolinite suspensions treated by the method of Schofield and Samson [59], and mixed with 0.67 mM unaged $FeCl_3$, at pH 6. (a), (b) and (c) are at increasing magnification.

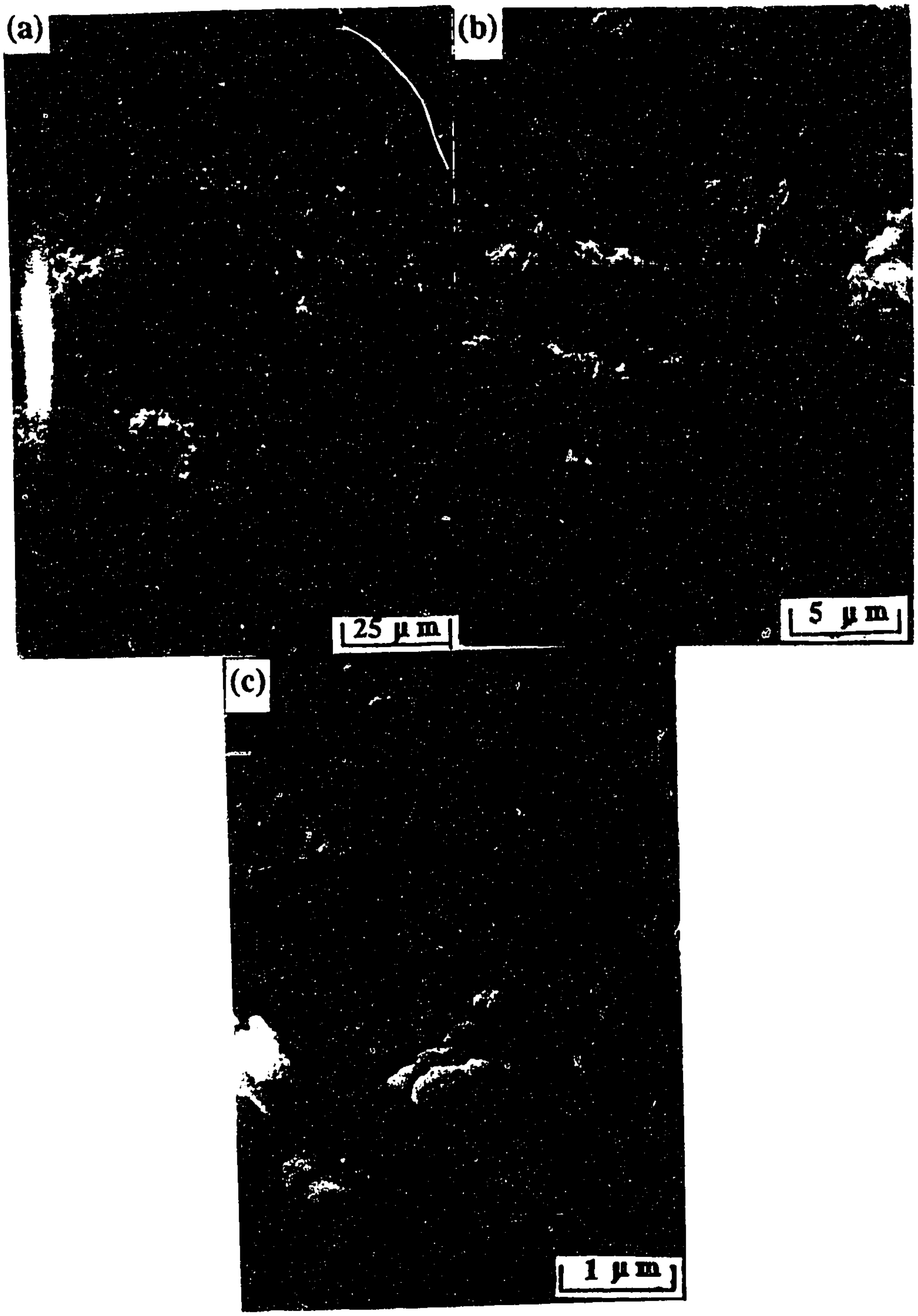

Fig. 6.1-8 - SEM micrographs at 10 kV of the sediments made from 0.5 % (by mass) kaolinite suspensions treated by the method of Schofield and Samson [59], and mixed with 0.67 mM unaged $FeCl_3$, at pH 9.5. (a), (b) and (c) are at increasing magnification.

6.2 - KAOLINITE WITH NEGATIVE CHARGES ON BOTH THE EDGES AND THE FACES

6.2.1 - Kaolinite sediments made with unaged $FeCl_3$

6.2.1.1 - Accumulated sediment

The SEM micrographs of an accumulated sediment from the sample without $FeCl_3$ are reported in Fig. 6.2-1. At low magnification, this sediment seems quite compact. However, at the highest magnification (Fig. 6.2-1c) it is porous. In the latter micrograph, the main particle association mode is mostly FF. Some EE association can also be observed.

Fig. 6.2-2 shows SEM micrographs of the accumulated kaolinite sediments made without $FeCl_3$ at pH=9.5. The suspension from which this sediment accumulated took a longer time to settle than the previous one at pH=4. At the lowest magnification (Fig. 6.2-2a and b) it was more compact than at pH 4. At the highest magnification the particles formed a type of structure with random particles packing.

In the accumulated sediment made with a $FeCl_3$ concentration of 3.3 mM, the micrographs in Figs. 6.2-3a & b show a very dense packing. Most of particles are associated in the FF mode (Fig. 6.2-3c).

6.2.1.2 - Flocculated sediment

The SEM micrographs of a flocculated sediment from the sample with the unaged $FeCl_3$ concentration of 0.67 mM, are reported in Fig. 6.2-4. The sediment architecture is different form the accumulated sediment, because more EE particles association can be observed (Fig. 6.2-4c and d). The micrographs actually show the presence of flocs. Each floc has a center area which is rather densely packed, while the floc becomes statistically less dense when going further from its center. Such a structure is qualitatively typical of

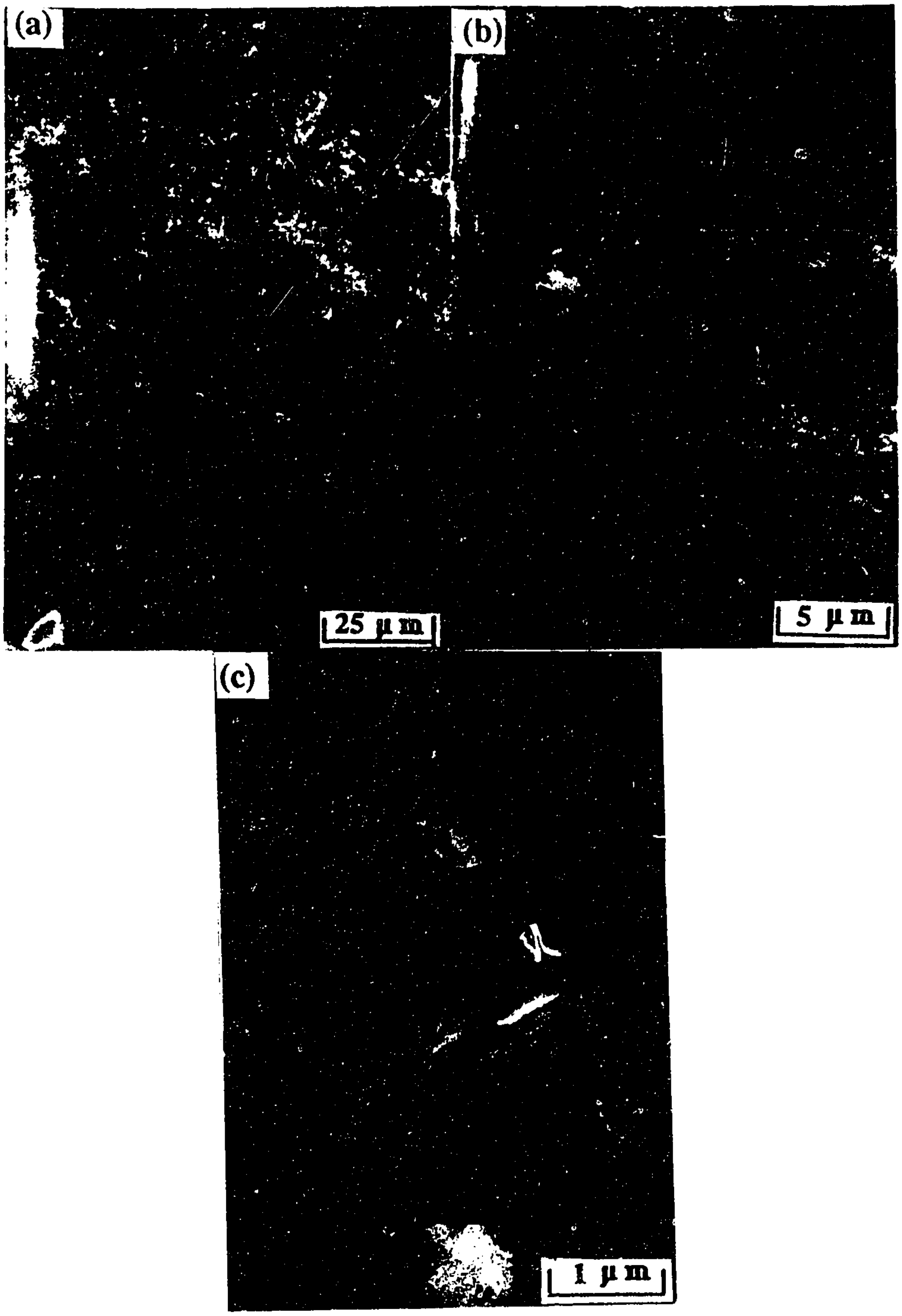
(a)
(b)
25 μm
5 μm
(c)
1 μm

Fig. 6.2-1 - SEM micrographs made at 10 kV and at several magnifications, of the accumulated kaolinite sediment without Fe additives at pH = 4.0.

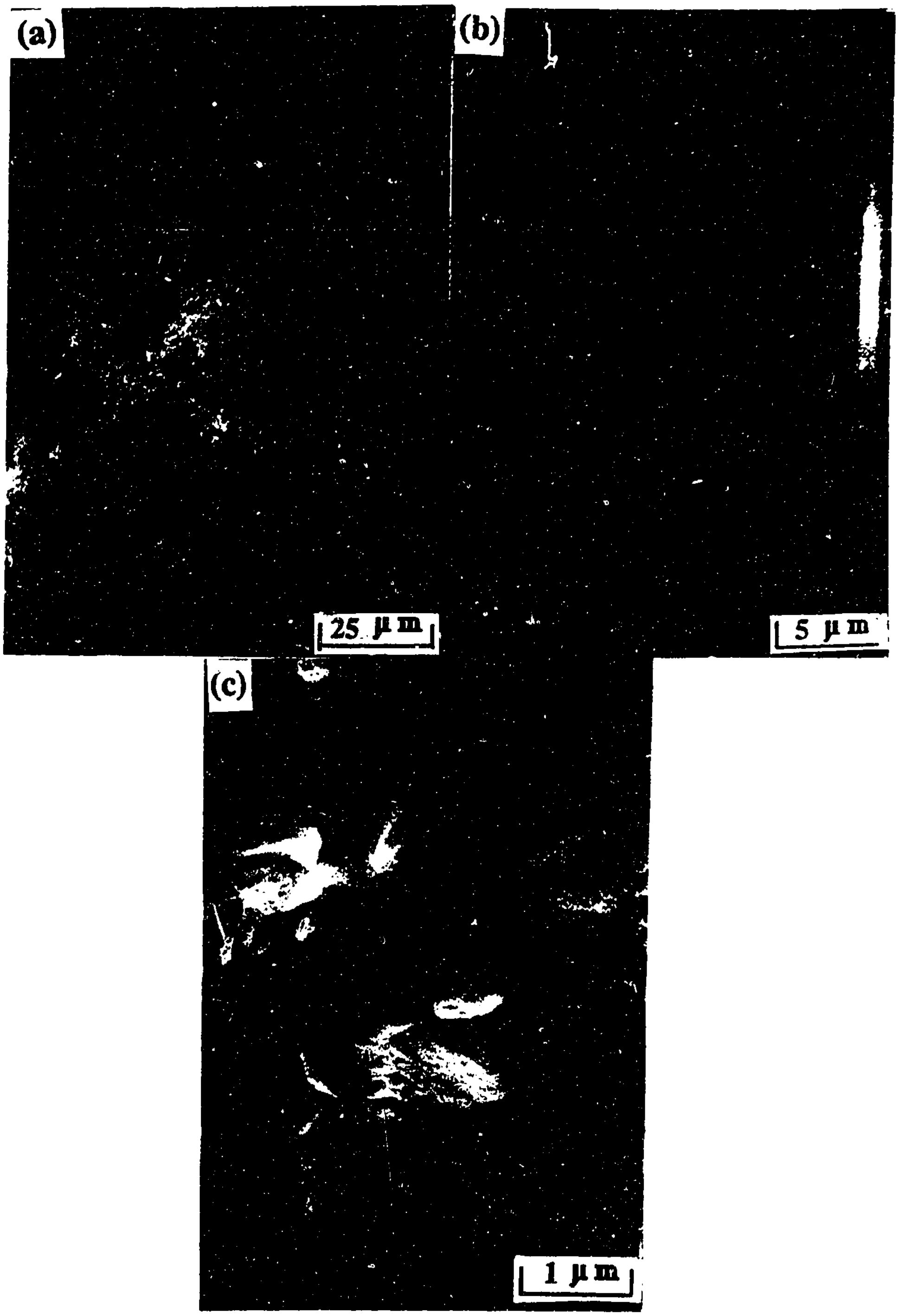
(a)
(b)
(c)
25 μm
5 μm
1 μm

Fig. 6.2-2 - SEM micrographs made at 10 kV and at several magnifications, of the accumulated kaolinite sediment without Fe additives, at pH = 9.5.

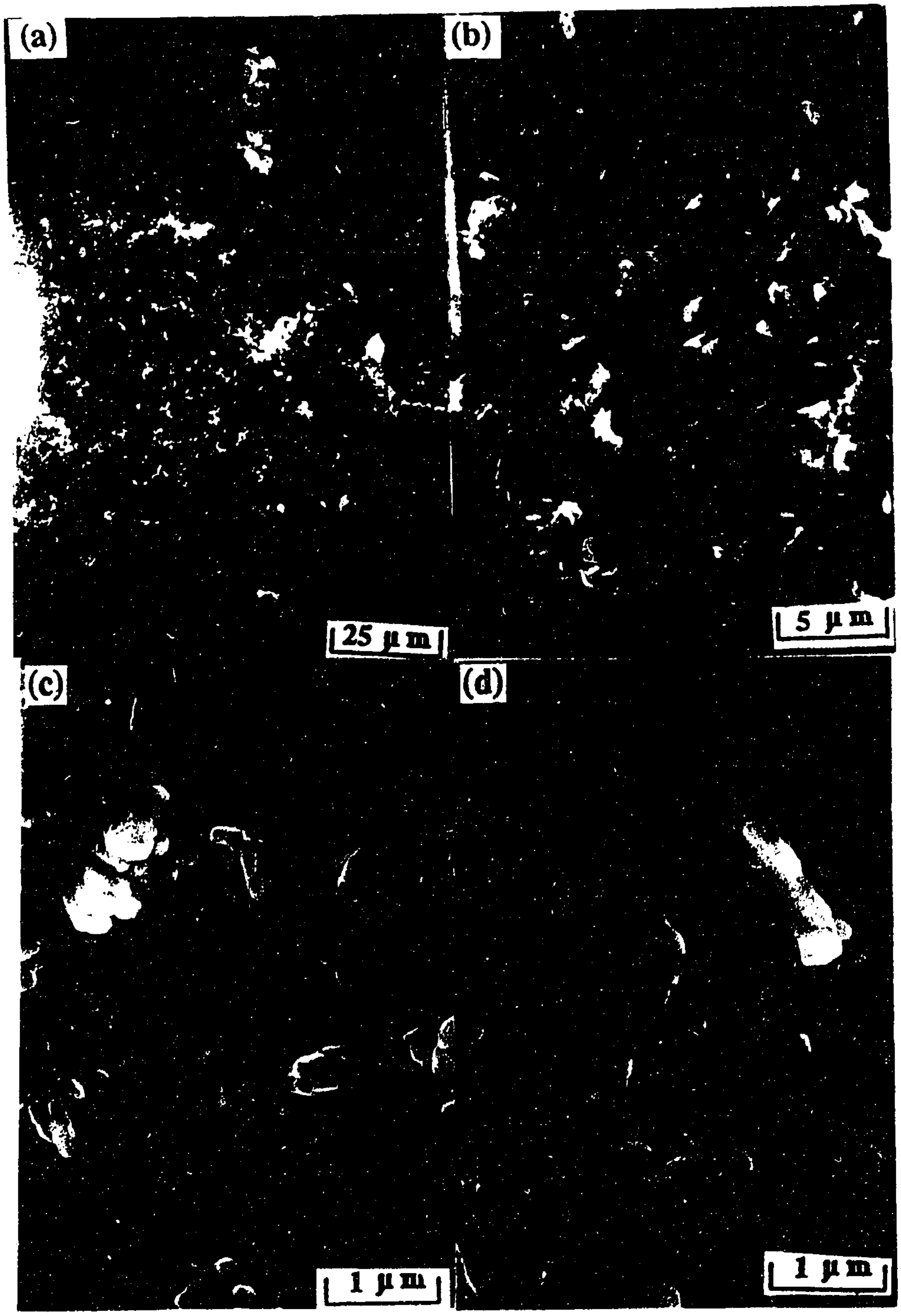
(a)
(b)
25 µm
5 µm
(c)
(d)
1 µm
1 µm

Fig. 6.2-3 - SEM micrographs made at 10 kV and at several magnifications, of the accumulated kaolinite sediment made at pH = 4.0 with unaged $FeCl_3$ at a concentration of 3.33mM.

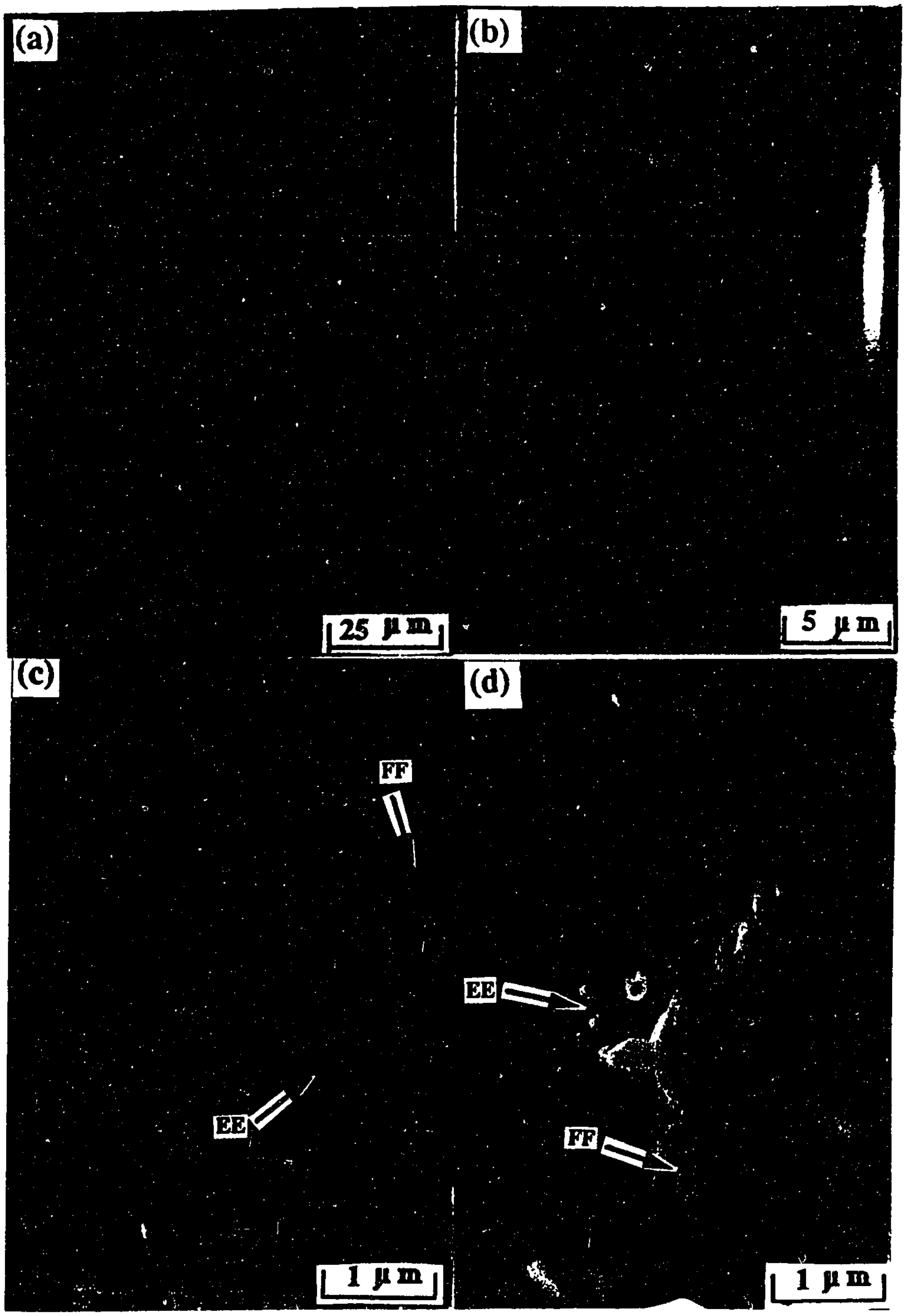
(a)
(b)
25 μm
5 μm
(c)
(d)
FF
EE
EE
FF
1 μm
1 μm

Fig. 6.2-4 - SEM micrographs made at 10 kV and at several magnifications, of the flocculated kaolinite sediment made at pH = 4.0 with unaged $FeCl_3$ at a concentration of 0.67mM.

the aggregates known as "DLA fractal aggregate", as presented in Section 2.2.3.2 [122,123].

6.2.1.3 - Mixed accumulated-flocculated sediments

SEM micrographs of a mixed accumulated-flocculated sediment from the sample with the unaged $FeCl_3$ concentration 1.67 mM are reported in Fig. 6.2-5. The upper part of the sediment has a microstructure which is typical of a flocculated sediment with a large porosity (Fig. 6.2-5a), while the lower part shows the character of an accumulated sediment (Fig. 6.2-5b).

6.2.2 - Kaolinite sediments made with aged $FeCl_3$

6.2.2.1 - Accumulated sediment

SEM micrographs of an accumulated sediment with an aged $FeCl_3$ concentration of 10 mM, at pH 9.5, are reported in Fig. 6.2-6. The structure of this sediment is rather compact, as this was found with unaged $FeCl_3$ in Fig. 6.2-3.

6.2.2.2 - Flocculated sediment

SEM micrographs of a flocculated kaolinite sediment made with an aged $FeCl_3$ concentration of 3.3 mM, at pH=9.5, are reported in Fig. 6.2-7. These micrographs clearly show flocs with a center which is rather densely packed, while bigger pores develop when going further from this center. The EE association mode of the kaolinite particles was quite frequent. However, some FF association could also be observed.

6.2.3 - Flocculated kaolinite sediments made with unaged $AlCl_3$

SEM micrographs of flocculated kaolinite sediments made at pH 2 with concentrations of unaged $AlCl_3$ of 0, 2 and 50mM, are respectively reported in Figs. 6.2-8

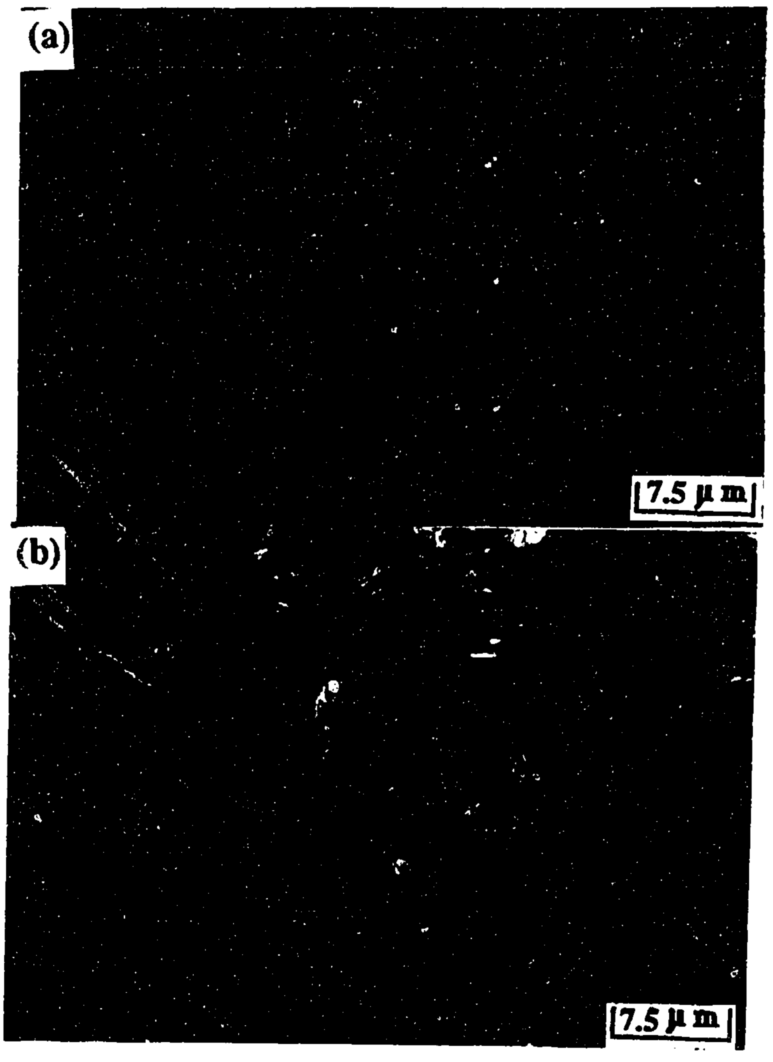

Fig. 6.2-5 - SEM micrographs at several magnifications, of the mixed accumulated-flocculated kaolinite sediment made at pH 4 with unaged $FeCl_3$ at a concentration of 1.67mM; (a) top part of the sediment; (b) bottom part of the sediment.

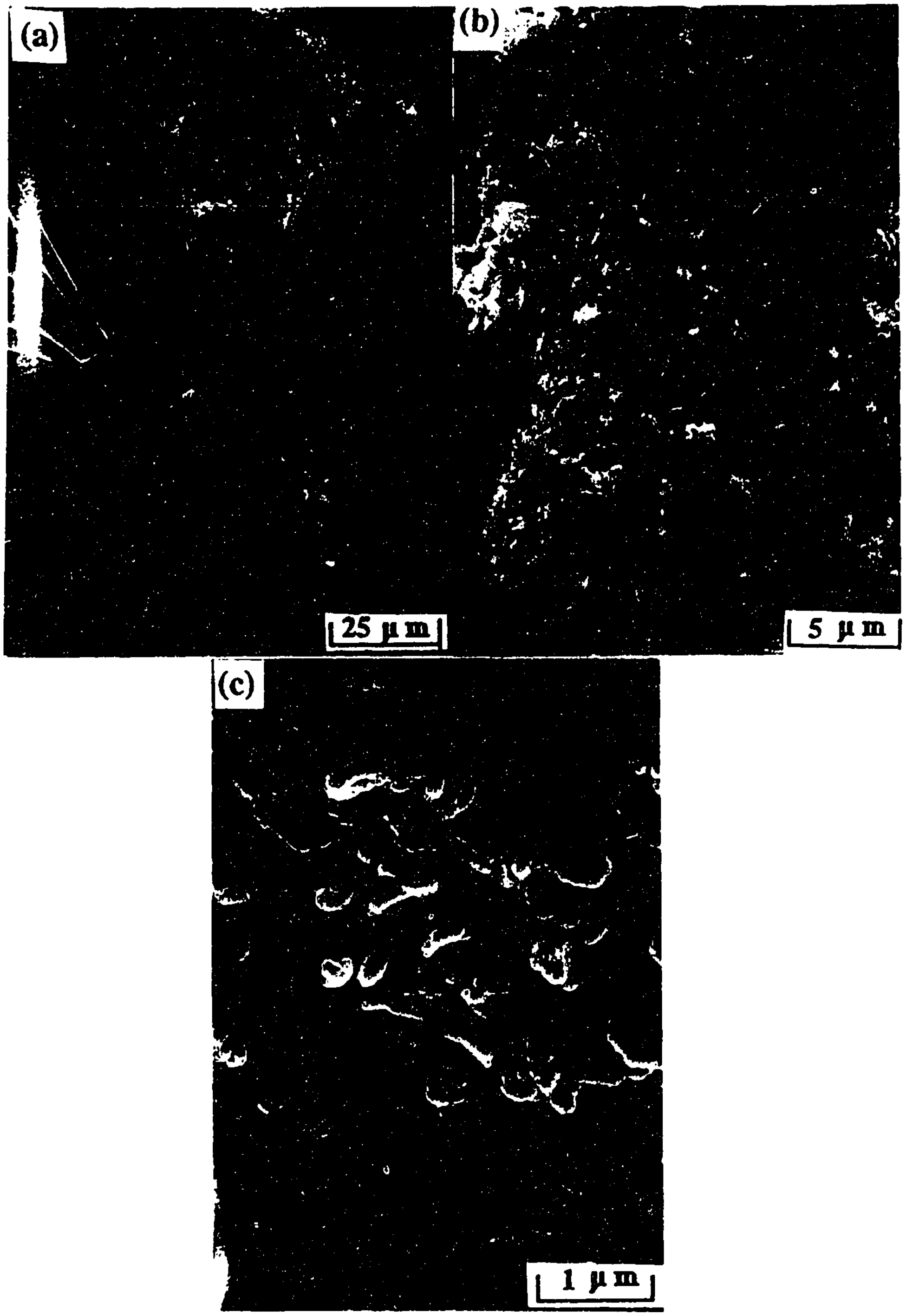

Fig. 6.2-6 - SEM micrographs made at 10 kV and at several magnifications, of the accumulated kaolinite sediment made at pH 9.5 with aged $FeCl_3$ at a concentration of 10mM.

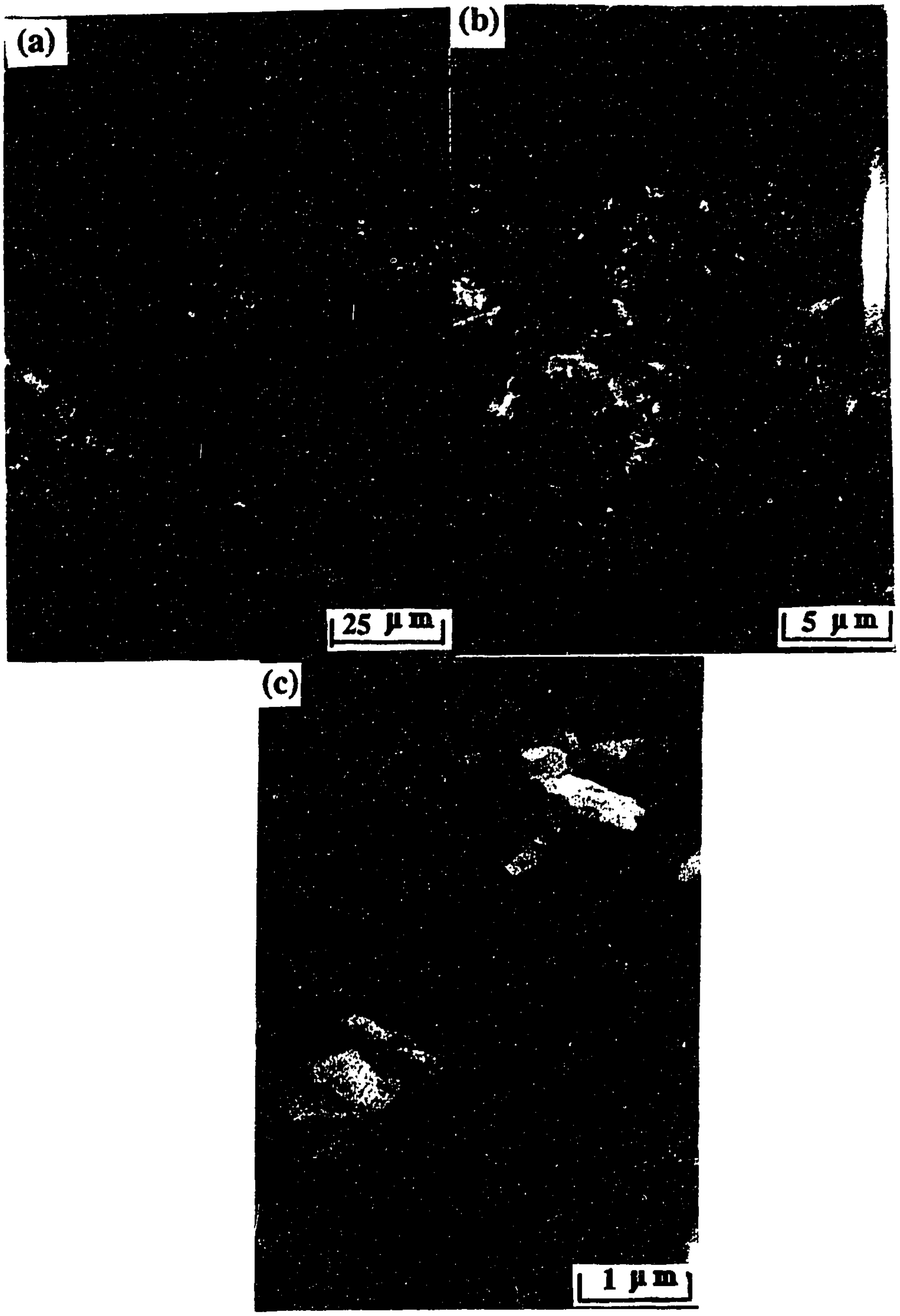

Fig. 6.2-7 - SEM micrographs made at 10 kV and at several magnifications, of the accumulated kaolinite sediment made at pH 9.5 with aged $FeCl_3$ at a concentration of 3.3mM.

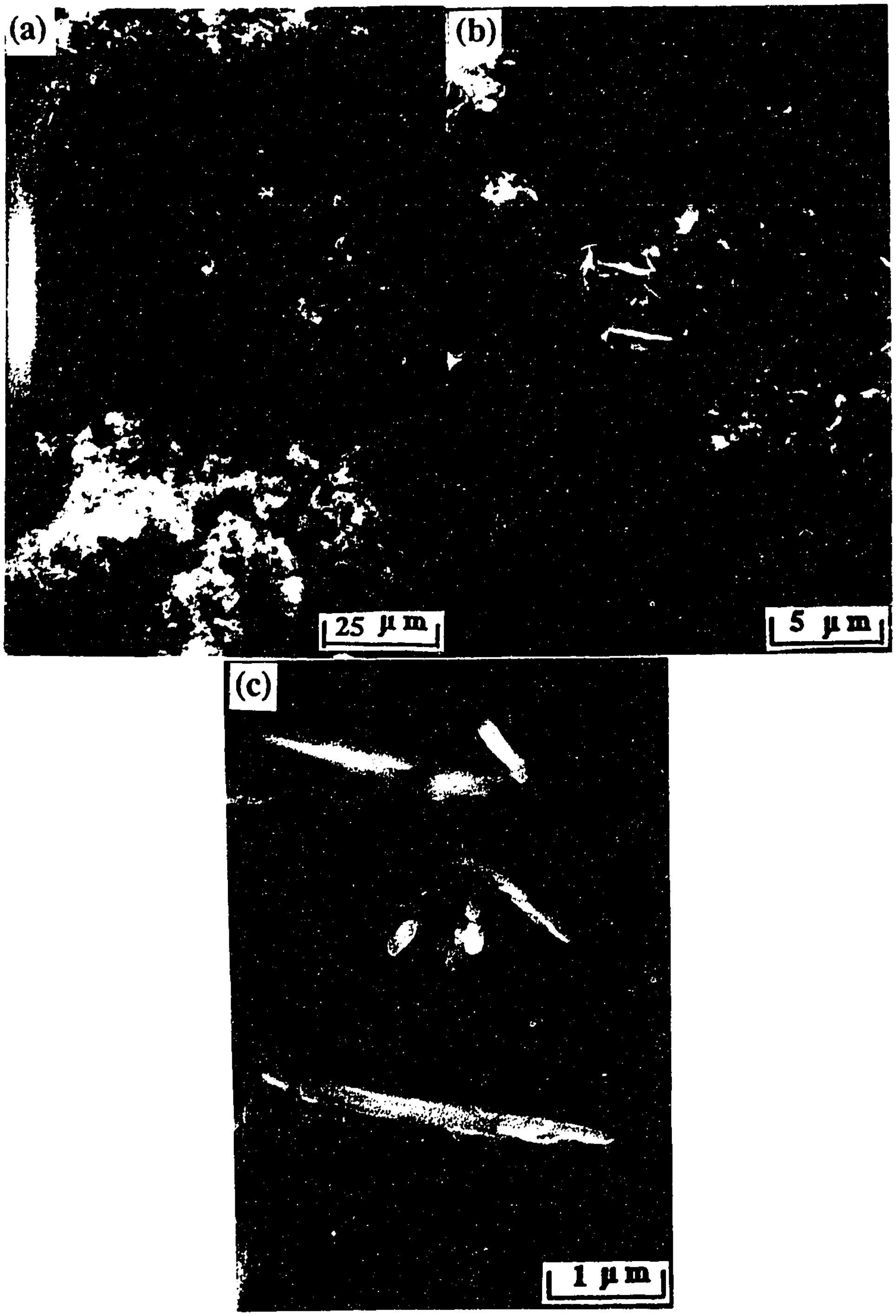
(a)
(b)
25 μm
5 μm
(c)
1 μm

Fig. 6.2-8 - SEM micrographs made at 10 kV and at several magnifications, of the flocculated kaolinite sediment made at pH 2 without $AlCl_3$.

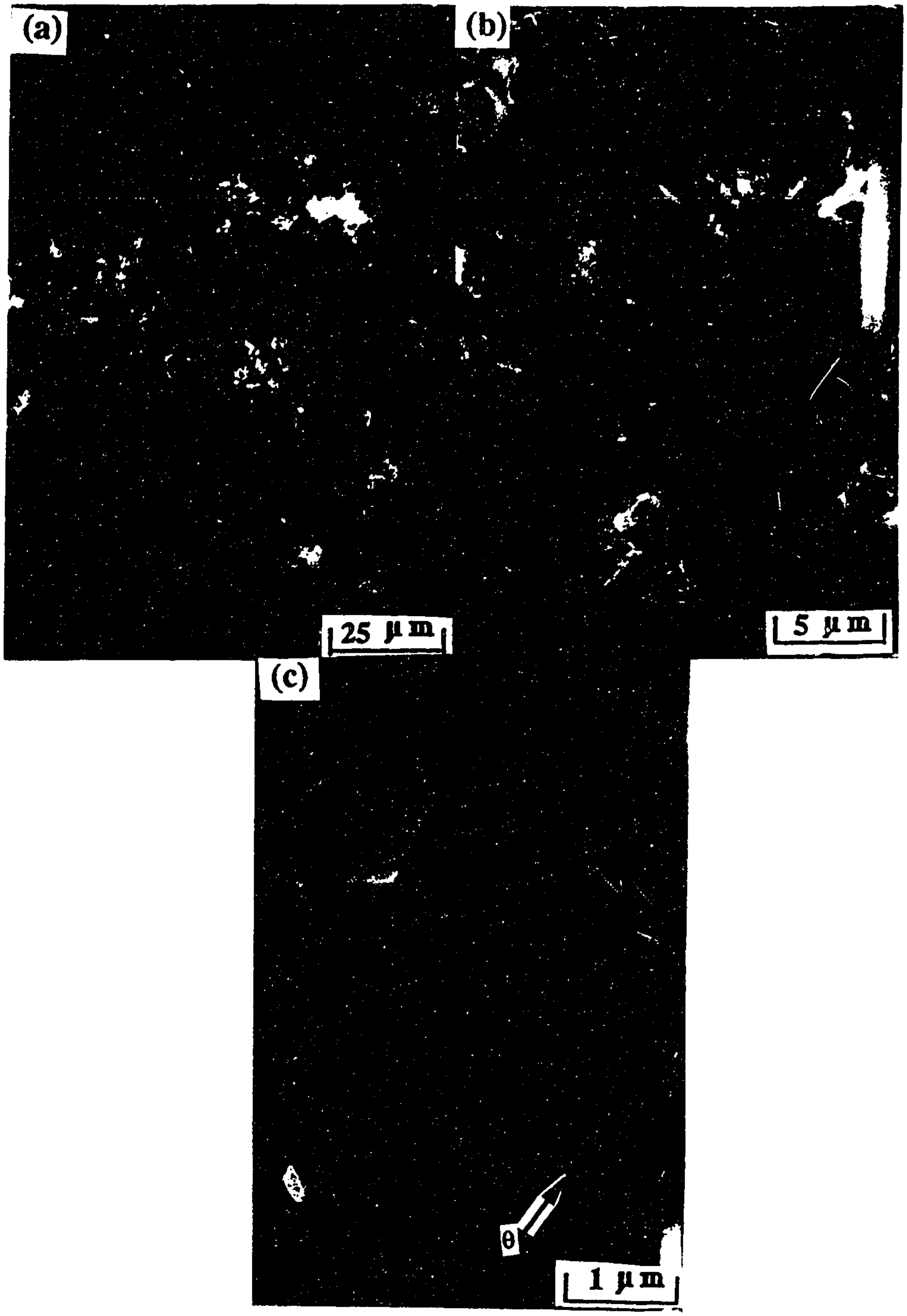

Fig. 6.2-9 - SEM micrographs made at 10 kV and at several magnifications, of the flocculated kaolinite sediment made at pH 2 with unaged $AlCl_3$ at a concentration of 2mM.

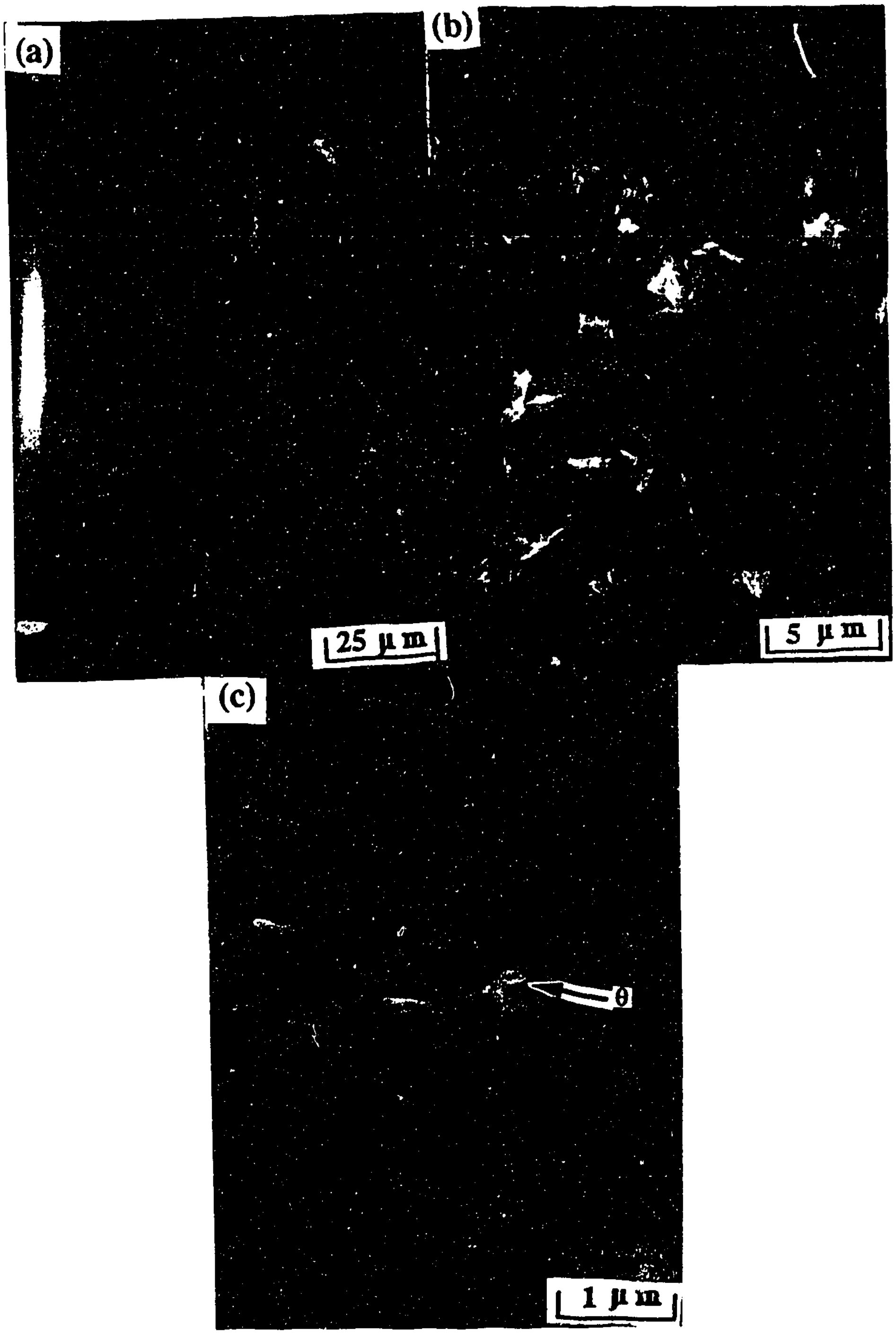

Fig. 6.2-10 - SEM micrographs made at 10 kV and at several magnifications, of the flocculated kaolinite sediment made at pH 2 with unaged $AlCl_3$ at a concentration of 50mM.

to 6.2-10. All the pictures show flocs which can be qualitatively described by the DLA model.

In Fig. 6.2-9c and 6.2-10c, some clay particles were associated with an angle, as indicated by arrows.

SEM micrographs of other flocculated kaolinite sediments made at pH=9.5 with unaged $AlCl_3$ at the concentrations of 2 and 50mM, are respectively reported in Fig. 6.2-11 and 6.2-12. The EE mode of particles association is well illustrated in Fig. 6.2-11c, while stair-step structures can clearly be seen in Fig. 6.2-12c.

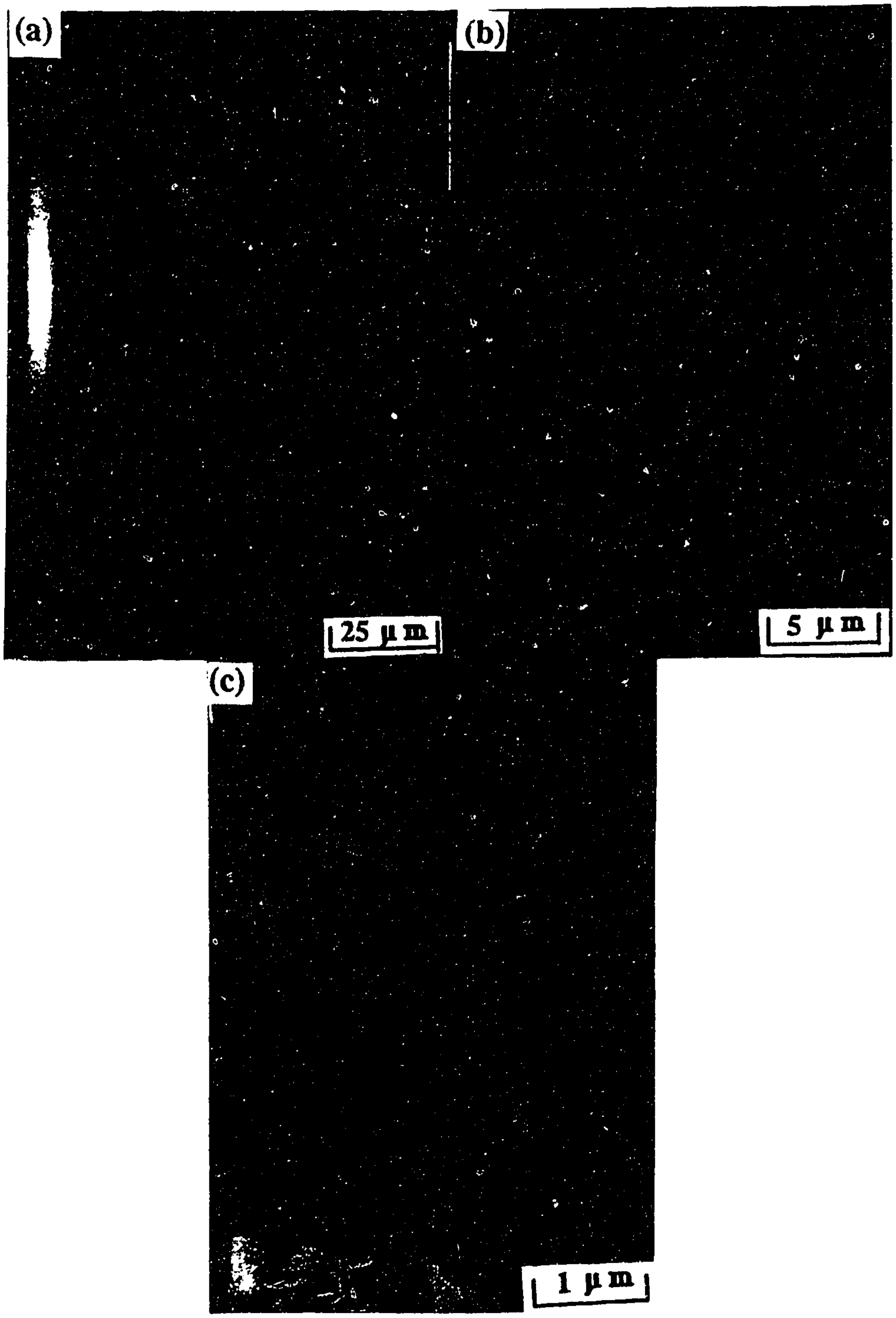

Fig. 6.2-11 - SEM micrographs made at 10 kV and at several magnifications, of the flocculated kaolinite sediment made at pH 9.5 with unaged $AlCl_3$ at a concentration of 2mM.

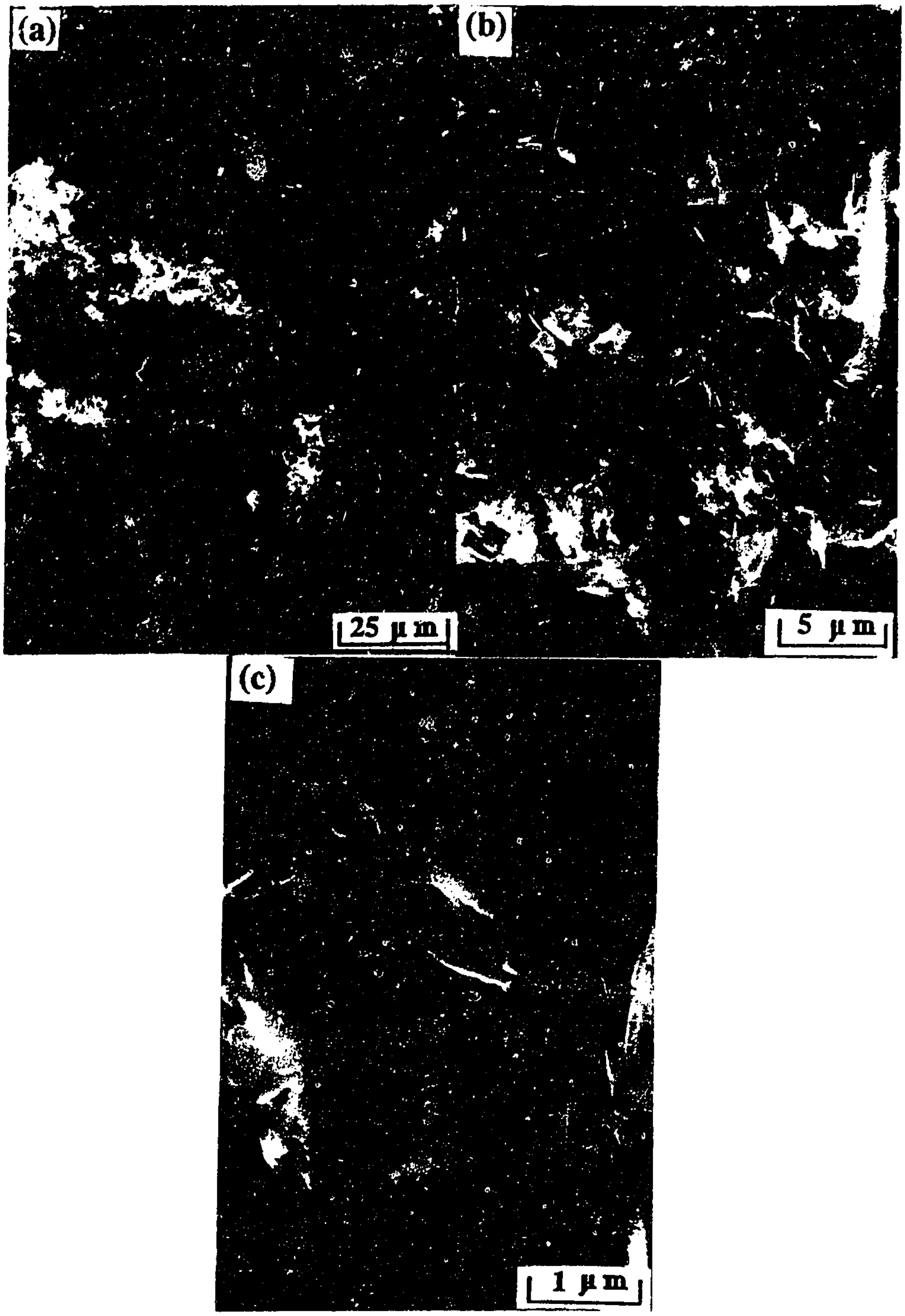

Fig. 6.2-12 - SEM micrographs made at 10 kV and at several magnifications, of the flocculated kaolinite sediment made at pH 9.5 with unaged $AlCl_3$ at a concentration of 50mM.

6.3 - MONTMORILLONITE

6.3.1 - Montmorillonite-aged FeCl$_3$ sediments

6.3.1.1 - Accumulated sediment

SEM micrographs of the accumulated sediment from a 1 % montmorillonite suspension mixed with aged FeCl$_3$ at a concentration of 0.33mM and at pH=9.5, are reported in Fig. 6.3-1. These pictures show a rather uniform and random packing of montmorillonite particles, with a uniform porosity.

6.3.1.2 - Flocculated sediment

The microstructure of a flocculated motmorillonite sediment is illustrated in the micrographs of Fig. 6.3-2. This sediment was obtained from a 1 % montmorillonite suspension mixed with aged FeCl$_3$ at a concentration of 5mM and at pH=9.5. The micrographs show fractal flocs, similar to the flocs previously described in Section 6.2 for kaolinite. In the present case, the montmorillonite particles were mostly associated according to the EE mode (Fig. 6.3-2c).

6.3.2 - Montmorillonite - hydroxoferric particles flocculated sediments

SEM micrographs of the flocculated sediments prepared from 1% Na-montmorillonite suspensions, mixed with hydroxoferric particles at the solid contents of 0.125% and 0.5% at pH = 9.5, are respectively reported in Fig. 6.3-3 and 6.3-4. With both hydroxoferric solid contents, fractal flocs similar to the flocs previously described in Section 6.3.1, were formed. However, in the present case, extensive curling of the montmorillonite particles occurred. Consequently, the mode of particle association, such as the EE mode, is difficult to describe with certainty. Also, the flocs appeared to be more compact than in the previous case.

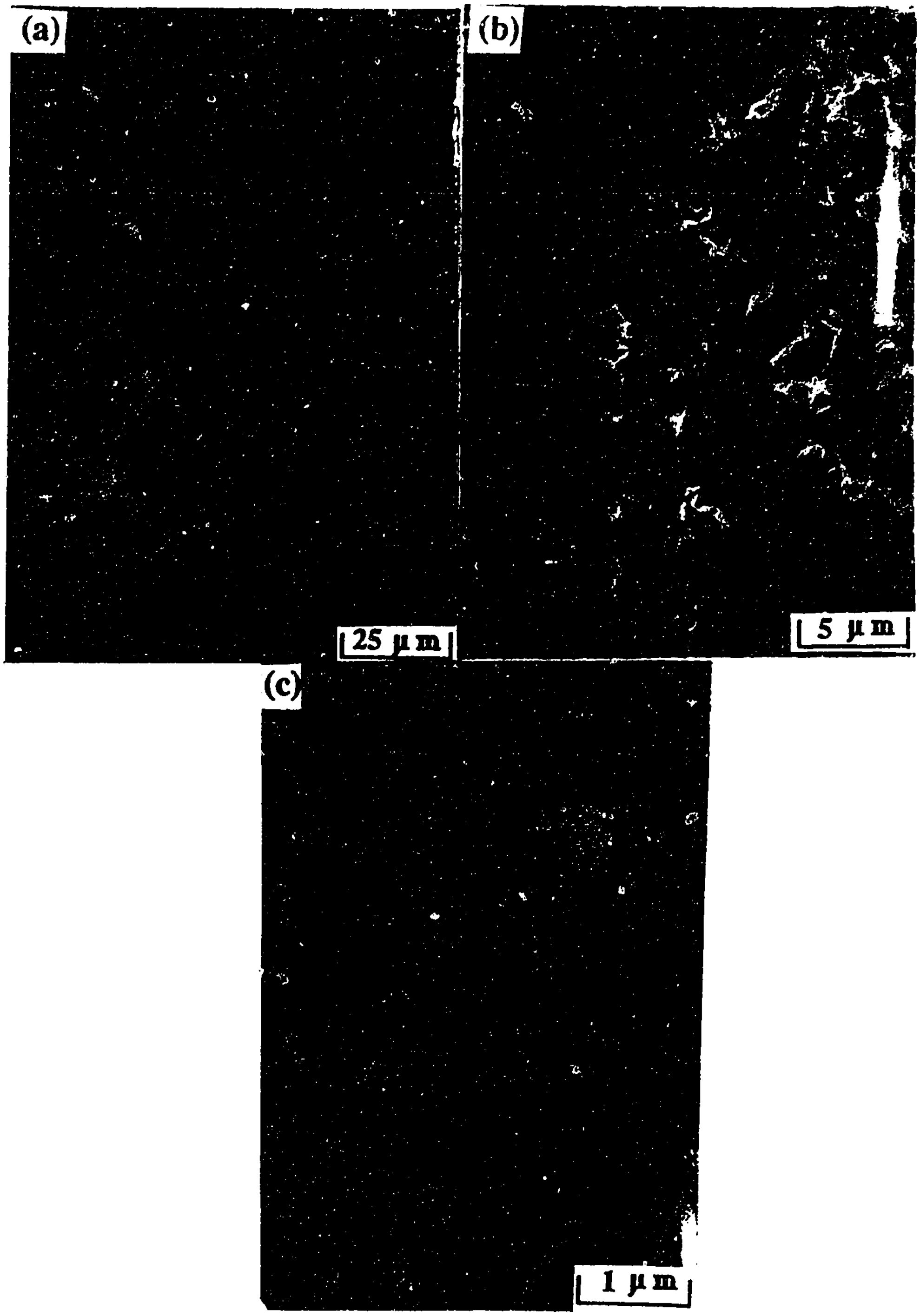

Fig. 6.3-1 - SEM micrographs made at 10 kV and at several magnifications, of the accumulated montmorillonite sediment made at pH = 9.5 with aged FeCl at a concentration of 0.33mM.

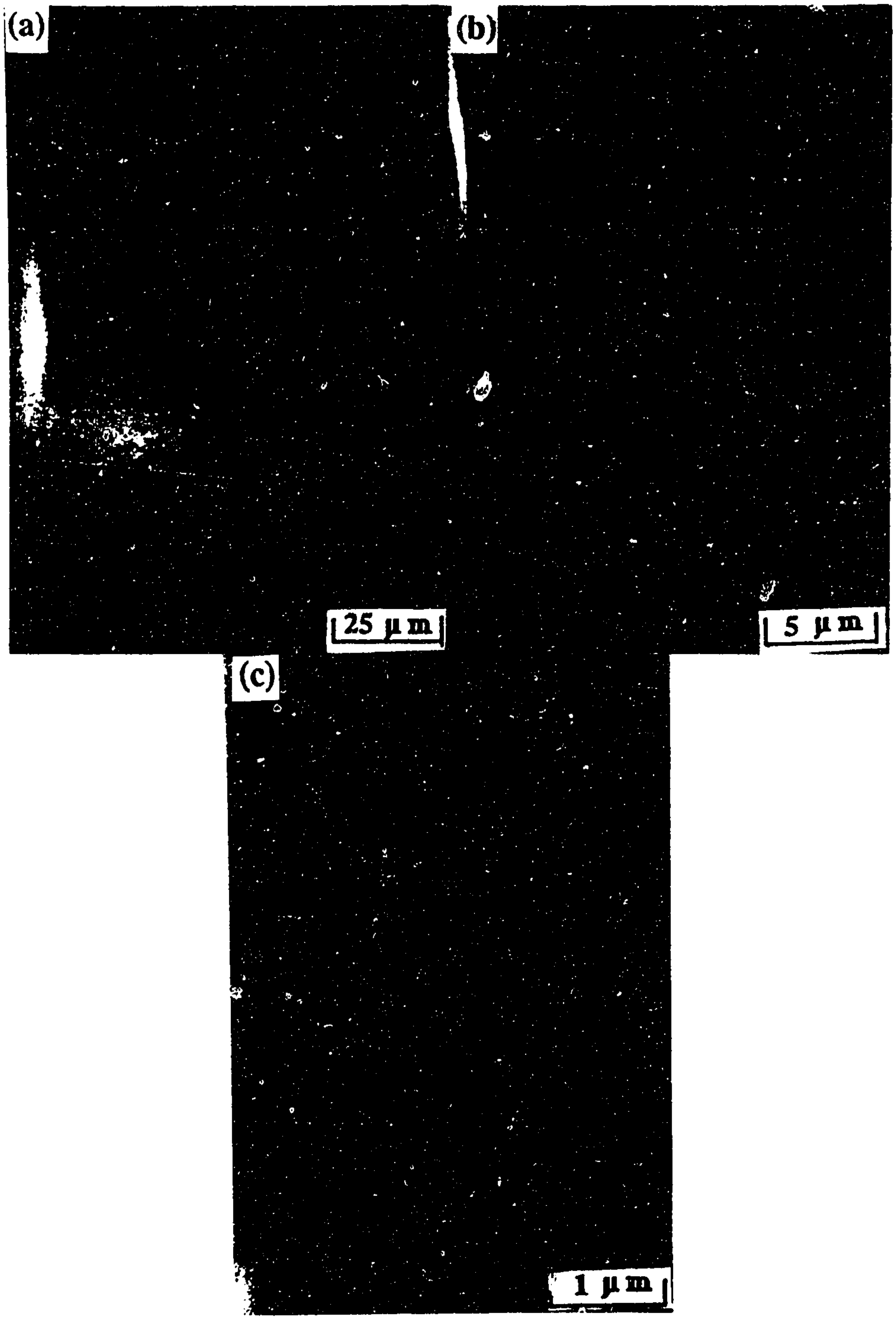

Fig. 6.3-2 - SEM micrographs made at 10 kV and at several magnifications, of the flocculated montmorillonite sediment made at pH = 9.5 with aged $FeCl_3$ at a concentration of 5mM.

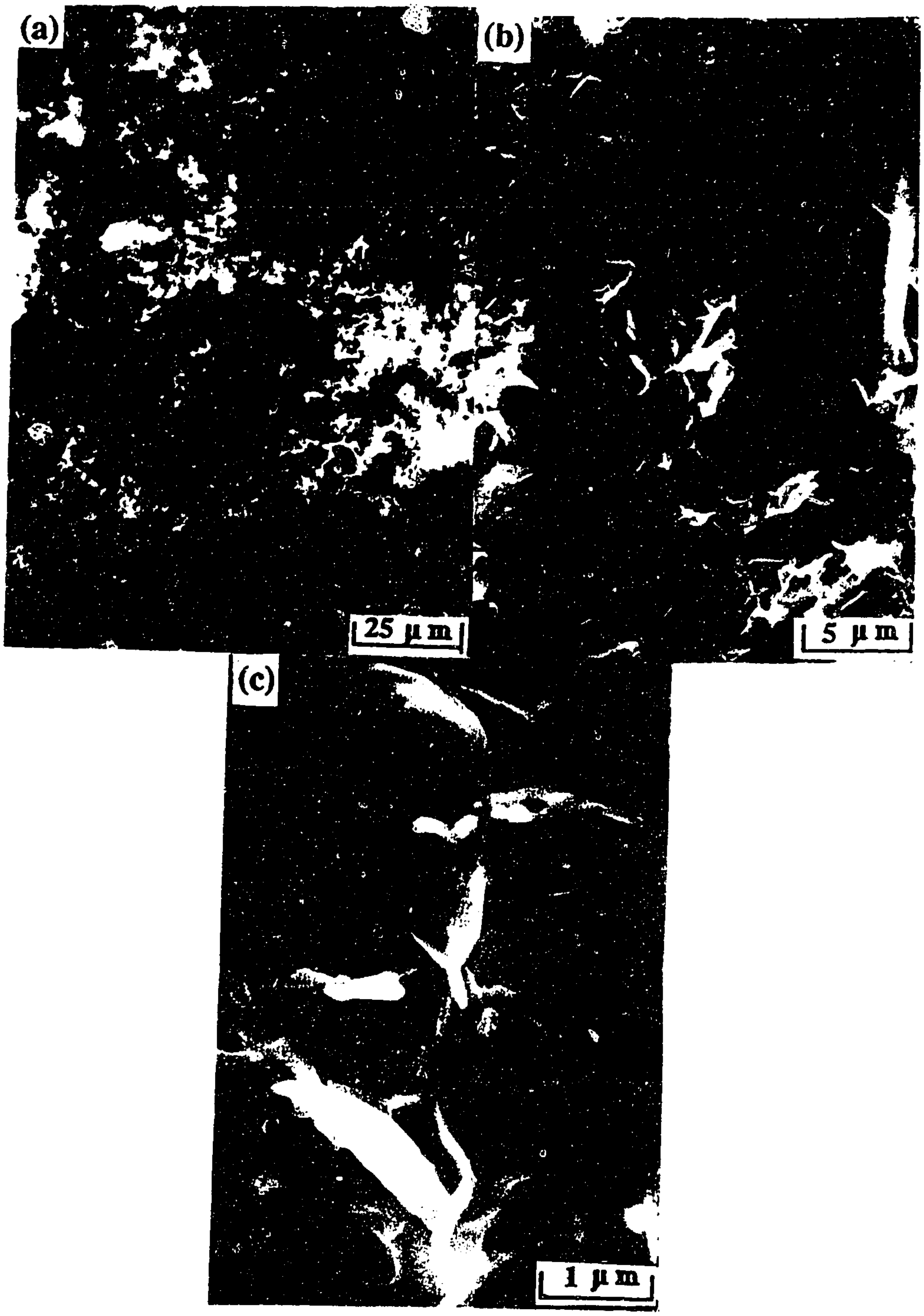

Fig. 6.3-3 - SEM micrographs made at 15 kV and at several magnifications, of the flocculated montmorillonite sediment made at pH = 9.5 with hydroxoferric particles at a solid content of 0.125 % by mass.

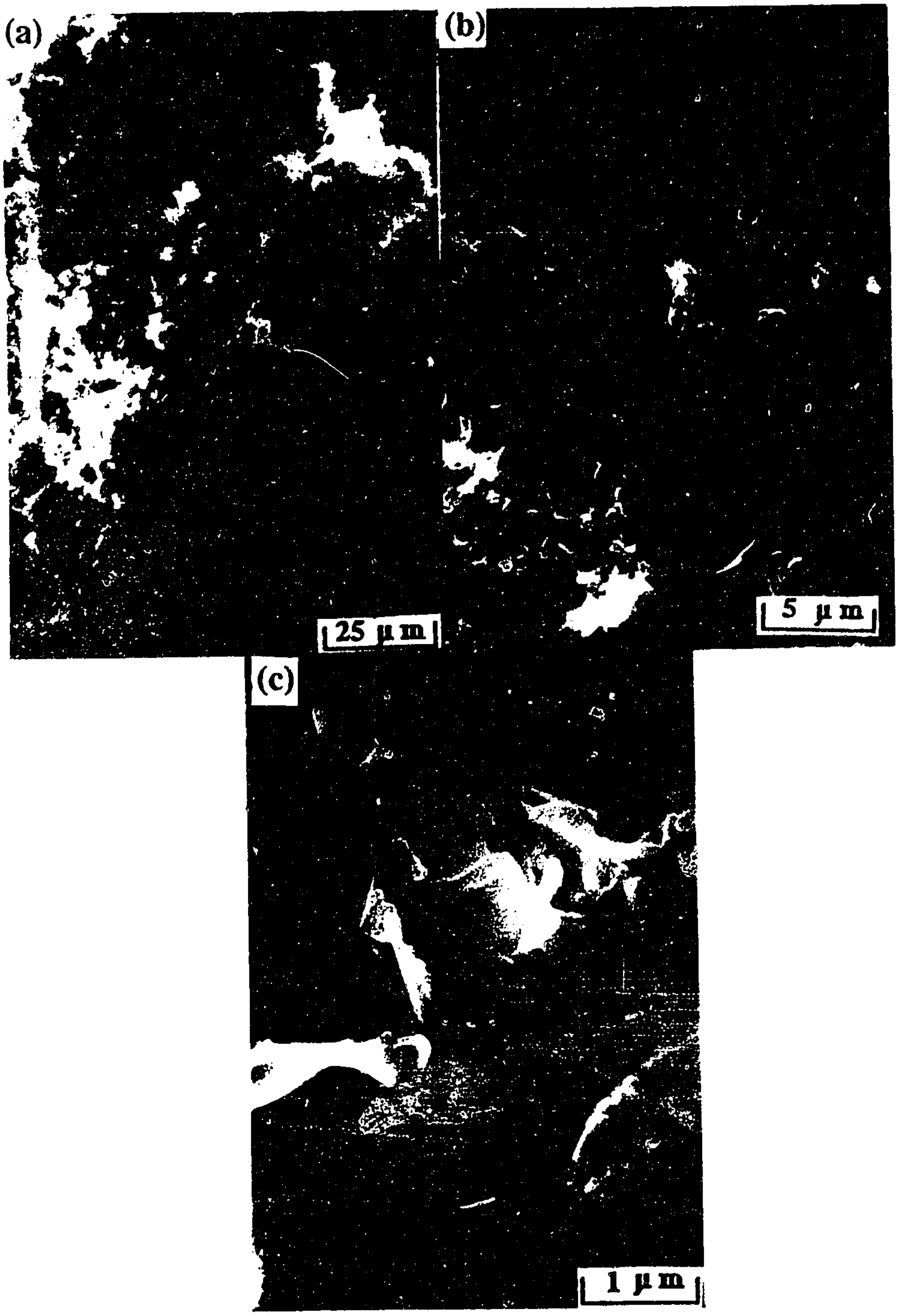

Fig. 6.3-4 - SEM micrographs made at 15 kV and at several magnifications, of the flocculated montmorillonite sediment made at pH = 9.5 with hydroxoferric particles at a solid content of 0.5 % by mass.

6.3.3 - Montmorillonite-unaged $AlCl_3$ flocculated sediments

Two series of SEM micrographs were made on the flocculated sediments from 1% montmorillonite suspensions mixed with unaged $AlCl_3$ at pH=9.5. The unaged $AlCl_3$ concentrations were respectively 2 and 5mM (Figs.6.3-5 and 6.3-6). These sediments appeared to be comprised of flocs with a fractal type aspect. The clay particles were mostly connected in the EE mode.

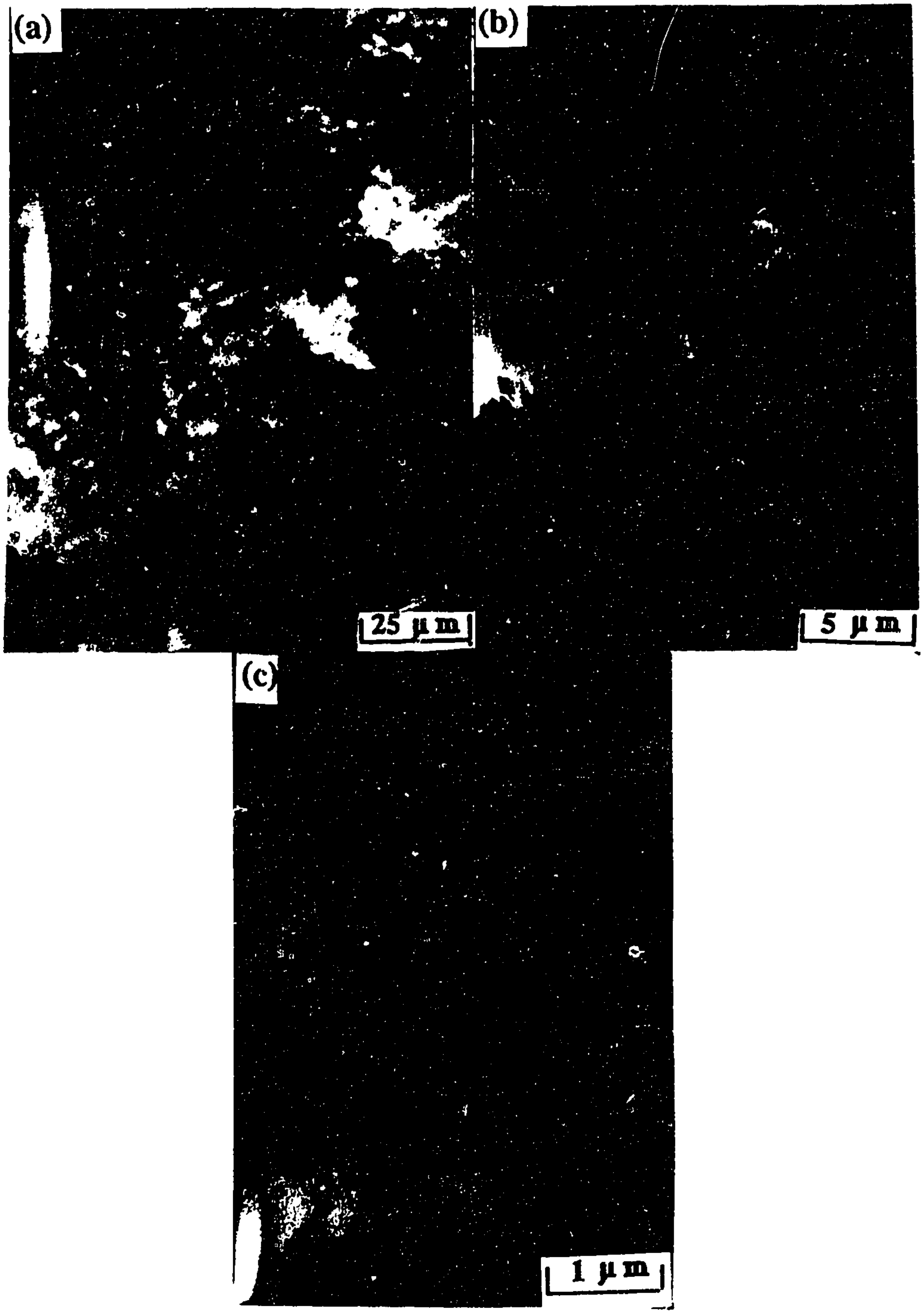

Fig. 6.3-5 - SEM micrographs made at 10 kV and at several magnifications, of the flocculated montmorillonite sediment made at pH = 9.5 with unaged $AlCl_3$ at a concentration of 2mM.

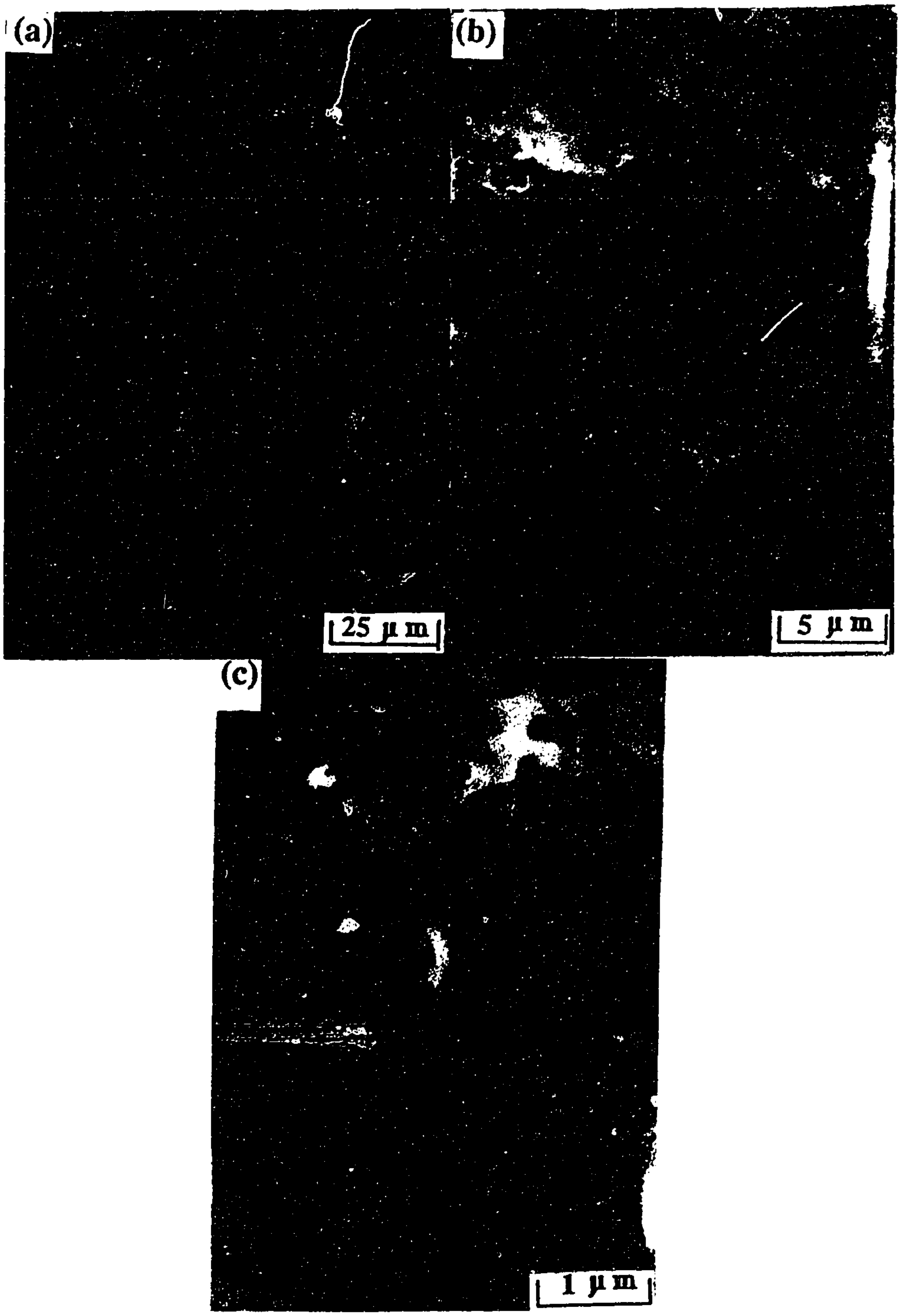

Fig. 6.3-6 - SEM micrographs made at 15 kV and at several magnifications, of the flocculated montmorillonite sediment made at pH = 9.5 with unaged $AlCl_3$ at a concentration of 5mM.

CHAPTER 7 - MATHEMATICAL MODELING

7.1 - INTRODUCTION TO THE MATHEMATICAL MODELING

As reviewed in Section 2.3, when flocculation occurs in a suspension of platelike kaolinite or montmorillonite particles, several different modes of particles association are possible, such as face-to-face (FF), edge-to-face (EF) and edge-to-edge (EE). In the present experimental investigation, a good correlation was found between the absolute value of the zeta potential of the clay particles and the type of sedimentation behavior, as reported in Section 5.4. More precisely, flocculation-sedimentation occurred when $|\zeta| < 0.01$ V, accumulation-sedimentation occurred when $|\zeta| > 0.015$ V, and mixed flocculation-accumulation sedimentation occurred when $0.01 \text{ V} \leq |\zeta| \leq 0.015$ V.

The objective of the present chapter is to use typical zeta potential values, as correlated with a type of sedimentation behavior according to our data, to compute the interaction between platelike particles, according to the DLVO theory. The calculation must take into account the full possible range of particle orientation with respect to each other, in order to determine if an EE, an EF, or any other particle association mode at any angle, is more probable. The results of the computation will eventually be compared with the SEM observations of the sediments dried by the supercritical method.

The calculations were only developed in the case where the clay particles had electric charges with the same sign (i.e. negative charges) on both the edges and the faces, because drastic differences between the microstructure of different sediments (i.e. accumulated or flocculated sediments) could only be observed in this case.

7.2 - FORMULATION OF THE MATHEMATICAL MODEL

7.2.1 - Geometrical configuration

The particle geometry used in the present study was derived from Tateyama et al. [64]. It is comprised of two identical platelike particles, which approach each other at an angle θ, as shown in Fig. 7.2-1. The two particles have the same length L_1, the same width L_2, the same thickness δ, and they are separated by the nearest distance of $2h_0$. The edge of the first particle is close to the edge of the second particle. Hence, this model differs from the stair-step model by O'Brien (Section 2.4.1), where the edge of the first particle is close to the face of the second particle, at any location.

For clay platelike particles, it is assumed that the faces carry a constant electric charge density σ_f, in agreement with the review in Section 2.3.2.1. On the other hand, the edges are considered to be at a constant electric potential ψ_e.

7.2.2 - Formulation of the van der Waals attraction energy

The mathematical expression for the van der Waals attraction energy $U_A(\theta)$ between two platelike particles at an angle θ ($0° \le \theta \le 90°$) was derived by Tateyama et al. [64]. This attraction term is:

$$
\begin{aligned}
U_A = {} & -\frac{A L_1 L_2}{12\pi\cos\theta} \\
& \times \left[\frac{1}{2h_0(2h_0 + L_2\sin\theta)} + \frac{1}{(2h_0 + L_2\sin\theta + \delta\cos\theta + \delta)(2h_0 + \delta\cos\theta + \delta)} \right. \qquad (7.2\text{-}1) \\
& \left. - \frac{1}{(2h_0 + L_2\sin\theta + \delta\cos\theta)(2h_0 + \delta\cos\theta)} - \frac{1}{(2h_0 + L_2\sin\theta + \delta)(2h_0 + \delta)} \right]
\end{aligned}
$$

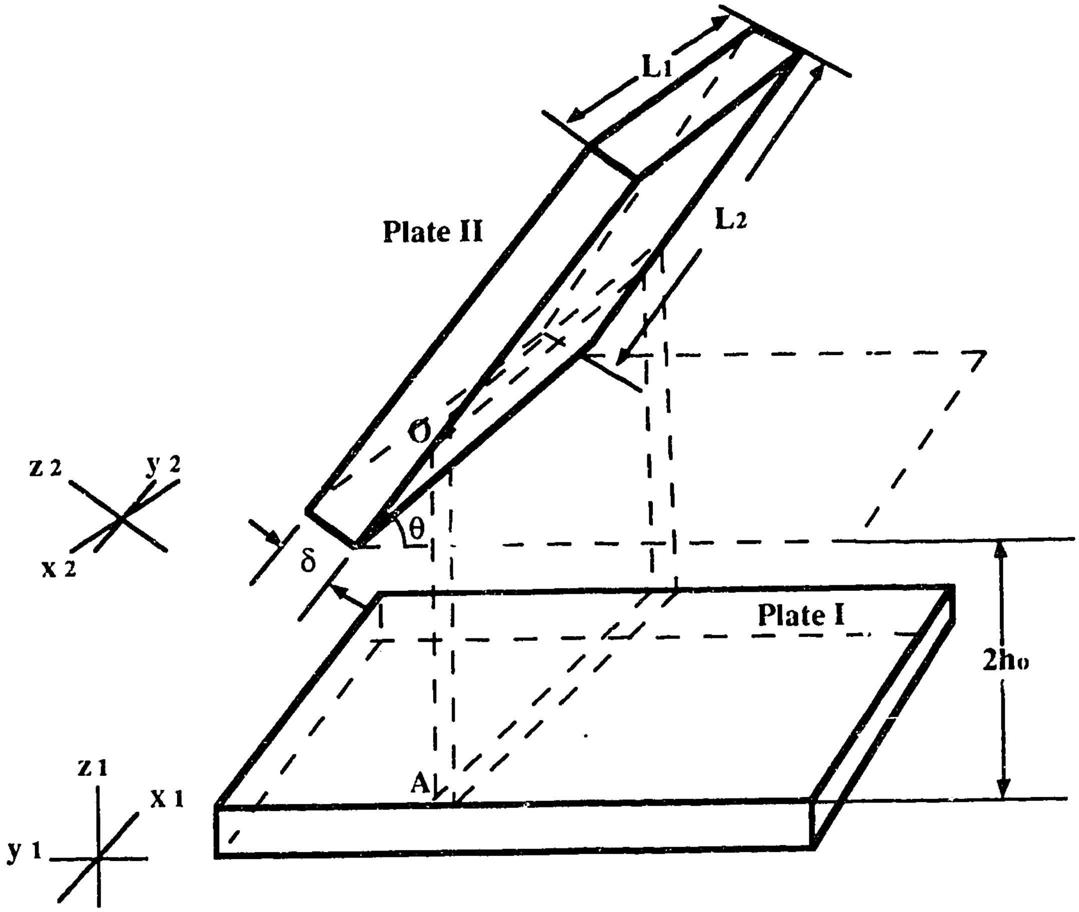
L1
Plate II
L2
σ
θ
δ
z 2
y 2
x 2
Plate I
2h0
A
z 1
x 1
y 1

Fig. 7.2-1 - Illustration of the geometrical model used to compute the interaction between two platelike particles at an angle θ.

When $\theta = 0$, equation (7.2-1) becomes

$$U_A = - \frac{AL_1L_2}{12\pi} \times \left[\frac{1}{(2h_0)^2} + \frac{1}{(2h_0+2\delta)^2} - \frac{2}{(2h_0+\delta)^2} \right] \qquad (7.2\text{-}2)$$

and when $\theta = 90°$, equation (7.2-1) becomes

$$U_A(90°) = - \frac{AL_1L_2\delta}{12\pi} \times \left[\frac{4h_0+L_2}{(2h_0)^2(2h_0+L_2)^2} - \frac{4h_0+L_2+2\delta}{(2h_0+\delta)^2(2h_0+L_2+\delta)^2} \right] \qquad (7.2\text{-}3)$$

7.2.3 - Formulation of the electrostatic interaction energy

The interaction of the two platelike particles in Fig. 7.2-1 can be calculated by a method summarized by Hiemenz [10]. This method consists in summing up the elementary interactions U_R $(2h = y_2\sin\theta + 2h_0)$ $(0° \leq \theta \leq 90°)$ between narrow rectangular and parallel plates at a distance $2h = (2h_0 + y_2\sin\theta)$ from each other. In these conditions, the interaction energy due to the electrostatic repulsion between the two platelike particles is given by the following equation [64] :

$$U_R(\theta) = \int_0^{L_1}\int_0^{L_2} U_R(2h = y_2\sin\theta + 2h_0)\cos\theta \, dx_2 dy_2 \qquad (7.2\text{-}4)$$

In this equation, the electrostatic interaction U_R $(2h = y_2\sin\theta + 2h_0)$ was expressed in Section 2.2.2.6, for various conditions.

7.2.3.1 - Electrostatic energy between two faces

Equation (2.2-27) is introduced into equation (7.2-4) and the integrations are from 0 to L_1 and from 0 to L_2 so that

$$U_R^{FF}(\theta) = \int_0^{L_1}\int_0^{L_2} \frac{\varepsilon\varepsilon_0\kappa}{2}\{(\psi_{f1}^2+\psi_{f2}^2)[\coth\kappa(y_2\sin\theta+2h_0) - 1]$$

$$+ 2\psi_{f1}\psi_{f2}\,\mathrm{cosech}\,\kappa(y_2\sin\theta+2h_0)\}\cos\theta \, dx_2 dy_2$$

$$= \frac{\varepsilon\varepsilon_0\kappa}{2}L_1\cos\theta(A + B) \tag{7.2-5}$$

where

$$\begin{aligned}
A &= \int_0^{L_2} (\psi_{f1}^2+\psi_{f2}^2)[\coth\kappa(y_2\sin\theta+2h_0) - 1]dy_2 \\
&= \frac{\psi_{f1}^2+\psi_{f2}^2}{\sin\theta\kappa}\left\{\ln\left(\frac{sh\kappa(L_2\sin\theta+2h_0)}{sh(2\kappa h_0)}\right) - L_2\sin\theta\kappa\right\} \\
&= \frac{\psi_{f1}^2+\psi_{f2}^2}{\sin\theta\kappa}\left\{\ln[\exp(L_2\sin\theta\kappa)] + \ln\left(\frac{1 - \exp[-2\kappa(L_2\sin\theta+2h_0)]}{1 - \exp(-4\kappa h_0)}\right) - L_2\sin\theta\kappa\right\} \\
&= \frac{\psi_{f1}^2+\psi_{f2}^2}{\sin\theta\kappa}\ln\left(\frac{1 - \exp[-2\kappa(L_2\sin\theta+2h_0)]}{1 - \exp(-4\kappa h_0)}\right)
\end{aligned} \tag{7.2-6}$$

and

$$\begin{aligned}
B &= 2\psi_{f1}\psi_{f2}\int_0^{L_2} \mathrm{cosech}\,\kappa(y_2\sin\theta+2h_0)dy_2 \\
&= 2\frac{\psi_{f1}\psi_{f2}}{\sin\theta\kappa}\ln\left(\frac{\tanh\frac{\kappa}{2}(L_2\sin\theta+2h_0)}{\tanh(\kappa h_0)}\right) \\
&= -2\frac{\psi_{f1}\psi_{f2}}{\sin\theta\kappa}\ln\left(\frac{\{1 + \exp[-\kappa(L_2\sin\theta+2h_0)]\}[1 - \exp(-2\kappa h_0)]}{\{1 - \exp[-\kappa(L_2\sin\theta+2h_0)]\}[1 + \exp(-2\kappa h_0)]}\right)
\end{aligned} \tag{7.2-7}$$

Combining equations (7.2-5) to (7.2-7). The electrostatic energy between two faces is

$$\begin{aligned}
U_R^{FF}(\theta) = &\frac{\varepsilon\varepsilon_0\cos\theta}{2\sin\theta}L_1[(\psi_{f1}^2+\psi_{f2}^2)\ln\left(\frac{1 - \exp[-2\kappa(L_2\sin\theta+2h_0)]}{1 - \exp(-4\kappa h_0)}\right) \\
&-2\frac{\psi_{f1}\psi_{f2}}{\sin\theta\kappa}\ln\left(\frac{\{1 + \exp[-\kappa(L_2\sin\theta+2h_0)]\}[1 - \exp(-2\kappa h_0)]}{\{1 - \exp[-\kappa(L_2\sin\theta+2h_0)]\}[1 + \exp(-2\kappa h_0)]}\right)
\end{aligned} \tag{7.2-8}$$

When $\psi_{f1} = \psi_{f2} = \psi_f$, equation (7.2-8) becomes

$$\begin{aligned}
U_R^{FF}(\theta) = &\frac{\varepsilon\varepsilon_0\cos\theta}{\sin\theta}L_1\psi_f^2[\ln\left(\frac{1 - \exp[-2\kappa(L_2\sin\theta+2h_0)]}{1 - \exp(-4\kappa h_0)}\right) \\
&-\ln\left(\frac{\{1 + \exp[-\kappa(L_2\sin\theta+2h_0)]\}[1 - \exp(-2\kappa h_0)]}{\{1 - \exp[-\kappa(L_2\sin\theta+2h_0)]\}[1 + \exp(-2\kappa h_0)]}\right)]
\end{aligned} \tag{7.2-9}$$

7.2.3.2 - electrostatic energy between a face and an edge

As shown in Fig. 7.2.1, when two faces approach each other with an angle θ, the face and the edge approach each other with an anle 90° - θ. Equation (2.2-29) is introduced into equation (7.2-4) and the integrations are from 0 to L_1 and from 0 to δ so that

$$\begin{aligned} U_R^{EF}(\theta) &= \int_0^{L_1}\int_0^{\delta} \frac{\varepsilon\varepsilon_0\kappa}{2}\{(\psi_e^2-\psi_f^2)[\tanh\kappa(y_2\cos\theta+2h_0) - 1] \\ &\quad + 2\psi_e\psi_f \operatorname{sech}\kappa(y_2\cos\theta+2h_0)\}\sin\theta dx_2 dy_2 \\ &= \frac{\varepsilon\varepsilon_0\kappa}{2} L_1 \sin\theta(A + B) \end{aligned} \tag{7.2-10}$$

where

$$\begin{aligned} A &= \int_0^{\delta} (\psi_e^2-\psi_f^2)[\tanh\kappa(y_2\cos\theta+2h_0) - 1]dy_2 \\ &= \frac{\psi_e^2-\psi_f^2}{\cos\theta\kappa}\{\ln\left(\frac{\operatorname{ch}\kappa(\delta\cos\theta+2h_0)}{\operatorname{ch}(2\kappa h_0)}\right) - \delta\cos\theta\kappa\} \\ &= \frac{\psi_e^2-\psi_f^2}{\cos\theta\kappa}\{\ln[\exp(\delta\cos\theta\kappa)] + \ln\left(\frac{1 + \exp[-2\kappa(\delta\cos\theta+2h_0)]}{1 + \exp(-4\kappa h_0)}\right) - \delta\cos\theta\kappa\} \\ &= \frac{\psi_e^2-\psi_f^2}{\cos\theta\kappa}\ln\left(\frac{1 + \exp[-2\kappa(\delta\cos\theta+2h_0)]}{1 + \exp(-4\kappa h_0)}\right) \end{aligned} \tag{7.2-11}$$

and

$$\begin{aligned} B &= 2\psi_e\psi_f\int_0^{\delta} \operatorname{sech}\kappa(y_2\cos\theta+2h_0)dy_2 \\ &= 2\frac{\psi_e\psi_f}{\cos\theta\kappa}\{\arcsin[\tanh\kappa(\delta\cos\theta+2h_0)] - \arcsin[\tanh(2\kappa h_0)]\} \\ &= 2\frac{\psi_e\psi_f}{\cos\theta\kappa}\{\arcsin\left(\frac{1 - \exp[-2\kappa(\delta\cos\theta+2h_0)]}{1 + \exp[-2\kappa(\delta\cos\theta+2h_0)]}\right) - \arcsin\left(\frac{1 - \exp(-4\kappa h_0)}{1 + \exp(-4\kappa h_0)}\right)\} \end{aligned} \tag{7.2-12}$$

Combining equations of (7.2-10) to (7.2-12), the electrostatic energy between the face and the edge is

$$U_R^{EF}(\theta) = \frac{\varepsilon\varepsilon_0 \sin\theta}{2\cos\theta} L_1 [(\psi_e^2 - \psi_f^2) \ln\left(\frac{1 + \exp[-2\kappa(\delta\cos\theta + 2h_0)]}{1 + \exp(-4\kappa h_0)}\right)$$
$$+ 2\psi_e\psi_f \{\arcsin\left(\frac{1 - \exp[-2\kappa(\delta\cos\theta + 2h_0)]}{1 + \exp[-2\kappa(\delta\cos\theta + 2h_0)]}\right)$$
$$- \arcsin\left(\frac{1 - \exp(-4\kappa h_0)}{1 + \exp(-4\kappa h_0)}\right)\}] \qquad (7.2\text{-}13)$$

7.2.4 - Total interaction energy when the faces of two platelike particles are at an angle θ.

This association mode corresponds to the general geometrical case which is illustrated in Fig. 7.2-1. The van der Waals attraction energy, as a function of the angle θ, can be calculated from equation (7.2-1). As for the electrostatic repulsion energy, it can be obtained by integrating equation (7.2-4). This electrostatic energy is comprised of two terms: (1) the electrostatic energy U_R^{FF} (θ) between the two faces which are identical in the present case; and (2) the electrostatic energy U_R^{EF}(θ) between the edge and the face. The total interaction energy between the two platelike particles, as a function of the angle θ and the distance $2h_0$, is given by

$$U_{Total}(\theta, 2h_0) = (7.2\text{-}1) + (7.2\text{-}9) + (7.2\text{-}13) \qquad (7.2\text{-}14)$$

7.2.5 - Total interaction energy for a few important modes of particles association

7.2.5.1 - Face-to-face (FF) association mode

When θ = 0° in Fig. 7.2-1, the two particles are connected in the face to face (FF) mode, as shown in Fig. 7.2-2(a). Assumi at the faces of the two clay particles carry the same constant surface charge density σ_f, this surface charge density σ_f can be replaced by the electric potential ψ_f when the two particles are separated by an infinite gap. In this case, equation (7.2-9) becomes:

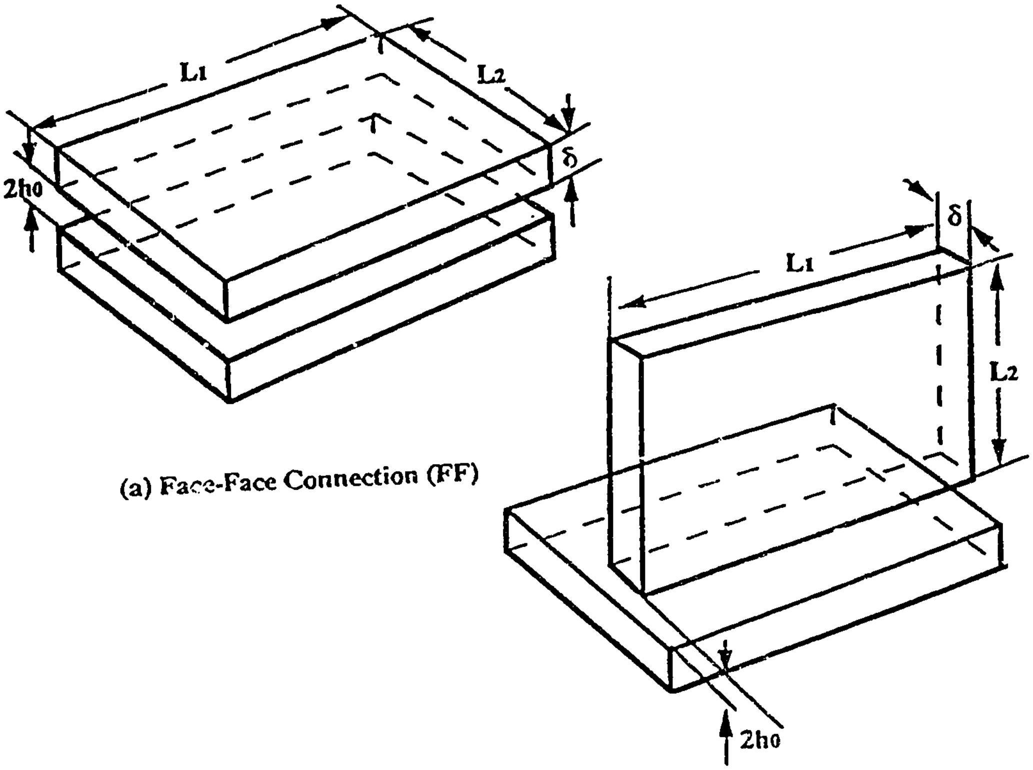
L1
L2
δ
2h0
δ
L1
L2
2h0

(a) Face-Face Connection (FF)

(b) Edge-Face Connection (EF)

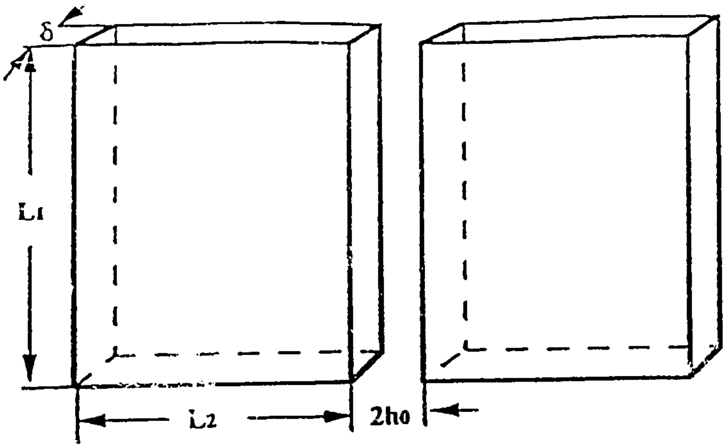

(c) Edge-Edge Connection (EE)

Fig. 7.2-2 - Platelike particles association modes: (a) FF mode; (b) EF mode; (c) EE mode.

$$\lim_{\theta\to 0} U_R^{FF}(\theta) = \frac{\varepsilon\varepsilon_0}{(tg\theta)'} L_1\psi_f^2\{[\ln\left(\frac{1 - \exp[-2\kappa(L_2\sin\theta+2h_0)]}{1 - \exp(-4\kappa h_0)}\right)]'$$

$$-[\ln\left(\frac{\{1 + \exp[-\kappa(L_2\sin\theta+2h_0)]\}[1 - \exp(-2\kappa h_0)]}{\{1 - \exp[-\kappa(L_2\sin\theta+2h_0)]\}[1 + \exp(-2\kappa h_0)]}\right)]'\}$$

$$= L_1L_2\varepsilon\varepsilon_0\kappa\psi_f^2\cos^3\theta\{\frac{2\exp[-2\kappa(L_2\sin\theta+2h_0)]}{1 - \exp[-2\kappa(L_2\sin\theta+2h_0)]}$$

$$+\frac{\exp[-\kappa(L_2\sin\theta+2h_0)]}{1 + \exp[-\kappa(L_2\sin\theta+2h_0)]} + \frac{\exp[-\kappa(L_2\sin\theta+2h_0)]}{1 - \exp[-\kappa(L_2\sin\theta+2h_0)]}\} \quad (7.2\text{-}15)$$

$$= L_1L_2\varepsilon\varepsilon_0\kappa\psi_f^2\{\frac{2\exp(-4\kappa h_0)}{1 - \exp(-4\kappa h_0)} + \frac{\exp(-2\kappa h_0)}{1 + \exp(-2\kappa h_0)} + \frac{\exp(-2\kappa h_0)}{1 - \exp(-2\kappa h_0)}\}$$

The electrostatic energy between two faces is

$$U_R^{FF} = L_1L_2\varepsilon\varepsilon_0\kappa\psi_f^2[(\coth 2\kappa h_0 - 1) + \mathrm{cosech}\, 2\kappa h_0] \quad (7.2\text{-}16)$$

The van der Waals attraction energy is provided by equation (7.2-2), and the total interaction energy between the two platelike particles in the FF association mode is:

$$U_{Total}(FF) = (7.2\text{-}2) + (7.2\text{-}16) \quad (7.2\text{-}17)$$

7.2.5.2 - Edge-to-face (EF) association mode

When $\theta = 90°$ in Fig. 7.2-1, the two particles are connected in the edge to face (EF) mode, as shown in Fig. 7.2.2(b). The constant charge density on the faces σ_1 can be replaced by the face electric potential ψ_f when the particles are far from each other. In this case, equation (7.2-13) becomes

$$\lim_{\theta\to 90^0} U_R^{EF}(\theta) = -\frac{L_1\varepsilon_0\varepsilon}{2(ctg\theta)'}[(\psi_e^2 - \psi_f^2)[\{\ln\left(\frac{1 + \exp[-2\kappa(\delta\cos\theta+2h_0)]}{1+\exp(-4\kappa h_0)}\right)\}'$$

$$+ 2\psi_e\psi_f\{\arcsin\left(\frac{1 - \exp[-2\kappa(\delta\cos\theta+2h_0)]}{1 + \exp[-2\kappa(\delta\cos\theta+2h_0)]}\right)\}']$$

$$=\frac{L_1\delta\varepsilon_0\varepsilon\kappa\sin^3\theta}{2}\{(\psi_e^2-\psi_f^2)\left(\frac{-2\exp[-2\kappa(\delta\cos\theta+2h_0)]}{1+\exp[-2\kappa(\delta\cos\theta+2h_0)]}\right)$$

$$+2\psi_e\psi_f\left(\frac{2\exp[-\kappa(\delta\cos\theta+2h_0)]}{1+\exp[-2\kappa(\delta\cos\theta+2h_0)]}\right)\} \qquad (7.2\text{-}18)$$

$$=\frac{L_1\delta\varepsilon_0\varepsilon\kappa}{2}\{(\psi_e^2-\psi_f^2)\left(\frac{-2\exp(-4\kappa h_0)}{1+\exp(-4\kappa h_0)}\right)+2\psi_e\psi_f\left(\frac{2\exp(-2\kappa h_0)}{1+\exp(-4\kappa h_0)}\right)\}$$

so that the electrostatic energy between the face and the edge is

$$U_R^{EF}=\frac{L_1\delta\varepsilon_0\varepsilon\kappa}{2}[(\psi_e^2-\psi_f^2)(\tanh 2\kappa h_0-1)+2\psi_e\psi_f\operatorname{sech}2\kappa h_0] \qquad (7.2\text{-}19)$$

When two platelike particles are associated according to the EF mode, as this is illustrated in Fig. 7.2-2b, the attraction energy U_A is given by equation (7.2-3).

The total interaction energy for the EF association mode is:

$$U_{Total}(EF) = (7.2\text{-}3) + (7.2\text{-}19) \qquad (7.2\text{-}20)$$

7.2.5.3 - Edge-to-edge (EE) association mode

Fig. 7.2-2c shows two platelike particles that are associated in the EE mode. By comparing Fig. 7.2-2a and Fig. 7.2-2c, the FF mode and the EE mode are similar to each other in geometry. The FF mode can be changed to the EE mode by exchanging the thickness δ with the width L_2. Hence, by comparing equation (7.2.2), the attraction energy for the EE mode, is given by equation (7.2-21):

$$U_A=-\frac{AL_1\delta}{12\pi}\times\left[\frac{1}{(2h_0)^2}+\frac{1}{(2h_0+2L_2)^2}-\frac{2}{(2h_0+L_2)^2}\right] \qquad (7.2\text{-}21)$$

Since the edges have a constant electric potential ψ_e, the electrostatic energy between them can be calculated from equation (2.2-25) which gives:

$$U_R^{EE}=\int_0^{L_1}\int_0^{\delta}\varepsilon\varepsilon_0\kappa\psi_e^2[(1-\coth 2\kappa h_0)+\operatorname{cosech}2\kappa h_0]\,dx_2dy_2 \qquad (7.2\text{-}22)$$

$$U_R^{EE} = L_1 \delta \varepsilon \varepsilon_0 \kappa \psi_e^2 [\, (1 - \coth 2\kappa h_0) + \operatorname{cosech} 2\kappa h_0] \qquad (7.2\text{-}23)$$

The total interaction between two platelike particles in the edge to edge mode is:

$$U_{Total}(EE) = (7.2\text{-}21) + (7.2\text{-}23) \qquad (7.2\text{-}24)$$

7.3 - RESULTS OF THE COMPUTATION OF INTERACTIONS IN A SELECTED CASES

7.3.1 - Computation for experimental conditions where accumulation sedimentation occurred

7.3.1.1 - Computation parameters

According to the results on the zeta potential, as reported in Section 5.4.2.1 for kaolinite suspension mixed with $FeCl_3$, accumulation sedimentation occurred when $|\zeta| > 0.015$ V. Examples of typical electrolyte conditions were at pH=9.5 and without unaged $FeCl_3$, where $|\zeta| \approx 0.025$ V. Although this zeta potential result provided only the average surface electrical potential of a particle in the suspension, the exact values of surface potential on faces or edges were not available. Hence, several combinations of electric potentials on edges and faces will be assumed in the following calculation in order to simulate the zeta potential of 0.025 V in a suspension.

In the present study, computations of interaction energy between platelike particles were made with the following characteristics according to the size of HUF clay particles and the experimental conditions:

(1) Identical platelike dimensions: $L_1 = L_2 = 4 \times 10^{-7}$ m, $\delta = 5 \times 10^{-8}$ m

(2) $T = 298K$

(3) $A = 2 \times 10^{-20}$ J

(4) (a) $\psi_f = -0.03$ V, $\psi_e = -0.02$ V; (b) $\psi_f = -0.02$ V, $\psi_e = -0.03$ V; (c) $\psi_f = \psi_e = -0.025$ V.

(5) In each group of combination of surface potentials on faces and edges, different concentrations of the 1:1 electrolyte are chosen. The interaction modes will be different at each chosen concentration. (For convenience, the concentration of the 1: 1 electrolyte in a suspension is represented by c_0).

7.3.1.2 - Comparison of FF, EF and EE association modes

When ψ_f = -0.03 V and ψ_e = -0.02 V, Figs. 7.3-1(a), (b) and (c) show the variation of interaction energy for the FF, the EF, and the EE association modes as a function of the distance between two particles at the concentration of the 1:1 electrolyte c_0 = 0.01 M, 0.03 M, and 0.06 M, respectively. From the calculation, no association should occur with the electrolyte concentration of 10 mM. With an increase in concentration of the electrolyte, the dispersed suspension will be flocculated. The platelike particles should connect in the EE mode at the electrolyte concentration of 30 mM. The EE and the FF modes should coexist and the FF mode is the most favored at c_0 =0.06 M according to this model.

When ψ_f = -0.02 V and ψ_e = -0.03 V, no particle assocations occur until the electrolyte concentration is 5 mM (Fig. 7.3-2a). In the case of $\psi_f = \psi_e$ = -0.025 V, no association should occur at the concentration of the electrolyte c_0 = 0.01 M (Fig. 7.3-2b). According to the calculation, particles should connect from the EE mode to a mixture of the EE and FF modes with an increase in concentration of the electrolyte in both cases (ψ_f = -0.02 V, ψ_e = -0.03 V; or $\psi_f = \psi_e$ = -0.025 V).

This result is consistent with that a sediment was made of randomly accumulated particles when $|\zeta| > 0.015$ V. Also, it confirms that clay particles were associated in the FF mode in the suspensions with high concentration of electrolytes.

7.3.1.3 - Effect of the platelike particles thickness on EE aggregation

The effect of the particles plate thickness δ on the total interaction energy, for the EE association mode and for 10 mM of a 1:1 indifferent electrolyte, is reported in Fig. 7.3-3. This figure shows that the energy barrier which opposes aggregation, decreases with the particles thickness. Hence, as the particles become thinner, EE aggregation has an increasing chance to occur.

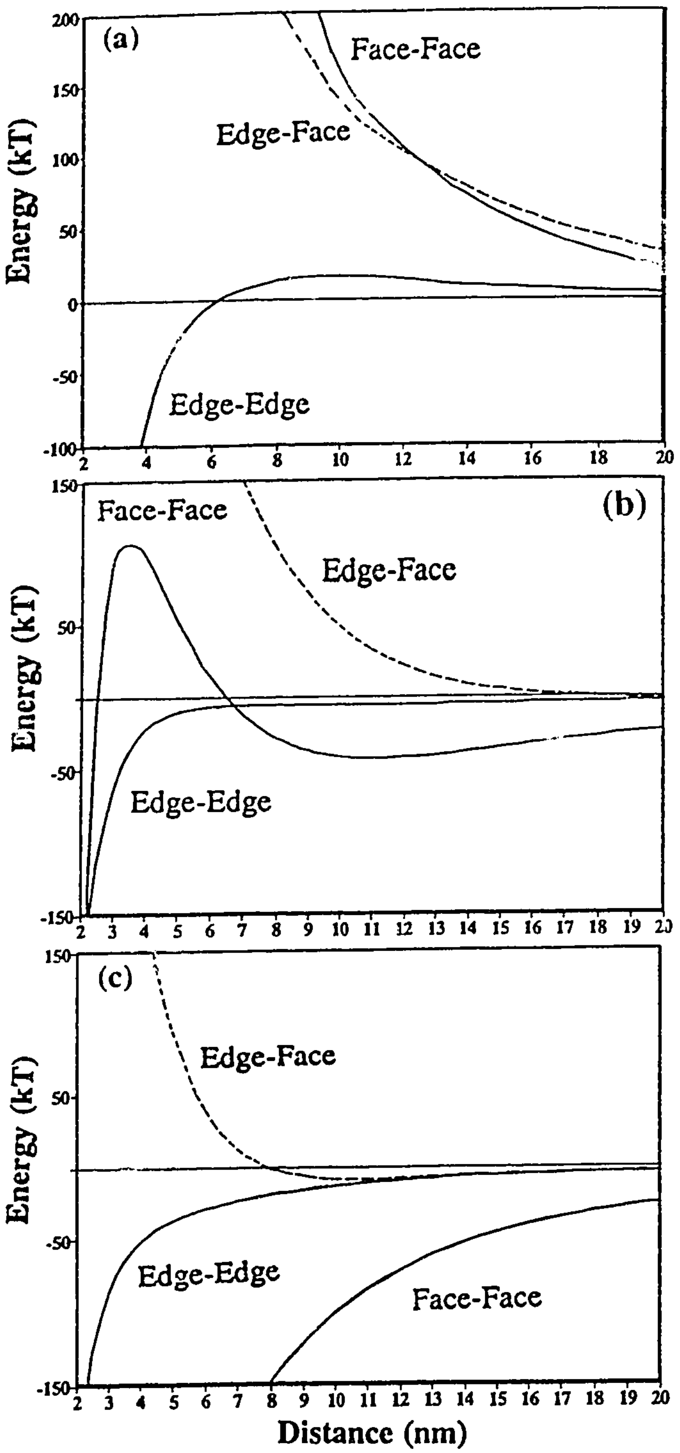

Fig. 7.3-1 - Total interaction energy between two platelike particles, as a function of the nearest separation distance between the particles, for FF, EF, and EE configurations. General conditions: $L_1 = L_2 = 4 \times 10^{-7}$ m, $\delta = 5 \times 10^{-8}$ m, T = 298K, $A = 2 \times 10^{-20}$ J, $\psi_f = -0.03$ V, $\psi_c = -0.02$ V, 1:1 type electrolyte at the concentrations: (a) 10mM; (b) 30mM; (c) 60mM.

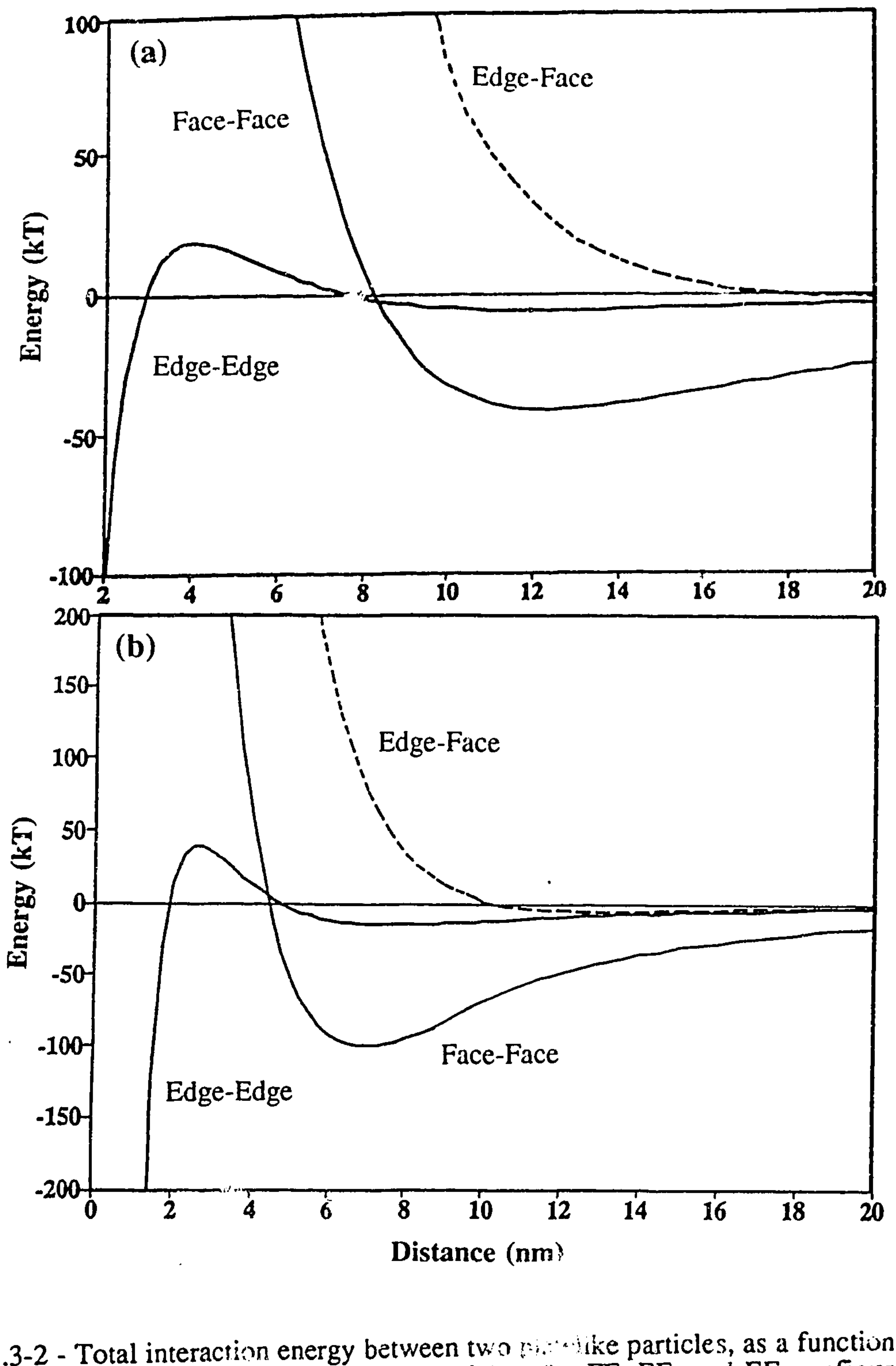

Fig. 7.3-2 - Total interaction energy between two plate-like particles, as a function of the nearest separation distance between the particles, for FF, EF, and EE configurations. General conditions: $L_1 = L_2 = 4 \times 10^{-7}$ m, $\delta = 5 \times 10^{-8}$ m, T = 298K, $A = 2 \times 10^{-20}$ J : (a) $\psi_f = -0.02$ V and $\psi_e = -0.03$ V, 1:1 type electrolyte at the concentrations of 5 mM; (b) $\psi_f = \psi_e = -0.02$ V, 1:1 type electrolyte at the concentrations of 10 mM.

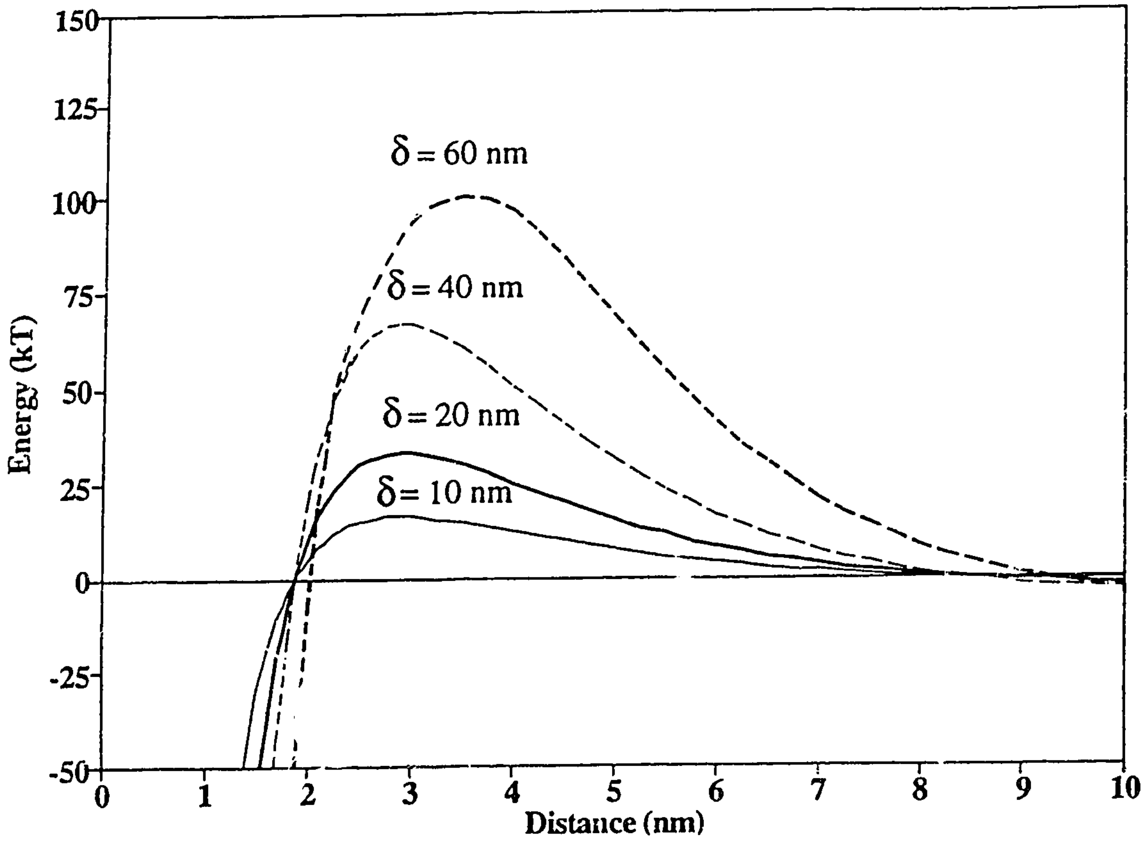

Fig. 7.3-3 - Total interaction energy between two platelike particles, as a function of the nearest separation distance between the particles, for the EE configuration. General conditions: $L_1 = L_2 = 4 \times 10^{-7}$ m, $\delta = 5 \times 10^{-8}$ m, T = 298K, A = 2×10^{-20} J, $\psi_f = \psi_e = -0.025$ V, 1:1 type electrolyte at the concentration of 10mM.

7.3.2 - Computation for experimental conditions where flocculation sedimentation occurred

7.3.2.1 - Computation parameters

According to the results on the zeta potential, reported in the Section 5.4.2.1 for kaolinite suspension mixed with $FeCl_3$, flocculation sedimentation occurred when $|\zeta| < 0.01$ V. An example of typical electrolyte conditions was at pH= 4 for the unaged $FeCl_3$ concentrations of 0.67 mM, where $|\zeta| \approx 0.004$ V.

In the present study, computations were made for platelike particles with the same geometrical characteristics as in 7.3.1 and with the following electrical characteristics:

(4) (a) $\psi_f = -0.015$ V, $\psi_e = -0.005$ V; (b) $\psi_f = -0.005$ V, $\psi_e = -0.015$ V; (c) $\psi_f = \psi_e = -0.01$ V

(5) Several different concentrations of 1:1 electrolytes were chosen using a similar method to Section 7.3.1.1(4).

7.3.2.2 - Comparison of FF, EF and EE association modes

The interaction energies for FF, EF and FF association modes, as a function of the nearest separation distance $2h_0$ between the particles, are reported in Fig. 7.3-4 for the case using $\psi_f = -0.015$ V and $\psi_e = -0.005$ V. According to these computations, EE association should occur with an indifferent electrolyte concentration of 0.1 mM (Fig. 7.3-4a). Then, the particles should connect in the EE and the FF modes with increasing of electrolyte concentration (Fig. 7.3-4b). At a high concentration of the electrolyte, three particle association modes can coexist according to the model (Fig. 7.3-4c). For the cases where (b) $\psi_f = -0.005$ V and $\psi_e = -0.015$ V, and (c) $\psi_f = \psi_e = -0.01$ V, EE association could occur at electrolyte concentration of the electrolyte as low as 0.1 mM, as shown in Fig. 7.3-5. This is consistent with a sedimentation which involves at least partially a flocculation process.

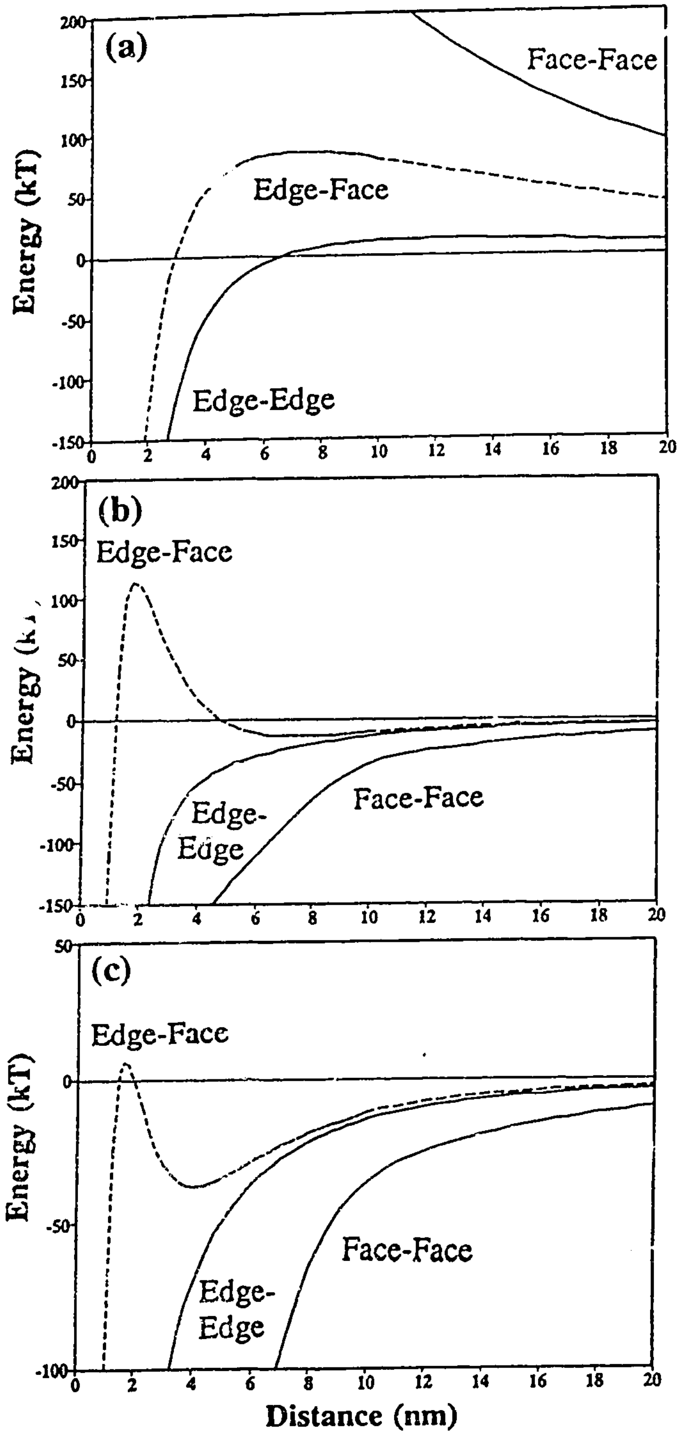

Fig. 7.3-4 - Total interaction energy between two platelike particles, as a function of the nearest separation distance between the particles, for FF, EF, and EE configurations. General conditions: $L_1 = L_2 = 4 \times 10^{-7}$ m, $\delta = 5 \times 10^{-8}$ m, T = 298K, $A = 2 \times 10^{-20}$ J, $\psi_f = -0.015$ V, $\psi_e = -0.005$ V, 1:1 type electrolyte at the concentrations: (a) 0.1 mM; (b) 10mM; (c) 20mM.

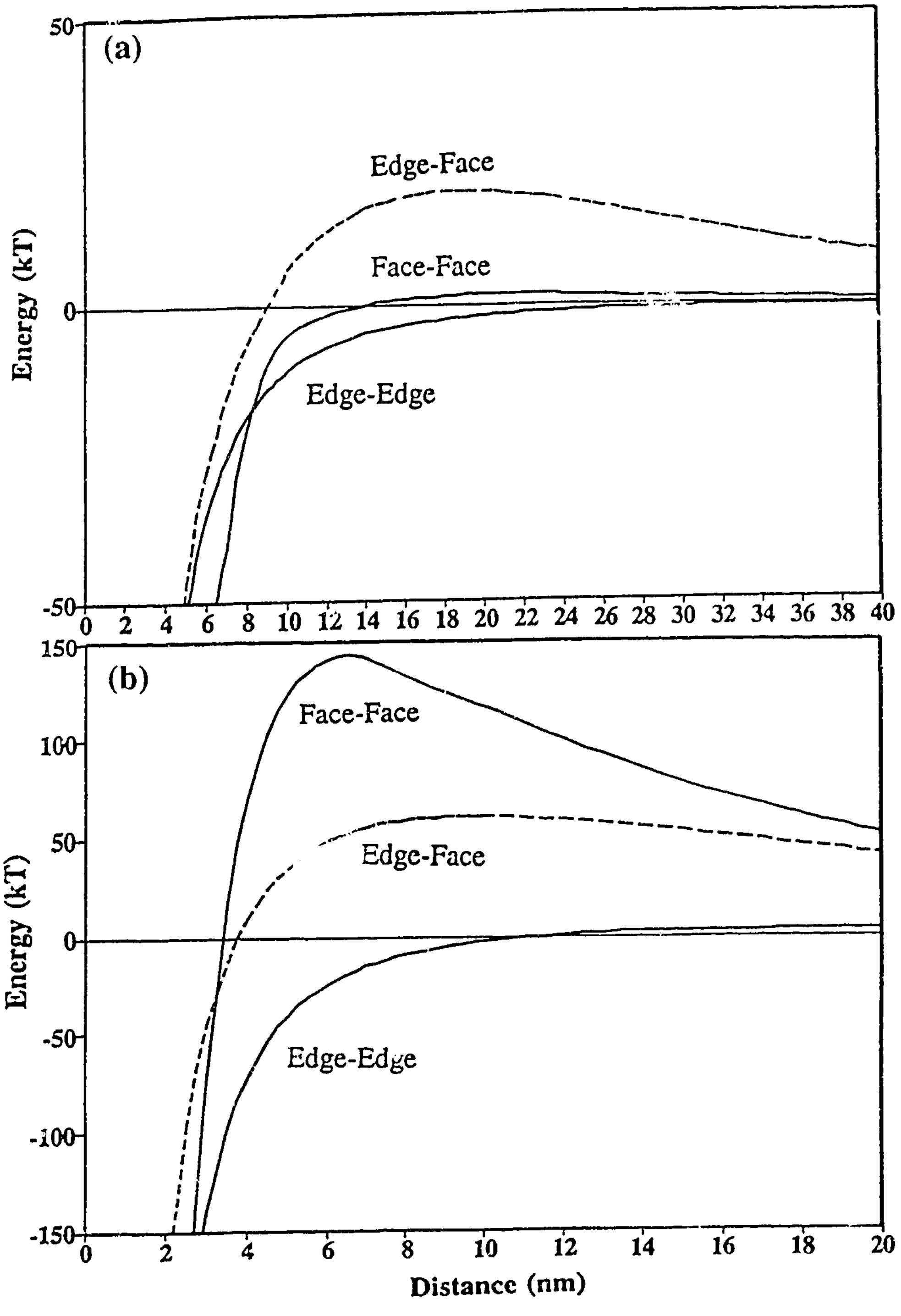

Fig. 7.3-5 - Total interaction energy between two platelike particles, as a function of the nearest separation distance between the particles, for FF, EF, and EE configurations. General conditions: $L_1 = L_2 = 4 \times 10^{-7}$ m, $\delta = 5 \times 10^{-8}$ m, T = 298K, $A = 2 \times 10^{-20}$ J : (a) $\psi_f = -0.005$ V and $\psi_e = -0.015$ V, 1:1 type electrolyte at the concentrations of 0.1 mM; (b) $\psi_f = \psi_e = -0.01$ V, 1:1 type electrolyte at the concentrations of 0.1 mM.

7.3.3 - Computation for experimental conditions where mixed accumulation-flocculation sedimentation occurs

7.3.3.1 - Computation parameters

The zeta potential was about 0.011 V when the kaolinite suspension was prepared at pH=4 and an unaged $FeCl_3$ concentration of 1.67mM. As mentioned in Section 5.4.2.1, the mixed accumulation-flocculation sedimentation occurred when $0.01\ V < |\zeta| < 0.015\ V$.

In the present study, computations were made for platelike particles with the same geometrical characteristics as in 7.3.1 and with the following electrical characteristics:

(4) (a) $\psi_f = -0.02$ V, $\psi_e = -0.01$ V; (b) $\psi_f = -0.01$ V, $\psi_e = -0.02$ V; (c) $\psi_f = \psi_e = -0.015$ V

(5) different concentration of 1:1 electrolyte were chosen according to the similar considerations in Section 7.3.1.1(4).

7.3.3.2 - Comparison of FF,EF and EE association modes

Fig. 7.3-6a shows the variation of interaction energy between two particles as a function of distance when the concentration of the electrolyte $c_0 = 0.001$M in the case of $\psi_f = -0.02$ V and $\psi_e = -0.01$ V. Platelike particles are not associated. Platelike particles are connected in the EE mode at an electrolyte concentration of $c_0 = 0.005$ M (Fig. 7.3-6b). According to the calculation, EE association dominates until c_0 increases to 11.8 mM. At high concentration of electrolytes , the face to face association becomes the most favored, as shown in Fig. 7.3-6c.

Fig. 7.3-7a shows the result when $\psi_f = -0.01$ V and $\psi_e = -0.02$ V. Flocculation can occur at a very low concentration of electrolyte (0.1mM) and platelike particles are associated in EE mode. However, when $\psi_f = \psi_e = -0.015$ V, two particles are not connected at $c_0 = 0.0005$ M (Fig. 7.3-7b).

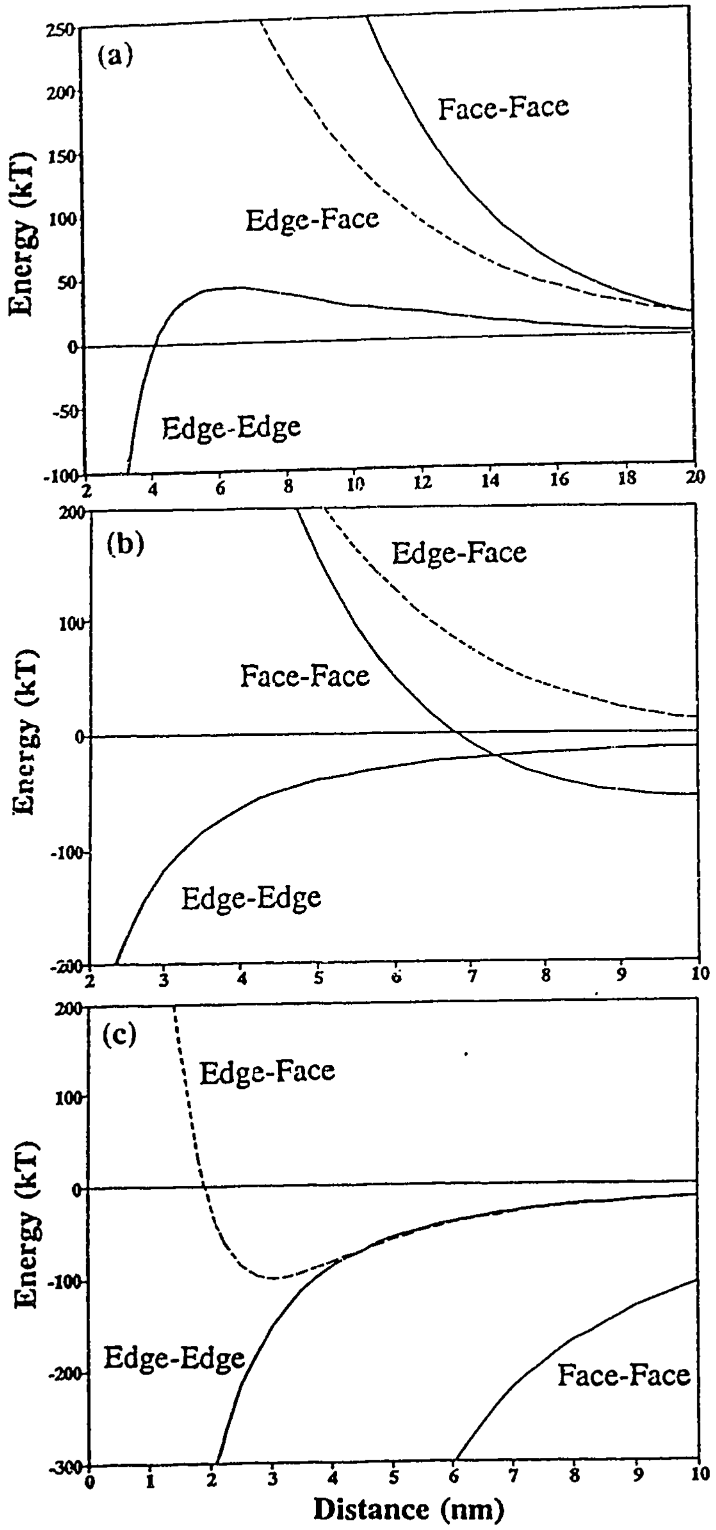

Fig. 7.3-6 - Total interaction energy between two platelike particles, as a function of the nearest separation distance between the particles, for FF, EF, and EE configurations. General conditions: $L_1 = L_2 = 4 \times 10^{-7}$ m, $\delta = 5 \times 10^{-8}$ m, T = 298K, $A = 2 \times 10^{-20}$ J, $\psi_f = -0.02$ V, $\psi_e = -0.01$ V, 1:1 type electrolyte at the concentrations: (a) 1 mM; (b) 5 mM; (c) 60 mM.

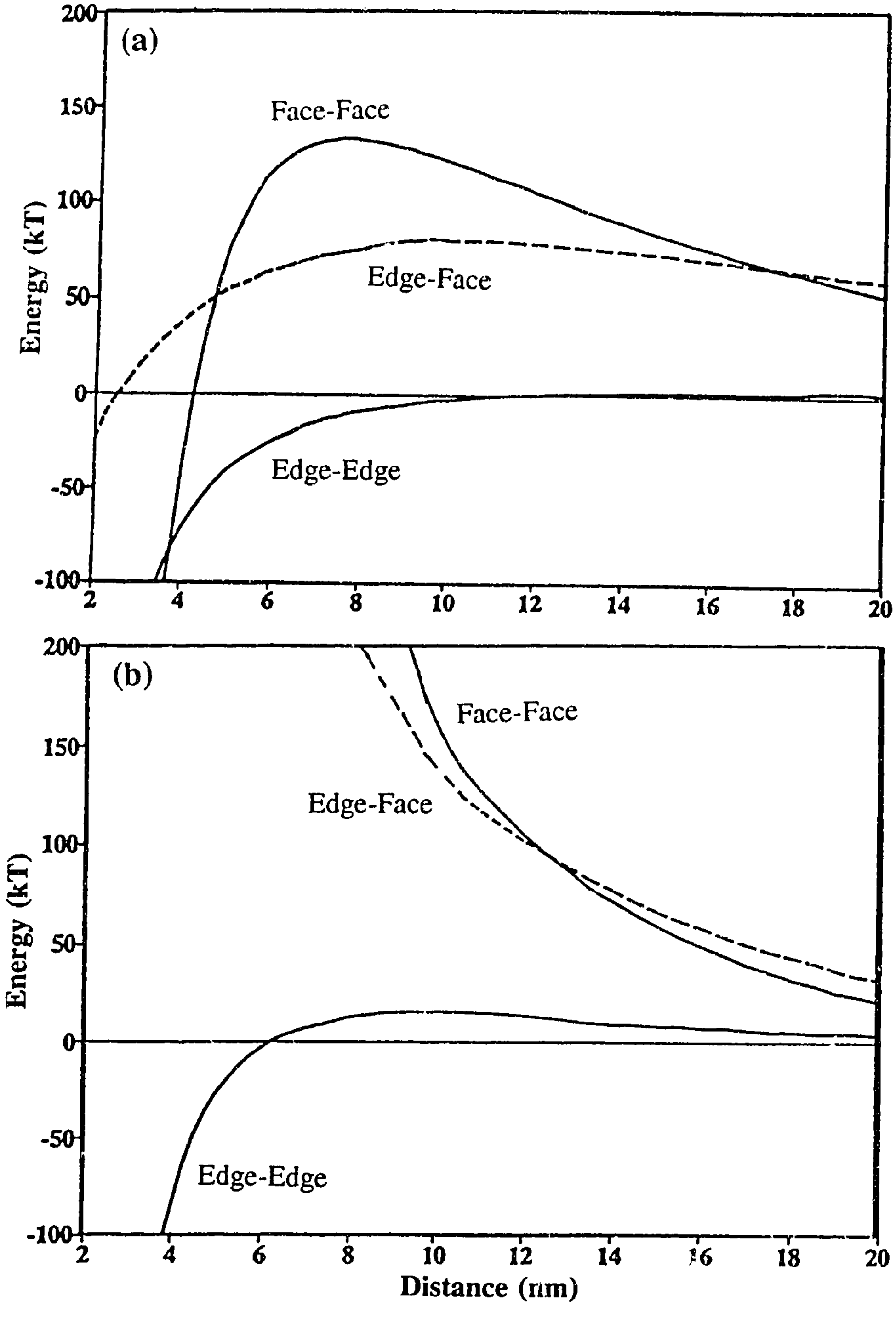

Fig. 7.3-7 - Total interaction energy between two platelike particles, as a function of the nearest separation distance between the particles, for FF, EF, and EE configurations. General conditions: $L_1 = L_2 = 4 \times 10^{-7}$ m, $\delta = 5 \times 10^{-8}$ m, T = 298K, A = 2×10^{-20} J : (a) $\psi_f = -0.01$ V and $\psi_e = -0.02$ V, 1:1 type electrolyte at the concentrations of 0.1 mM; (b) $\psi_f = \psi_e = -0.015$ V, 1:1 type electrolyte at the concentrations of 0.5 mM.

7.3.4 - Summary

The calculations show that when the average electric potential of a particle is over |0.015 V|, the suspension is always dispersed with a low or intermediate electrolyte concentration, no matter what the exact electric potentials are on faces and edges. However, when the average electric potential is less than |0.01 V|, flocculation should occur in a suspension even with very little electrolyte added. The situation becomes complicated when the average electric potential is in the range of $0.01\ V \leq |\zeta| \leq 0.015\ V$. In the case of a higher surface potential on faces and a lower one on edges, or electric potentials of the same order on both faces and edges, no particle associations can occur without addition of electrolyte. A suspension will be brought to flocculate by adding a small amount of electrolyte. On the other hand, flocculation happens in a suspension with almost no addition of electrolytes if a lower electric potential is on faces and a higher one is on edges. It means that flocculation and dispersion compete with one other in a suspension with $0.01\ V \leq |\zeta| \leq 0.015\ V$. Consequently, a mixed dispersion-flocculation sedimentation should occur in such a suspension.

Furthermore, according to the calculation, the EF connection is the most unfavourable mode under all conditions. The EE connection should occur under the condition of low or intermediate electrolyte concentration while the FF connection occurs under higher concentration. The behavior of dispersion-flocculation and the variation of particle association modes with the variation of zeta potential and concentration of the electrolyte in suspensions by the theoretical analysis, correspond qualitatively with the present experimental results.

7.3.5 - Angle at Stair-Step Configuration

As early as 1971, O'Brien (1971) observed that clay particles connected with an angle in the sediment. O'Brien (1971) suggested a stair-step microstructure for clay sediments or gels, as shown in Fig. 2.4-4(a). In the present study, the stair-step microstructure was observed in some kaolinite sediments (Fig. 6.2-12c) As mentioned previously, this model differs from the stair-step model but the model will at least show that platelike particles can connect with an angle.

7.3.5.1 - Edges and faces with relatively low surface potentials

This computation was carried out for $\psi_f = 0.012$ V and $\psi_e = 0.02$ V by equation (7.2-7). The selected concentration of 1:1 indifferent electrolyte was 1 mM.

The value of the total interaction energy, as a function of the angle θ and the nearest separation distance $2h_0$ between the particles, is reported in Fig. 7.3-8. The energy barriers are over 15 kT as two particles approach each other when $\theta \leq 6°$ and $\theta \geq 60°$ The particles can be associated for $6°<\theta<60°$. The minimum barrier occurs at $\theta \approx 10°$.

7.3.5.2 - Edges and faces with relatively high surface potentials

This computation was carried out for a concentration of 30 mM of 1:1 non potential determining electrolyte, also known as indifferent electrolyte. The selected values for the electric surface potentials were $\psi_f = 0.03$ V and $\psi_e = 0.05$ V.

The value of the total interaction energy, as a function of the angle θ and the nearest separation distance $2h_0$ between the particles, is reported in Fig. 7.3-9. This figure shows that the particles can easily approach each other at an angle $4° < \theta < 30°$. In this orientation range, the total interaction energy is negative, which corresponds to an attraction. Further calculations showed that this kind of situation occurred for a 1:1 indifferent electrolyte concentration in the range from 27mM to 36.2mM.

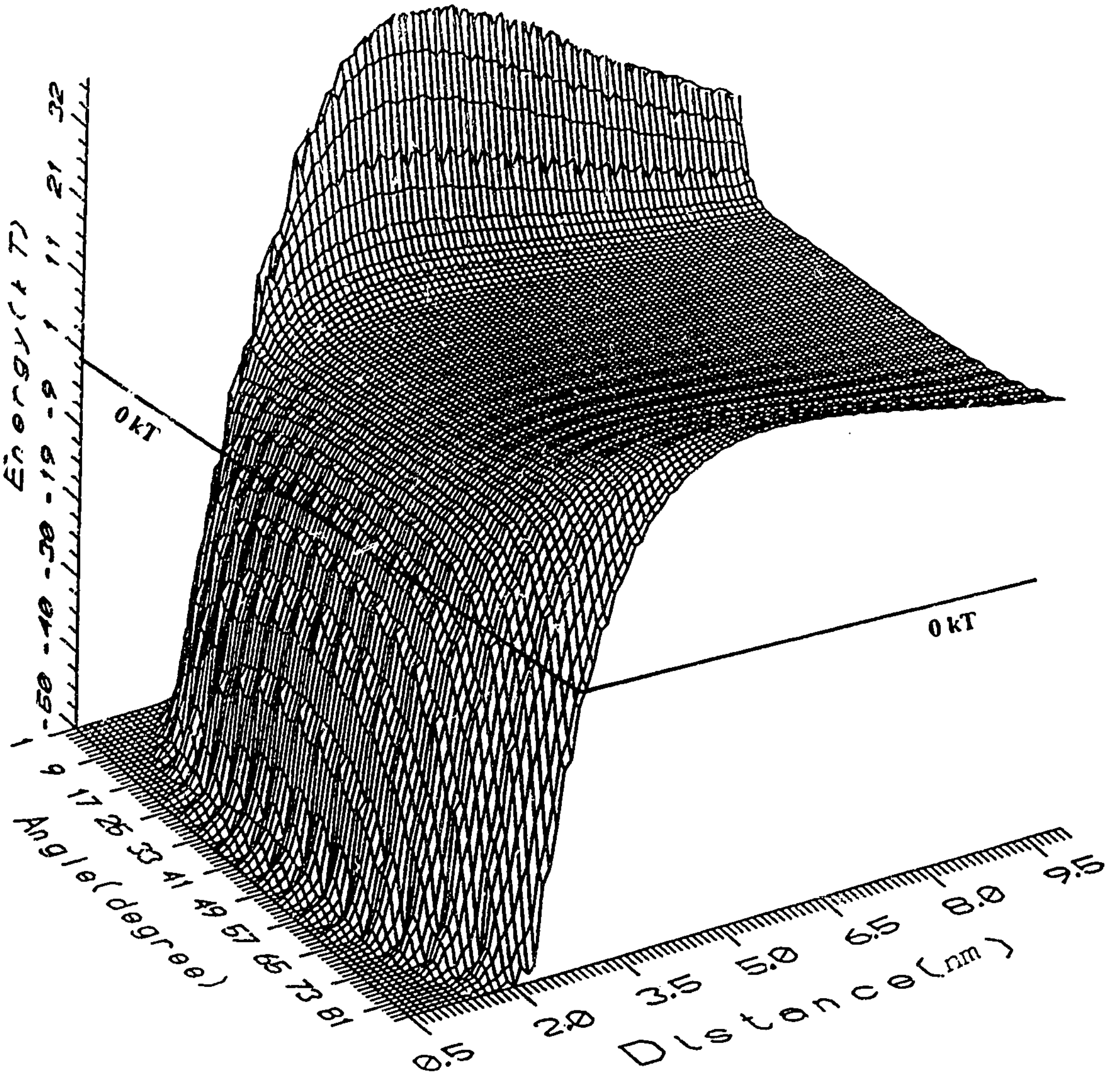

Fig. 7.3-8 - Total interaction energy between two platelike particles, as a function of the nearest separation distance and the angle θ between them, for the configuration in Fig. 7.2-1. General conditions: $L_1 = L_2 = 4 \times 10^{-7}$ m, $\delta = 5 \times 10^{-8}$ m, T = 298K, A = 2×10^{-20} J, $\psi_f = 0.012$ V, $\psi_e = 0.02$ V, 1:1 type electrolyte at a concentration of 1mM.

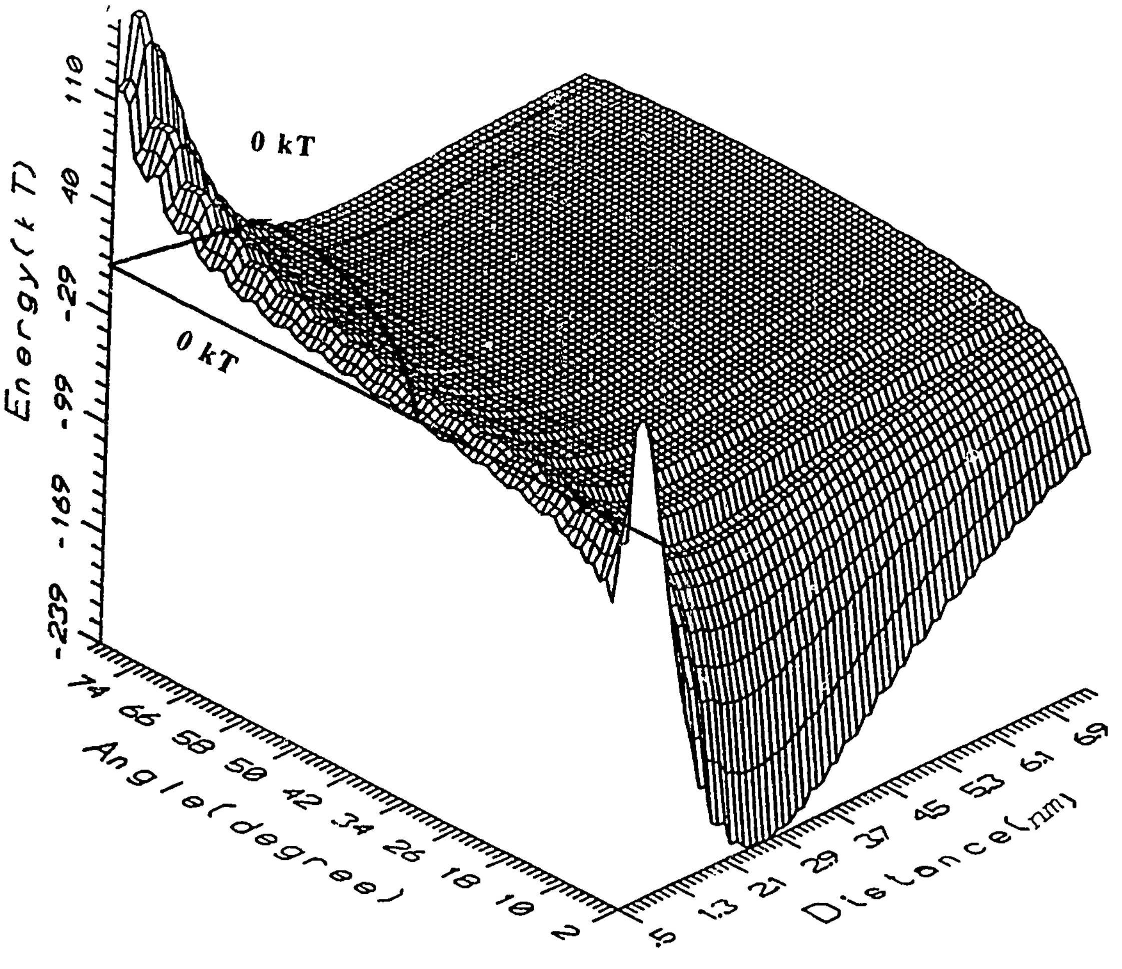

Fig. 7.3-9 - Total interaction energy between two platelike particles, as a function of the nearest separation distance and the angle θ between them, for the configuration in Fig. 7.2-1. General conditions: $L_1 = L_2 = 4 \times 10^{-7}$ m, $\delta = 5 \times 10^{-8}$ m, T = 298K, A = 2×10^{-20} J, $\psi_f = 0.03$ V, $\psi_e = 0.05$ V, 1:1 type electrolyte at a concentration of 30mM.

CHAPTER 8 - DISCUSSION

8.1 - AGGREGATION OF Na-KAOLINITE WITH NEGATIVE CHARGES ON BOTH THE EDGES AND THE FACES

8.1.1 - Aggregation with unaged Fe electrolyte

In Chapter 4, the sedimentation behavior of Na-kaolinite suspensions after treatment with $Na_4P_2O_7$, was found to occur according to one of the three following behaviors: (1) accumulation; (2) flocculation; and (3) mixed accumulation-flocculation.

The SEM observations of sediments dried by the supercritical method made it possible to relate these three sedimentation behaviors to three different types of kaolinite particle aggregation. Moreover, accumulated sediments could themselves be divided in two different types of structures, depending on the added concentration of Fe electrolyte. In turn, the zeta potential measurements made it possible to relate the type of aggregation behavior to the electrical double layer of the kaolinite particles.

When the electrical conditions around the particles were modified with unaged Fe electrolyte additives, a synthetic view of the main typical sedimentation behaviors could be presented as follows.

8.1.1.1 - Typical randomly accumulated sediment

The SEM micrographs showed that a first category of sediments made by accumulation, consisted of kaolinite particles connected in a random way, due to the settlement under gravity of individual kaolinite particles. Hence, this type of sediment could be termed randomly accumulated sediment.

Sedimentation leading to the formation of such random sediments occurred more readily in basic conditions, either without or with a low Fe electrolyte concentration. For example, such kaolinite sediments formed at pH = 4.0 and 9.5, without Fe or with a small concentration of Fe additive.

Under these conditions, our data in Section 5.4 showed that the zeta potential had a relatively high absolute magnitude ($|\zeta| > 0.015$ V), compared to the range of zeta potentials measured in the present thesis. This corresponds to a relatively high surface potential with a thick electrical double layer.

According to the bibliography statements, in Sections 2.3.2.2 & 3.2.1.3, kaolinite particles are known to only carry negative charges both on their edges and their faces, after they are treated with $Na_4P_2O_7$. Moreover, the adsorbed negative phosphate anions are known not to desorb easily during further chemical treatments [27]. These properties were confirmed by our measurements of the zeta potential of HUF Na-kaolinite, since Fig. 3.2-1 shows that the phosphate treated HUF kaolinite had a negative zeta potential at all pH, while the untreated kaolinite had a z.p.c at pH = 4.2.

A consequence of these properties is that as long as either no Fe, or a small amount of Fe electrolyte is added, the electrostatic repulsion between the kaolinite particles is strong. The initial kaolinite particles could not aggregate, and they remained dispersed in the suspension for a time depending on their weight, but typically of the order of half an hour.

During sedimentation, the heaviest particles settled first under gravity and they formed an accumulated sediment at the bottom of a cylinder. The smaller particles remained suspended for a longer period in a sol. Also, because of the size distribution, the population density of particles in this suspension decreased progressively at an increasing height in the cylinder. That is to say, a diffuse transition-zone with the clear supernatant liquid was observed, as shown in Fig. 4.2-1a.

The sediment volume slowly increased with time and the final sediment volume was the smallest of the various types of sediments made in the present thesis. SEM micrographs, such as in Fig. 6.2-2, confirmed this was a very compacted sediment. The porosity was rather uniform, and there was no preferred orientation of the particles.

A structure of this type, termed dispersed structure, was suggested by Lambe [124]. Sides and Barden [87] observed such structures in an SEM, in kaolinite and in illite sediments prepared by simple air-drying. The present study is consistent with these previous observations. As a new result, it clearly showed that these structures formed in conditions where the surface potential was high and the electrical double layer was thick, in qualitative agreement with the DLVO theory.

8.1.1.2 - Typical flocculated sediment

When a moderate concentration of Fe electrolyte is added to a kaolinite suspension, cations such as Fe^{3+} and its hydrolysis products act as the counterions for the negatively charged kaolinite particles. Because of the high valence state of these counterions, a moderate concentration of unaged $FeCl_3$ such as 0.67 mM at pH = 4.0, drastically decreased the absolute magnitude of the zeta potential. A zeta potential value $\zeta = -0.004$ V was measured in these conditions (Fig. 5.4-2). Hence the surface electrical potential was drastically reduced and, according to the DLVO theory, aggregation could occur.

The computation showed that this aggregation involved a significant probability of EE association (Fig. 7.3-6). The EF association mode was less probable. In practice, the particles had time to build flocs before undertaking any significant settling. SEM observations showed that these flocs had a much more open structure than the previous randomly accumulated sediment. The floc characteristics in the micrographs (Fig. 6.2-4) typically looked like what is known as the DLA fractal aspect, described in Section 2.2.3. A floc network of this type is consistent with random collisions due to the Brownian motion, as this is supposed to occur according to the DLVO theory. The supercritical drying technique is the only one able to make monolithic dry aerogels with a huge specific surface area, and it is the only one to have shown such fractals in clay, as expected by the theory, contrary to the techniques of air-drying and freeze-drying where the long range fractal network is broken [51]. We consider this as an important success of the present thesis.

Actually, the flocs were sufficiently large to be in contact with each other. Consequently, a uniformly flocculated, voluminous and apparently homogeneous sediment could be observed very soon after dispersing a suspension. This flocculated sediment was separated by a sharp interface, according to a visual observation, from the supernatant liquid.

The fractal arms of the flocs were flexible and they could slowly deform under gravity during aging. Hence a compaction process of the flocculated sediment, sometimes known as consolidation [1], slowly occurred. This satisfactorily explains the decrease in the volume of the sediment with time (Fig. 4.2-2a), in agreement with previous reports quoted in the bibliography (Fig. 2.3-7).

The Fe electrolyte had an influence which goes beyond just modifying the electrical double layer. However, this aspect deserves a special analysis which is the subject of Section 8.1.2.

8.1.1.3 - Typical packed accumulated sediment

Such sediments were formed with a higher Fe electrolyte concentration than the flocculated sediments. A typical example was at pH = 4.0 with the unaged $FeCl_3$ concentration of 3.3 mM.

With respect to the visual aspect of the settling process, it did not appear to behave very differently from the randomly accumulated sediment, except that it was faster. As for random accumulation, the zeta potential magnitude was high ($|\zeta| > 0.015V$). However, this zeta potential was positive instead of being negative. For instance, the zeta potential was about +0.017 V for the kaolinite suspension mentioned at the beginning of this Section (Fig. 5.4-2a). TEM observations also showed that Fe hydrolysis product had deposited on the kaolinite faces, so that the positive zeta potential was due to a Fe product coating (Section 5.2).

From DLVO theory, and in spite of this high zeta potential, the high Fe electrolyte concentration was sufficient to drastically compress the electrical double layer thickness of the kaolinite particles. The anions played an important role as the counterions to compress the electrical double layer, in agreement with the shorter field for flocculation-sedimentation with $FeCl_3$ than with $Fe_2(SO_4)_3$ (Fig. 4.2-3). This effect is consistent with the higher valence state of SO_4^{2-} than Cl^-, according to the DLVO theory. The double layer compression went to the extent that FF association of the kaolinite particles occurred. The computation reported in Fig. 7.3-1 supports this view.

The frequent occurrence of FF association was confirmed by SEM observations, as in Fig. 6.2-3. These micrographs showed that rather compact kaolinite aggregates were formed. The aggregates did not entangle in a unique network, as in flocculation sedimentation. Instead, they settled individually under gravity. Hence, a packed accumulated sediment slowly accumulated.

8.1.1.4 - Mixed sediments

Mixed flocculation-random accumulation and mixed flocculation-packed accumulation occurred in intermediate conditions. In both cases, the zeta potential had an absolute value $0.01\ V < |\zeta| < 0.015\ V$ (Fig. 5.4-2).

For instance, the first of the above mixed regime occurred when the flocculation kinetics and the settling kinetics of individual kaolinite particles were comparable. A typical example was at pH = 4 and the unaged $FeCl_3$ concentration of 1.67mM. The zeta potential of the kaolinite particles was 0.011V. The double layer thickness was such that flocculation was slow. Consequently, accumulation proceeded, until flocculation had time to operate with the remaining particles in the suspension (Fig. 4.2-1c). Two sharp interfaces could be successively followed in the same cylinder: (1) a sharp interface between the accumulated layer and the remaining suspension, at the beginning of the settling process; (2) a sharp interface between the flocculated layer and the clear supernatant liquid, at the end. The final sediment was composed of an accumulated sediment and a flocculated sediment, with the flocculated sediment on top of the accumulated sediment, as shown in Fig. 6.2-5.

8.1.1.5 - Effect of the kaolinite content

According to the kinetic theory of flocculation by Smoluchowski [10, 125], the rate of flocculation is proportional to the square of the solid particles concentration in a sol. The data in Fig. 4.2-2a showed that a short induction time was necessary to form a sharp interface between the flocculated sediment layer and the clear supernatant liquid, when the kaolinite concentration was 0.5%. On the other hand, flocculation immediately occurred for higher kaolinite contents. Hence, the present study was consistent with the Smoluchowski theory.

During sedimentation, the settling velocity of a particle depends on its size and its weight. For instance flocs which have a very open structure settle more slowly than dense flocs, and this effect becomes very drastic if the open flocs form a single entangled network as in flocculation sedimentation. For some clay concentrations, the settling velocity increased in the first stage, because heavier and bigger flocs than the initial particles started to form, while these flocs had not started to entangle. Such a settling kinetics was already reported and termed "settling curve b" by Michael and Bolger [42] (Fig. 2.3-7). Also, the field of conditions ($FeCl_3$ concentration, pH) where flocculation sedimentation occurred, increased with the kaolinite content in the suspension, as shown in Fig. 4.2-16 and Fig. 4.2-17.

The qualitative agreement between the type of sedimentation behavior and DLVO theory, which was analyzed in the previous sections of this chapter, held as the kaolinite content increased. For instance, as shown in Fig. 4.2-17, flocculation sedimentation was favored by a lower pH and a higher concentration of unaged $FeCl_3$ for 2% HR kaolinite suspensions. The data on the initial settling rate (Fig. 4.2-11) and on the floc size (Fig. 4.2-15) indicate that the flocs were bigger and less dense with 5mM unaged $FeCl_3$

than with 10 mM. With 5 mM $FeCl_3$, the kaolinite particles were frequently associated according to the EE mode and the flocs had a fractal aspect.

8.1.1.6 - Effect of the kaolinite particle size

As indicated in Section 3.2.1.1, two types of kaolinite with a different median particle size were compared. For the HR kaolinite, the median particle size was 0.77 µm, while for the HUF kaolinite it was 0.2 µm. The other properties of both kaolinites were similar and they were pretreated according to the same procedure with $Na_4P_2O_7$.

For the same solid kaolinite content (by mass) in a suspension, a smaller number of particles were present with the HR kaolinite than with the HUF kaolinite. Hence, the chance of collisions between particles was lower with the HR than with the HUF kaolinite. Flocculation leading to a single entangled network was expected to be more difficult with the HR kaolinite than with the HUF kaolinite, at a given pH and a given $FeCl_3$ concentration.

The data reported in Figs. 4.2-16 and 4.2-17 are in agreement with the expectations, especially when the kaolinite concentration was low (0.5%) (Figs. 4.2-3a and 4.2-17a). These diagrams on the sedimentation behavior show that the mixed accumulation-flocculation field is much larger for the HR kaolinite than for the HUF kaolinite, for a given pH and $FeCl_3$ concentration. This is due to the fact that with the HR kaolinite, the flocs had some difficulty in making a single entangled network. The bigger HR flocs could settle quickly and individually, while the smaller flocs or even the single particles remained dispersed for a longer time.

As the kaolinite concentration increased, the difference in sedimentation behavior between the HR and the HUF kaolinite attenuated so that flocculation occurred in almost the same field of conditions (pH values and $FeCl_3$ concentrations) for a kaolinite content of 5 % (Fig. 4.2-16c and 4.2-17d).

8.1.2 - Action of Fe in the aggregation of kaolinite particles

8.1.2.1 - Possible actions of Fe additives

Potentially, the Fe^{3+} cations and their hydrolysis products can have a triple role on the aggregation of kaolinite particles:

(1) As counterions for the negatively charged kaolinite particles.

(2) As exchange cations for the cations in the kaolinite.

(3) As bonding agent between the kaolinite particles by intermediate Fe hydrolysis products.

A comparison of the action of unaged Fe electrolytes and aged Fe electrolytes may cast some light on the special action of Fe.

8.1.2.2 - Fe additives as counterions for kaolinite

Considering that the kaolinite particles were negatively charged before adding the Fe electrolytes, the Fe^{3+} cations and their hydrolysis products obviously had a major role as counterions. This is supported by the result that, as the initial Fe electrolyte increased, the aggregation behavior of the kaolinite particles progressively changed from no aggregation to fractal aggregation. This evolution in the aggregation mode is consistent with a progressive decrease in the double layer thickness due to the counterions, as analyzed in detail in Section 8.1.1. In terms of the sedimentation regime, these types of aggregation respectively led to random accumulation sedimentation and to flocculation sedimentation.

A third type of aggregation regime, termed packed accumulation sedimentation, was not due to an action of the Fe products as counterions. Rather, these products were deposited on the kaolinite particles and this is analyzed in the next section. Generally, the action of Fe^{3+} and its hydrolysis products as counterions was more effective at low concentrations.

Such a progressive evolution due to an increasing Fe additive concentration was observed both with the unaged and with the aged Fe electrolytes. The greatest effect of using aged Fe electrolytes, instead of unaged electrolytes, was to decrease the ability of Fe^{3+} and its hydrolysis species as counterions. A comparison of Figs. 4.2-3a and 4.2-8 shows that the field of conditions where accumulation sedimentation occurred was enlarged with aged $FeCl_3$.

This indicates that the population of high charge Fe species in solution was less with the aged Fe electrolytes, which is consistent with an important reduction in the adsorbed Fe on the clay particles from the unaged $FeCl_3$, by comparison with aged $FeCl_3$ (Section 5.1.1). Consequently, the electrical double layer was less compressed with the aged Fe electrolytes. In turn, the formation of large and light fractal flocs was less frequent with the aged Fe electrolytes.

The above difference in the difficulty to make fractal flocs was also consistent with the differences in the initial settling rate and the final sediment volume. The initial settling rate of the sediments with aged $FeCl_3$ was always higher than that of sediments with unaged $FeCl_3$, for a given Fe concentration and pH value. The effect was opposite on the final sediment volume (Fig. 4.2-9a and b).

8.1.2.3 - Fe additives as an exchangeable cation source for kaolinite

Fe^{3+} and its hydrolysis products could also exchange for cations such as Na^+ in the clay, which was consistent with the data on the residual amounts of Fe and Na in the supernatant liquid, after sedimentation (Section 5.1.1). The cation exchange process could help to anchor Fe hydroxoferric complexes into the clay particles [66]. They could also help to strengthen the bonds between two clay particles by intermediate Fe compounds. In this way, Fe contributed to the success of the supercritical drying technique, because it made the fractal network more resistant to the stresses which may have developed during fluid exchange and drying.

8.1.2.4 - Fe additives as bonding intermediates between the kaolinite particles

When the Fe^{3+} electrolyte concentration in the suspension was sufficiently high, the present TEM observations (Section 5.2) and the present zeta potential measurements (Section 5.4) showed that the clay particles were coated with complex Fe products. Because of such Fe coatings, the charge on the kaolinite particles changed from negative to positive. Also, the kaolinite particles associated mostly according to the FF mode, so as to form dense flocs which easily settled under gravity.

As summarized in the bibliography (Section 2.3.6), the Fe electrolytes make their own precipitates or gels. The nature of these products largely depends on the anions (NO_3^-, Cl^-, SO_4^{2-}) and on the pH [68]. For instance, the hydrolysis of $Fe_2(SO_4)_3$ is more complex than that of $FeCl_3$. It gives rise to a larger variety of complexes such as $Fe_3(SO_4)_2(OH)_5{\cdot}2(H_2O)$, $Fe_4(SO_4)(OH)_{10}$ [126], or the insoluble complex $Na[Al_{13}O_4(OH)_{24}(H_2O)_{12}(SO_4)_4]$ [127].

All these Fe products could deposit on the clay particles and cement these particles together as if "closing the pages of a book" [128,129]. They also increased the strength of the clay flocs, as shown by the data on the Bingham yield stress of montmorillonite suspensions mixed with hydroxoferric particles, shown in Section 5.3.2. Actually, the importance of Fe gelation or precipitation to coat the clay faces, increased with the pH. At high pH, the precipitation of Fe hydrolysis products was abundant (Section 5.2). The action of Fe hydrolysis products as counterions disappeared. Instead, a mixed clay-Fe made the sediment.

With respect to this action of coating the kaolinite particles, the main difference between unaged Fe electrolytes and aged Fe electrolytes was that the aged Fe electrolytes more easily coated the kaolinite particles. Also, the electrical charge of the particles changed sign with a lower amount of aged $FeCl_3$ than unaged $FeCl_3$. Then, the zeta potential increased faster with the aged Fe electrolytes (Fig. 5.4-2a and b). Consequently, packed accumulation sedimentation occurred with a lower concentration of aged $FeCl_3$ than unaged $FeCl_3$ (Figs. 4.2-3a and 4.2-8).

8.1.3 - Aggregation of kaolinite particles with the help of Al electrolytes

Both the Fe electrolytes and the Al electrolytes provide trivalent cations in aqueous solutions. Also, both trivalent cations undertake hydrolysis reactions which depend on the nature of the anions. The main characteristics concerning the transformations of these cations in solutions were summarized in Sections 2.3.6 and 2.3.7.

The main difference is that various Fe compounds easily precipitate from $FeCl_3$, while amorphous and transparent boehmite gels always form in acidic conditions from $AlCl_3$. In the present study, we actually found that precipitation quickly occurred after dissolving $FeCl_3$ in distilled water, and aged $FeCl_3$ preparations contained an abundant brown-red precipitate. The concentration of Fe in a 0.5 mM solution was reduced to 0.33 mM after 1 month aging. On the other hand, aged $AlCl_3$ solutions were still as clear as water and contained no precipitate, even after a long aging time.

To a large extent, the Fe and the Al electrolytes had a similar action in terms of providing counterions for negatively charged kaolinite particles. Hence, as the cation concentrations increased, the double layer was increasingly compressed and a transition from accumulation sedimentation to flocculation sedimentation occurred. The flocculated sediments made with unaged $AlCl_3$ were comprised of nice fractal structures which could also be observed in the SEM, after supercritical drying (Fig. 6.2-11).

With respect to the mode of particle association, the micrographs of kaolinite sediments made with Al electrolytes showed stair-step structures, for instance at pH = 9.5 and at high $AlCl_3$ concentration of 50 mM (Fig. 6.2-12). In these conditions, the edges and the faces of the kaolinite particles were both positively charged, because of the adsorption of Al^{3+} hydrolysis products, and Cl^- was a counterion. Such an experimental situation was similar to the conditions selected for the computation in Section 7.3.5. In the same way, the SEM micrographs of kaolinite sediments made at pH = 2 with the low $AlCl_3$ concentration of 2 mM (Fig. 6.2-9) showed clay particle association with an angle.

As summarized in Section 2.4.1, the stair-step organization of platelike particles was proposed by O'Brien [88]. This researcher also observed that the angle θ between the two particles was smaller than 30°, with a more frequent value near 10°. These results are consistent with the computations reported in Section 7.3.5.

One of the main differences between Al and Fe concerned the exchange capability of both cations. Al^{3+} is one of the main cations in the atomic structure of a clay itself. Hence, this is a potential determining ion. The data on the adsorption of cations by kaolinite showed that more Fe (Fig. 5.1-1) than Al (Fig. 5.1-2) was adsorbed by the kaolinite particles, under similar conditions. This did not mean anything in terms of the charge on the clay particles, since positive charges could be created by cutting the bonds from the Al atoms at the edge of a clay particle. Practically, the data showed that the zeta potential increased faster, algebraically, with the concentration of unaged $AlCl_3$ (Fig. 5.4-5) than with the concentration of unaged $FeCl_3$ (Fig. 5.4-2). With respect to the anions, and according to the sedimentation diagrams in Fig. 4.2-20, NO_3^- was less effective than Cl^- in making the suspensions flocculate after reversal of the charge on the clay particles (Fig. 4.2.20). $SO_4^=$ was intermediate between the two previous anions.

According to El-Swaify and Emerson [78], an $Al(OH)_3$ precipitate could bond the clay particles even more efficiently than the precipitates from the Fe electrolytes. However, this statement could not be confirmed in the present study since such precipitates could not be observed in the TEM, as was done with the Fe electrolytes. Besides, at a high Al electrolyte concentration, the kaolinite particles were positively charged. However, no packed accumulation by FF association of the clay particles in dense aggregates was observed, contrary to the observations made with the Fe electrolytes. Also, no significant difference was observed between unaged and aged $AlCl_3$ concerning the flocculation of kaolinite and the sediment microstructures were similar.

8.2 - AGGREGATION OF Na-MONTMORILLONITE

8.2.1 - Aggregation with aged Fe electrolyte

Of the three sedimentation behaviors reported for the kaolinite suspensions, only two were also found to occur with the montmorillonite suspensions mixed with aged $FeCl_3$. They were: (1) random accumulation sedimentation; and (2) flocculation sedimentation. These two sedimentation regimes lead to the same sediment structures as with kaolinite, according to the SEM observations. Also, the results with aged $FeCl_3$ are very similar to the results obtained by Zou on 0.5% montmorillonite suspensions with unaged $FeCl_3$ [1].

Random accumulation occurred at low Fe concentration and at medium or high pH, for instance with an aged $FeCl_3$ concentration of 0.33mM and at pH =9.5 (Fig. 6.3-1). Flocculated sedimentation occurred in a large field of conditions (Fig. 4.3-4a). The sedimentation diagram of 1% montmorillonite suspensions with aged $FeCl_3$ (Fig. 4.3-4a) looks like the sedimentation diagram of 1% kaolinite with unaged $FeCl_3$ (Fig. 4.2-16).

The structure and the formation conditions for random accumulated sediments and flocculated sediments can, respectively, be described in the same way as the equivalent kaolinite sediments in Sections 8.1.1.1 and 8.1.1.2. The DLVO theory applies qualitatively as well in both cases. The flocculated sediments were comprised of fractal aggregates, illustrated in Fig. 6.3-2 ,with a solid volume fraction as low as 0.5%. In these flocs, the particles were mostly associated according to the EE mode. The montmorillonite particles were charged negatively. With the addition of aged $FeCl_3$, the electric double layers around montmorillonite particles were compressed by the counterions. As a result, the montmorillonite sediments had a tendency to transform from a flocculated structure to an accumulated structure as the pH increased.

same % by mass, the montmorillonite flocs occupied more space than the kaolinite flocs. Also, collisions to form the flocs were more frequent.

The fact that no packed accumulated sediments were discovered in montmorillonite sediments can be considered as a consequence of the high specific area of this type of clay. However, a special flocculated sediment, characterized by a sharp interface with the clear supernatant liquid was reported by Zou [1] for a $FeCl_3$ concentration of 10 mM. This sediment was comprised of flocs with a strong preferred organization of the momtmorillonite particles in packed parallel domains.

8.2.2 - Aggregation with hydroxoferric particles

In this study, the excess ions were removed from the hydroxoferric particles by dialysis in distilled water. In this way, the effect of Fe^{3+} and its hydrolysis products as counterions and as exchange cations were cancelled. The influence of these ions and of the hydroxoferric particles could be compared.

It turned out that the zeta potential of montmorillonite particles increased at all pH with the solid content of hydroxoferric particles (Fig. 5.4-6). Hence, the adsorption of hydroxoferric particles on the surfaces of the clay particles resulted in a reduction of the repulsion between these particles, in a way similar to the counterions.

In this study, it was difficult to describe the association mode between the clay particles according to the SEM micrographs, because extensive curling of the particles occurred (Fig. 6.3-3 & 6.3-4). However, the data on the zeta potential and on the Bingham stress made it possible to derive some conclusions (Fig. 5.4-7). The Bingham yield stress increased roughly linearly as the zeta potential absolute magnitude decreased. Hence, the hydroxoferric particles coating on the montmorillonite particles, had both decreased the charge on the clay and increased the sediment strength as a bonding glue.

Flocs were also made, as with the electrolytes. However with 0.5% by mass hydroxoferric particles content, these flocs had a more globular spherical aspect (Fig. 6.3-4a) than the fractal flocs observed under other conditions, which can be explained by a deformation of the montmorillonite particles by a significant hydroxoferric coating.

8.2.3 - Action of Fe on the aggregation of montmorillonite particles

The analysis in Section 8.1.2, of the action of Fe^{3+} cations and their hydrolysis products on the aggregation of kaolinite, applies as well to montmorillonite. It includes: (1) a counterion effect to compress the electrical double layer of the negatively charged kaolinite particles; (2) an exchange capacity effect for the other cations in the clay, such as Na^+. The exchange capacity of montmorillonite is known to be much higher than that of kaolinite (Table 2.3-2). Hence this effect should be much larger for montmorillonite; and (3) a cementing effect. At high $FeCl_3$ concentration, Fe compounds were precipitated and they coated the montmorillonite particles and they could bond them to each other as was described for kaolinite. Such Fe compound coatings were observed in the TEM and reported in Fig. 5.2-3. However, because the montmorillonite particles were thinner than the kaolinite particles, the Fe hydrolysis products could not cover the surface of montmorillonite particles to the same extent as the kaolinite particles.

The hydroxoferric particles qualitatively had an effect similar to the counterions, as they are deposited on the clay particles. They decreased the absolute electrical charge magnitude of the clay particles, and they acted as a cementing agent.

The hydroxoferric particles deposited on the montmorillonite particles were well illustrated in the TEM micrographs. At pH = 2 (Figs. 5.2-5 & 5.2-6), the positively charged hydroxoferric particles repulsed each other and they were adsorbed by the negatively charged faces of the montmorillonite particles. They were rather uniformly distributed on these faces. However, they were more scarce near the edges of the montmorillonite particles, which can be an indication that these edges are positively charged.

At pH = 9.5, which is slightly above the z.p.c. of the hydroxoferric particles, these particles have a slight negative charge (Section 2.3.6.2). Hence, they made their own aggregates. These aggregates were repulsed by the stronger negative charge on the faces of the montmorillonite particles. The dry montmorillonite samples mixed with hydroxoferric particles, observed in TEM (Figs. 5.2-8 & 5.2-9), show hydroxoferric particles flocs, apparently resting on some areas of the montmorillonite faces, while other areas of these faces have no Fe deposit. A number of hydroxoferric particles flocs remained separated from the clay sediment , in the supernatant liquid to which they gave an uneven color from brown to yellow color, at pH 9.5 and 12. This indicated a poor attraction or a slight repulsion, between the hydroxoferric particles and the clay.

8.2.4 - Aggregation of Na-montmorillonite particles with the help of Al electrolytes

The aggregation of Na-montmorillonite suspensions with the help of Al electrolytes, basically follows the same pattern as for kaolinite, analyzed in Section 8.1.3.

One of the main differences is that a small concentration of $AlCl_3$, 1 mM, is sufficient to reverse the charge on montmorillonite particles from a negative value to a positive one (Fig. 5.4-8). Flocculation occurred, and the initial settling rate drastically decreased (Fig. 4.3-11).

Also, the exchange capability of Al in montmorillonite follows a special pattern. It depends on the pH, in relation with the hydrolysis transformations described Section 2.3.7. The monomeric Al species which intercalate in between the atomic montmorillonite layers, can polymerize in situ. Hence the properties of the clay can be largely modified. The most significant modification concerns the interlayer spacing which expands. In this way, the specific area of montmorillonite could increase up to a value of the order of 1000 m^2/g [62, 79].

The main difference between aged and unaged $AlCl_3$ is that, with aged $AlCl_3$, the settling rate increased again, to reach a maximum near a concentration of 3 mM. This could be explained by a decreasing ability of Al^{3+} to operate as an exchange cation, due to the formation of Al hydrolysis complexes during aging. Overall, nice fractal flocs could be formed with the Al electrolytes (Fig. 6.3-6), as this was found for kaolinite.

8.3 - AGGREGATION OF Na-KAOLINITE WITH NEGATIVELY CHARGED FACES AND POSITIVELY CHARGED EDGES

8.3.1- Aggregation of kaolinite suspensions without Fe additives

As summarized in the bibliography, in Section 2.3.2, it is generally admitted that Na-kaolinite particles carry negative electric charges on their faces and positive charges on their edges, unless they are treated with compounds such as the phosphates. For instance, Méring [58] observed that negatively charged colloidal gold particles were only adsorbed on the edges of kaolinite particles, not on the faces.

The observations of Méring were confirmed, in the present study, by SEM observations on Na-kaolinite mixed with colloidal silica particles (Section 5.5). The micrographs were consistent with kaolinite particles carrying negative charges on their faces and positive charges on their edges at a low pH, instead of only negative charges both on their faces and their edges at high pH.

Many data analyses rely on a EF association mode of the clay particles, due to electrical charges with a different sign on the edges and the faces. Rand et al. [44] relied on this type of association mode to explain their rheological data on kaolinite suspensions, and the present report on the relationship between the Bingham Yield Stress and the pH in kaolinite suspensions without Fe additive (Fig. 5.3-1), was similar to the report by Rand et al. The maximum Bingham Yield Stress occurred at pH $\approx$ 4, near the isoelectrical point of kaolinite, which is consistent with the highest association probability of the clay particles.

However, in the present study (Section 6.1), the EF particles association mode seemed to be scarce at low pH, according to our SEM micrographs. Instead, kaolinite particles were more frequently associated according to the FF mode. Actually, some calculations by Flegmann [63], supported the result that EF and FF associations could concurrently occur when the clay particles have faces and edges with electric charges of opposite sign. Such a behavior was explained by the fact that the particles association mode not only depended on the interaction energy between the particles, but also on the collision frequency. And the collision frequency for the FF configuration was higher than for the EF configuration.

Hence, particles domains made by FF association were formed. Once a domain had reached a sufficient size, it settled rapidly under gravity. During the settling process, collisions between domains lead to the formation of a bookhouse structure, such as those reported in the Fig. 6.1-2 and 6.1-3. The building of such a structure also contributed to an increase in the Bingham yield stress of a suspension.

Similar SEM observations were made at high pH (Fig. 6.1-4). However, the charges had the same sign on the edges and the faces, so that both the FF and the EF bonding were supposed to be weaker than at low pH, which was consistent with a lower Bingham yield stress.

8.3.2 - Aggregation of kaolinite suspensions with unaged $FeCl_3$

After addition of unaged $FeCl_3$ to a kaolinite suspension, the Fe^{3+} cations and their hydrolysis products could act as counterions to compress the electrical double layer of the clay faces. Hence, the FF asociation mode should have been even more favored than without Fe additive. However, the SEM micrographs did not show any significant difference in terms of FF association, between the two types of sediments.

The present data showed that the Bingham yield stress was almost independent of the pH in the range pH 2 to 6, and slightly lower than without Fe additive (Fig. 5.3-1). With the increase of pH, the repulsion between clay particles became strong that the originally connected particles started to be disconnected. Hence, the increase of the pH resulted in a rapid decrease of the Bingham yield stress.

CHAPTER 9 - CONCLUSIONS

The sedimentation behavior of kaolinite suspensions, treated with $Na_4P_2O_7$ to have negative charges both on the faces and on the edges of the particles, was studied. When such suspensions were mixed with unaged or with aged Fe or Al electrolytes, the sedimentation behavior could be classified into three categories: (1) accumulation sedimentation; (2) flocculation sedimentation; and (3) mixed accumulation-flocculation sedimentation.

The technique of supercritical drying with liquid CO_2 was successfully applied at elucidating the structure of the corresponding sediments. The most striking result was achieved with the flocculated sediments. These sediments were shown to be comprised of a network with a fractal character, illustrated by micrographs made in the SEM. In this network, an edge to edge (EE) association of the particles was frequent.

The accumulated sediments were comprised, either of a random accumulation of individual kaolinite particles, or of an accumulation of dense aggregates mostly made by face to face (FF) association of the clay particles. The randomly accumulated sediments formed when the Fe or the Al electrolyte concentration was low, while the packed accumulated sediment formed with a sufficiently high Fe electrolyte concentration.

The mixed accumulated-flocculated sediments were comprised of two layers, one with an accumulated structure at the bottom, the other with a fractal flocculated structure on top of the first layer.

Similarly, the sedimentation behavior of montmorillonite suspensions mixed with Fe or Al electrolytes, or with hydroxoferric particles, could also be classified into accumulation sedimentation or flocculation sedimentation. The flocculated sediments also had a fractal type network.

Physical chemical data, especially about the zeta potential, showed that the above results were at least in qualitative agreement with the DLVO theory. The Fe^{3+} or the Al^{3+}

cations and their hydrolysis products, acted as counterions for the negatively charged clay particles. They compressed the electrical double layer of the clay and made it possible for flocculation to occur. However, at high Fe or Al electrolyte concentrations, an Fe or an Al product deposited on the clay particles. These coatings changed the sign of the clay particles from a negative one to a positive one. They also helped to link the clay particles to each other with an intermediate Fe or Al gel cement.

In the cases where the kaolinite particles had opposite charges on the edges and on the faces, the traditional cardhouse structure often considered in theory was not really observed. Instead, a bookhouse structure could be observed. This structure was comprised of domains where the kaolinite particles were associated in the FF mode, while the domains were themselves associated by the EF or the EE mode.

In the treatment of oil sands tailing sludge, not only the sediment volume should be small but also solid particles should settle fast. The present study showed that the addition of ferric electrolytes up to a certain concentration can result in packed accumulation sedimentation. This kind of sedimentation produces a small sediment volume relatively quickly. Hence, it could be efficient to treat oil sands tailing sludge with a sufficient concentration of ferric electrolytes. The oil sands tailing sludge in Alberta is a complex system comprised of kaolinite as one main component, while the presence of montmorillonite or illite is controversial. In this thesis, kaolinite and montmorillonite were extensively studied. Illite should also be investigated in future work. In order to approach a real oil sands tailing sludge system, more attention should be addressed to different multiple components systems, such as kaolinite-montmorillonite-Fe electrolytes, and kaolinite-montmorillonite-illite-Fe electrolytes. The interactions between different types of clay particles play an important role in sedimentation behavior and microstructure formation in such systems. Understanding this role may provide a more efficient and economical way to treat the oil sands tailing sludge.

CHAPTER 10 - REFERENCES

1 - Zou, J. (1991) "*Colloidal Study of a Montmorillonite-Fe-Water Oil Sands Sludge Model* ", MSc, University of Alberta.

2 - Greenland, D.L. (1975) Charge characteristics of some kaolinite-iron hydroxide complexes: *Clay Miner.*, **10**: 407-416.

3 - Rengasamy, P. and Oades, J.M., (1977), Interaction of monomeric and polymeric species of metal ions with clay surfaces. I. Adsorption of iron(III) species; II. Changes in surface properties of clays after addition of iron(III): *Aust. J. Soil. Res.*, **15**: 221-242.

4 - Camp, F.W., (1976) "Processing Athabasca tar sands- Tailing disposal", 26th Canadian Chemical Engineering Conference, Toronto.

5 - Kessick, M.A. and Jobson, A.M., (1977) "Clay tailing from Alberta oil sands and other sources: A review", Alberta Environment Report.

6 - Mackinnon, M.D. and Retallack, J.T. (1982) "Preliminary characterization and Detoxification of tailings pond water at the Syncrude Canada Ltd. Oil Sands Plant", in "*Land and water issues related to energy development* ", 4th Conference, Denver, Colorado, 1981, Ed. Rand, P.J., Ann Arbor Science, 185.

7 - Kasperski, K.L., (1988) "*Studies of the Physical Chemistry of Clays* ", Ph.D. Thesis, The Department of Chemistry, University of Alberta.

8 - C-H Synfuels Limited, (1984) "Dry tailings disposal from oil sands mining", Unpublished report, Industrial Programs Branch, Environmental Protection Service, Environment Canada.

9 - Hardy Association Ltd., (1979) "Athabasca oil sands tailings disposal beyond surface mineable limits", Alberta Environment Report.

10 - Hiemenz, P.C. (1977) "*Principles of Colloid and Surface Chemistry* ", Marcel Deker, Inc., New York and Basel.

11 - van Olphen, H. (1987) "Dispersion and Flocculation" in "*Chemistry of clays and clay minerals* ", ed. Newman, A.C.D., Longman Scientic & Technical, Mineralogical Society, pp. 203-224.

12 - Pierre, A.C. (1992) "*Introduction aux procédés Sol-Gel* ", Septima, Paris.

13 - Flory, J.P. (1953) "*Principles of Polymer Chemistry* ", Cornell University Press., Ithaca, New York.

14 - Masliyah, J.H. [1994], "*Electrokinetic transport Phenomena*", Aostra technical publication, Edmonton.

15 - Derjaguin, B.V., Churaev, N.V., and Miller, V.M. (1987) "*Surface Force* " Consultants Bureau, New York, NY.

16 - Verwey, E.J.W. and Overbeek, J.Th.G. (1948) "*Theory of the Stability of Lyophobic Colloids* ", Elsevier, New York, NY.

17 - Overbeek, J.Th.G. (1982) "Colloids, a fascinating subject: Introductory lecture" in "*Colloidal Dispersion* ", Goodwin, J.W., Ed., Special publication 43, Royal Society of Chemistry, London.

18 - Hunter, R.J., (1982), "*Zeta Potential in Colloid Science* " Academic Press Inc, San Diego.

19 - Hunter, R.J. (1987) "*Foundations of Colloid Science* ", Clarendon Press, Oxford.

20 - Gouy, J., (1910) Sur la constitution de la charge electrique à la surface d'un electrolyte, *J. Phys* ., **9**: 457-467.

21 - Chapman, D.L. (1913) A contribution to the theory of electrocapillarity, *Phil. Mag*., 25(6):475-481.

22 - Shaw, D.J. (1980), "*Introduction to Colloid and Interface Chemistry*, Butterworths, 3rd. Ed., London

23 - Stern, O. [1924], Zur Theorie der electrolytischen doppelschicht, *Zeitschrift fur Elecktrochemie*, **30**: 508-517.

24 - Adamson, A.W., (1982) "*Physical Chemistry of Surfaces* " 4th Ed..John Wiley & Sons, New York.

25 - Grahame, D.C., (1947) The electrical double layer and the theory of electrocapillarity, *Chem. Rev.*, **41**: 441-501.

26 - Bockris, J. O'M., Devanathan, M.A.V., and Muller, K., (1963) On the structure of charged interface, *Proc. Roy. Soc. London* (Series A), **274**: 55-79.

27 - van Olphen, H. (1977) "*Introduction to Clay Colloid Chemistry* ", 2nd ed. New York, John Wiley & Sons.

28 - Hogg, R., Healy, T.W., and Fuerstenau, D.W., (1966) Mutual coagulation of colloidal dispersions, *Trans. Faraday Soc.*, **62**: 1638-1651.

29 - Wang, G.T (1990) " *The Sability of Colloidal Systems*" , Scientific Publication (In Chinese).

30 - Wiese, G.R. and Healy, T.W., (1970) *Trans. Faraday Soc.*, **66**: 490.

31 - Kar, G., Chander, S., and Mika, T.S. (1973] The potential energy of interaction between dissimilar electrical double layers, *J. Colloid. Interface Sci.*, **44**: 347-355.

32 - Hench, L.L. and West, J.K. (1990) The sol-gel process, *Chem. Rev.*, **90**: 33-72.

33 - Stauffer, D., Coniglio, A., and Adam, M. (1982) " Gelation and Critical Phenomena" in "*Advances in Polymer Science 44* ", Springer-Verlag Berlin Heidelberg, pp. 103-158.

34 - Mandelbrot, B.B. (1977) "*Fratals: Form, chance and dimension* ", W.H. Freeman, San Fransiso.

35 - Chander, S. and Hogg, R. (1987) "Sedimentation and consolidation in destabilized suspensions" in "*Flocculation in biotechnology ans separation system* ", proceedings of the international symposium on flocculation in biotechnology and saparation systems, San Francisco, July, 1986, ed. Attia, Y.A., Elsevier, Amsterdam, pp. 279-286.

36 - Pierre, A.C (1992) The gelation of colloidal platelike particles, *J. Canadian Ceramic Soc.*, **61**: 135-138.

37 - Mandelbrot, B.B. (1990) "Fractal geometry: what is it, and what does it do?" in "*Fractals in the natural science*", Ed. Fleischmann, F.R.S., Tildesley, D.J., and Ball, R.C., Princeton University Press, NJ, USA,

38 - Pfeifer, P. and Avnir, D. (1983) Chemistry in noninteger dimensions between two and three. I. Fractal theory of heterogeneous surfaces, *J. chem. Phys.*, **79**: 3558-3565

39 - Jullien, R. and Botet, R. (1987) "*Aggregation and fractal aggregates* ", World Scientific Publishing Co Pte Ltd, Singapore.

40 - Brinker, G.J. and Scherer, G.W. (1990) "*Sol-gel Science* ", Acasemic Press, Inc., U.S.A.

41 - Meakin, P. (1983) Diffusion-controlled cluster formation in two, three, and four dimensions, *Phy. Rev. A* , **27**: 604-607.

42 - Michaels, A.S. and Bolger, J.C. (1962) Settling rates and sediment volumes of flocculated kaolin suspensions, *I & FC Fundam.*, **10**: 24-33

43 - R. Buscall and L.R. White, (1987) The consolidation of concentrated suspensions: Part 1. - The theory of sedimentation, *J. Chem. Soc., Faraday Trans. I* , 873-891

44 - Moore, F. (1965) "*Rheology of Ceramic Systems* ", Maclaren & Sons, Ltd., London.

45 - Michaels, A.S. (1958) "Rheological Properties of Aqueous Clay Systems" in "*Ceramic Fabrication Processes*", ed. Kingery, W.D., MIT and John Wiley & Sons, Inc., New York, pp. 23-30.

46 - Frisch H.L. and Simha R. (1956), The viscosity of Colloidal Suspensions and Macromolecular solutions", in *Rheology*, vol. 1, F.R. Eirich, ed., Academic Press, New-York, pp. 525-613

47 - Kingery, W.D., Bowen, H.R., and Uhlmann, D.R. (1976) "*Introduction to Ceramics* ", 2nd ed., John Wiley & Sons, New York.

48 - Brindley, G.W. (1958) "Ion exchange in clay Minerals" in "*Ceramic Fabrication Processes*" ed.W.D. Kingery, MIT and John Wiley & Sons, Inc., New York, pp. 7-22.

49 - Worrall, W.E. (1986) "*Clays and Ceramic Raw Materials* ", 2nd ed. Elsevier Applied Science Publishers, London and New York.

50 - Durrant P.J. (1964), "*General and Inorganic Chemistry* ", 3rd Edition, Longmans, Green and Co. Ltd., London

51 - Bennett, R.N. and Hulbert, M.H. (1986) "*Clay Microstructure*", International Human Resorces Development Corporation.

52 - Goldberg, S and Glaubig, R.A., (1987) Effect of saturating cation, pH and aluminium and iron oxide on the flocculation of kaolinite and montmorillonite, *Clays & Clay Min.* **35**: 220-227.

53 - Williams, D.J.A. and Williams, K.P. (1978), Electrophoresis and zeta potential of kaolinite, *J. Colloid and Interface Sci.*, **245**: 645-662.

54 - Yong, R.N. and Ohtsubo, M. (1987) Interparticle action and rheology of kaolinite-amorphous iron hydroxoide (ferrihydrite) complexes, *Appl. Clay Sci.*, **2**: 63-81

55 - Newman, A.C.D., (1987) "The interaction of water with clay mineral surfaces" in "*Chemistry of clays and clay minerals* ", ed. A.C.D. Newman, Longman Scientic & Technical, Mineralogical Society, pp. 237-274.

56 - N. Street, N., (1956) The rheology of kaolinite suspensions, *Australian J. Chem.*, **9**: 467-479.

57 - Thiessen, P.A., (1947) Kennzeichnung submikroskopischer grenzflächenbereiche verschiedener wirksamkeit, *Z. Anorg. Chem.*, **253**: 161-169.

58 - Méring, J., Mathieu-Sicaud, A., and I. Perrin-Bonnet, I., (1953) Fixation des particules d'or colloidal sur la kaolinite, *Compt. rend. congr. Geol. Int. Alger* , 1952, section 18, pp.103-107.

59 - Schofield R.K. and Samson, H.R.(1954), Flocculation of kaolinite due to the attraction on oppositely charged crystal faces: *Discuss. Faraday Soc.*, **18**: 135-145.

60 - Rand, B. and Melton, I.E. (1977) Particle interactions in aqueous kaolinite suspension, I; II; *J. Colloid and Interface Sci.*, **60**: 308-320.

61 - Ohtsubo, M., Yoshimura, A., Wada, S., and Young, R.N. (1991) Particle interaction and rheology of illite-iron oxide complexes, *Clay & Clay Min.*, **39**: 347-354.

62 - Avena, M.J., Cabrol, R., Pauli, C.P.D., (1990), Study of some physicochemical properties of pillared montmorillonites: Acid-base potentiometric titrations and electrophoretic measurements, *Clay & Clay Min.* **38**: 356-362.

63 - Flegmann, A.W. (1969) Rheological studies on kaolinite suspensions, *Proc. Br. Ceram. Soc.*, pp.31-45

64 - Tateyama, H, Hirosue, H., Nishimura, S., Tsunematsu, K. Jinnai, K., and K. Imagama, K., (1988) "Theoretical aspects of interaction between colloidal particles with various shapes in liquid" in "*Untrastructure Processing of Advanced Ceramics*". ed. J.D. Mackenzie and D.R. Ulrich, John Wiley & Sons, pp.453-461.

65 - Gaudin, A.M., Fuerstenau, M.C., and Mitchell, (1959), Effect of pulp depth and initial pulp density in batch thickening, *Min. Eng.*, **11**: 613-616.

66 - Zou, J. and Pierre, A.C., (1992) SEM observation of "card-house" structures in montmorillonite gels, *J. Mater. Sci. Lett.*, **11**: 664-666.

67 - Chen, J.S., Cushman, J.H., Low, P.F., (1990), Rheological Behavior of Na-montmorillonite suspensions at low electrolyte concentration, *Clay & Clay Min.*, **38**: 57-62.

68 - Henry, M., Jolivet, J.P., and Livage, J., (1990), Aqueous chemistry of metal cation: hydrolysis, condensation, and complexation, *Structure and Bonding* , **25**: 1-64

69 - Livage, J., Henry, M., and Sancgez, C., (1988) Sol-gel chemistry of transition metal oxides, *Prog. Solid State Chem.*, **18**: 259-374.

70 - Baes, C.F. Jr and Mesmer, R.E. (1976) "*The hydrolysis of cations*", John Wiley & Sons, New York.

71 - Schneider, W., (1984) Hydrolysis of ion(III) - Chaotic versus Nucleation, *Comments Inorg. Chem.*, **3**: 205-223

72 - Sylva, R.N. (1972) "The Hydrolysis of Iron(III)", *Rev. Pure and Appl. Chem.*, **22**: 115-132.

73 - Thomas, G. W., and Swoboda, A.R., (1962) Cation exchange in Kaolinite-iron oxide system,*Clay & Clay Min.* **10**: 321-326.

74 - Blackmore, A.V., (1973), Aggregation of clay by the products of iron(III) hydrolysis: *Aust. J. Soil Res.*, **11**: 75-82

75 - Rengasamy, P. and Oades, J.M., (1978), Interaction of monomeric and polymeric species of metal ions with clay surfaces. III. Aluminium(III) and Chromium(III): *Aust. J. Soil. Res.*, **16**: 53-66.

76 - Oades, J.M., (1984), Interaction of polycations of aluminum and iron with clays, *Clay & Clay Min.*, **32**: 49-57.

77 - Greenland, D.L., and Oades, J.M., (1968) Iron Hydroxides and clay surfaces, *Trans. 9th Int. Congr. Soil Sci.*, **Vol.I**: 657-668.

78 - El-Swaify S.A. and Emerson W.W. (1975), "Changes in the physical properties of soil clays due to precipitated aluminum and iron hydroxides: I: Swelling and aggregate stability after drying", *Soil Sci.*, **39**:1056-1063.

79 - Hsu, P.H., (1992) Reaction of OH-Al polymer with smectites and vermiculites: *Clays & Clay Min.*, **40**: 300-305.

80 - Sloan, R.L. and Kell, T.R. (1966) The frabic of mechanically compacted kaolin, *Clay & Clay Min.*, **14**: 289-296.

81 - Smalley, L.J. and Cabrera, J.G. (1969) Particle association in compacted kaolin, *Nature*, **222**: 80-81.

82 - C.F. Moon, C.F., (1972) The microsdtructure of clay sediments, *Earth-science Reviews*, **8**: 303-321.

83 - Lambe, T.W. (1958) (1) The Structure of compacted clay; (2) The engineering behavior of compacted clay , *Journal of the Soil Mechanics and Foundation Division, Proceedings of the American Society of Civil Engineerings*, **v.84**: pp.1654-1 to 1654-34; pp.1655-1 to 1655-35

84 - Terzaghi, K. (1925) "*Erdbaumechanik auf bodenphysikalischer grundlage* ", Leipzig und Wien, Franze Dutike.

85 - Casagrande, A., (1932), The structure of clay and its importance in foundation engineering, *Journal of the Boston Society of Civil Engineers*, pp. 168.

86 - Aylmore, L.A.G. and Quirk, J.P. (1960) Domain or turbostratic structure of clays, *Nature*, **187**: 1046-1048.

87 - Sides, G. and Barden, L. (1971) The microstructure of dispersed and flocculated samples of kaolinite, illite, and montmorillonite, *Canadian Geotechnical Journal*, **8**: 391-399.

88 - O'Brien, N.R. (1971) Fabric of kaolinite and illite floccules, *Clay & Clay Min.*, **19**: 353-359

89 - Ingles, O.G. (1968) "Soil chemistry relevant to the engineering behavior of soils" in "*Soil Mechanics-Selected Topics* ", ed. by Lee, I.K., New York, Elservier, pp.1-57.

90 - Pusch, P. (1970) Microstructural changes in soft quick clay at failure, *Canadian Geotechnical Journal*, **7**: 1-7.

91 - O'Brien, N.R., (1972) Microstructure of a laboratory flocculated illitic sediment, *Can. Geothech. J.*, **9**: 120-2 .

92 - Smart, P and Tovey, N.Y. (1982) "*Electron microscopy of soils and sediments: samples* ", Clarendon Press, Oxford.

93 - Tovey, N.K., (1971) Soil structure analysis using optical techniques on scanning electron micrographs, in *Proc. 4 SEM symp. IIT Research Institute*, Chicago, pp.49-56.

94 - Tovey, N.K., (1970) Electron microscopy of clays, Ph.D. thesis, Cambridge.

95 - Tovey, N.K., (1971) Discussion to session 1. Stress-strain behavior of soils, *Proc. Roscoe Mem. Symp.* (ed. R.H.G. Parry), pp.116-20.

96 - Green-Kelly, R., (1972), The application of modern structure method to clay soil, *Br. Soc. Soil Sci.*, **2**: 43-52.

97 - Gillott, J.E. (1969) Study of the fabric of fine-grained sediments with the scanning electron microscope, *J. Sedi. Petrol.*, **39**: 90-105.

98 - Luyet, B.J. (1960) "On the Mechanism of growth of ice crystals in aqueous solutions and on the effect of rapid cooling in hindering crystallization" in *Recent Research in Freezing and Drying*, ed. A.S. Parkes and A.U. Smith, , pp. 3-22.

99 - H.T. Meryman, H.T., (1957) Physical limitation of the rapid freezing methods, *Proc. R. Soc.B*, **147**: 452-9.

100 - Higuchi, K., (1964), Tyndall figures formed in crystallographic plane perpendicular to basal plane of ice crystals, *Nature*, **202**: 485-487.

101 - Lincoln, J. and R. Tettenhorst, R. (1971) Freeze-dried and thawed clays, *Clay & Clay Miner.*, **19**: 103-7.

102 - Rosenqvist, I.T., (1959) Physico-chemical properties of soils: mechanical properties of soil water systems, *Trans. Am. Soc. civ. Engrs.*, **126**: 745-67.

103 - Mikula R.J., Payette C., Munoz V., Lam W.W., (1991) "Microscopic observation of structure in oil sands sludge", Conference of the Petroleum Society of CIM and AOSTRA, AOSTRA 91-120, pp.1-9.

104 - Naymik, T.G., (1974) "The Effects of drying techniques on clay-rich soil texture" in Proceedings of the 32 Annual Meeting of the Electron Microscopy Society of america, C.J. Arceneaux ed., St Louis, Missouri, Clayton Publishing Division, Baton-Rouge, Louisiana, pp. 446-467.

105 - Kistler, S.S, (1932) Coherent expanded aerogels, *J. Phys. Chem.*, **36**: 52-64.

106 - Bhasin, R.N, (1975), Pore size distribution of compacted soils after critical region drying, National Tech. Inf. ser., US Department of commerce, Springfield, VA.

107 - McHugh, M.A. and Krukonis, V.J. (1968) "*Supercritical Fluid Extraction* ", Butterworth.

108 - Gillott, J.E, (1968) "*Clay in Engineering Geology* ", Elsevier, Amesterdam.

109 - Tovey, N.K. and Wong, K.Y., (1973) The preparation of soils and other geological materials for the SEM, **vol.1**, pp.59-67, in *Proc. Int. Symp. Soil Struct. Geothenburg*, Swedish Geotechnical Society , Stockholm.

110 - Coleman, J., (1986), in "*Principles of analytical electron Microscope*", Joy, D.C., Romig, A.D., and Goldstein, J.L., Eds., Plenum Press, New-York, pp. 361-383.

111 - Mattiat, B., (1969), Eine methodz zur elektronenmikroskopischen untersuchung des mikrogefuges in toningen sedimenten, *Gel. Jber.*, **88**: 87-111.

112 - Stawinski, J., Wierzchos, J., and Garcia-Gonzalez, M.T., (1990) Influence of calcium and sodium concentration on the microstructure of bentonite anf kaolin, *Clay &Clay Min.*, **38**: 617-622.

113 - Smart, P and Tovey, N.Y. (1981) "*Electron microscopy of soils and sediments: techniques* ", Clarendon Press, Oxford.

114 - Lanier, W.P. and D.L. Jones, D.L., (1979) Scanning electron microscope (SEM) study of the texture relationships of kaolinite clay flocculated in increasingly saline solutions, *Scanning Electron Microscopy*, **vol.1** pp.525-530.

115 - N.R. OBrien, N.R. (1970) Clay flake orientation in flocculated illite- an electron microscope study, *Maritime Sediments*, **6**:79-80.

116 - Jernigan D.L. and Mcate, J.L., Jr, (1975) Critical point drying of electron microscope samples of clay minerals, *Clays &Clay Min.*, **23**: 161-162

117 - Georgia Kaolin Company, Inc., (1990), Information about properties of Hydrite UF kaolinite particles.

118 - Yaalon, D.H., (1976), "Calgon" no longer suitable, *Soil Sci. Soc. Am. J.*, **40**: 333

119 - Stöber, W., Fink. A., and Bohn, E., (1968) Controlled growth of monodisperse silica spheres in the micron size range, *J. Colloid and Interface Sci.*, **26**: 62-69

120 - Plitt, L.R. (1993) "*Mineral Processing* ", Text Book, Department of Mining, Metallurgical and Petroleum Engineering, University of Alberta.

121 - Schwertmann, U. and Taylor, R.M. (1989) "Iron oxides" in "*Minerals in Soil Environments* ", ed. Dixon, J.B. and Weed, S.B., Soil Sci. Soc. Am., Madison, WI, pp.379-427.

122 - Winter, H.H and Chambon, F. (1987) Analysis of linear viscoelasticity of a crosslinking polymer at the gel point, *J. of Rheology* , **30**: 367-382.

123 - Witten, T.A. Jr and Meakin, P. (1983) Diffusion limited aggregation at multiple growth sites, *Phys. Rev.* **B28**: 5632-5642.

124- Lambe,T.W. (1953) "The structure of inorganic soil" in "*Proceedings of the American Society of Civil Engineers* ", **v.79**, separate 315: pp.1-49

125 - Smoluchowski, M.Z., [1917] Versuch einer mathematischen theorie der koagulationskinetik kolloider losungen, *Z. Phy. Chem.* , **92**:129

126 - Matijetivic, E., Sapieszko, R.S. and Melville, J.B., (1975), Ferric hydrous oxide sols: I. Monodispersied basic iron(III) sulfate particles: *J. Colloid Interface Sci.*, **50**: 567-581

127 - Segal, D.L., (1984) Time-dependent properties of colloidal dispersions of ferri-hydroxy polycations, *J. Chem. Tech. Biotechnol* , **34A**:355-362

128 - Ma, K. and Pierre, A.C. (1992) "Packing patterns in clay colloids" in "*Ceramics adding the value* ", Proceedings of the international ceramic conference, **Vol.1**, Australia.

129 - Ma, K. and Pierre, A.C. (1992) Sedimentation behavior of a fine kaolinite in the presence of fresh Fe electrolyte, *Clay & Clay Min.*, **40**: 586-592.